Study of Supersonic Nozzle Flows in Low-pressure Environments: Starting Jets and Lunar Plume-Surface Interactions

Ziqu Cao

Submitted in fulfilment of the requirements for the degree of
Doctor of Philosophy

Aerospace Science
James Watt School of Engineering
College of Science & Engineering
University of Glasgow

May, 2023

Declaration

I confirm that this thesis presented for the degree of Doctor of Philosophy of Aerospace Science, has

- been composed entirely by myself
- been the result of my own work
- not been submitted for any other degree or professional qualification

Ziqu Cao
May 17, 2023

Abstract

Supersonic nozzle flows play an important role in aerospace engineering, e.g. controlling motions, attitudes, and orbits of space vehicles using various propulsion systems. Supersonic nozzle flows include free nozzle flows and restricted nozzle flows, such as plume-surface interactions if a surface obstructs the flow propagation.

When compressed gas is discharged from a nozzle into a low-pressure environment in the case of free nozzle flows, the shock wave diffracts around the nozzle lip and a vortex loop forms. These phenomena have attracted much attention in the continuum flow regime, but how the shock diffraction and vortex behave under rarefied flow conditions has received less attention. Understanding transient flow in rarefied conditions is helpful for increasing thrust vector control and avoiding potential contamination and erosion of spacecraft surfaces.

Furthermore, comprehending plume-surface interactions is critical for the design of lander modules and future bases on bodies such as the moon, as it is necessary to anticipate surface erosion patterns and the transport of displaced regolith material. Extraterrestrial conditions are difficult to recreate experimentally (e.g. the effects of low gravity, strong radiation and extreme temperature difference). Available numerical techniques for modelling regolith entrainment and subsequent movement suffer from limited accessibility and different levels of sophistication.

In this thesis, a design for an open-ended shock tube connected to a vacuum chamber is presented. This is used to release a shock wave into a low-pressure environment and study the subsequent vortex ring formation as the gas diffracts around the shock tube exit. Schlieren visualisation and pressure measurements of the vortex ring formation are conducted. The flow structure degenerates through a decrease in the strength of the embedded shock waves and an increase in their thickness, and the counter-rotating vortex ring when the environmental pressure decreases. The existence of the vortex ring is confirmed through spectral analysis when the environmental pressure is as low as 1.0 kPa.

Due to limitations with experimental measurement equipment and techniques, the shock wave diffraction problem should be complemented with numerical techniques. A program to generate ensemble-averaged direct simulation Monte Carlo (DSMC) results is designed. Computational

fluid dynamics (CFD) and ensemble-averaged DSMC methods are implemented to simulate the formation of a two-dimensional vortex loop due to shock wave diffraction around a 90° corner. The influence of the Mach number and rarefaction on the development and growth of the vortex loop are studied. A concept, called rorticity, was used to investigate the transient structures of vortex loops. The simplification of the internal structure of vortex loops and postponement of the vortex loop formation due to the increase of the rarefaction level are confirmed. Two properties from the decomposition equation of vorticity to quantify the vortex strength; rorticity flux (i.e. representing the vortex rotational strength), and the shear vector flux (i.e. representing the vortex shear movement strength), are derived. A mutual transformation relationship between the rorticity and shear vectors has been identified, suggesting that this concept can be employed to better explain vortex flow phenomena. It is found that the increase of the Knudsen number thickens the Knudsen layer, causing the failure of the generation of the vortex sheet and the subsequent formation of vortex loops.

A new solver based on *dsmcFoamPlus – rarefiedMultiphaseFoam*, is developed for solving rarefied multiphase flows. The solver is extended to include a two-way coupling model and a particle phase change model. Additionally, the solid stochastic collison model and the multiphase particle-in-cell (MPPIC) method for solving dilute and dense granular flows, respectively, have been implemented in the new solver. The models mentioned are rigorously benchmarked against analytical solutions and previous results in the literature. The benchmarking results of the two-way coupling method show excellent agreement with analytical results. The results of a reproduced uniform gas-solid flow and a purely gravity-controlled granular flow sedimentation agree well with previous numerical results in the literature. A solid particle is allowed to experience a physical and continuous phase change and diameter variation using the updated phase change model.

Finally, the *rarefiedMultiphaseFoam* solver is used to simulate two lunar plume-surface interaction (PSI) cases using the stochastic collision model and the MPPIC method, respectively. Both methods are applied to a scaled down version of the Apollo era lunar module descent engine and comparisons are made between the two simulation results. The results show that the transient effects are essential to both the gas and solid phase evolution and the entrained dust particles significantly influence the evolution of the gas flow. In the PSI simulations, the MPPIC method is more reliable than the stochastic collision method because it takes enduring contacts and the close-packing limit into account. Furthermore, it is identified that the breakdown of the locally free-molecular flow assumption has a significant impact on the solid particle temperatures.

Acknowledgements

Words cannot express my gratitude to my supervisors, Prof. Konstantinos Kontis and Dr. Craig White, for their timely guidance, advice, patience, support and encouragement over the last three and a half years. Thanks all the things, including the experiment design, the usage of a Linux system, programming of OpenFOAM, and paper writing you have taught me. It is my honor and fortune to be your Ph.D student.

Prof. Hosano Hamid, who works at the University of Kumamoto University, has been helpful in the advice of the design of the shock tube during my first year and thanks to Dr. Muhammed Burak Agir for teaching me the basic installation and usage of OpenFOAM and the collaboration of programming in OpenFOAM. A special thanks to Dr Guoshuai Li, who was a PhD student of Prof. Kontis and graduated from the University of Glasgow in 2020, for the introduction of the lab and the schlieren imaging system. I am also grateful to Dr. Senthilkumar Subramanian, Mr. Ting Tsung Chang and Ms. Gaargi Jain for setting up the Schlieren system and the help of the experiments. Thanks all in Room 734 in the James Watt South building for the helps and joys. Also, thanks to the difficulties I faced that force me to become stronger and more confident during this PhD project.

I would like to thank my family, who have supported me emotionally and financially without any hesitation throughout my whole life and education, and especially, my wife, Ms Danqing Xu, who married me in Jan 2021 and quit her high-paying job and came to Glasgow to offer accompany and support to me during the third year of my research. I could not have undertaken this journey without them. Finally, I would like to remember my maternal grandfather and uncle, who passed away when I was in the United Kingdom. I regret that I was unable to go back to China to mourn during the COVID-19 pandemic.

Ziqu Cao
May 17, 2023

Contents

List of Tables

List of Figures

Nomenclature

Symbols

α	the fraction of gas atoms which experience isothermal diffuse reflection in the $(1-\varepsilon)$ fraction of incident atoms in Equation 4.1 and 4.2	
β	shock wave angle in Equation 2.1/ a constant in Equation 4.47/ an index in Equation 4.11	
χ	polar angle	rad
δ	deflection angle	rad
$\dot{m}$	mass erosion rate	$\mathrm{kg\,s^{-1}\,m^{-2}}$
Γ	circulation	$\mathrm{m^4\,s^{-1}}$
γ	ratio of specific heat	
Λ	number of degrees of freedom of a gas molecule	
λ	gas mean free path	m
μ	dynamic viscosity	$\mathrm{Pa\cdot s}$
Ω	solid angle	rad
Φ	flux of a property	
ϕ	angle in Figure 4.3	rad
ρ	density	$\mathrm{kg\,m^{-3}}$
a	speed of sound	$\mathrm{m\,s^{-1}}$
E	kinetic energy of a vortex ring	J
I	hydrodynamic impulse of a vortex ring	$\mathrm{m^3\,s^{-1}}$

p	component of relative velocity in a relative coordinate system	$\mathrm{m\,s^{-1}}$
U	propagation speed of a vortex ring	$\mathrm{m\,s^{-1}}$
σ	collision cross-section	
τ	stress	
$\mathbf{T}$	rotation matrix	
θ	volume fraction	
υ	kinematic viscosity	$\mathrm{m^2\,s^{-1}}$
ε	the fraction of specularly reflected gas atoms among the incident atoms in Equation 4.1/ a small value on the order of 10^{-7} in Equation 4.47	
φ	azimuthal angle	rad
φ_0	repose angle of soil	rad
$\vec{\omega}$	vorticity	$\mathrm{m^2\,s^{-1}}$
$\vec{a}$	discrete particle acceleration	$\mathrm{m\,s^{-2}}$
$\vec{e}$	a random vector sampled from a unit sphere	
$\vec{F}$	external force per unit mass in Equation 3.1/momentum transfer rate in Equation 4.1 and 4.3	N
$\vec{g}$	gravitational acceleration	$\mathrm{m\,s^{-2}}$
$\vec{p}$	relative velocity in local coordinate system	$\mathrm{m\,s^{-1}}$
$\vec{R}$	rorticity	$\mathrm{m^2\,s^{-1}}$
$\vec{r}$	position vector	m
$\vec{S}$	shear vector	$\mathrm{m^2\,s^{-1}}$
$\vec{v}$	velocity vector	$\mathrm{m\,s^{-1}}$
ξ	strain rate	
A	surface area or surface of a function integrated over	$\mathrm{m^2}$
a	thermal accommodation coefficient of a solid particle/a fractional coefficient in Equation 5.3	
Ac	acoustic number	

b	impact parameter	
$bins$	the number of bins in the histogram	
c_p	solid specific heat capacity	$\mathrm{J\,kg^{-1}\,K^{-1}}$
c_v	gas specific heat capacity at a constant volume	$\mathrm{J\,kg^{-1}\,K^{-1}}$
d	diameter	m
e	energy of an individual gas atom/molecule	J
E_ρ	fractional error of the volume-averaged density	
E_p	fractional error of the volume-averaged pressure	
E_T	fractional error of the volume-averaged temperature	
E_u	fractional error of the volume-averaged velocity	
f	particle velocity distribution function/ a sign of function if in the form of $f()$	
H	nozzle exit altitude	m
h	semi-height of a 2D nozzle	m
k_B	the Boltzmann constant	$\mathrm{m^2\,kg\,s^{-2}\,K^{-1}}$
Kn	Knudsen number	
L	characteristic length in Equation 1.1/path of a function integrated over in Equation 3.17	m
M	number of samples	
m	atom/molecule mass or mass of a solid particle if a subscript p is added	kg
Ma	Mach number	
N	number of computational particles	
n	number density	$\mathrm{m^{-3}}$
N_A	Avogadro constant	
p	scalar pressure	Pa
P_s	constant in Harris and Crighton model	

Q	heat transfer rate	$\mathrm{J\,s^{-1}}$
R	radius	m
r	atom/molecule radius or solid particle radius if a subscript p is added	m
r_1	the ratio of crystallization front radius to the solid particle radius	
R_f	random number between 0 to 1	
r_{32}	the Sauter mean radius	
Re	Reynolds number	
T	temperature	K
t	time	s
t_0	time when the vortex loop formed	s
$t_{s,0}$	time when the shock wave reaches the 2D nozzle exit	s
U	normal velocity component in the normal coordinate system	$\mathrm{m\,s^{-1}}$
u, v, w	velocity vector component in x, y, z direction of cartesian coordinate system	$\mathrm{m\,s^{-1}}$
V	tangential velocity component in the normal coordinate system	$\mathrm{m\,s^{-1}}$
W	number of actual particles represented by a computational particle	
x, y, z	spatial cartesian coordinate	m
e	restitution coefficient	
V	volume	$\mathrm{m^3}$

Superscripts

$*$	post-collision property
$-$	arithmeric average
loc	property in local coordinate system
$[r]$	property in a $X^{[r]}Y^{[r]}Z^{[r]}$ coordinate system, which is transformed from the xyz cartesian coordinate system, where the fluid-rotational axis is parallel to the axis $Z^{[r]}$

Subscripts

∞	far field
b	background property
c	property in chamber of a thruster
$cell$	property of a cell
co	cohesive
cp	closed packing
D	solid particle damping
D'	"obtained by collapsing the velocity dependence of particle distribution function to a delta function centered about the local mass-averaged particle velocity"
$drag$	property caused by drag force
eq	equivalent property
f	solid particle nucleation
G	solid particle return-to-isotropy
g	property of gas phase
G'	solid particle equilibrium isotropic
GLL	local gradient-length
i	index number
$inlet$	property at the inlet boundary
ip	inter-particle property
j	index number
L	property of liquid phase of solid particles
lp	liquid phase
m	solid particle equilibrium melting
max	maximum value
min	minimum value
n	property of a nozzle

$outlet$	property at the outlet boundary
p	property of a solid particle
ppc	particles per cell
R	property of rorticity
r	relative property
rot	local rotational property
S	property of shear vector
s	property of a shock wave
sel	selected property
sp	solid phase
ss	surface shear
$stag$	property at the stagnation point
T	transformed property with the same magnitude
t	local translational property
tot	total property
ts	threshold
vfc	vortex filament core
vr	vortex ring
w	weighted
x, y, z	vector component in x, y, z direction of cartesian coordinate system
$\vec{S}_T$	transformed shear vector
1	property before the shock wave or in the driven section of a shock tube before the rupture of the diaphragm
2	property after the shock wave
3	property after the contact surface
4	property in the driver section of a shock tube before the rupture of the diaphragm

exit property at the exit of a shock tube or a nozzle

Acronyms

BGK Bhatnagar, Gross, and Krook

CFD computational fluid dynamics

CPFD Computational Particle Fluid Dynamics

CRVR counter-rotating vortex ring

DAQ data acquisition

DDPM-KTGF Dense Discrete Phase Model incorporated with the Kinetic Theory of Granular Flow

DEM Discrete Element Method

DPM Discrete Phase Model

DSMC direct simulation Monte Carlo

HPC high performance computing

LEO low Earth orbit

MFP mean free path

MPPIC multiphase particle-in-cell

NSF Navier-Stokes-Fourier

NTC no time counter

OpenFOAM Open Field Operation and Manipulation

PC personal computer

PSI plume-surface interaction

List of publications

Journal articles:

- Z. Cao, C. White, K. Kontis. *Numerical investigation of rarefied vortex loop formation due to shock wave diffraction with the use of rorticity*. Physics of Fluids, 2021. 33(6): 067112. DOI: https://doi.org/10.1063/5.0054289
- Z. Cao, M.B. Agir, C. White, and K. Kontis, *An open source code for two-phase rarefied flows: rarefiedMultiphaseFoam*. Computer Physics Communications, 2022. p.108339. DOI: https://doi.org/10.1016/j.cpc.2022.108339
- Z. Cao, C. White, M. B. Agir, and K. Kontis, *Lunar plume-surface interactions using rarefiedMultiphaseFoam*, Frontiers in Mechanical Engineering, Frontiers, 2023, Vol 9, p. 2. DOI: https://doi.org/10.3389/fmech.2023.1116330
- Z. Cao, K. Kontis, H. Hosano, C. White, T. Chang, and M. B. Agir, *Vortex ring formation following shock wave diffraction in low-pressure environments*, Flow, Turbulence and Combustion, 2023, (Submitted)

Chapter 1

Introduction

1.1 Motivation

A supersonic nozzle flow is produced when a compressible gas flow passes through a nozzle and is accelerated to supersonic speed. Such applications, including free nozzle flows (i.e. free expansion flow), shown in Figure 1.1(a), and restricted nozzle flows (i.e. a surface exists downstream of the nozzle exit and impedes the flow from propagating freely), shown in Figure 1.1(b), play a fundamental and essential role in controlling the motions, attitudes, and orbits of space vehicles operating in rarefied conditions.

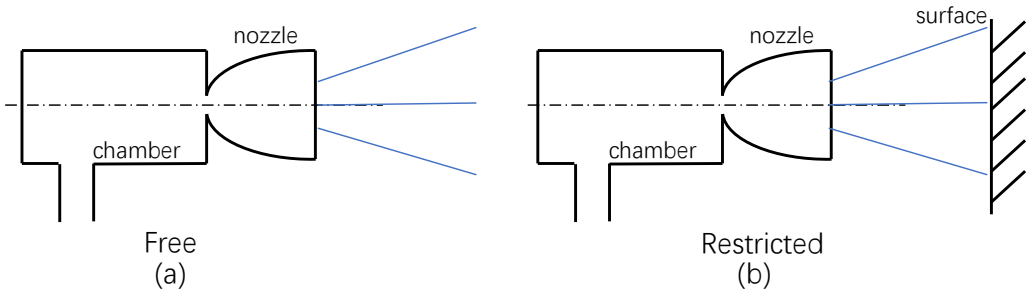

Figure 1.1: **Jet categories.**

Typical examples can be found not only in specialized propulsion systems of cost-effective micro-satellites that can provide thrusts in the micro- and milli-Newton range in low Earth orbit (LEO) for the purposes of earth observation, telecommunication, and navigation [1, 2], but also in the main thrusters of space stations and unmanned landing modules of sample return missions from the Moon [3], Mars [4] and asteroids [5].

When the nozzle operates in rarefied backflow condition, the physics of the flow ejected from a convergent-divergent nozzle cannot be fully and accurately described by the Navier-Stokes-Fourier (NSF) equations; rarefied and non-equilibrium gas dynamic effects must be considered. Rarefied gas dynamics is the study of gas where the local mean free path (MFP), noted as λ, is comparable to a characteristic length scale of the problem, L [6]. The rarefaction level is described by the Knudsen number Kn, expressed as

$$Kn = \frac{\lambda}{L}. \tag{1.1}$$

The flow from a nozzle in vacuum will experience a continuous change of Knudsen number regime from the continuum regime ($Kn < 0.001$) in the combustion or stagnation chamber, to the slip and transition flow regime ($0.001 < Kn < 10$) as the flow passes through the nozzle, and finally to the free-molecular regime ($Kn > 10$) when the flow is far away from the nozzle exit [7].

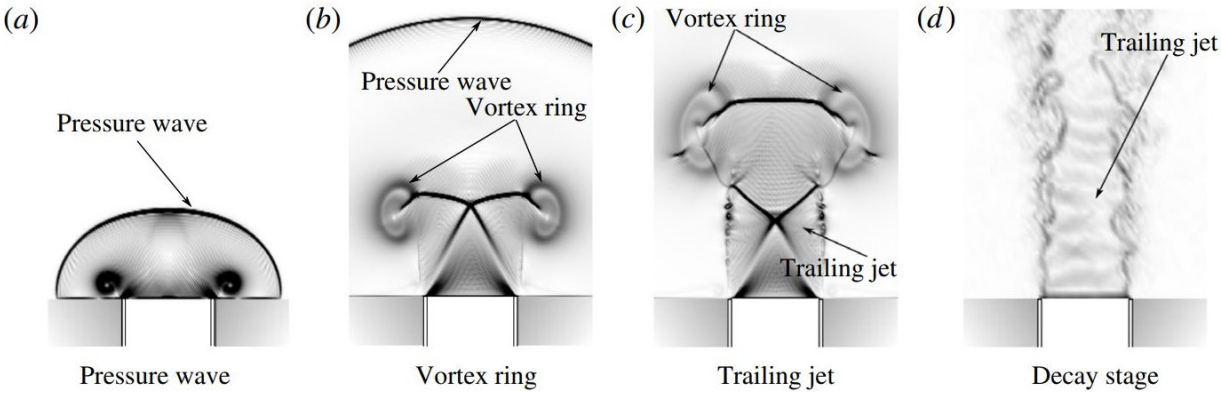

Figure 1.2: **Stages of a supersonic starting jet [8].**

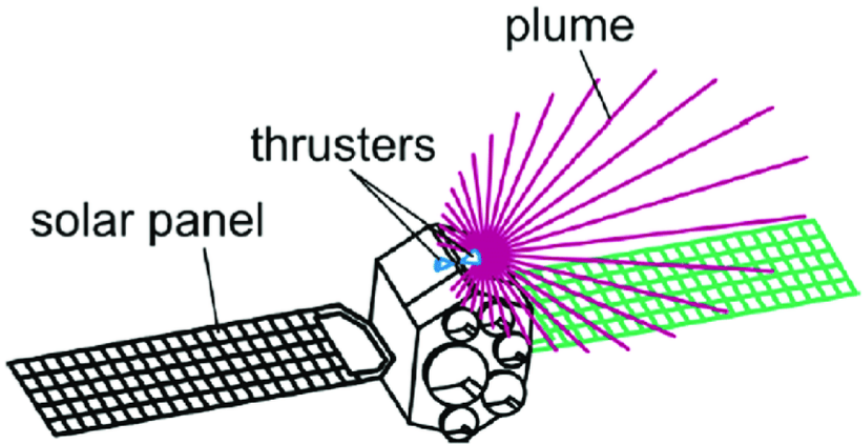

Figure 1.3: **Schematic of an exhaust plume interfering with the surfaces of a satellite [9].**

A supersonic starting jet is formed when the high-speed gas flow reaches the nozzle exit surface and experiences shock wave diffraction around the nozzle lip, with the potential to generate

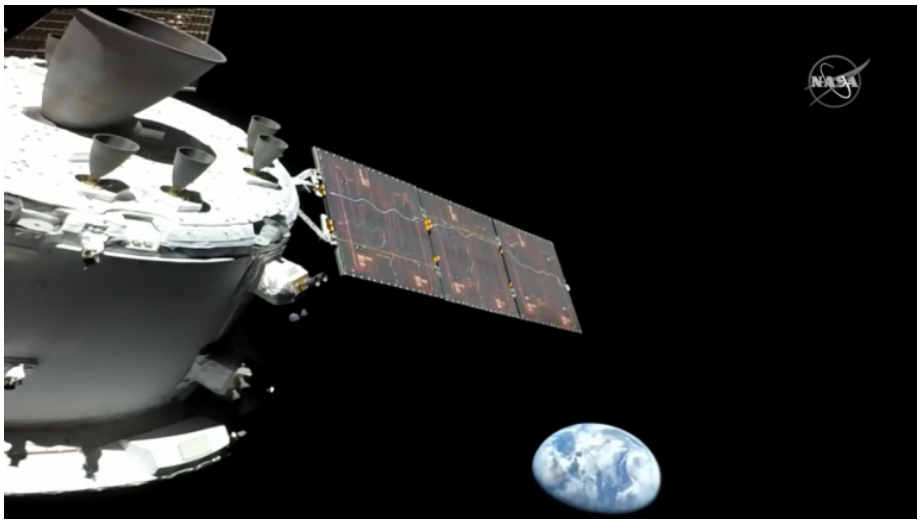

Figure 1.4: **Image of Artemis I Orion capsule [10].**

a vortex loop in a rarefied environment. An example under atmospheric conditions is shown in Figure 1.2. In general, three aspects of vortex loops have received attention; sound generation, transport and mixing, and vortex interactions [11]. First, the sound field created by the discharged gas flow is closely connected to the structure of the flow field (laminar/turbulent). The sound pressure level and sound frequency spectrum of the sound field created by a rarefied flow with a low Reynolds number is likely to be significantly different from those in the continuum regime, which could result in uncertain and unanticipated vibrations. Second, the flow discharged from the nozzle of liquid and solid rocket propulsion systems may comprise tiny solid particles and liquid droplets. With the aid of shock wave diffraction and the subsequent vortex loop, these particles and droplets may impact sensitive surfaces, see Figure 1.3. The impingement will pollute or degrade the surfaces of space vehicles, for example there have been reports of damage to the International Space Station [12] and satellites [13]. However, the evolution of this transient flow phenomenon remains unclear. Third, multiple thrusters are generally used at the same time in practice, such as the Artemis I Orion capsule shown in Figure 1.4, and complicated phenomena involving shock interactions and vortex interactions will be difficult to comprehend without a fundamental knowledge of rarefied vortex loops. Furthermore, provided that the gas MFP at the nozzle exit is sufficiently large, or the nozzle dimension is sufficiently small, the high Knudsen number will have an impact on the subsequent flow development. Previous studies of compressible vortex loops are limited to the continuum regime, with Knudsen number $0 < Kn < 0.001$, where the Reynolds number is high and the flow is often idealised as inviscid, and therefore, the Euler equation can give a reasonably accurate model of the flow. However, under rarefied flow conditions, viscous effects remain important [14].

Despite decades of research vortex loops are yet to be fully understood; the generation, subsequent propagation, and flow impingement of vortex loops have not been investigated in any

depth under low-pressure or even rarefied circumstances like those found in LEO. The influence of the reduced environmental pressure, or rarefaction level, on the shock wave diffraction, vortex loops internal structures, along with their propagation ability and coverage remain unknown. Understanding these may help with thrust vector management and avoid potential contamination and erosion of spacecraft surfaces [15]. Without knowledge of these rarefied transient flows, accurate prediction of the disturbing forces and heat loads is not achievable.

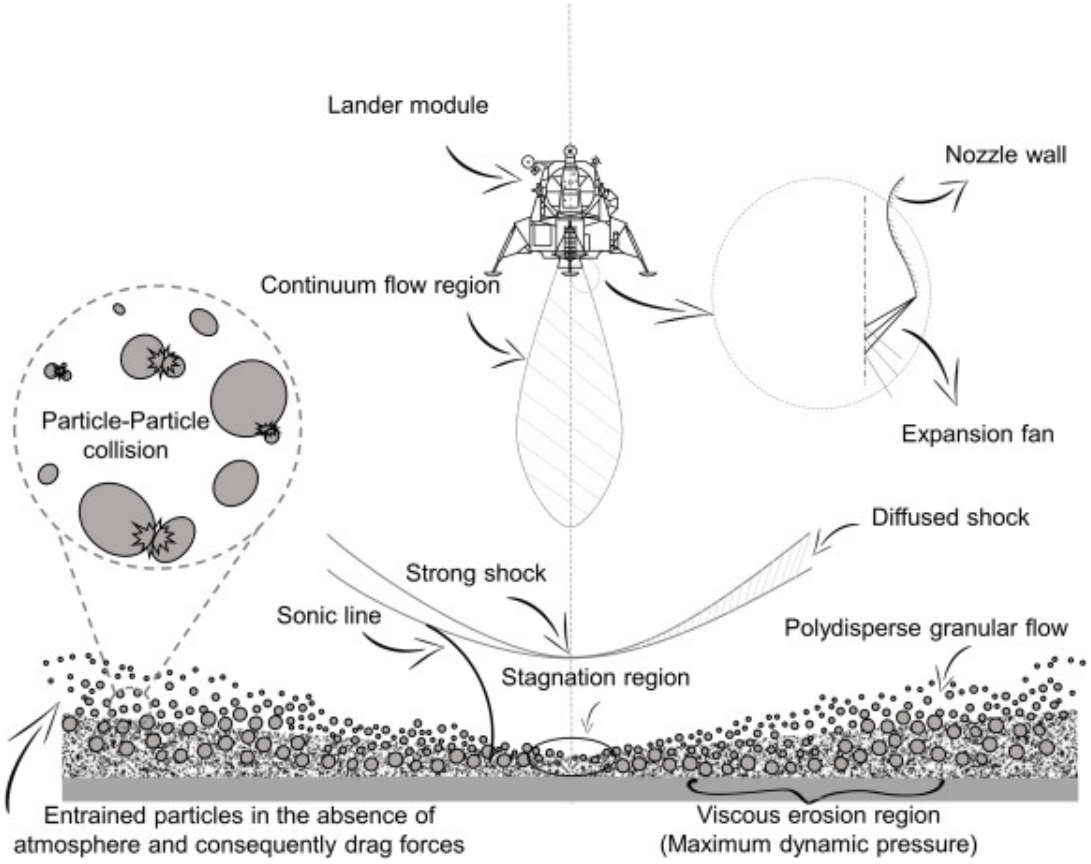

Figure 1.5: **A schematic of complex flow phenomena found in PSI problems [16].**

If supersonic nozzle flows from reverse-thrusters or the main-thruster of a landing module impinge on the ground of extra-terrestrial bodies with atmospheres that present rarefied conditions, e.g. the Moon and asteroids, regolith granules can be fluidised and entrained in the flow field around the landing module during soft-landing manoeuvres, leading to a phenomenon called plume-surface interaction (PSI), shown in Figure 1.5.

The supersonic starting jet plays an important role in PSI because when the thruster begins to fire, the starting jet, involving the diffracted shock wave, will first hit the uneroded (i.e. during an initial landing process) or cratered (i.e. during a return process) surface, followed by the impingement of the potential vortex loop and its propagation in the thruster radial direction. The variation of the strength of the diffracted shock wave and the internal structure of the vortex loop also has significant impact on the regolith granule movements. The flow may

re-enter the transition, slip, and continuum regimes if there is significant compression near the surface during the process of PSI. The process in which regolith granules are fluidised, lifted and then entrained into the flow field by the rocket plume is called surface erosion [16]. Five mechanisms contributing to the surface erosion have been defined as follows: viscous erosion, diffused gas eruption, bearing capacity failure, diffusion-driven shearing, and diffusive gas explosive erosion [17, 18]. Surface erosion is fully transient, coupled, and sensitive to variations in the gas flow field. Entrained regolith particles have the potential to cause obstruction of vision, impingement and erosion on the surfaces of the rocket's propulsion device, contamination of sensitive devices on the module, underestimation of disturbing forces and heat loads [19], and damage to nearby facilities (e.g. outposts or bases). The lunar regolith has been found to attach to surfaces, forming a dust coating layer on thermal radiators, space suits, and astronauts during the Apollo program [20]. Future manned missions using larger landing modules with greater thrust and numerous landings at a settled outpost or base will result in more severe threats and cumulative damage [21].

The comprehension of the complexity of PSI is vitally important in protecting hardware around the landing site and the landing module itself and it is meaningful and helpful in the design and exploitation of space vehicles [20] for sample collections or base building [22, 23] in the future.

Creating a full-scale and realistic extra-terrestrial environment, including high vacuum, low gravity, and strong radiation, to study PSI is difficult on Earth [24–26]. As a result, there is a clear need for an effective and efficient numerical framework to simulate this complex flow field. The direct simulation Monte Carlo (DSMC) method is the standard tool for dealing with these dilute flows, but rarefied multiphase solvers are less common due to the complexity of the essence of rarefied multiphase flow phenomena.

However, existing codes and solvers [24, 27–30] are private codes with restricted accessibility and extensibility. The transient interaction between the dust layer and the gas flow field remains to be correctly simulated; it cannot be achieved using an inlet surface to replace the dust layer or a stochastic collision model where enduring contacts are not considered. Although the DEM method can solve dense granular phases, it suffers from high computational expense for large numbers of solid particles. Therefore, an open source approach for rarefied multiphase flow with enduring contacts an efficient algorithm to solve the evolution of a dense solid phase is in high demand to simulate this complicated phenomenon with multi-scale and multi-physics characteristics.

1.2 Aims and objectives

This thesis aims to study transient phenomena that occur when a gas is ejected from a supersonic nozzle and impinges on a regolith-coated surface in low pressure environments. The fundamen-

tal flow physics of the supersonic starting jet is investigated both experimentally and numerically. Supersonic flow from an open-ended shock tube is used in the study of the supersonic starting jets, rather than a contoured nozzle, since a shock tube is the simplest nozzle and the supersonic flow from a shock tube is representative. PSI occurs when a regolith-coated surface obstructs the path of the free nozzle flow. The dynamics of the gas phase and the kinematics of regolith particulates will be studied using a newly-built numerical tool.

The details of the objectives of this research are to:

- Design a shock tube connected to a vacuum chamber and conduct schlieren visualisation and pressure measurement of the supersonic starting jets in low pressure environments to find the limits of the shock tube and the schlieren imaging system applicability and to study the physics of supersonic starting jets operating in reduced pressure conditions.
- Model the vortex loop formation due to shock wave diffraction around a 90° corner through the established transient ensemble averaged DSMC method and the compressible CFD method, examine the influence of the shock Mach number and the rarefaction level on vortex loop formation, and identify the structures and developments of vortex loops in rarefied conditions using the concept called "rorticity".
- Update an open source code, *rarefiedMultiphaseFoam*, for solving rarefied gas-solid multiphase flows with models for solid-solid interactions, including a stochastic collision model for dilute granular phase and the MPPIC method for dense granular phase, and benchmark the two-way coupling model, solid phase change model and the reproduced MPPIC method.
- Conduct two lunar PSI simulations with the stochastic collision model and the MPPIC method respectively using a scaled down version of the Apollo era lunar module descent engine, and compare the transient results.

1.3 Thesis outline

The thesis is constituted by the following chapters:

Chapter 2 presents a review literature of supersonic starting jets, including a demonstration of the fundamental theories of shock waves and shock tubes, followed by the details of the design of the shock tube that is connected to a vacuum chamber and an description of the experimental layout. Experimental results, including schlieren images and pressure distributions with different background pressures, of a study of vortex ring formation in low-pressure conditions (i.e. background/environmental pressure is lower than 1 atm but higher than 900 Pa) are presented.

Chapter 3 starts with introductions to the modified CFD method for simulating fluid phenomena in the near continuum regime and the DSMC method for solving rarefied gas dynamics, followed by an introduction of a new post-processing method for vortex dynamics. Then, the simulation results of vortex loop formation due to shock wave diffraction around a 90° corner in rarefied conditions (i.e. $Kn > 0.001$) will be discussed. The shock Mach number and the Knudsen number effects on the vortex loop formation are discussed. The structures and evolution of vortex loops are analysed using the rorticity concept.

Chapter 4 includes a detailed overview of the open source code for solving rarefied multiphase flows, *rarefiedMultiphaseFoam*, and the newly developed models will be presented after a review of existing codes. The results of benchmarking tests of the new open source code for rarefied multiphase flows will subsequently presented. The validations of the interphase coupling model, particle phase change model, and the MPPIC method are discussed.

Chapter 5 includes the numerical results of lunar plume-surface interactions using the *rarefiedMultiphaseFoam* solver with the addition of models considering the solid-solid interactions. In one case with low solid number density, the stochastic collision model is used, and in the other case with high solid particle number density, the MPPIC method is applied. The whole transient evolution of both phases in the two cases are presented. The gas flow field and the regolith layer evolution from both solid-solid interaction models are discussed in detail.

Chapter 6 summarises the key findings of this research followed by a discussion of possible future work based on the conclusions on this thesis.

1.4 Main contributions

The main contributions of this work are listed below:

- The physics of supersonic starting jets operating in reduced pressure conditions ($Kn < 0.001$) have been studied using a shock tube connected to a vacuum chamber with schlieren visualization and pressure measurement for the first time. It is proven that the internal flow structures in a vortex loop degenerate as the environmental pressure decreases. The existence of the vortex ring is confirmed through spectral analysis when the environmental pressure is as low as 1.0 kPa.

- The influence of the shock Mach number and the rarefaction level on vortex loop formation due to shock wave diffraction around a 90° corner under rarefied conditions has been investigated through the established transient ensemble averaged DSMC method and the compressible CFD method. The failure of the formation of the vortex loop is well explained as the result of the increase in Knudsen layer thickness.

- The concept called "rorticity" is applied to identify the internal structures and developments of vortex loops for the first time. Two properties called "rorticity flux" and "shear flux" are defined to quantify the fluid rotational and shear strengths, respectively. The mutual transformation between the rotational and shear movements has been observed, and the quantity of this transformation is equivalent.

- An open source code, *rarefiedMultiphaseFoam*, has been extended to include a two-way coupling model, a solid phase change model, and a stochastic collision model for dilute granular interactions. It has been extended to take solid-solid enduring contacts into account and is coupled with the MPPIC method for dense granular interactions to solve rarefied gas-solid multiphase flows. The two-way coupling model, solid phase change model, and reproduced MPPIC method have been benchmarked and agree well with analytical and previous numerical data.

- Two lunar PSI simulations are conducted with the stochastic collision model and the MPPIC method, respectively, using a scaled-down version of the Apollo era lunar module descent engine to study the transient interaction between the plume and the dust layer and the effect of the solid-solid enduring contacts on the PSI. It is found that the transient influence and the entrained solid particles have significant impacts on the development of the gas flow field. The numerical result from the MPPIC method is more realistic because the enduring contacts and the close-packing limit are considered.

Chapter 2

Supersonic starting jet from an open-ended shock tube in low-pressure environments

Nozzles have been widely employed inside a vacuum chamber [31–34] to study steady jet flows in vacuum, but fewer attempts have been made to connect a shock tube to a vacuum chamber [35] to investigate the formation of vortex rings/loops in low pressure environments. Furthermore, the basic optical techniques extensively used in the study of compressible flows, including schlieren, particle image velocimetry, and planar laser-induced fluorescence, have never been applied to the visualization of compressible vortex rings/loops in low-pressure environments or rarefied conditions.

Before considering rarefied conditions, the specific objectives of this chapter are to present the design of a shock tube connected to a vacuum chamber, to validate the feasibility of the shock tube, to provide preliminary schlieren visualisation, and conduct pressure measurements of vortex rings from an open-ended shock tube when the environmental pressure is lower than ambient atmosphere, which is followed by a literature review of supersonic starting jets.

2.1 A review of supersonic starting jets

Supersonic starting jets have piqued the interest of researchers due to their effectiveness for various application, such as improving mixing and combustor performance, noise suppression, heat transfer, and thrust vector control [36]. The flow patterns of supersonic jet flows depend on the pressure ratio p_{exit}/p_b, where p_{exit} is the pressure at the nozzle exit and p_b is known as the

back pressure or the atmospheric pressure. As shown in Figure 2.1, according to the pressure ratio, supersonic jet flows can be divided into [37, 38]:

- overexpanded jet: When $p_{exit} < p_b$, the gas from a nozzle will be compressed by the relatively high pressure outside of the nozzle and oblique shock waves attached to the nozzle exit can be found.
- ideal jet: When $p_{exit} = p_b$, no waves can be found at the nozzle exit.
- underexpanded jet: When $p_{exit} > p_b$, the gas from a nozzle will continue to expand after it leaves the nozzle, and a series of expansion waves can be observed at the nozzle exit.

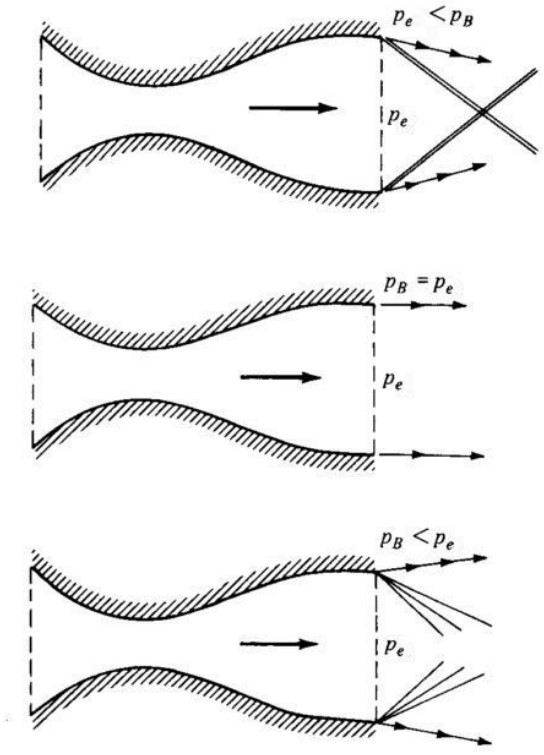

Figure 2.1: **Three kinds of free jets. From top to bottom; overexpanded jet, ideal jet, and underexpanded jet [37]**.

Figure 1.2 depicts a typical numerical work of the stages of a supersonic starting jet. After a relatively high-pressure gas flow is ejected from a nozzle or tube, the primary shock wave diffracts at the nozzle exit, resulting in the formation of a vortex sheet or shear layer, which is described as a thin gas layer with velocity discontinuity or a high velocity gradient in the normal direction [39], and later, the formation of a vortex pair. Then, by engulfing the surrounding fluid, the vortex sheet tends to roll up into a vortex ring. This vortex ring expands axially and radially until it reaches a critical size [40]. A rearward-facing shock wave is formed between the cores of the vortex ring in the case of a high shock Mach number. This shock wave is noted as a diaphragm shock [41] or embedded shock wave [42]. During the propagation of the vortex ring,

it separates from the trailing jet and continues its path. This separation is known as "pinch-off". Later, the trailing jet will interact with the vortex ring, leading to shock–shear layer–vortex ring interaction and noise generation [40].

2.1.1 Shock waves

As long as a body moves at supersonic speed in the gas flow, a shock wave can be seen. The shock wave is a strong compression wave, and it is a negotiation of the flow with the fast-moving body [37]. Usually, in the atmosphere, shock waves are extremely thin and highly viscous regions where the gas flow properties change abruptly.

Shock waves can be separated into steady and unsteady shock waves.Steady shock waves include bow shocks and oblique shocks according to the deflection or turning angle. There is a maximum flow deflection angle for a given Mach number Ma. When the flow deflection angle is smaller than the maximum angle, an oblique shock wave occurs, while a bow shock, or a normal shock wave, forms if the flow deflection angle is greater than the maximum angle.

$$\tan\delta = 2\cot\beta \frac{Ma^2\sin^2\beta - 1}{Ma^2(\gamma + \cos 2\beta) + 2} \tag{2.1}$$

According to Equation (2.1), for a given Mach number and deflection angle, the downstream flow conditions after an oblique shock wave includes the production of a weak shock and a strong shock [37]. The downstream flow is still supersonic in the weak shock condition, but it is subsonic after passing through a strong shock. Oblique shock waves are common targets to be controlled in aerodynamic applications [43, 44], such as controlled oblique shock waves at the intake and inside of the propulsion system of a supersonic vehicle to reduce total pressure loss, and optimized oblique shock waves attached at the front of the vehicle to decrease drag force.

The formation of bow shock waves usually happens around blunt bodies [45, 46]. A typical bow shock wave can be found in front of the re-entry module of a spacecraft during the re-entry process. The process when flow passes the bow shock is non-isentropic and the drag force on the body is significantly increased once a bow shock has formed.

The oblique shocks and the bow shocks mentioned are typically stationary shock waves. If a shock wave propagates freely in space and the flow field is related to both space and time, this shock wave propagation is considered unsteady [47]. Examples of unsteady or moving shock can be seen in the process of an explosion of a bomb or a balloon. The common method to generate a moving shock wave is to use a facility called a shock tube, as will be described in the following sections.

The fundamental derivations of the relations before and after shock waves can be found in many

fundamental textbooks [37, 38, 48], so they are not repeated in this thesis.

2.1.2 Shock wave diffraction

Shock wave diffraction is the result of a moving shock wave encountering a sudden expansion [49] and has been investigated for a wide range of Mach numbers. Figure 2.2 shows an example of shock wave diffraction.

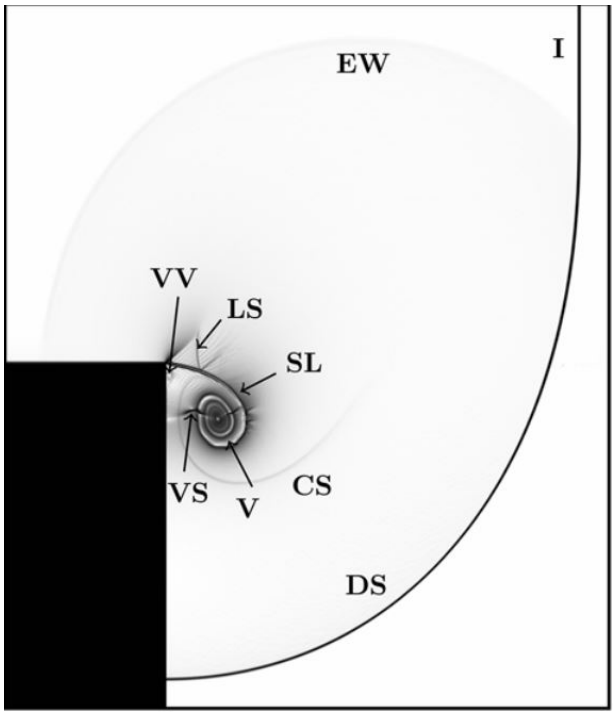

Figure 2.2: **Numerical schlieren image of the shock wave diffraction. I: incident shock wave. DS: diffraction shock wave. EW: expansion shock wave. CS: contact surface. SL: shear layer. LS: lambda shock. VV: viscous vortex. VS: vortex shock. V: cortex core [50].**

When a shock wave diffracts at a corner, an expansion wave emerges that propagates in the opposite direction of the primary shock wave. Then a vortex propagates a short distance and a slipstream occurs, which is explained as the failure adaptation of the shocked gas to the corner. The presence of the contact surface and the second shock are recognised in the case of a high shock Mach number. When the shock Mach number exceeds 2.068, the expansion wave cannot go upstream [51]. Sun and Takayama [52] found that small vortices form in the shear layer as a result of the enhanced interaction between the viscous effect and the baroclinic effect, resulting in the characteristic Kelvin–Helmholtz instability structure. Furthermore, it has been proposed [53] that the vorticity created by the slipstream is a critical part of the total vorticity and that vorticity production is positively associated with the wall angle. Because of the formation of flow instabilities, boundary layers, and the flow transition, the shear layer separation and flow evolution were found to be different as the size of the experimental facilities increased [54].

Attempts have been made to analytically predict the joint of the incident shock wave and the expansion wave. Whitham's theory was widely used for estimations of the shape of the diffracting shock wave [55, 56], but corrections were made due to the intolerable differences between the experimental results and predictions [49]. There are also some novel shock wave diffraction investigations, such as diffraction around slotted splitters [57], diffraction with the presence of a co-flow jet [58], diffraction at a curved exit from the shock tube [59], the interaction of two perpendicular diffracting shock waves [60], and vortex merging caused by shock wave diffraction in three dimensions [61].

2.1.3 Compressible vortex loops

Since 1952, when Elder and Haas [62] were the first to capture the compressible vortex ring at a shock tube exit using schlieren, researchers have been drawn to the "beauty" of compressible vortex rings. Vortex loops have been studied intensively for decades, both experimentally and numerically, to better understand their evolution.

The subsequent phenomenon of the ejection of a moving shock wave from a shock tube is the production of a shear layer with a strong velocity gradient in the radial direction of the shock tube. This shear layer then rolls up and entrains the gas around it to form a forward-moving vortex ring [63]. Through analysis of the vorticity field, this vortex ring was found to separate from the trailing jet and move forward alone [64]. In general, the compressible vortex ring has a high Reynolds number, and its propagation speed is fast and dependent on the pressure in the shock tube's driver section. When the Reynolds number is sufficiently high, turbulence occurs in the vortex ring [63].

Some substructures emerge during the formation and propagation of a compressible vortex ring, resulting in more complicated phenomena. Brouillette and Hébert [65] discovered a link between the structure variation of compressible vortex rings and the shock Mach number. There is no shock wave in the vortex ring if the shock Mach number is less than 1.43. There is an embedded rearward-facing shock wave in the vortex ring if the shock Mach number is between 1.43 and 1.6, which was also observed by Baird [66], and secondary vortex rings form ahead of the primary vortex ring if the Mach number is more than 1.6. In addition, when the shock Mach number is higher than 1.4, a pair of vortex-induced shock waves occur on opposite sides of the main vortex core [67]. These phenomena were also observed in the works of Murugan *et al.* [42]. They found that the maximum axial velocity along the centerline, the dimensionless mean core radius, and the propagation velocity of vortex rings increase the shock Mach number, and they no longer increase when the embedded shock wave forms [68]. A secondary counter-rotating vortex ring was observed ahead of the primary vortex ring when the shock Mach number reaches 1.63 [63]. Kontis *et al.* [69] found secondary counter-rotating vortex rings inside a vortex ring as a result of a Kelvin-Helmholtz type instability of the vortex sheet [70]/slipstream beginning from

the triple point of the Mach disc and subsequent vortex coupling [71], which was proved by the numerical results of Zhang *et al.* [72]. These vortices were strongly dependent on the strength of the embedded shock wave and the length of the jet. In addition, the strength of the embedded shock wave will be increased by the tube radius, and its lifetime will be extended with a longer driver section [70]. The vortex ring's entrainment phenomena generates vortex-induced shock waves in the vortex ring's recirculating zone. These shock waves are connected to the embedded shock wave and perform as incident shock waves, causing shock-vortex interactions. Within the primary vortex, weak shock–vortex interactions coexist with strong ones, and they will eventually becoming strong interactions [41]. The shock waves created will deteriorate the shear layer's stability, resulting in smaller vortices surrounding the vortex centre [73, 74]. The vortex ring will interact with the trailing jet as it propagates, including the shock–shear layer–vortex interaction and the shear layer–vortex interaction. It is pointed out that a key Reynolds number determines the creation of the shock–shear layer–vortex interaction. The noise produced by the shock–shear layer–vortex interaction has a sound pressure level equivalent to that of a continuous jet [8]. In the condition of the existence of the co-flow around the vortex ring, the circulation of the primary vortex ring and the strength of the embedded shock and vortex-induced shock wave decreases with the increase in the speed of the co-flow [75].

In incompressible vortex theory, a vortex is quantified by the circulation, hydrodynamic impulse, angular impulse, kinetic energy, and helicity [39, 74]. Shivamoggi [76] extended the equation of the hydrodynamic impulse, denoted as I, and the kinetic energy, denoted as E, to compressible vortices, and they are expressed as

$$\mathrm{I} = \frac{1}{2}\int_{\mathrm{V}} \vec{r} \times (\nabla \times \rho\vec{v})\, d\vec{r} \tag{2.2}$$

and

$$\mathrm{E} = \frac{1}{2}\int_{\mathrm{V}} \rho\vec{v}^2 d\vec{r}. \tag{2.3}$$

The expression for the incompressible thin-cored vortex ring ($R_{VRc}/R_{VR} \ll 1$) [73] propagation speed, which is expressed as

$$\mathrm{U} = \frac{\Gamma}{4\pi R_{vr}}\left[\log\frac{8R_{vr}}{R_{vfc}} - \frac{1}{4}\right], \tag{2.4}$$

is theoretically extended to the compressible case by Moore [77], resulting in

$$\mathrm{U} = \frac{\Gamma}{4\pi R_{vr}}\left[\log\frac{8R_{vr}}{R_{vfc}} - \frac{1}{4} - \frac{5}{12}Ma_{vr}^2 + O\left(Ma_{vr}\right)\right], \tag{2.5}$$

where Ma_{vr} is a Mach number that expressed as $\Gamma/2\pi R_{vfc}\mathrm{a}_\infty$, R_{vr} is the vortex ring radius, and R_{vfc} is the radius of vortex filament core. Mariani and Kontis [78] observed that a converging nozzle accelerates vortex ring propagation while a diverging nozzle decelerates it, and that the vortex ring propagation speed distribution is proportional to the cross-sectional area and pressure

in the driving section.

It is identified that the vortex rings are sensitive to the nozzle geometry. Qin *et al.* [79] studied the effect of straight, diverging, and converging nozzles on the vortex ring evolution using schlieren. The vortex ring dimension from the diverging nozzle is larger than that from a converging nozzle, but the propagation speed of the vortex ring from the converging nozzle is greatest among the three types of nozzles [79]. When the shape of a tube or nozzle exit is non-circular, vortex rings become vortex loops. Non-circular jets have been identified as an effective passive flow control technology, and they have been utilised to improve the performance of material mixing, combustion, noise suppression, heat transfer, and thrust vector control [80]. The vortex loop evolution, including formation, stable laminar phase, unstable phase, and turbulent phase, is very sensitive to the exit cross-section [36]. The common shapes of non-circular exit cross-sections are triangular, square, and elliptical [74]. Zare-Behtash *et al.* [69] used schlieren, shadowgraph, and particle image velocimetry to explore the propagation of vortex loops expelled from various exit geometries and found that non-circular vortex loops are extremely three-dimensional. Square vortex loops have much more vorticity in the shear layer and are more prone to stretching. The introduction of corners at the tube or nozzle exit would accelerate the pace of vortex loop propagation. Entrainment in noncircular jets is intensified by a self-induced Biot-Savart deformation and the interaction of azimuthal and streamwise vorticity. The Biot-Savart self-induction causes the vortex part with a small radius of curvature to travel faster and the vortex loop to deform, leading to the axis-switching phenomenon of supersonic square vortex loop [81]. This deformation gets more complicated during vortex loop convection and redistributes the energy of azimuthal and streamwise vortices [80]. Through large eddy simulations by Zhang *et al.* [82], comparisons have been made between circular and square vortex loops. Strong stretches of square vortex loops were also observed, and these stretches, in combination with the outward-wash effect, caused the lateral axis switching phenomenon in the propagation of square vortex loops, demonstrating that a square vortex loop generated a more effective mixing and entrainment phenomenon. The highly three-dimensional square vortex loop and accompanying shock waves were discovered in their subsequent study [81]. The shock wave surfaces would suppress the flow boundary at the corner in the diagonal direction while speeding up the flow boundary in the symmetry direction, and an ascent in the pressure ratio would enhance the growth of the boundary in the symmetry direction [81].

Vortex rings become more interesting when they interact with surfaces [84]. A schematic of a compressible vortex ring impingement on a wall is shown in Figure 2.3. The surface distance influences the vortex ring development during impingement. When the surface is near to the shock tube exit, the vortex ring is underdeveloped and when the distance is large, the vortex ring is completely formed. The following shock and vortex interaction in the impingement process will also be influenced by the vortex ring at different stages [83]. Kontis *et al.* [63]

investigated the interactions of compressible vortex rings with a solid wall experimentally. In all of their tests, they demonstrated that the state of vortex rings changed from laminar to turbulent during propagation due to Kelvin-Helmholtz instability. When the primary shock wave hit the wall and reflected, the reflected wave interacted with the vortex loop, causing the generation of acoustic waves. The vortex ring then impinged on the wall and spread radially, creating sound waves that were amplified by the shock Mach number. As the vortex ring gets closer to the wall, the boundary layer produced on the wall separates, resulting in the formation of a wall vortex. During the vortex ring-plane wall interactions, the radial dimension of the vortex ring is positively correlated with the pressure in the driver section and the interactions between the reflected shock wave and the vortex ring strengthen the noise level [63]. A shocklet is formed between the primary and wall vortices at the same moment [85]. Some bodies, such as a circular cone, a sphere, and a cube, interacted with vortex rings, and the vortex rings grew radially as a result of the interaction.

Some other research groups focused on the vortex ring acoustic characteristics [86, 87]. The noise of vortex ring evolution has been found to be dominant in the range of 25° to 50° from the nozzle axis, and the noise generated from the interactions between shear-layer vortices and the trailing jet is noticeable [87]. The sound generated during the formation and propagation of a counter-rotating vortex ring is larger than that of the primary vortex ring [86]. The three main sources of the far-field noise from the normal impingement of a compressible vortex ring on a flat plate include the formation and evolution of the vortex ring; the interaction between

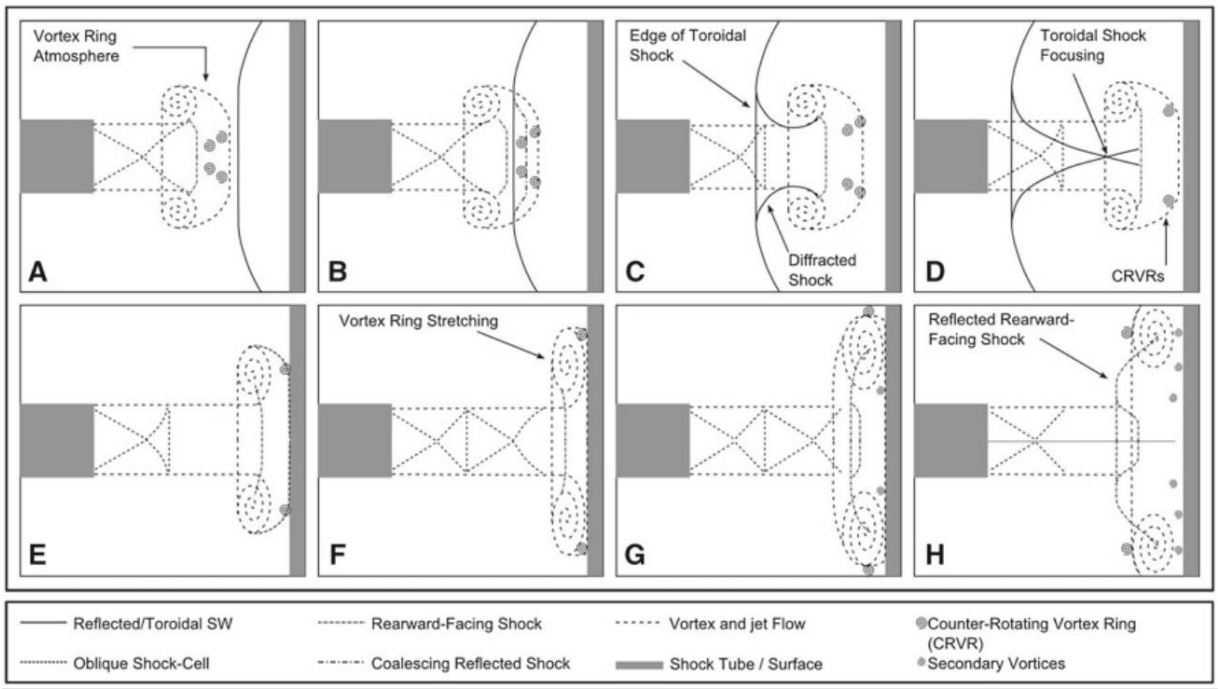

Figure 2.3: **A schematic of compressible vortex ring impingement on a surface perpendicular to the nozzle axis [83].**

the vortex ring and the reflected shock wave; and the vortex ring impingement. The noise of the vortex ring-wall interaction dominates in the range of 10° to 40° from the nozzle axis [88].

The preceding studies are restricted to the continuum regime, in which the Knudsen number $0 < Kn < 0.001$, where the Reynolds number is high, and the flow is idealized as inviscid. The effect of the low-pressure and rarefied conditions on the shock wave diffraction and the subsequent vortex loop formation and propagation remains unknown. Questions such as how the internal structures (e.g. embedded shocks, CRVR and shock intrusions) change and whether a vortex ring can be formed in low-pressure and rarefied conditions still require to be answered.

2.1.4 Summary

Supersonic starting jets have been studied intensively for decades, both experimentally and numerically, in the continuum flow regime, but no previous study has investigated vortex ring formation and transport in low-pressure environments (i.e. the environmental pressure is lower than 1 atm) or even rarefied conditions (i.e. $Kn > 0.001$). In addition, no experimental evidence of compressible vortex loops or vortex rings in low-pressure or rarefied conditions is available in the literature. Hence, a conventional shock tube is designed to work with a vacuum chamber for the first time so that the formation and internal flow structures of supersonic starting jets can be studied in low-pressure environments.

2.2 Experimental apparatus and method

2.2.1 Shock tube

A shock tube is a fundamental instrument to generate various straight blast waves and moving shock waves. It is often used to investigate compressible gas phenomena, such as shock waves, vortex loops, high temperature combustion reactions, and hypersonic gas flow [38]. A shock tube, as shown in Figure 2.4, mainly consists of a driver section which contains high pressure gas, p_4, and a driven section with lower pressure gas, p_1. The part separating both sections is called a diaphragm. When the diaphragm is ruptured, a moving shock wave is generated due to the sudden discontinuity that is introduced and immediately spreads downstream. In the opposite direction, a series of expansion waves will be generated at the diaphragm position and propagate into the driver section. p_2 and p_3 are the pressures after the initial shock wave and the expansion wave inside the shock tube, respectively. If the shock tube is open-ended, the shock wave diffracts at the exit.

In the continuum flow regime, the ratio of the macroscopic properties on both sides of the shock wave, considering an ideal gas where the vibrational and electronic modes are not excited, is

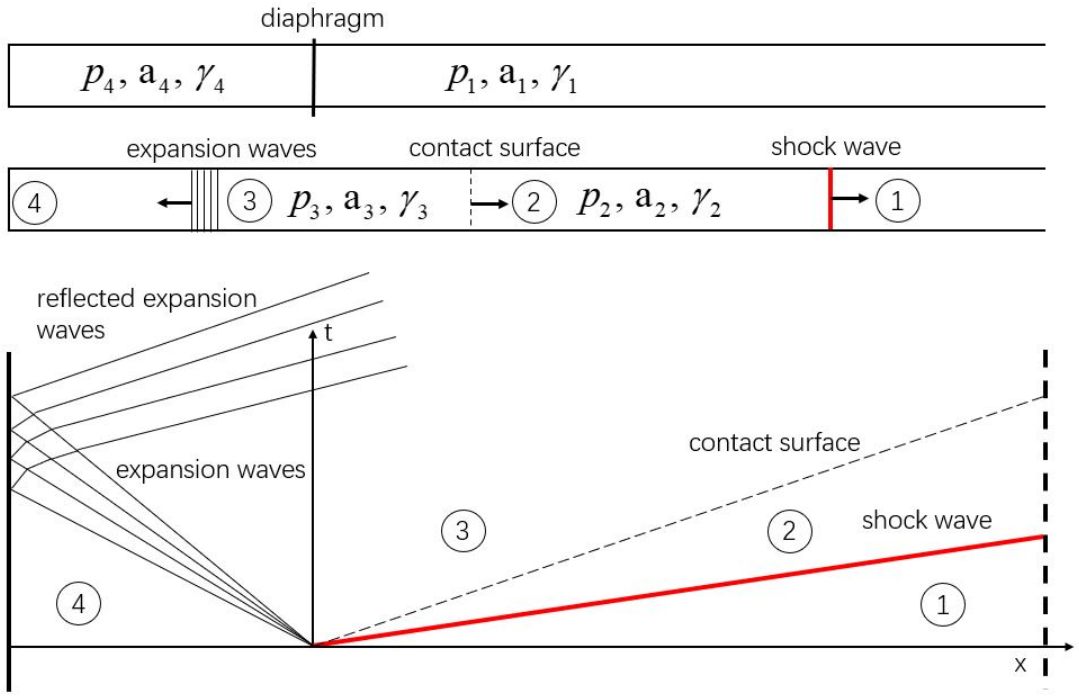

Figure 2.4: **A schematic of an open-ended shock tube and the x-t waves diagram.**

derived according to the continuity, momentum, and energy equations [38]:

$$\frac{p_2}{p_1} = 1 + \frac{2\gamma_1}{\gamma_1 + 1}\left(Ma_s^2 - 1\right), \tag{2.6}$$

$$\frac{\rho_2}{\rho_1} = \frac{(\gamma_1 + 1)Ma_s^2}{(\gamma_1 - 1)Ma_s^2 + 2}, \tag{2.7}$$

$$\frac{T_2}{T_1} = \frac{\left[\frac{\gamma_1 - 1}{\gamma_1 + 1}\left(Ma_s^2 - 1\right) + M_s^2\right]\left[\frac{\gamma_1 - 1}{\gamma_1 + 1}\left(Ma_s^2 - 1\right) + 1\right]}{Ma_s^2}. \tag{2.8}$$

The pressure ratio p_2/p_1 is considered as the shock strength. Based on the isentropic flow relation and the Riemann invariants [38], the pressure ratio of the driver and driven section is

$$\frac{p_4}{p_1} = \frac{2\gamma_1 Ma_s^2 - \gamma_1 + 1}{(\gamma_1 + 1)\left[1 - \frac{a_1}{a_4}\frac{\gamma_4 - 1}{\gamma_1 + 1}\left(Ma_s - \frac{1}{Ma_s}\right)\right]^{\frac{2\gamma_4}{\gamma_4 - 1}}}. \tag{2.9}$$

Equation (2.9) is applicable when different types of ideal gases are used in the driver and driven sections and it implies that a higher shock Mach number can be achieved through increasing the gas temperature or using a lighter gas in the driver section [47].

Many attempts have been made to allow design novel shock tubes with lower costs and easier operation for the purposes of studying shock and blast wave phenomena. The diaphragm has

been found to be avoidable using a fast acting valve [89–91]. In order to avoid filling gas into the driver section to generate high pressure, detonations [92] and lasers [93] have also been used to create the initial pressure discontinuity.

However, there has been less previous literature related to shock tubes with the driven side attached to a vacuum chamber [35] to study transient high-speed flow physics in low pressure environments. A conventional and simple shock tube connected to a vacuum chamber is designed in this research to study shock wave diffraction and vortex ring formation in low pressure environments.

Design of the shock tube

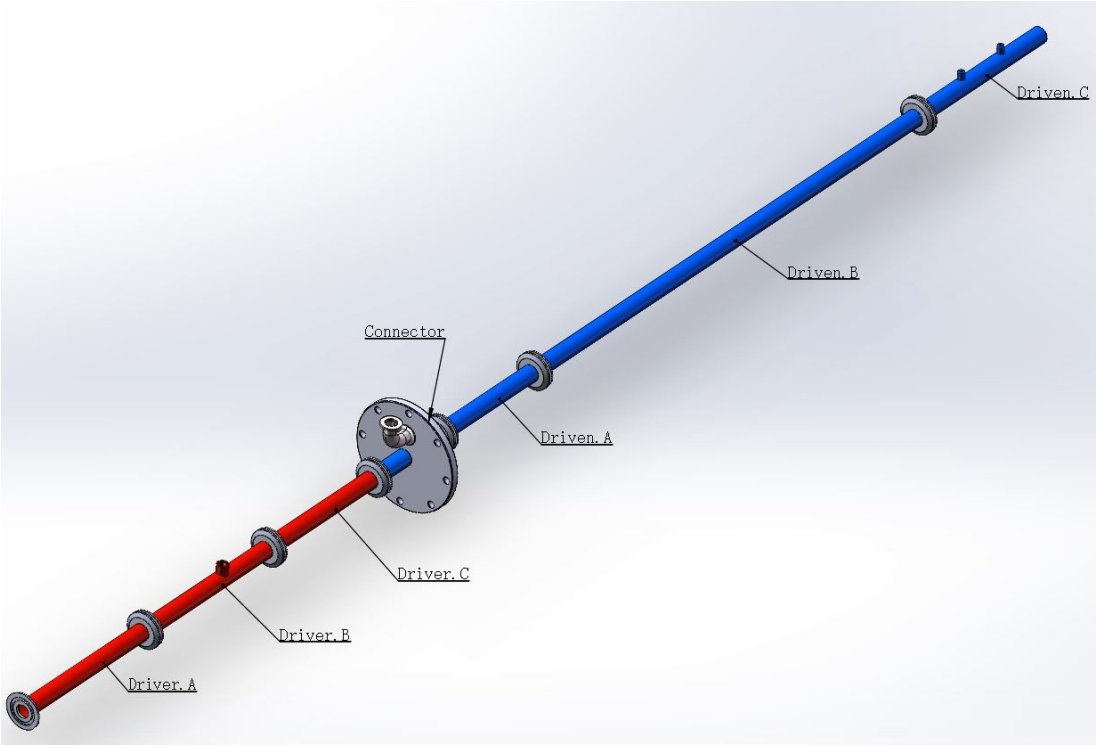

Figure 2.5: **Overview of the shock tube.**

Figure 2.5 shows an open-ended shock tube connected to a vacuum chamber. The small flanges sealed with aluminium clamps between the tubes are KF40 type vacuum flanges. The outer diameter of the tube is 25 mm and the inner diameter, denoted D, is 20 mm. The connector, which is machined from an ISO200 blank flange, is used to connect the shock tube to the vacuum chamber whose diameter is around 2.5 m. The red sections are the driver section, while the blue sections are the driven portion, whose environmental pressure decreases as the vacuum chamber is evacuated. The lengths of the driver and driven sections are 742 mm and 1405.7 mm, corresponding to $37D$ and $70D$, respectively. The length of the driven section is substantially longer than the recommended minimum length (i.e. $8D$–$10D$) [94], allowing for shock wave formation. The lengths of the driver and driven sections can be adjusted by adding or removing

tubes. As a diaphragm, 20 micron thick aluminium foil is installed at the flange connection between the vacuum flange and driver part C. Before any additional improvements are considered, the feasibility of the shock tube must be proven, hence no diaphragm-breaking system is included in the current work. The pressure difference between the driver and driven sections spontaneously breaks the diaphragm. The details of the dimensions of the individual shock tube parts are available in Appendix D.

2.2.2 Schlieren and experimental setup

Thanks to Robert Hooke, schlieren was developed according to the refractive index difference in non-uniform medium in the 17th century [95] and it has become a standard optical tool to visualise various flows with density gradients caused by temperature or velocity changes. The basic difference between the schlieren and shadowgraph photography is that the schlieren technique uses a knife to intercept some of the deflected light in front of the camera and the shadowgraph photography does not require the knife edge.

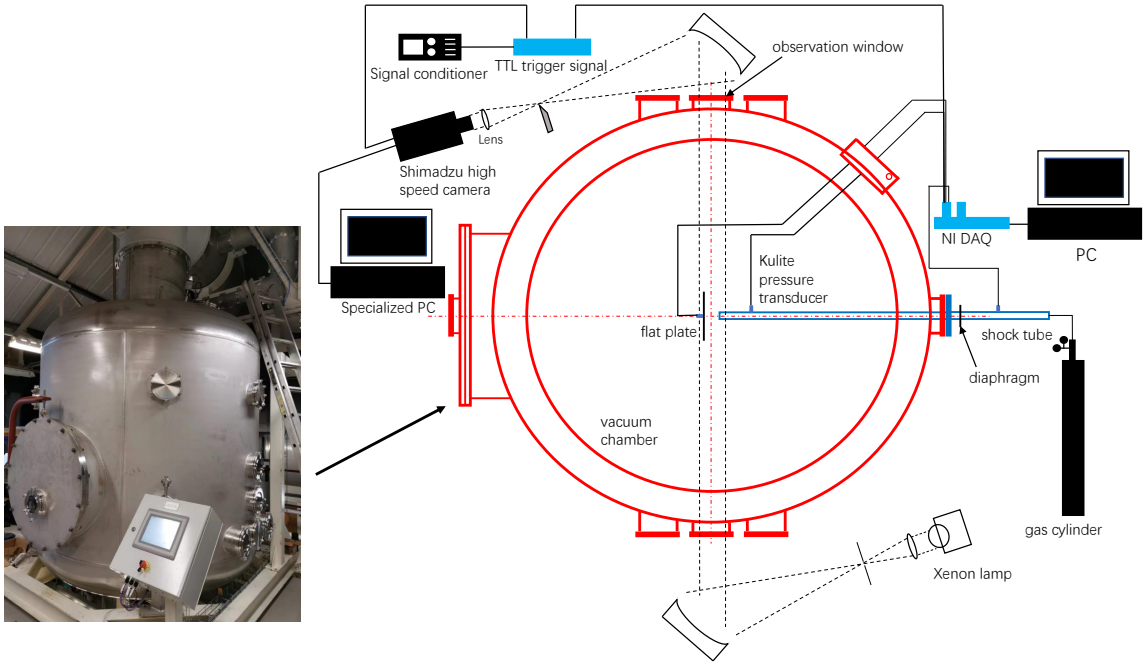

Figure 2.6: **Overview of the experimental layout.**

The experimental layout is presented in Figure 2.6. The red line is the cross-section of the vacuum chamber, with an outer diameter of 2.52 m and a height of 3.02 m. The shock tube is connected at a flange opposite the access door to the chamber.

A typical Z-type schlieren system is used outside the vacuum chamber. The system includes a 450–1000 W continuous light source with a Xenon arc lamp (Newport, model: 66921), a pair of 203.3 mm diameter parabolic mirrors with a focal length of 1829 mm, a knife edge to block

part of the light, and a Shimadzu HPV-1 high-speed camera. The sudden pressure rise signal induced by the primary shock wave is used as a trigger to the camera. To trigger the camera shutter and the data acquisition system, a signal conditioner is required to adjust the output voltage from the transistor-transistor logic trigger signal. The threshold output voltage is related to the over pressure signal changing with the pressure value inside the vacuum chamber and must be adjusted before any images are recorded.

Pressure signals were received using Kulite XTE-190M pressure transducers installed in the driver and driven parts to calculate the pressure ratio. The pressure signal was collected with an NI-9223 module (National Instruments Corp., 1 MS/s, 16 bit, 4 channels) and an NI-9178 compact data acquisition (DAQ) system controlled by LabVIEW, resulting in a resolution approximately 700 Pa. To obtain high-frequency data, a sampling rate of 100 kHz was chosen.

The whole optical system, however, is less sensitive than that used to visualise loud sounds and weak shock waves [96], so it becomes difficult to capture any images when the pressure in the driver section decreases below a threshold value. To gather information below that low pressure level, a flat plate with a pressure transducer in the centre is placed in front of the shock tube, normal to the shock tube exit, as illustrated in Figure 2.6. The distance between the exit of the shock tube and the flat plate is 55 mm.

2.2.3 Image processing

In comparison with the image background, shock waves usually appear in the form of darker or lighter lines or parts in schlieren images and it is a common method to distinguish flow features through brightness intensity extracted from schlieren images. However, a contaminated background will severely disturb the estimation of the flow features [97]. Typical contamination of the schlieren image background is caused by some mild scratches and dust attached on the lens or mirrors or issues with camera senors, such as overheating. Reportedly, the background noise can be partially removed by cleaning the lens and mirrors, but image processing algorithms are necessary and effective to provide clean and clear schlieren images. Typical approaches to remove the background noise consist of background subtraction, image thresholding, image filters (including convolution, mean filter, Gaussian filter, median filter, bilateral filter [98], Sobel filter [99], *etc.*) and image resampling [47].

It is pointed out that background image subtraction in the frequency domain is effective in eliminating noise [47]. Li [47] has detailed the image processing method and the corresponding code based on Matlab and an image processing toolbox, so the image processing theory, validation, and the code will not be repeated here. All the schlieren images in this chapter are processed using the background image subtraction in the frequency domain.

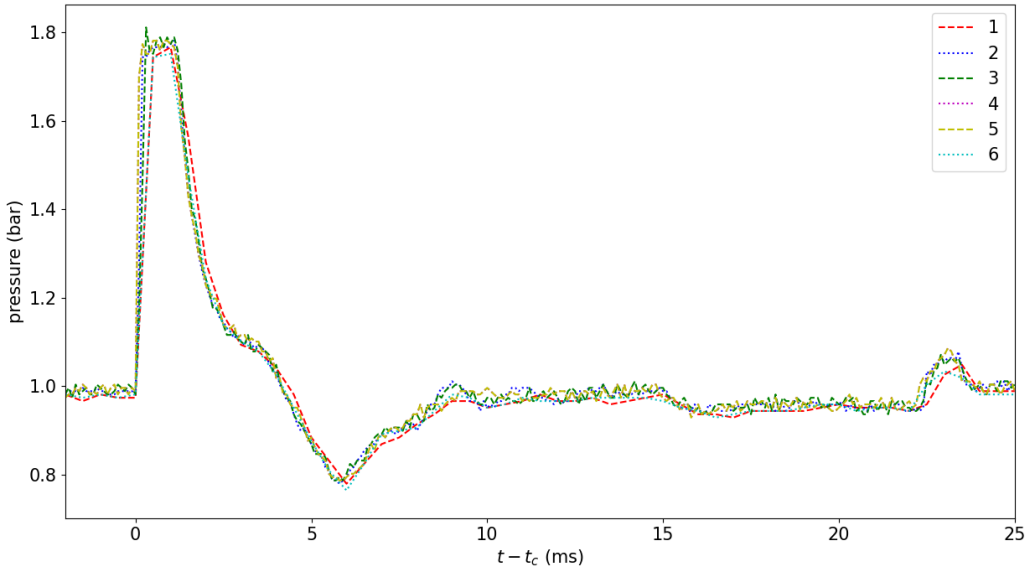

Figure 2.7: **Pressure distributions of shock tube repeatability tests.**

2.3 Shock tube repeatability validation

The shock tube repeatability is validated by repeating the pressure measurements 6 times with the same lengths of the driver and driven sections. For the reason that no diaphragm-breaking mechanism is installed; the 20 μm aluminium foil being used as the diaphragm will be spontaneously ruptured by the pressure difference between the driver and driven sections. Hence, the time when the diaphragm is broken is related to the pressurisation speed in the driver section, but the pressure signal distribution should be identical. The time at which the pressure starts to surge to the peak is considered as the reference time, denoted as t_c. Figure 2.7 presents the pressure distributions due to the passing of the shock wave inside the shock tube through the pressure transducer. The results show good agreement and the measured overpressure is 1.7735 bar with $\pm 2.5\%$ discrepancies (corresponding to a shock wave of approximately Mach 1.3), proving that the combination of the shock tube and the aluminium foil is able to produce repeatable shock waves.

2.4 Results and discussions

The experimental matrix is presented in Table 2.1. The schlieren images of typical starting jets with background pressures p_1 of to 1 bar, 0.36 bar, and 0.2 bar are shown in Figures 2.8, 2.9, and 2.10. The pressure ratios, p_4/p_1, of these three cases are 4.2, 8.8 and 15.8, respectively, corresponding to shock Mach numbers of 1.37, 1.57 and 1.75.

The primary shock waves in all cases diffract at the shock tube exit, followed by the formation of the shear layer and the subsequent flow separation and rolling up. Finally a vortex ring is

Table 2.1: **Experimental matrix.**

Back pressure p_1	Free-expansion	Flow impingement
1 bar	✓	✓
0.556 bar		✓
0.487 bar		✓
0.36 bar	✓	
0.2 bar	✓	✓
0.184 bar		✓
0.01 bar		✓

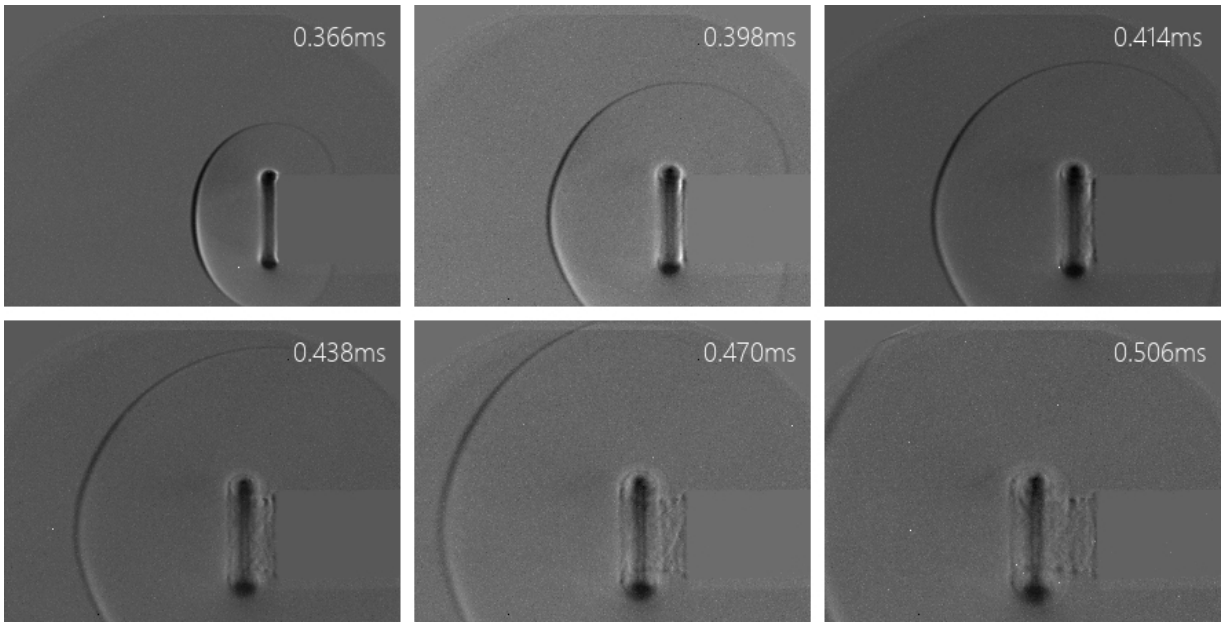

Figure 2.8: **Schlieren with p_1 = atmosphere. p_4/p_1 = 4.2, corresponding to a shock Mach number of 1.37.**

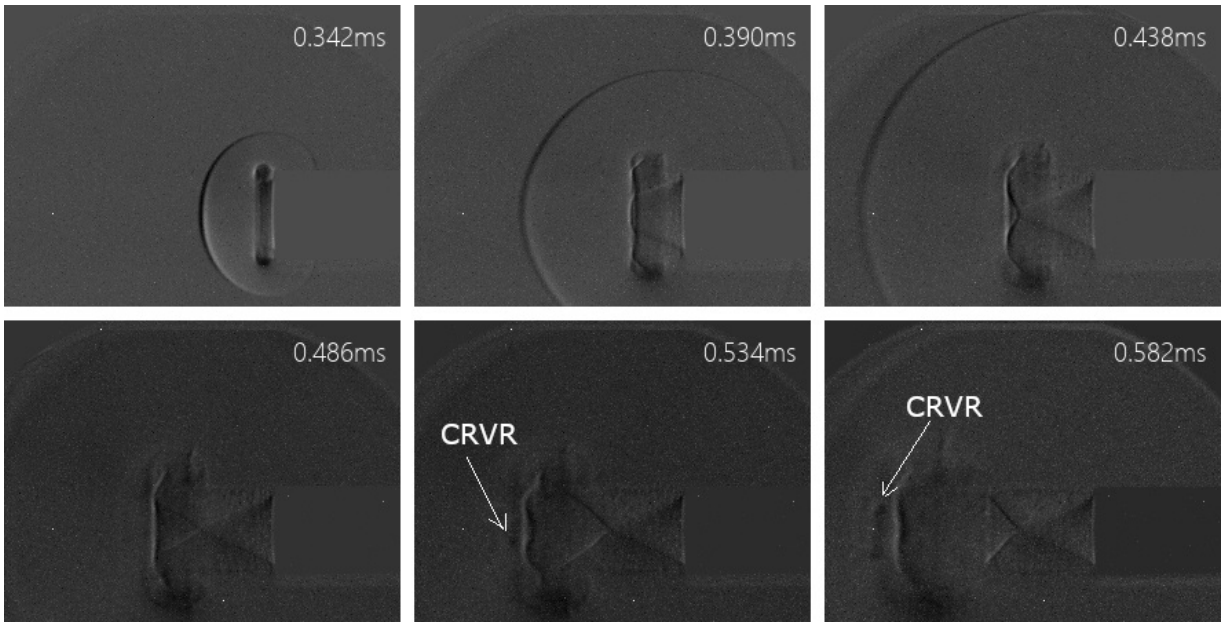

Figure 2.9: **Schlieren with p_1 = 0.36 bar. p_4/p_1 = 8.8, corresponding to a shock Mach number of 1.57.**

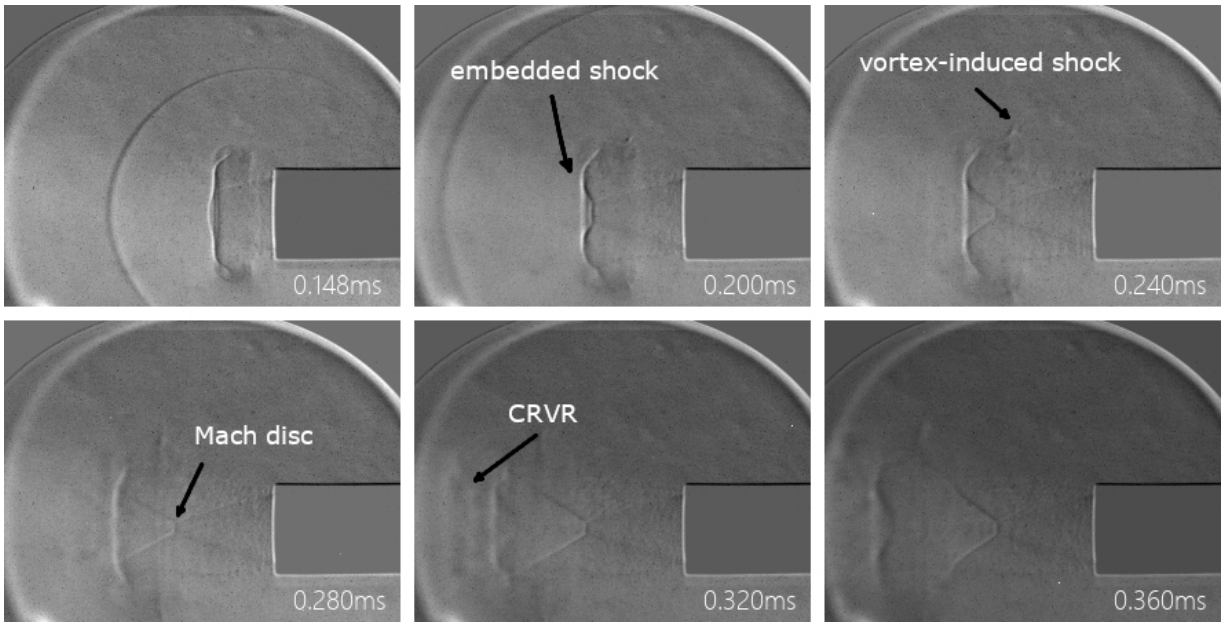

Figure 2.10: **Schlieren with p_1 =0.2 bar. p_4/p_1 = 15.8, corresponding to a shock Mach number of 1.75.**

generated, as shown in Figures 2.8 (0.366 ms), 2.9 (0.342 ms), and 2.10 (0.104 ms). After the diffraction, the primary shock wave turns into a spherical shock wave. At the same time, the vortex ring gradually grows at the nozzle exit and begins to propagate forwards: Figures 2.8 (0.414 ms), 2.9 (0.390 ms), and 2.10 (0.148 ms). In Figures 2.8 (0.470 ms), 2.9 (0.486 ms), and 2.10 (0.240 ms), relatively small vortices are generated within the shear layer and the laminar structures inside the vortex rings become turbulent due to the instability waves around the circumference of the vortex ring. The small vortices in the shear layer are important for the development of the vortex ring because they continuously feed vorticity into the primary vortex ring, helping the vortex ring growing in size with time.

It is already known from Ref. [65] that the vortex ring is shock-free when the shock Mach number is lower than 1.4, as shown in Figure 2.8. The shock structures, including the embedded shock wave and the x-shape oblique shock waves in Figure 2.9 are consistent with those in Figure 5 of Ref. [63]. The embedded shock wave appears inside the vortex ring (0.39 ms in Figure 2.9 and 0.2 ms in Figure 2.10) and the joint of the x-shape oblique shock waves at 0.486 ms in Figure 2.9 becomes a small Mach disc in Figure 2.10 at 0.2 ms because of the increase in the pressure ratio. The existence of the counter-rotating vortex ring (CRVR) has been highlighted in Refs. [63] and [72]. Vortex induced shock waves are visible in Figures 2.9 (0.438 ms and 0.486 ms) and 2.10 (0.240 - 0.28 ms). The length of the vortex induced shock is approximately tripled at 0.582 ms compared with that at 0.486 ms when $p_1 = 0.36$ ms and a similar growth can also be observed in Figure 2.10. It is interesting that CRVRs appear when the environmental pressure is 0.36 bar and 0.2 bar in Figures 2.9 and 2.10. The formation of these representative structures in a low-pressure environment proves that as long as the pressure ratio, p_4/p_1, reaches the threshold values and the gas conditions are in the continuum flow regime, these structures can be produced by decreasing the environmental pressure.

Flow structures in Figures 2.9 and 2.10 gradually become hard to recognise as the vortex ring propagates forward. First, the CRVRs are less apparent compared with those observed in atmosphere, such as the Figure 5 in Ref. [63] and numerical results in Ref. [72]. Secondly, the vortex-induced shock is weakened and becomes difficult to distinguish at 0.582 ms in Figure 2.9 and 0.36 ms in Figure 2.10. Third, the vortex ring has a clear boundary during its propagation in Figure 2.8, while this boundary becomes more diffuse and unrecognisable in Figures 2.9 and 2.10. The primary shock wave significantly thickens from 0.39 ms to 0.438 ms in Figure 2.9 and from 0.148 ms to 0.2 ms in Figure 2.10, respectively. Figure 2.11 shows the trends in the thickness of the primary and embedded shock waves in different conditions. The thicknesses of all the shock waves increase during the propagation of the vortex ring, and especially the primary shock wave with $p_1 = 0.2$ bar is thickened rapidly within 0.1 ms, compared with the other two cases. The thickness of the primary shock wave is greater than that of the embedded shock wave because the primary shock wave is the leading structure of the whole supersonic jet.

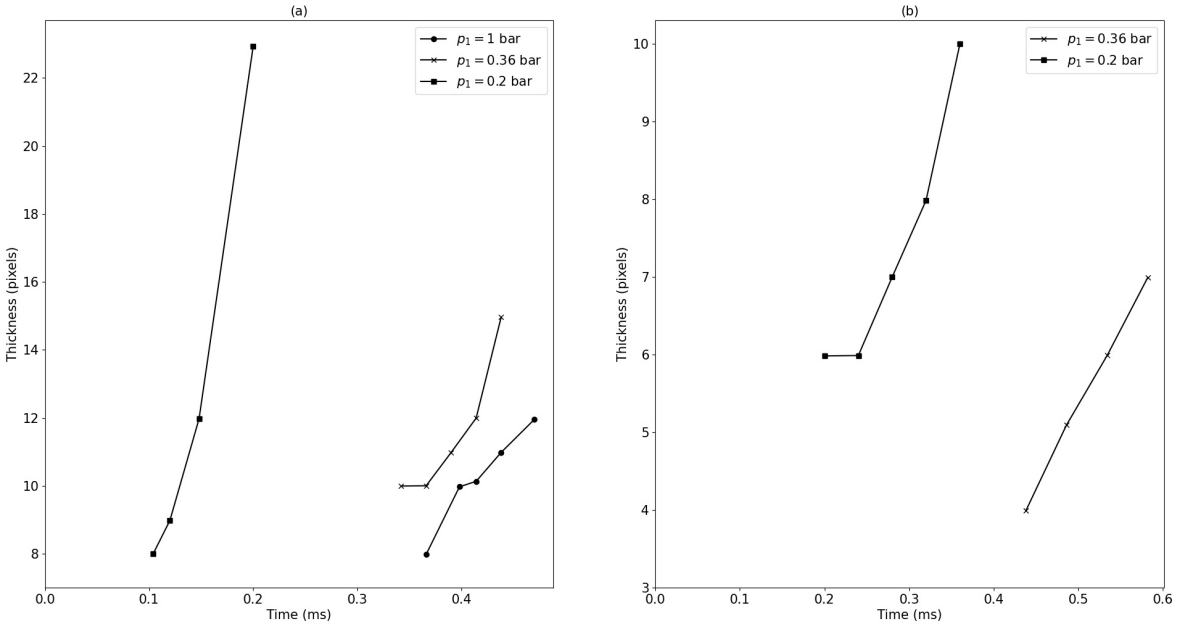

Figure 2.11: **Thickness of shock waves in different environmental pressures ((a) primary shock wave, (b) embedded shock wave). The thickness is calculated using the brightness intensity profile extracted from schlieren images in Matlab.**

The increase in the thickness of all the shock waves in the supersonic starting jets due to the decrease in environmental pressure indicates a decrease in the strength of the shock wave. The rapid expansion of the vortex ring under low-pressure conditions drags and forces the internal flow features to grow. The growth in dimension of these flow features reduces the local pressure and pressure gradient, making it difficult to distinguish them in schlieren images. These phenomena imply that in rarefied conditions, if the environmental pressure, p_1, is continuously reduced, flow features such as shock waves and CRVRs degenerate and eventually disappear.

Through our tests, it is found that it was not possible to capture any visible structures when the background pressure is lower than approximately 0.15 bar using the experimental apparatus described in Section 2.2.2, due to insufficient sensitivity of the mirrors and the frame rate of the camera in the schlieren imaging system. Therefore, a flat plate with a pressure transducer at its centre is placed in front of the shock tube exit to record the pressure signal and identify the possible footprints of vortex rings when $p_1 < 0.1$ bar.

Figure 2.12 shows the flow evolution in 1 atm, which is similar to that of Figure 2 in Ref. [83]. The incident shock wave impinges on the flat plate, followed by its reflection. The reflected shock wave is then diffracted by the vortex core during the interaction with the oncoming vortex ring. Due to the rotation inside the vortex core, a toroidal shock wave forms [83] at 0.594 ms and focuses at the centre at 0.618 ms. In Figure 2.13, the reflected shock wave becomes the shape of the embedded shock wave after the interaction with the primary vortex ring at 0.308

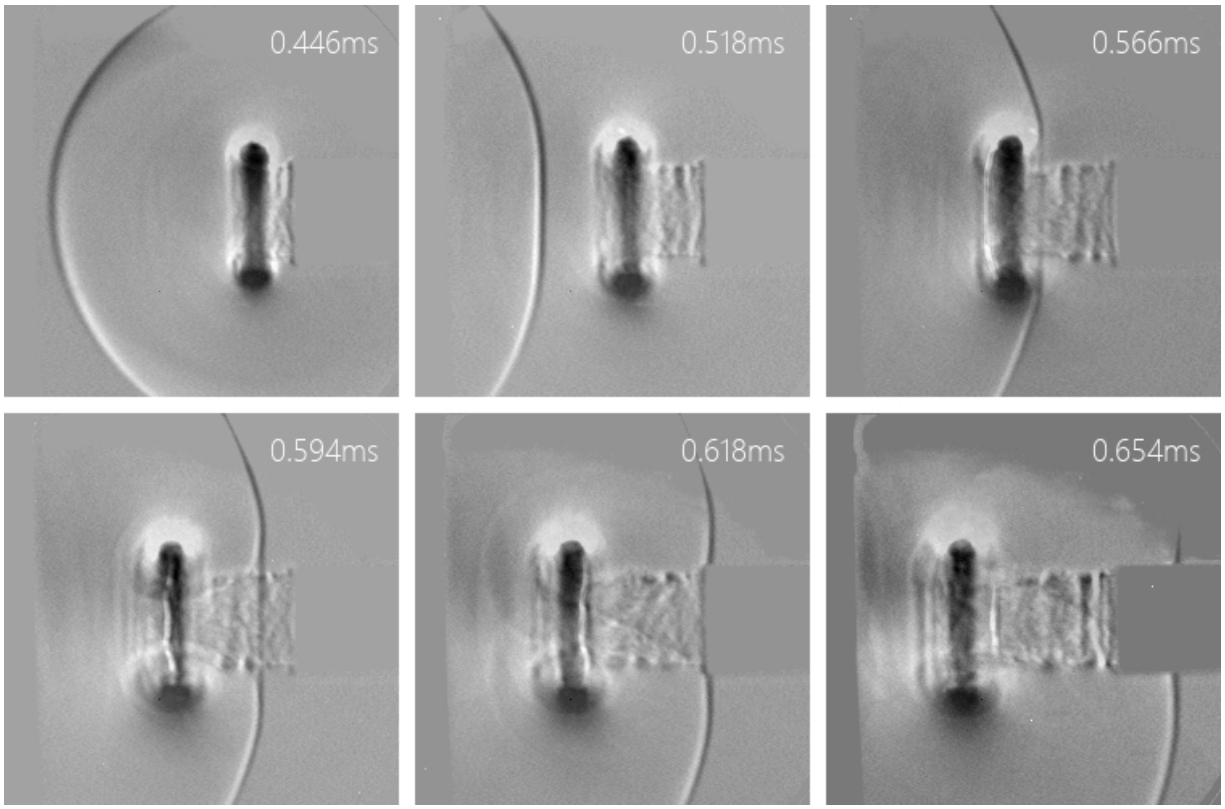

Figure 2.12: **Schlieren with p_1 = 0.928 bar.**

ms, and the formed CRVR in front of the primary vortex ring becomes the first vortex ring to hit the surface (0.444 ms), which is identical to the description in Ref. [100]. The impingement of the starting jet forms a boundary layer on the flat plate and this boundary layer extends in the radial direction. Subsequently, the embedded shock wave inside the main vortex ring hits the surface and is reflected towards the shock tube exit, as shown in Figure 2.13 at 0.524 ms.

In Figure 2.14(a), the normalised pressure distribution at the centre of the flat plate in the different background pressures is presented and the increase in the slope of the primary shock wave indicates the growth in the strength of the shock wave due to the changes of the pressure ratio. Compared with the result in atmosphere (0.928 bar), the signal distributions of the other three cases (0.556 bar, 0.487 bar and 0.184 bar) are significantly different, but the primary shock wave and the main vortex ring are still recognisable. This should be attributed to the flow structure changes, such as the formation of the CRVRs and the embedded shock waves. However, the pressure signal is too noisy to recognise any flow structure of the supersonic starting jet because of the limited resolution of the DAQ system, shown in Figure 2.14(b). The resolution is limited to around 700 Pa using the combination of the 16-bit NI-9223 module and the full scale output of the Kulite XTE-190M pressure transducers. The $t - t_i$ time is limited to 4 ms in Figure 2.14(b) due to an unnatural pressure surge and fluctuation caused by the impingement of diaphragm debris. Since the flow features at p_1 =1.0 kPa cannot be resolved through Figure 2.14(b), the fast

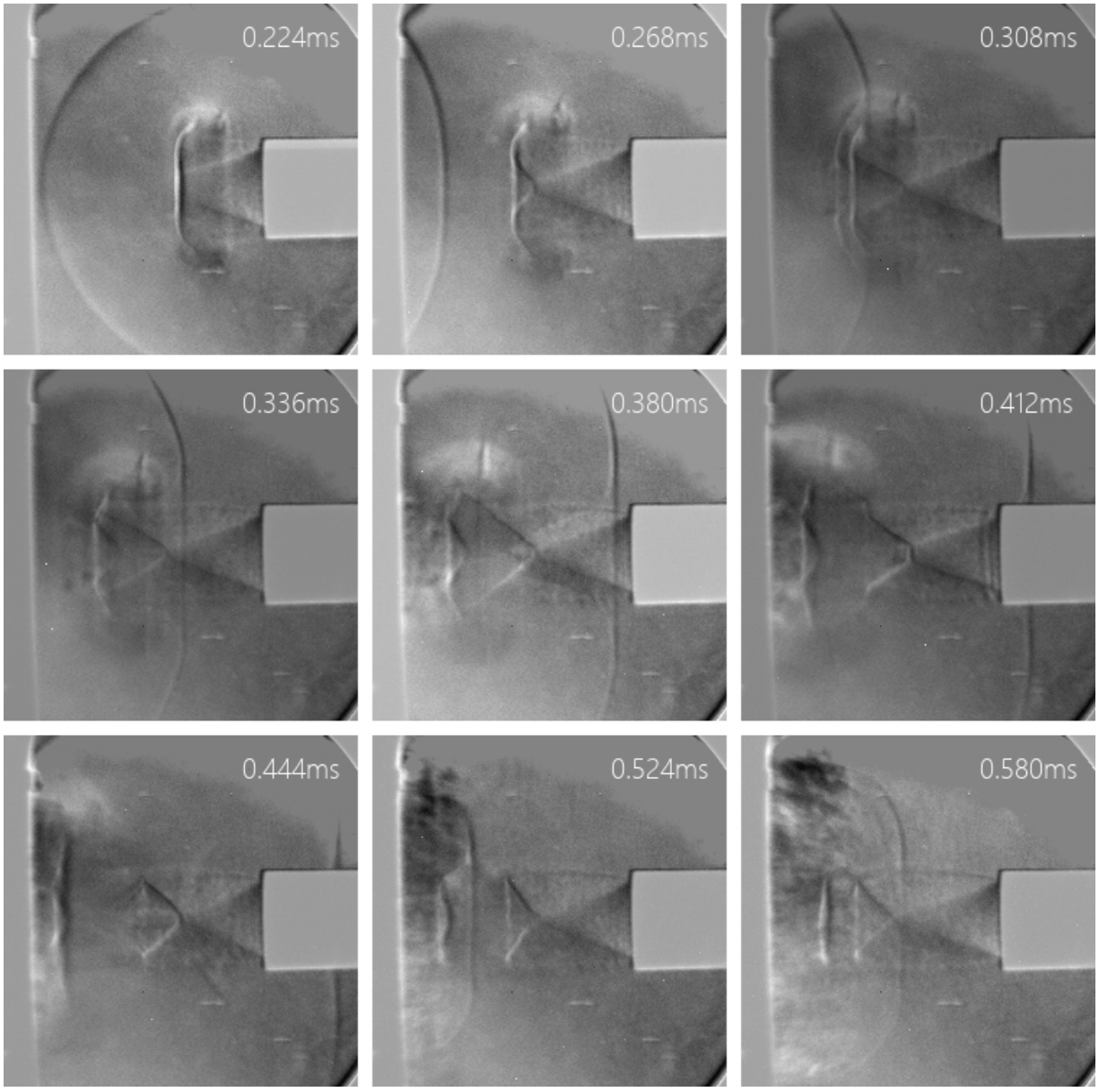

Figure 2.13: **Schlieren with p_1 = 0.228 bar. p_4/p_1 = 13.4.**

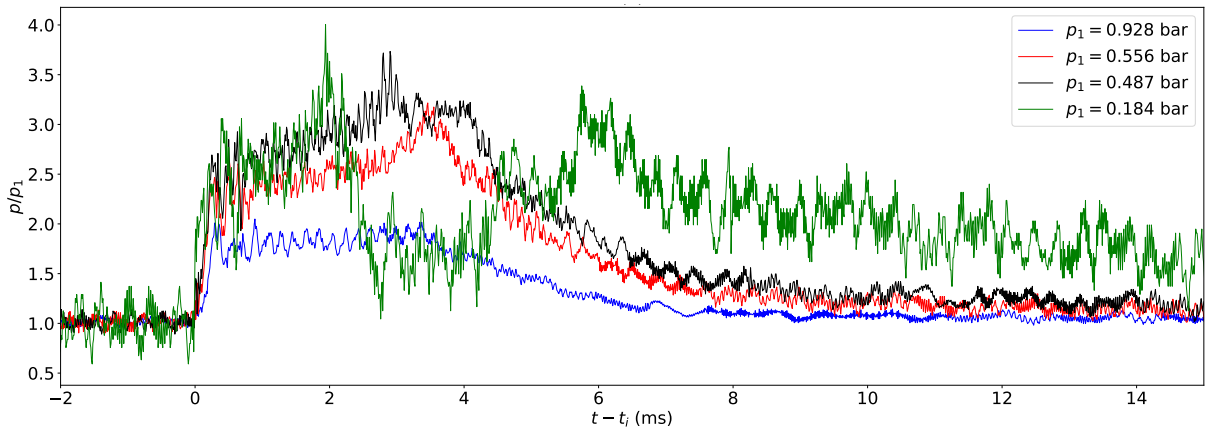

(a)

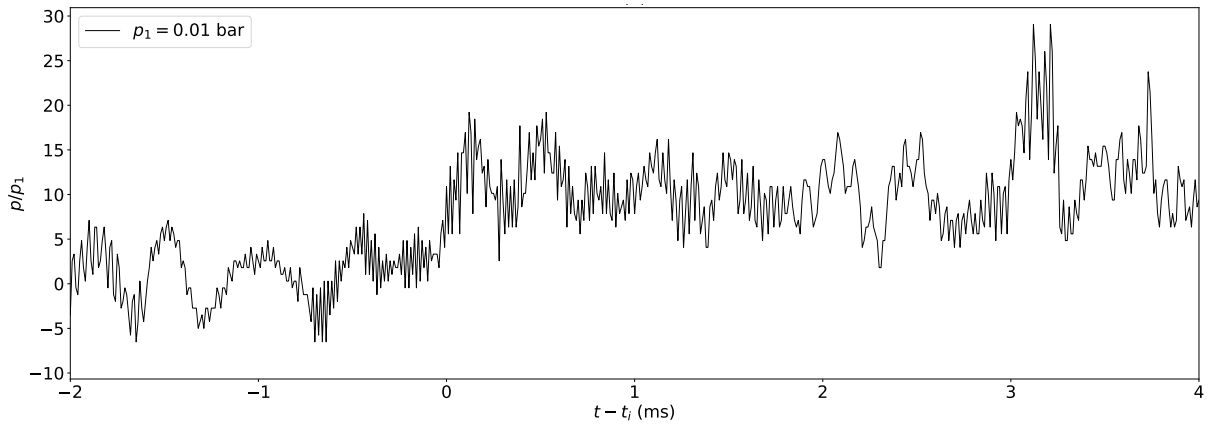

(b)

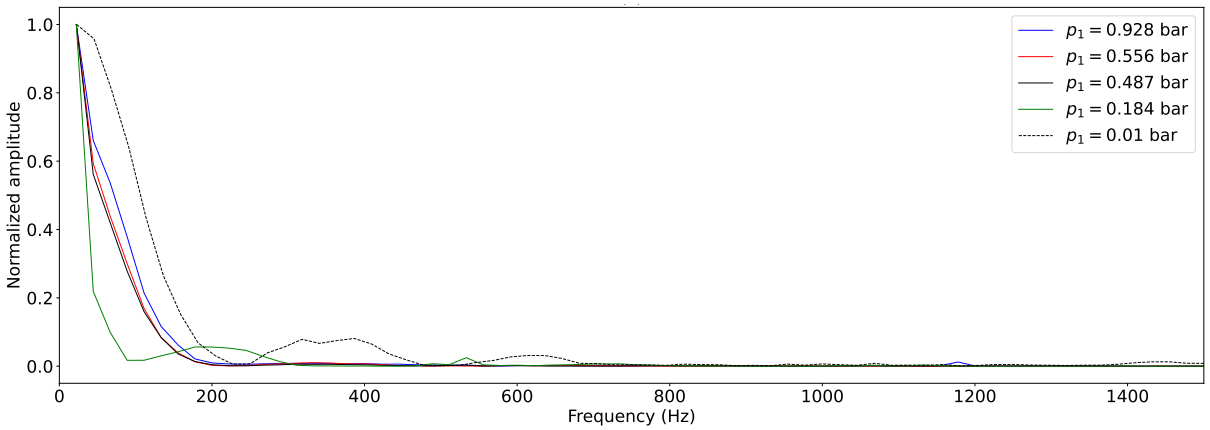

(c)

Figure 2.14: **(a), (b): Normalized pressure distribution with time at the center of the flat plate. t_i is the time that the pressure start to increase due to the shock wave. (c) Frequency distribution of the pressure signal using Fast Fourier transform.**

Fourier transform is used to turn the pressure signal from the time domain into the frequency domain. The frequency profiles of p_1 =0.556 bar and p_1 =0.487 bar are in excellent agreement, indicating the consistency of the basic flow structures during impingement. The profile difference between the case of p_1 =0.928 bar and that of p_1 =0.556 bar is caused by the different internal structures of the vortex ring due to the increase in the shock Mach number. The three cases prove that similar flow features will give a similar frequency distribution in the frequency domain. It is confirmed that the vortex ring is generated when the environmental pressure is in the vicinity of 0.2 bar and the frequency distribution with p_1 =0.01 bar is highly similar to that with p_1 =0.184 bar, implying the existence of the vortex ring impingement when p_1 = 1.0 kPa.

2.5 Summary

An experimental study of supersonic starting jets from an open-ended shock tube under low-pressure conditions has been conducted. It has been experimentally confirmed that the decrease of the background pressure will increase the thickness of the primary and embedded shock wave of vortex rings. The trend of the flow structure degeneration as the environmental pressure decreases is described. The CRVR sill can be found in reduced pressure environments as long as the pressure ratio reaches the threshold values, but its strength decreases during its propagation because of the reduction of the background pressure. The existence of a vortex ring is confirmed when the environmental pressure is approximately 1.0 kPa. However, the flow regime is still in the continuum flow regime when the back pressure is around 1.0 kPa using the spectral analysis. To investigate the rarefaction effect on the vortex loop formation and evolution, numerical tools will be used in the next chapter.

Chapter 3

Numerical simulations of vortex loop formation due to shock diffraction in rarefied conditions

An overview of schlieren imaging and pressure measurement of vortex rings in low-pressure environments is discussed in Chapter 2. However, due to insufficient DAQ resolution and the sensitivity of the mirrors of the schlieren imaging system, no flow structures are recognizable when the environmental pressure is lower than 1000 Pa. The supersonic starting jet in the near continuum flow regime or rarefied conditions has never been studied in any depth. The effect of the rarefaction level on the shock wave diffraction and vortex loop formation is not fully understood. This chapter provides numerical simulation results of 2D vortex loop formation due to shock wave diffraction in rarefied conditions ($Kn > 0.001$) after a series of validation tests. The influence of the shock Mach number and the rarefaction level on the vortex loop formation will be discussed. The interior structures and development of vortex loops will be identified using the concept called "rorticity".

To begin with, the numerical methods used in this thesis will be introduced, including the CFD solver and the DSMC solver, both of which are implemented in OpenFOAM, followed by a description of the method for rorticity calculation.

3.1 Numerical method I: Near continuum regime

As the gas MFP increases, the gas atoms/molecules collide less frequently with surfaces, leading to non-equilibrium regions close the surface and failure of the no-slip boundary condition where the gas velocity and temperature at the surface is not equivalent to the surface values. This boundary condition failure is known as velocity slip and temperature jump [6]. The validity of

the NSF equations has been extended to the near continuum flow regime through the addition of Maxwell's velocity slip [101] and Von Smoluchowski's temperature jump [102] boundary conditions. In addition, it is computationally expensive to use the DSMC method to simulate gas flows in the near continuum regime because of the large number of cells demanded by the small gas MFP and the large number of gas simulators. To increase efficiency, the *hy2Foam* [103] solver in Open Field Operation and Manipulation (OpenFOAM) is used to perform the numerical simulations in the near continuum flow regime.

The *hy2Foam* solver is a density-based Navier-Stokes-Fourier code for solving hypersonic flow problems, including the effects of chemical reactions. The translational and rotational temperatures are assumed to be always remain equal in a trans-rotational mode, while the electron, electronic, and vibrational temperatures are assumed to be equal in a vibrational-electron-electronic temperature. It was specifically built for simulating high-speed flow in the near continuum region, which is computationally costly when using a DSMC solver. It has been validated under hypersonic flow conditions with and without chemical reactions [103]. This solver is developed from the *rhoCentralFoam* solver and is hence based on the Kurganov-Tadmor central-upwind differencing schemes. A more detailed introduction to the *hy2Foam* solver can be found in Ref. [103].

Polyatomic gas molecules may have enough energy behind a shock wave with high Mach number for the vibrational mode to become excited and for chemical reactions, such as dissociation, to occur. However, as the Mach numbers in the current study are relatively low, the two-temperature model will be reduced to a single temperature model. The temperature behind the shock wave will be insufficient to excite the vibrational and electronic modes and chemical reactions are not likely to be induced. The no-slip boundary condition is unacceptable due to the Knudsen numbers studied, hence Maxwell's velocity slip [101] and Von Smoluchowski's temperature jump boundary [102] conditions are applied to simulate the velocity slip and temperature jump phenomena in the vicinity of solid wall boundaries. The Reynolds number is low due to the small length scales and low density, hence the flow can be assumed to be laminar.

3.2 Numerical method II: Rarefied gas flows

The importance of the gas non-equilibrium effects continuously increases as the Knudsen number increases. The assumptions of molecular chaos and binary inter-molecular collisions are the prerequisite for the validity of the Boltzmann equation controlling the gas in rarefied conditions from moderate to high Knudsen numbers. For a single species monatomic gas, the Boltzmann

equation is expressed as:

$$\frac{\partial n_g f}{\partial t} + \vec{v}\frac{\partial n_g f}{\partial \vec{r}} + \vec{F}\frac{\partial n_g f}{\partial \vec{v}} = \int_{-\infty}^{\infty}\int_{0}^{4\pi} n_g^2 \left(f^* f_1^* - f f_1\right) |\vec{v}_r| \, \sigma d\Omega d\vec{v}_1, \tag{3.1}$$

where n_g is the local gas number density, $\vec{v}$ is the velocity, $\vec{r}$ is the position in physical space, $\vec{F}$ is the external force per unit mass here, f is the velocity distribution function and f^* is the post-collision particle velocity distribution. The on-linear integral term on the right hand side is the collision term. f_1 and ${f_1}^*$ are the pre- and post-collision particle distribution function at class $\vec{v}_1$, respectively. σ is the particle collision cross-section and Ω is the solid angle [104]. The non-linearity of the collision term, and the integro-differential nature of the equation as a whole, are the main obstructions in acquiring solutions to the Boltzmann equation [104]. Neglecting the collision term in the free-molecular flow regime brings convenience in solving the Boltzmann equation. However, the consideration of the collision term in the slip and the transition flow regime still brings difficulty to find solutions. The existing methods of solving the Boltzmann equation analytically depend on making assumptions about the forms of the velocity distribution function, known as the Moment methods [104, 105] including the regularised 13 moment [106] and 26 moment equations [107], or on simplification of the collision term, such as the Bhatnagar, Gross, and Krook (BGK) method [108]. Unfortunately, the Moment methods mentioned are unable to solve problems with complex three-dimensional geometries and the BGK method is only suitable for small perturbations from equilibrium.

Other numerical methods have also seen significant progress in finding solutions of the Boltzmann equation. As a standard, and the most successful tool for studying rarefied gas flows, the DSMC method [104] has been used to simulate a wide range of problems in dilute gas flows, such as multiphase plumes [27], hypersonic vehicles [109], rarefied jets [110], and even astrophysical flows [111]. The DSMC method is a particle-based stochastic approach that can provide numerical solutions of the Boltzmann equation that governs the behaviour of dilute gases by simulating the physics of real inter-particle processes.

A large number of real atoms or molecules are represented by each statistically representative simulator particle, which reduces the computational cost of a simulation in the DSMC method. Additionally, the movements and collisions between representative particles are decoupled over a small time step, which is a valid assumption so long as the time-step remains much smaller than the local mean collision time of the gas. Gas-surface interactions, e.g. a diffuse reflection, are handled during this movement phase.

A stochastic collision process occurs after all of the particles have been moved. To achieve a realistic transfer of mass, momentum, and energy, collisions must happen between particles that are near neighbours and within distances that are smaller than the local gas mean free path. A

computational mesh is implemented to enforce this, using cells that should be smaller than the local gas mean free path. The computational cells are also used to obtain volumes for reporting on macroscopic flow parameters, such as density and temperature. All DSMC solvers obey the basic algorithm shown in Figure 3.1.

The *dsmcFoamPlus* solver in OpenFOAM, developed by White *et al.* [112], is used for all the DSMC simulations in this thesis. In *dsmcFoamPlus*, the numerical cells are separated into 8 individual collision cells using a virtual sub-cell method. When using the NTC method to determine the number of probable collision pairs, the number of particles in each cell must be adequate to minimise statistical error in the estimated collision rates; commonly, at least 20 DSMC particles per cell are required [113]. Due to changes in local number density and cell size throughout the domain, the number of DSMC particles per cell may vary. This study does not focus on the impact of collision schemes on flow fields, and only the NTC approach is considered, but alternative collision schemes, including simplified and generalised Bernoulli trial collision schemes [114, 115] are available in the literature.

Several modifications, described in Appendix A, to the *dsmcFoamPlus* solver have been made to allow numerous ensembles of the same transient simulation to be run. The number of ensembles, noted as M, is related to the fractional error of the volume-averaged quantities of interest, such as velocity E_u, density E_ρ, temperature E_T, and pressure E_p, which can be expressed as

$$E_u = \frac{1}{\sqrt{\gamma Ac^2 M N_{ppc} Ma^2}}, \tag{3.2}$$

$$E_\rho = \frac{1}{\sqrt{M N_{ppc}}} \frac{1}{Ac}, \tag{3.3}$$

$$E_T = \frac{1}{\sqrt{M N_{ppc}}} \sqrt{\frac{k_B}{c_v / N_A}}, \tag{3.4}$$

and

$$E_p = \frac{Ac\sqrt{\gamma}}{\sqrt{M N_{ppc}}}, \tag{3.5}$$

respectively, where γ is the ratio of specific heats, Ac is the acoustic number, and N_{ppc} is the average number of DSMC particles in the cell. In the current work, Ac can be approximated to 1 [116]. According to the desired fractional error of the local velocity E_u and the local flow Mach number Ma for each transient case in the DSMC method, the number of ensembles M is determined through

$$M = \frac{1}{\gamma Ac^2 N_{ppc} Ma^2 E_u^2}. \tag{3.6}$$

For example, at a Mach number of 0.1, 286 ensembles with 25 particles in each cell are required to get a 10% error in the velocity of nitrogen gas. The fractional error is decreased to 3.33%

when the local Mach number is increased to 0.3.

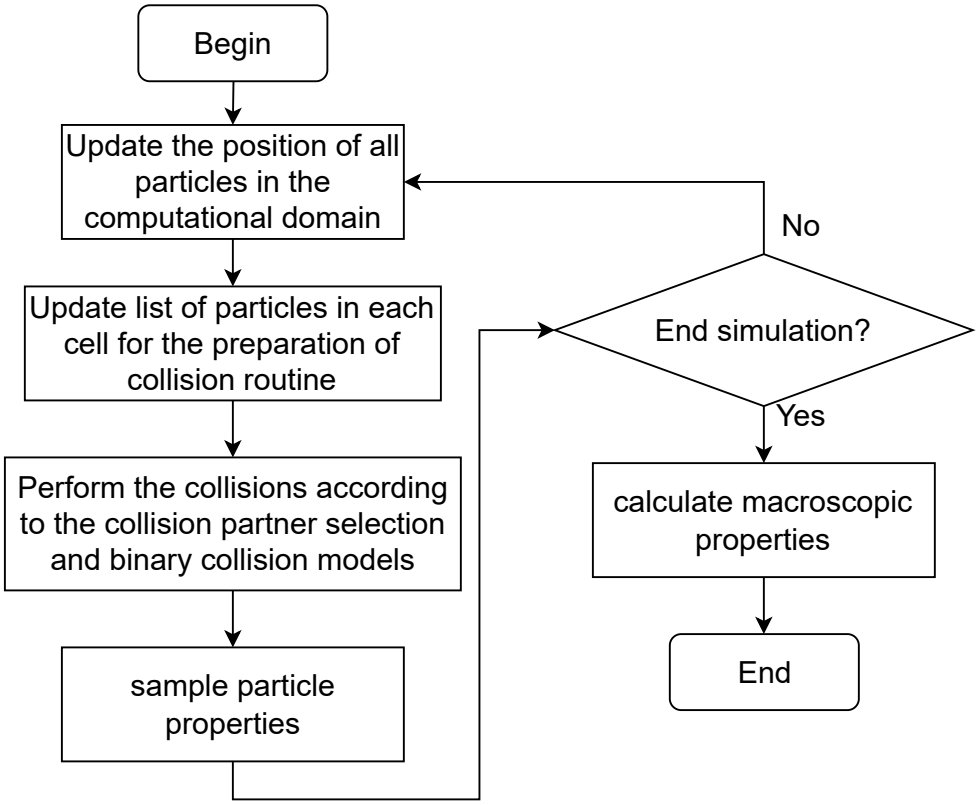

Figure 3.1: **Basic algorithm of DSMC method.**

Transient DSMC simulations are run, with the procedure outlined in Figure 3.1 applied to each case in the ensemble, after the determination of the number of ensembles, M. The procedure for acquiring ensemble averaged DSMC results through a Python script is outlined below:

Step 1. Start the first DSMC simulation according to the flow chart in Figure 3.1.

Step 2. Copy the macroscopic properties of interest and save them in a new directory called *First-Calculation*.

Step 3. Conduct the DSMC simulation again from the beginning according to the flow chart in Figure 3.1 - ensuring that a different random seed is used for each ensemble so that different results are obtained.

Step 4. Append the latest results with to those stored in *FirstCalculation*.

Step 5. Check if the number of ensemble, M, is met. If yes, go to Step 6; if no, go back to Step 3.

Step 6. Average the macroscopic properties in *FirstCalculation* and end the simulation.

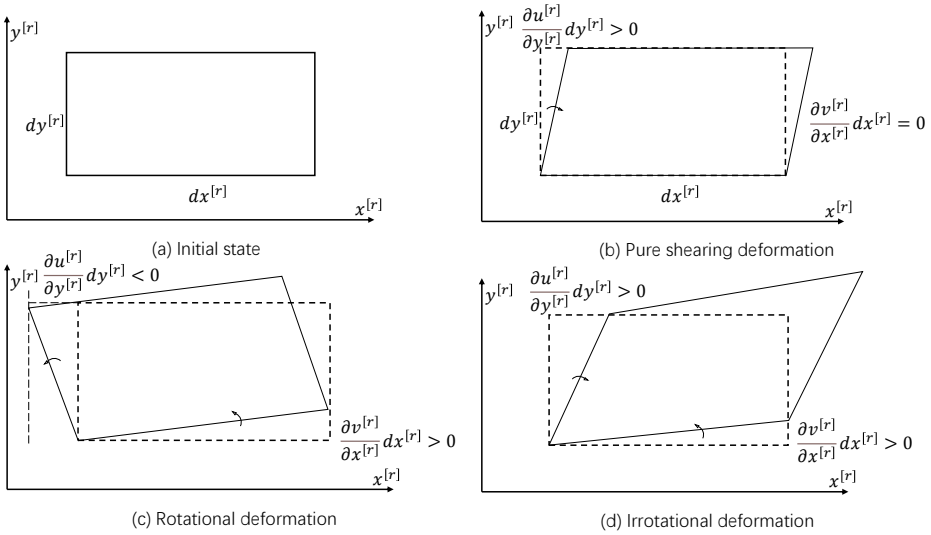

Figure 3.2: **Deformation of a 2D fluid element.**

3.3 Post-processing method: Introduction of rorticity

A vortex is traditionally defined as a connected area of relatively high vorticity that is characterised by vortex lines or tubes. Conventionally, whether vorticity is zero determines if the flow is irrotational or rotational (i.e. the angular velocity of the fluid elements is non-zero.). The strength of a vortex is quantified by the circulation, Γ [117], which is the sum of the vorticity within a closed loop in the domain. Unfortunately, this definition is imprecise, and in some cases, the presence of a vortex cannot explain the vorticity concentration. For instance, in the boundary layer of laminar flow, there is a velocity gradient along the wall's perpendicular direction so that the vorticity in this area is non-zero, but no rotational movements can be found and hence no vortex exists. Examples can also be found in the inconsistency between the vortex axis direction and the direction of vortex tubes in turbulent flow. It is unable to distinguish rotational vortical structures from a shear layer [117], because both rotation and local shear movements can create vorticity. An example is shown in Figure 3.2. The vorticity of the $x^{[r]}y^{[r]}$ plane is $\frac{\partial v^{[r]}}{\partial x^{[r]}} - \frac{\partial u^{[r]}}{\partial y^{[r]}}$ and the deformations in Figure 3.2(b)-(d) can easily create a non-zero vorticity, but not all non-zero vorticity means the fluid element is rotating. Therefore, it can be concluded that the vorticity is unable to reveal all vortical structures effectively and Liu *et al.* [118] has pointed out that vorticity should be decomposed into a rotational part and a shear part, but they did not provide any expression of this decomposition. Attempts have been made to build vortex identification criteria, such as the Q-criterion and λ_{ci}-criterion [119], but these eigenvalue-based criteria are scalars which cannot show the rotation axis and direction and they can be contaminated by shear motions. Vortex identification, such as the average co-rotation [120], is a vector, but it suffers from calculation difficulties when investigating transport properties in vortices of turbulent flows.

The theoretical work of the vorticity decomposition was performed by Tian *et.al* [117] and the new vector vortex identification is called rorticity in this work. The introduction of the rorticity can effectively separate the vorticity, $\vec{\omega}$, into a rotational part, rorticity, $\vec{R}$, and an irrotational part, the shear vector, $\vec{S}$, such that

$$\nabla \times \vec{v} = \vec{\omega} = \vec{R} + \vec{S}, \tag{3.7}$$

The rorticity is defined as "a vector quantity which represents the local fluid rotation" and its magnitude is equal to twice the fluid-rotational angular velocity (i.e. $\beta^{[r]} \pm \alpha^{[r]}$) [117], which is also named as vortex vector [117] or rortex [121], such that

$$\vec{R} = \begin{cases} 2 \times (\beta^{[r]} - \alpha^{[r]}) \times \vec{r}^{[r]}, \text{ if } {\beta^{[r]}}^2 - {\alpha^{[r]}}^2 > 0, \ \beta^{[r]} > 0 \\ 2 \times (\beta^{[r]} + \alpha^{[r]}) \times \vec{r}^{[r]}, \text{ if } {\beta^{[r]}}^2 - {\alpha^{[r]}}^2 > 0, \ \beta^{[r]} < 0 \\ 0, \text{ if } {\beta^{[r]}}^2 - {\alpha^{[r]}}^2 \leq 0 \end{cases} \tag{3.8}$$

where $\vec{r}^{[r]}$ is a unique unit vector representing the vortex local rotation axis, and

$$\beta^{[r]} = \frac{1}{2}\left(\frac{\partial v^{[r]}}{\partial x^{[r]}} - \frac{\partial u^{[r]}}{\partial y^{[r]}}\right) \tag{3.9}$$

$$\alpha^{[r]} = \frac{1}{2}\sqrt{\left(\frac{\partial u^{[r]}}{\partial x^{[r]}} - \frac{\partial v^{[r]}}{\partial y^{[r]}}\right) + \left(\frac{\partial v^{[r]}}{\partial x^{[r]}} + \frac{\partial u^{[r]}}{\partial y^{[r]}}\right)} \tag{3.10}$$

$x^{[r]}$, $y^{[r]}$, $u^{[r]}$, and $v^{[r]}$ are the x, y coordinate components and velocity components in x and y direction in a coordinate system that is perpendicular to the vortex rotation axis direction $\vec{r}^{[r]}$. Then, the shear vector is defined as

$$\vec{S} = \vec{\omega} - \vec{R}, \tag{3.11}$$

where

$$|\vec{S}| = 2\alpha^{[r]} \tag{3.12}$$

according to Ref. [121]. In their work [117], a vortex is re-defined as a connected region with non-zero rorticity.

It's worth noting that fluid rotation differs from rigid body rotation. Within the same vortex, fluid rotations allow for different rotational directions and intensities at different points [117]. Rorticity is a vector separated from the vorticity so that flow visualisation benefits from the rorticity field and rorticity lines. With the help of rorticity, a vortex can be displayed through calculating the rorticity vector field, rorticity lines, rorticity tubes, and rorticity surfaces [121].

As the derivation of the roticity is independent of the continuum assumption or the Navier-Stokes

equations and the rorticity is calculated using the gradient of the velocity field of a domain and the procedures of calculations are purely mathematical [117, 121], the roticity is applicable to any flow condition and may be considered as a component of vorticity. A Python script for calculating the rorticity and the shear vector from simulation results from OpenFOAM has been developed and more details can be found in Appendix B.

3.4 Validation

3.4.1 Rorticity calculator validation

In Section 3.3, the concept of rorticity has been introduced, and the rorticity calculator mentioned in Appendix B must be validated before conducting any post-processing and data analysis. The script is validated by studying a Burgers vortex superposed on a shearing motion [119]. As an exact solution of the Navier-Stokes equation, the velocity field of the Burgers vortex is expressed as

$$u = -\xi x - \frac{\Gamma}{2\pi r^2}\left(1 - e^{-\frac{r^2\xi}{2\upsilon}}\right) y - C\frac{\mathrm{Re}\xi}{\tilde{r}_0^2} y, \tag{3.13}$$

$$v = -\xi y - \frac{\Gamma}{2\pi r^2}\left(1 - e^{-\frac{r^2\xi}{2\upsilon}}\right) x, \tag{3.14}$$

$$w = 2\xi z, \tag{3.15}$$

where ξ is the strain rate, υ is the kinematic viscosity, and the last term on the right hand side of the x-component of velocity is a shearing motion superposed on to the vortex field. C is a user-defined constant, Re is the Reynolds number which is defined as $\mathrm{Re} = \Gamma/(2\pi\upsilon)$, $\tilde{r}_0$ is a non-dimensional vortex size, equal to 1.5852. C, Re, ξ, and the circulation are given as 1, 10, 1, and 63 m^2/s, respectively, in the validation. The spatial resolution in the XY plane is 250×250.

Figure 3.3(a) shows the contours of constant vorticity from the rorticity calculator, and the result agrees well with that in Figure 3.3(b) from Ref. [119]. Only the $z-$component of the rorticity is nonzero here. Figure 3.4 is plotted along $x = 0$ in Figure 3.3(a), and shows that the sum of the $z-$ component of rorticity and shear vectors is equal to the $z-$ component of the vorticity vector, proving the accuracy of the rorticity calculator that has been implemented in the post-processing of this chapter.

3.4.2 Mesh and time-step independence study of CFD

Because the *hy2Foam* solver is based on the traditional CFD approach, a mesh and time-step independence study with varied mesh level and time-step conditions is performed at $Kn = 0.005$ and $Ma_s = 1.6$ to confirm that the discretisation errors have been minimised. Figure 3.5 presents the computational geometry. A first-order implicit Euler scheme is used to discretise the time

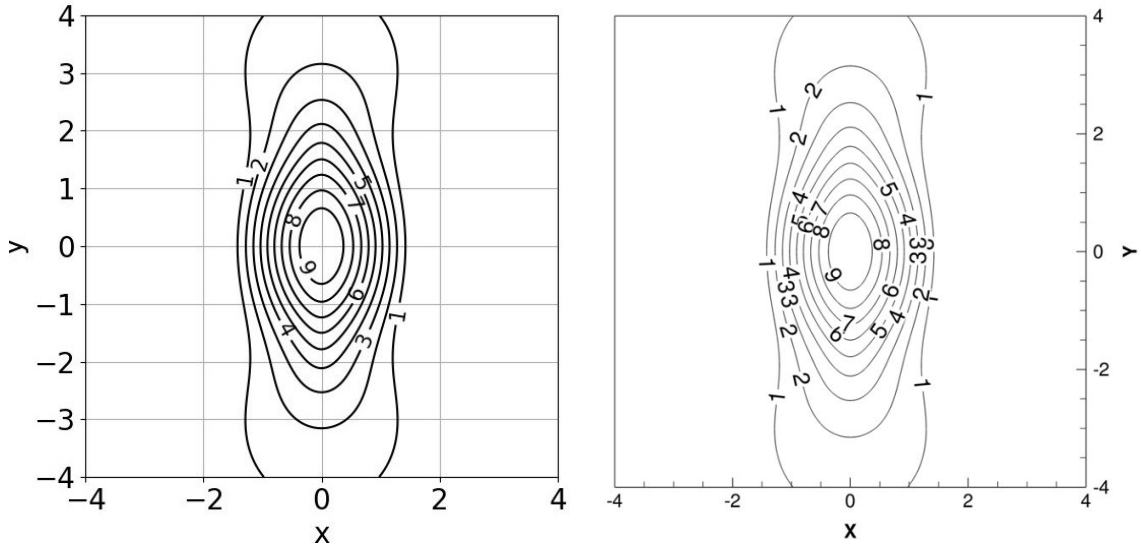

Figure 3.3: **Comparison of contours of constant vorticity in a Burgers vortex in the XY plane calculated from (a) the rorticity calculator used in the current work, and (b) from Ref. [119].**

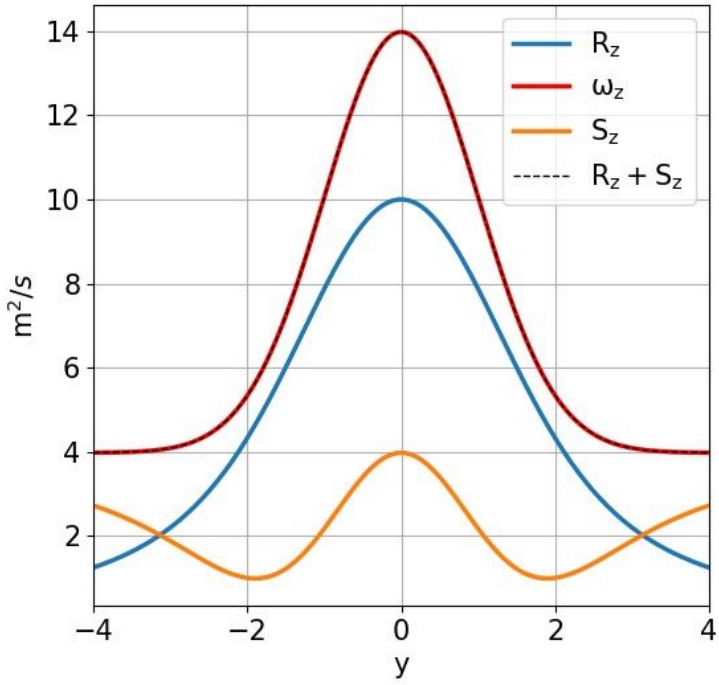

Figure 3.4: $z-$**component of vorticity** $\vec{\omega}_z$**, rorticity** $\vec{R}_z$**, shear vector** $\vec{S}_z$**, and the sum of the rorticity and shear vector** $\vec{R}_z + \vec{S}_z$ **along a 1D line through the Burgers vortex.**

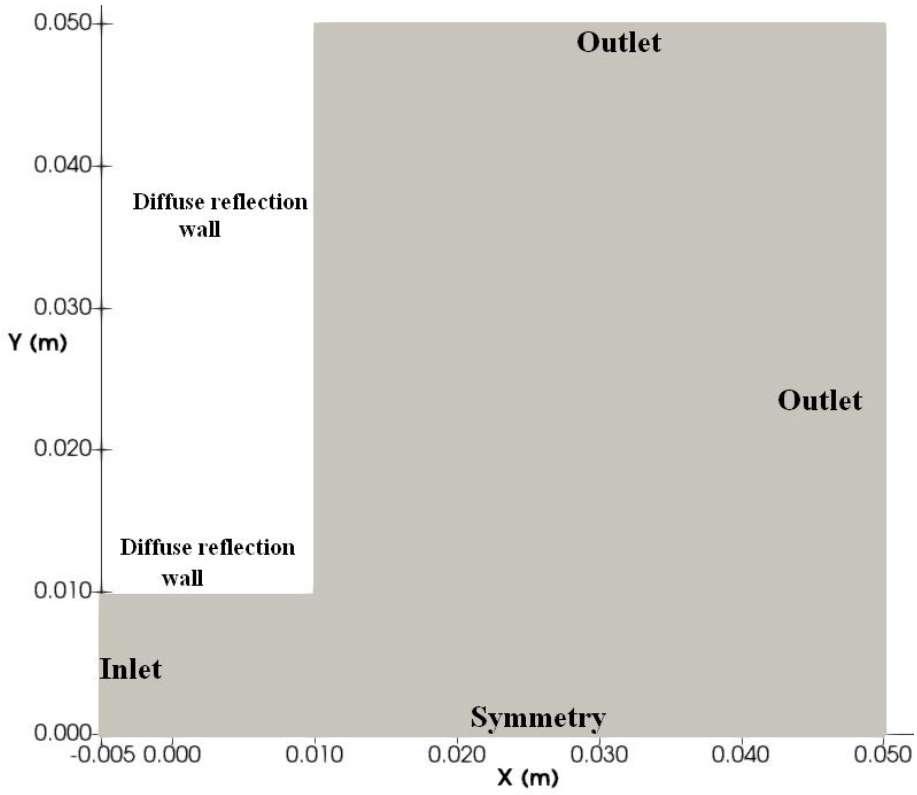

Figure 3.5: **The computational domain used to perform the simulations of vortex loop formation in rarefied conditions.**

derivative, and a second-order central-upwind differencing scheme is used to discretise the gradient terms, divergence terms, and diffusive terms, as well as to interpolate the cell centre values to the cell faces.

Table 3.1: **Mesh and time-step independence study.**

Case label	Mesh name	Grid resolution (mm)	Time-step (s)
A	Coarse	1.0	5×10^{-8}
B	Medium	0.33	5×10^{-8}
C	Fine	0.25	1×10^{-7}
D	Fine	0.25	5×10^{-8}
E	Fine	0.25	2.5×10^{-8}

Three levels of grid sizes and time-steps were tested, as shown in Table 3.1. The computational domain is large enough to avoid contact between the primary shock wave and the wall. The axial pressure profile at 0.1 ms has been plotted in Figure 3.6.

No distinguishable difference between the results of cases B and C is observed. As the computational cost of the fine mesh is acceptable and it has better spatial resolution, the fine mesh with a grid size of 0.25 mm is used in all the CFD cases in this chapter. The pressure distributions of cases C-E with the variation of time-steps agree well. A time step of 5×10^{-8} s is selected for all of the *hy2Foam* cases to ensure that the Courant–Friedrichs–Lewy (CFL) number is in the

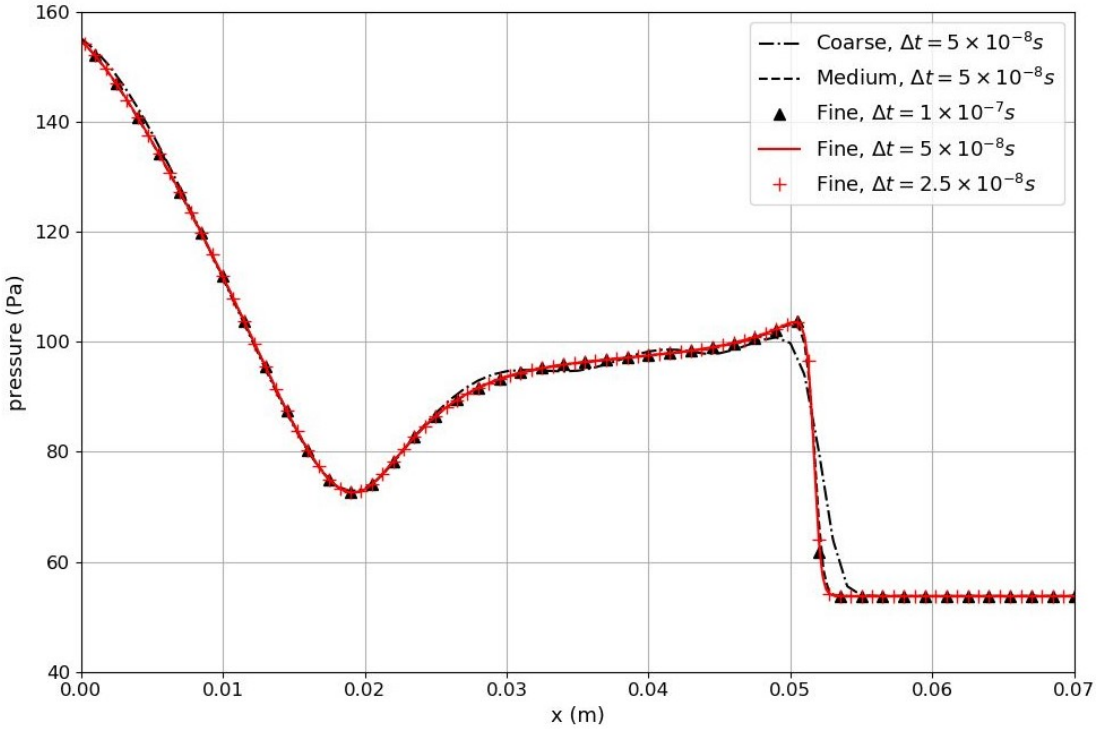

Figure 3.6: **Axial pressure distribution at $t = 0.1$ ms, for different mesh densities and time steps.**

vicinity of 0.1.

3.5 Simulation detail

The working gas of the simulations is nitrogen, and the non-dimensional characteristics, such as the Knudsen number and the Reynolds number, are calculated using the semi-height of the shock tube, which is 10 mm. The mean free path of the Knudsen number is determined based on the parameters of the primary shock wave within the shock tube. The macroscopic parameters, including pressure, temperature, and velocity, of each simulation are calculated using the Rankine–Hugoniot relations; the simulation setup is presented in Tables 3.2 and 3.3.

In the *dsmcFoamPlus* solver, the NTC method is used for collision partner selection, and the variable hard sphere model with Larsen-Borgnakke energy redistribution is used to perform the collisions. The inverse rotational energy collision number is 5. Again, the planar two-dimensional computational domain is shown in Figure 3.5. It is known that the decrease in the Knudsen number will increase the computational cost, so that the size of the domain downstream of the shock tube exit changes with different cases. As an illustration, the DSMC case of $Kn = 0.005$ is the most computationally expensive one, so the domain outside the shock tube exit is the smallest.

Table 3.2: **DSMC case parameters.**

Case number	1	2	3
Knudsen number Kn	0.005	0.025	0.05
Shock Mach number Ma_s		1.6	
Inlet flow velocity $\vec{v}_{inlet}$ (m/s)		(277.7274 0 0)	
Shock Reynolds number Re_s	168.72	33.75	16.87
Inlet pressure p_2 (Pa)	152.6314	30.3291	15.1645
Outlet pressure p_1 (Pa)	53.77	10.755	5.3775
Inlet number density n_{inlet} (m^{-3})	2.8159×10^{22}	5.6323×10^{21}	2.8161×10^{21}
Outlet number density n_{outlet} (m^{-3})	1.39×10^{22}	2.7722×10^{21}	1.386×10^{21}
Temperature after shock T_2 (K)		390.0192	
Temperature before shock T_1 (K)		281	
Time step Δt (s)		1×10^{-7}	
Number of samples	620	2000	2500
Case number	4	5	6
Knudsen number Kn	0.125	1.25	12.5
Shock Mach number Ma_s		1.6	
Inlet flow velocity $\vec{v}_{inlet}$ (m/s)		(277.7274 0 0)	
Shock Reynolds number Re_s	6.75	0.67	0.07
Inlet pressure p_2 (Pa)	6.0658	0.60658	0.06066
Outlet pressure p_1 (Pa)	2.151	0.2151	0.02151
Inlet number density n_{inlet} (m^{-3})	1.1265×10^{21}	1.1265×10^{20}	1.1265×10^{19}
Outlet number density n_{outlet} (m^{-3})	5.5443×10^{20}	5.5443×10^{19}	5.5443×10^{18}
Temperature after shock T_2 (K)		390.0192	
Temperature before shock T_1 (K)		281	
Time step Δt (s)		1×10^{-7}	
Number of samples	2205	2205	3000

Table 3.3: **CFD case parameters.**

Case number	1	2	3	4	5
Kn			0.005		
Ma_s	1.3	1.4	1.5	1.6	2.0
u_{inlet} (m/s)	151.1889	195.3248	237.3839	277.7274	427.273
Re_s	99.05	124.58	147.68	168.72	235.21
p_2 (Pa)	125.267	133.56	142.3375	151.6314	193.05
p_1 (Pa)	69.4	63	57.9	53.77	42.9
T_2 (K)	334.6352	352.569	370.9807	390.0192	474.1875
T_1 (K)			281		

3.6 Results and discussions

3.6.1 Vortex loop structure

According to the normalised density gradient, $\nabla\rho/|\nabla\rho|_{\max}$, pseudo-schlieren images at $t = 0.16$ ms from *hy2Foam* are presented in Figure 3.7. No apparent shock structure within the vortex loop can be found, as can be seen in Figure 3.7(a)-3.7(b), until the shock Mach number reaches 1.5. Brouillette and Hébert [65] first observed that the vortex loop is shock-free when the shock Mach number is lower than 1.43. This conclusion is still valid in the near continuum regime. A weak embedded shock wave appears inside the vortex loop when the shock Mach number exceeds 1.5, and its strength climbs as the shock Mach number increases, as shown in Figure 3.9.

The intensified pseudo-schlieren images for $Kn = 0.005 - 0.05$, from *dsmcFoamPlus*, are shown in Figure 3.8. The shock wave thickness is positively correlated to the Knudsen number. In comparison with the shock thickness from CFD in Figure 3.7(d), the shock wave thickness in Figure 3.8(a) at $Ma_s = 1.6$ calculated from DSMC is thicker, which was also noted in Ref. [122]. Shock wave thickness is known to increase with flow rarefaction level, and the Navier-Stokes equations are not capable of capturing this physics. The vortex-induced shock pair appears due to high velocity within the shear layer of the primary vortex loop in the continuum flow regime, as demonstrated in experiments [63, 78] and simulations [8, 72]. From the schlieren images, it can be found that the vortex-induced shock pairs and oblique shocks in the primary vortex loop degenerate and disappear under the rarefied environment. Embedded shock waves and shear layers are still visible in Figure 3.7 and Figure 3.8(a) in the near continuum flow regime. The embedded shock and the shear layer degrade further as the Knudsen number grows. In addition, the thickness increase of the shock waves and mistiness in the CRVR images in Chapter 2 during the expansion of supersonic starting jets in low-pressure environments have been observed. It can be concluded that the internal structures of the compressible vortex loop will be simplified as the rarefaction level increases.

3.6.2 Characteristics of the flowfield

Velocity and pressure field comparisons

Comparisons of the axial speed and pressure distribution for $Kn = 0.005$ and $Kn = 0.025$ with $Ma_s = 1.6$ at $t = 0.16$ ms from both *hy2Foam* and *dsmcFoamPlus* are shown in Figure 3.10. Except for the underestimation of the primary shock wave thickness, the axial velocity and pressure distributions from the two solvers agree well in the near continuum regime.

Boyd [123] suggested a parameter called the local gradient-length Knudsen number for measuring the level of local continuum breakdown, and an improved expression was proposed in

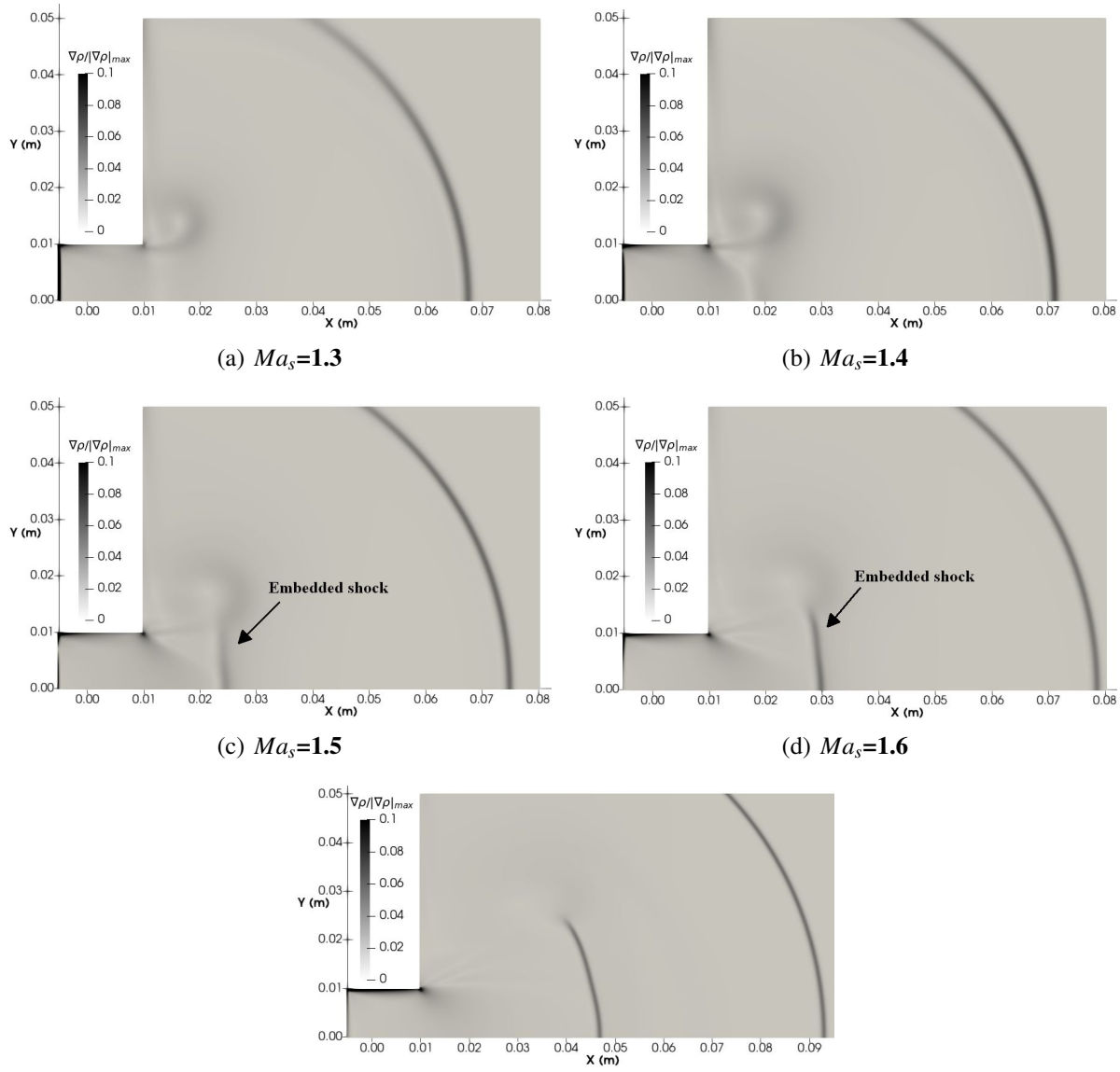

(a) Ma_s**=1.3**

(b) Ma_s**=1.4**

(c) Ma_s**=1.5**

(d) Ma_s**=1.6**

(e) Ma_s**=2.0**

Figure 3.7: (a) - (e) **Comaprison of pseudo-schlieren images for** $Kn = 0.005$ **at** $t = 0.16$ **ms from the CFD. The value of** $\nabla\rho/|\nabla\rho|_{\max}$ **is limited to 0.1 for visualisation purposes.**

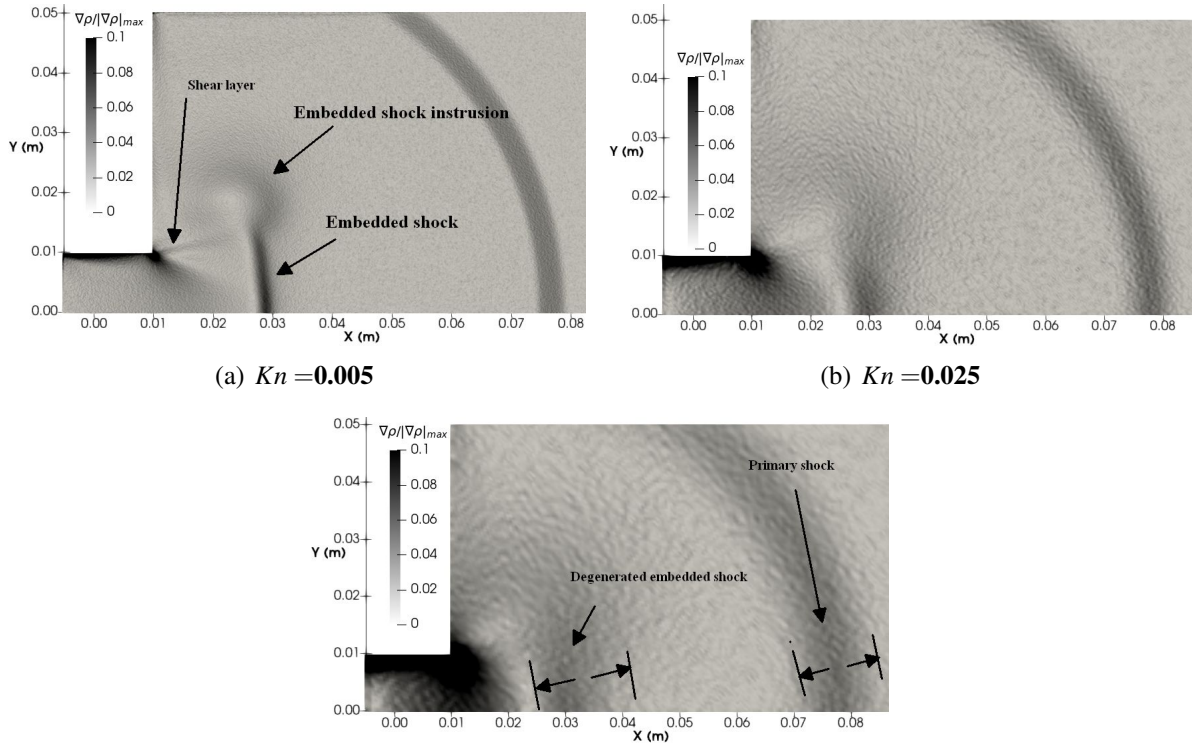

(a) Kn =**0.005** (b) Kn =**0.025**

(c) Kn =**0.05**

Figure 3.8: (a) - (c) **Comaprison of pseudo-schlieren images at** t =**0.16 ms for** $Ma_s = 1.6$ **from the DSMC solver.**

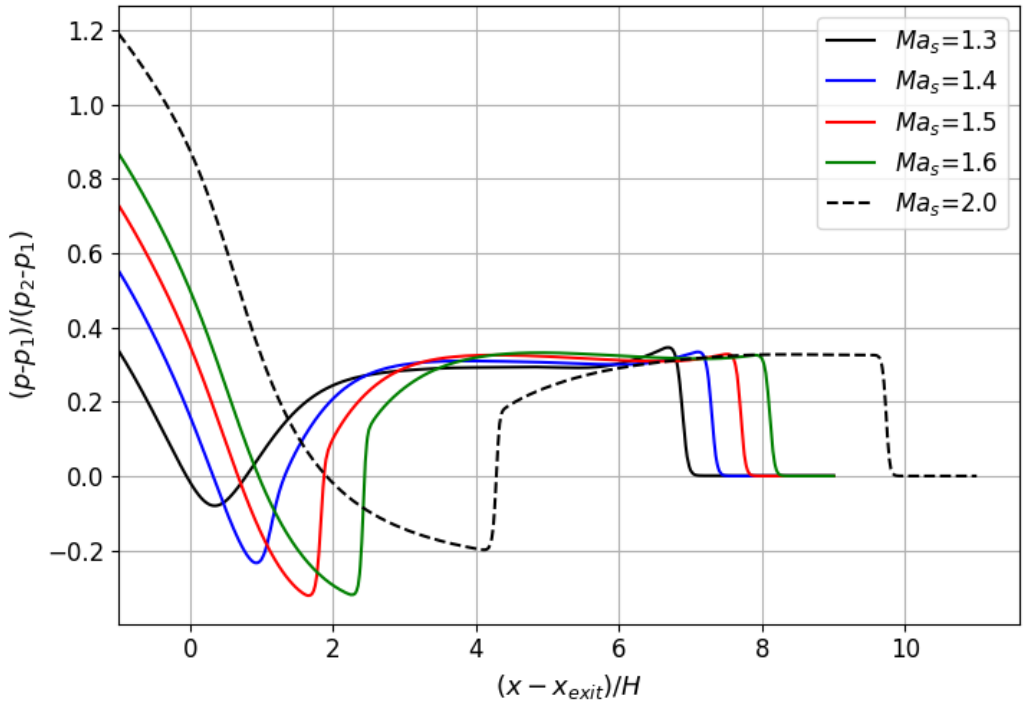

Figure 3.9: **Dimensionless axial pressure distributions at** $t = 0.19$ **ms for different shock Mach numbers, as predicted by *hy2Foam*.** x_{exit} **is the** x**-coordinate of the shock tube exit.**

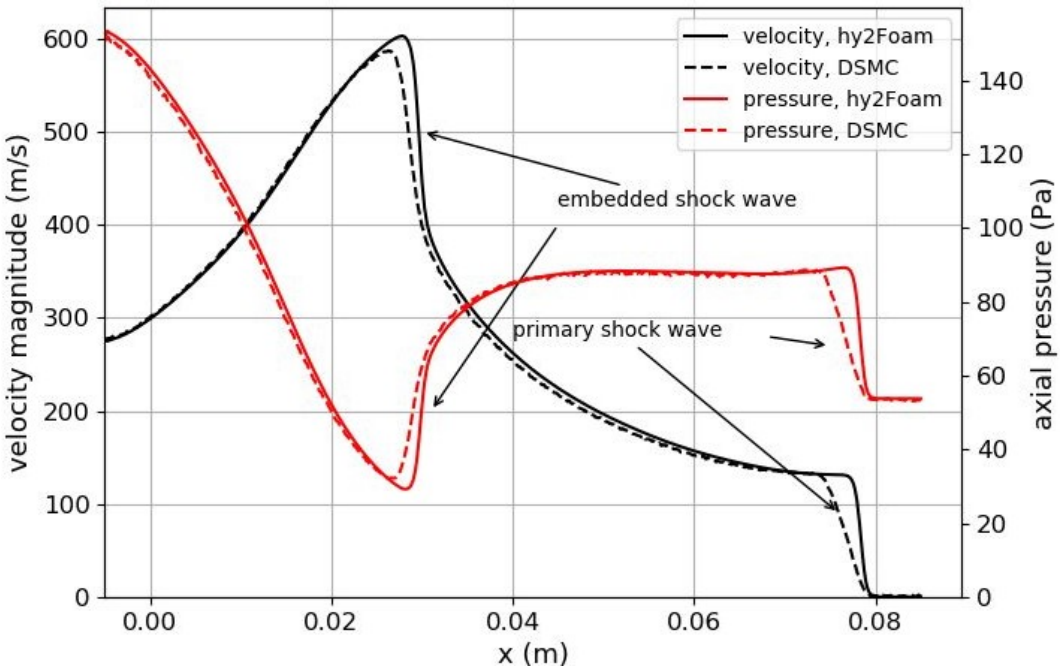

(a) **Kn=0.005**

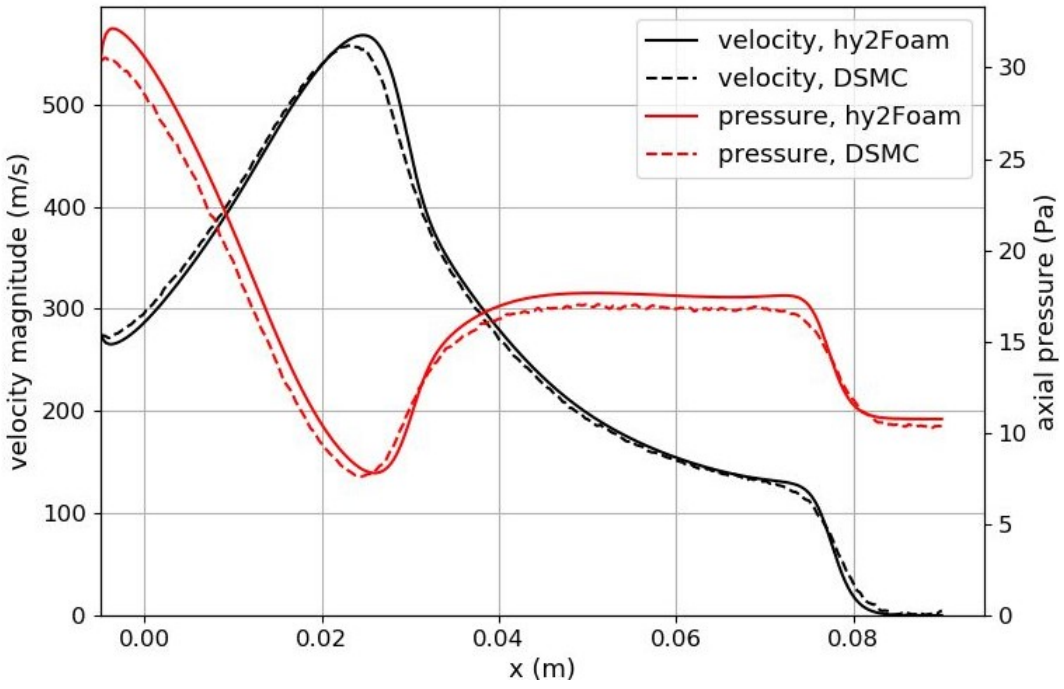

(b) **Kn=0.025**

Figure 3.10: **Axial velocity magnitude and pressure comparisons of the results from *hy2Foam* and *dsmcFoamPlus* at $t = 0.16$ ms for (a) $Kn = 0.005$ and (b) $Kn = 0.025$ with $Ma_s = 1.6$.**

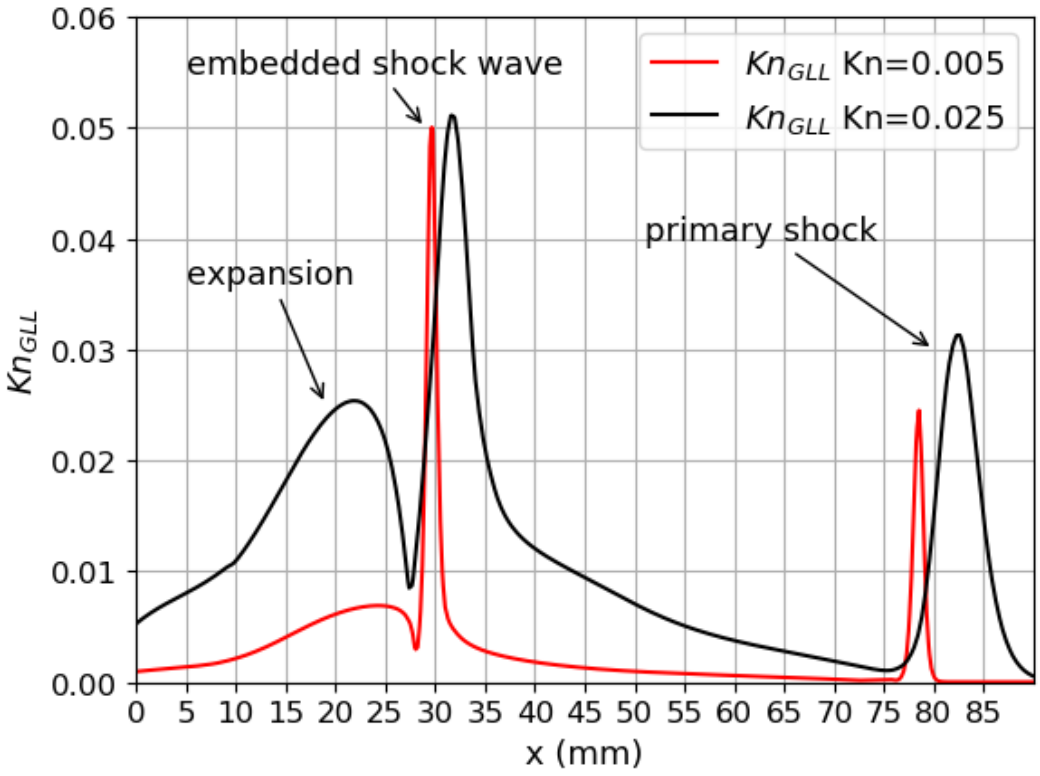

Figure 3.11: **Axial Kn_{GLL} distribution of $Kn = 0.005$ and $Kn = 0.025$ from *hy2Foam*.**

Ref. [103]:

$$Kn_{GLL} = \max(Kn_{GLL-\rho}, Kn_{GLL-T}, Kn_{GLL-|\vec{v}|}, 5 \times \frac{T_t - T_{rot}}{T_{rot}}), \tag{3.16}$$

where $Kn_{GLL-\phi}$ is the local gradient-length Knudsen number based on macroscopic property ϕ, T_t is the local translational temperature and T_{rot} is the local rotational temperature. The axial profile of Kn_{GLL} is presented in Figure 3.11. The local Knudsen number increases in the expansion at the exit and surges in the embedded and primary shock wave. The peaks of Kn_{GLL} are approximately at $x = 0.03$ m and $x = 0.077$ m for $Kn = 0.005$ and $x = 0.032$ m and $x = 0.083$ m for $Kn = 0.025$, which coincide with the positions of the discrepancies, where the embedded and the primary shock wave are located in Figure 3.10. Through comparison between Figures 3.10 and 3.11, the difference in the axial pressure and speed in Figure 3.10 from the two solvers can be explained as a result of the increase in local rarefaction level, especially in the primary shock and the embedded shock. In addition, the peak of Kn_{GLL} in the case of $Kn = 0.025$ is higher than that of $Kn = 0.005$ and this explains the more obvious inconsistency of the results from two solvers in Figure 3.10(b).

Figure 3.12 plots the normalised axial pressure distribution at $t = 0.12$ ms. As previously concluded, the escalation of Knudsen number attenuates and thickens the primary shock wave and the weak embedded shock, as shown in Figure 3.8, which is distinct in the slip flow regime ($Kn < 1$). As the flow gradually approaches the transition regime, the shock wave strength

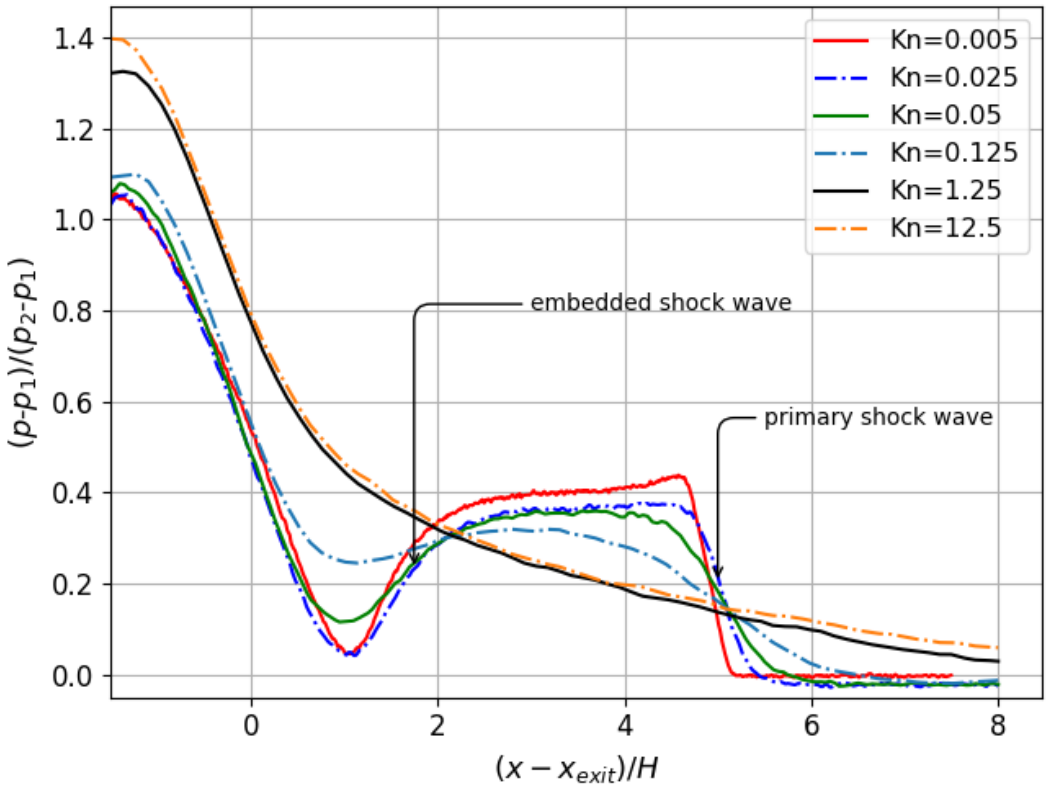

Figure 3.12: **Rarefaction effect on normalised axial pressure distribution at** $t = 0.12$ **ms from *dsmcFoamPlus*.** x_{exit} **is the** $x-$ **coordinate of the tube exit.**

drops. The distinct normalised pressure gradient due to the two weak shock waves is only distinguishable at $Kn = 0.005$, $Kn = 0.025$, and $Kn = 0.05$. The axial pressure distribution profile of higher Knudsen number regimes differs from that of slip flow. The normalised pressure distribution in the transition regime, $Kn = 1.25$, remarkably resembles that of the free-molecule flow, $Kn = 12.5$; in both cases, the flow expands smoothly, and the primary shock wave and the embedded shock wave in the slip flow regime have disappeared and degenerated to a smooth pressure expansion.

Rorticity and shear vector field

In Section 3.3, it is mentioned that the rorticity can be decomposed into a rorticity and a shear vector. Hence, the vorticity field around and within the vortex atmosphere, which is formed by closed-loop streamlines, can be decomposed into a rorticity field and a shear vector field, and the movement of the fluid in a computational cell can be understood. It is noteworthy that the Euler description of fluid motion can still be used to observe fluid motions in rarefied conditions. Figures 3.13 and 3.14 show contours of the rorticity field and streamlines around the vortex loop before and after the formation of the isolated rorticity region with different shock Mach numbers in the near continuum flow regime, as calculated by the two solvers. The comma-like shape of the rorticity loop cross-section is changed to a mushroom shape due to the increase in the shock

Mach number.

Interestingly, the fluid in the cells within the expansion fan is fluid-rotational, especially at the sharp corner. It's worthwhile to mention that when the shock Mach number is above 1.4, the local intensity of fluid rotation at the corner is stronger than that at the vortex centre. The rorticity magnitude equals twice the fluid-rotational angular velocity, according to Equation (2.22) in Ref. [117]. The large rorticity magnitude at the corner of the expanding fan indicates that the fluid in this region undergoes a considerable increase in rotational kinetic energy. This may imply that the internal energy is transformed to kinetic energy as a result of expansion at a sharp corner through fluid-rotation.

The shapes of the rorticity loop cross-section from *hy2Foam* and *dsmcFoamPlus*, shown in Figures 3.14(a)-3.14(d) are in good agreement. The periphery of the rorticity loop cross-section from both solvers is not perfectly consistent, and this may be caused by an insufficient number of ensemble samples of the case with the *dsmcFoamPlus* solver. It is not anticipated that the rorticity loop cross-section covers the core and most of the vortex atmosphere rather than the whole vortex atmosphere. This can also be observed and supported by the Direct Numerical Simulation result of a 2D Blasius-profile mixing layer flow in Ref. [117] for the validation of the rorticity calculation. However, if a vortex is stationary, such as in a Taylor-Green vortex sheet or a Burgers vortex, which means that the vortex rotational axis does not move in the radial direction, the corresponding rorticity field always overlaps with the vortex atmosphere. Therefore, it can be concluded that the rorticity field does not coincide with the vortex atmosphere when the vortex translates.

The shear layer with strong velocity gradient in the radial direction close to the nozzle exit mentioned in Section 2.1.3 is usually called a vortex sheet [39, 74, 124] and according to Equation (3.7), the vorticity inside the vortex sheet can be separated into a rorticity sheet, as in Figures 3.13-3.14, and a shear vector sheet, as shown in Figure 3.15. In Figure 3.15, shear movement intensity within the boundary layer and the vortex sheet is stronger than that of the vortex atmosphere. The fluid in the periphery of the vortex core is dominated by shear movements, and even the vortex core of the vortex atmosphere is under the influence of the shear vector field. This indicates that fluid in the vortex atmosphere core rotates and shears at the same time, but the rotational movement plays a leading role.

3.6.3 Evaluation of the rotational strength of the vortices

The strength of a vortex is usually measured by circulation, denoted as Γ, and can be expressed as

$$\Gamma = \oint_L \vec{v} \cdot d\vec{l} = \oint_A \vec{\omega} \cdot d\vec{A}. \tag{3.17}$$

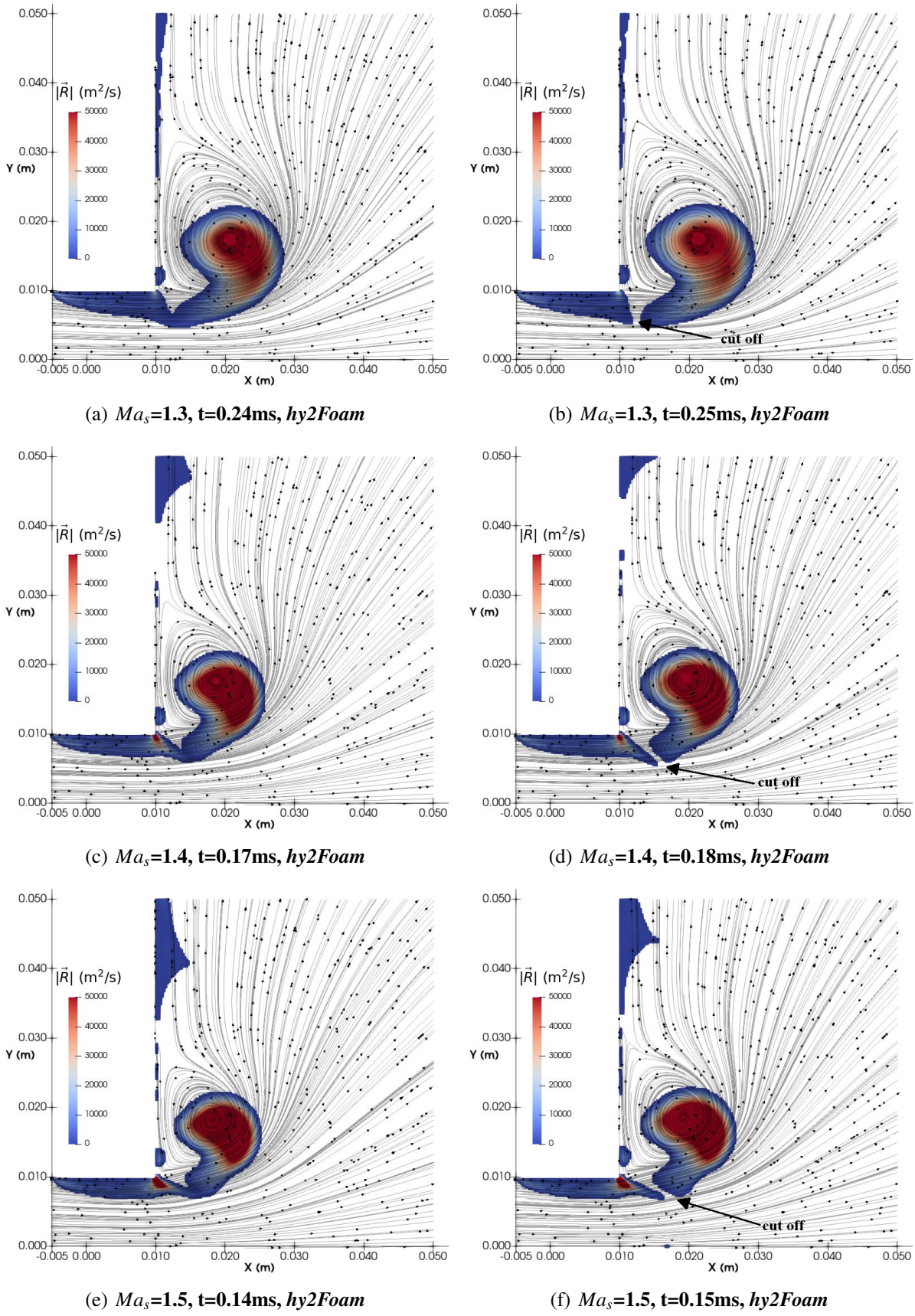

(a) Ma_s=1.3, t=0.24ms, ***hy2Foam***

(b) Ma_s=1.3, t=0.25ms, ***hy2Foam***

(c) Ma_s=1.4, t=0.17ms, ***hy2Foam***

(d) Ma_s=1.4, t=0.18ms, ***hy2Foam***

(e) Ma_s=1.5, t=0.14ms, ***hy2Foam***

(f) Ma_s=1.5, t=0.15ms, ***hy2Foam***

Figure 3.13: **Rorticity magnitude field and streamlines calculated by *hy2Foam* at *Kn* = 0.005 before and after the formation of the isolated rorticity region. The rorticity magnitude, $|\vec{R}|$, is limited to 5 $\times$ 10^4 m^2/s to aid field visualisation.**

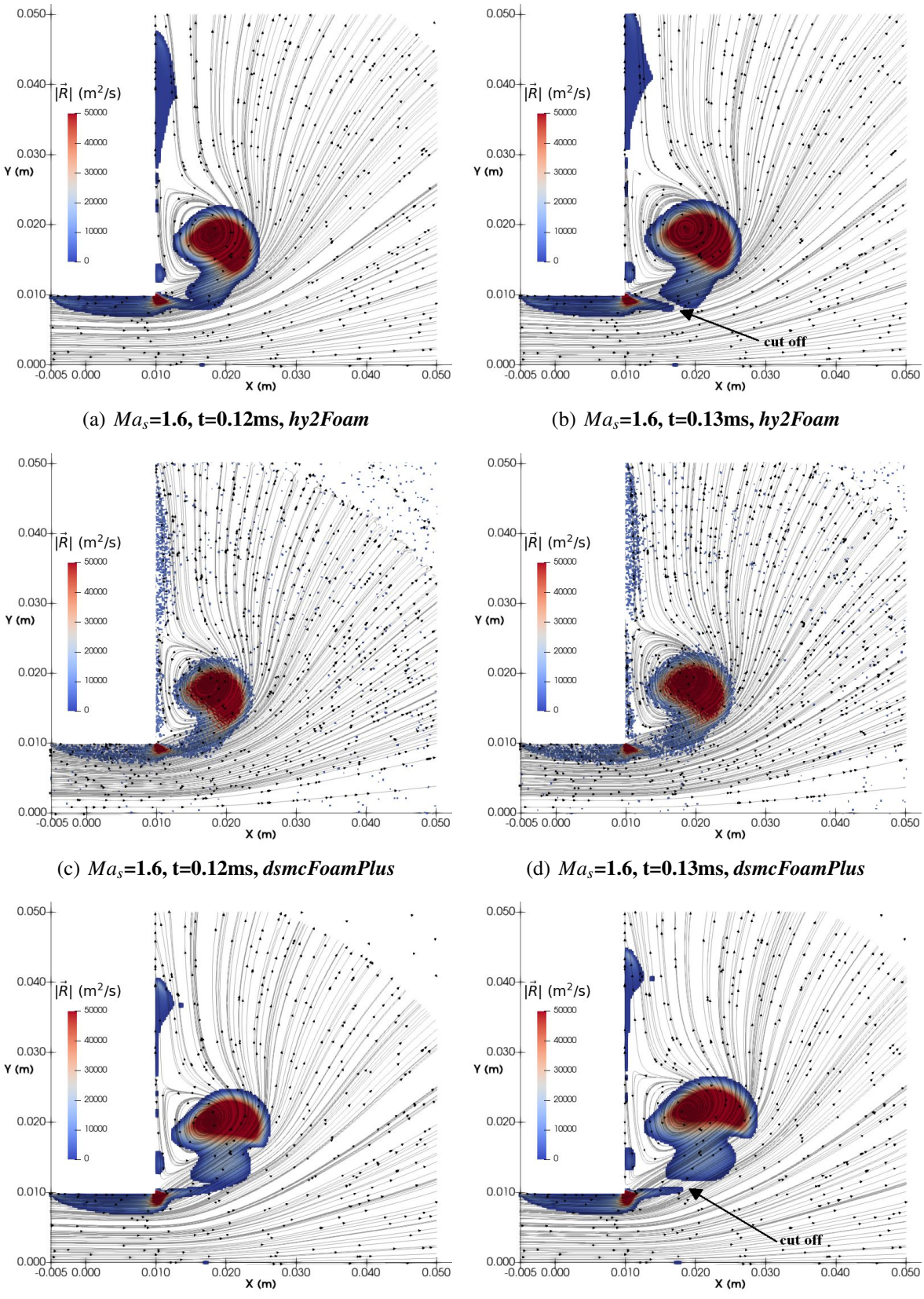

(a) Ma_s=1.6, t=0.12ms, ***hy2Foam***

(b) Ma_s=1.6, t=0.13ms, ***hy2Foam***

(c) Ma_s=1.6, t=0.12ms, ***dsmcFoamPlus***

(d) Ma_s=1.6, t=0.13ms, ***dsmcFoamPlus***

(e) Ma_s=2.0, t=0.09ms, ***hy2Foam***

(f) Ma_s=2.0, t=0.1ms, ***hy2Foam***

Figure 3.14: **Rorticity magnitude field and streamlines with Kn = 0.005 before and after the formation of the isolated rorticity region. The rorticity magnitude, $|\vec{R}|$, is limited to 5 $\times$ 10^4 m^2/s and the lower limit of $|\vec{R}|$ in the *dsmcFoamPlus* results is 6800 m^2/s to aid field visualisation.**

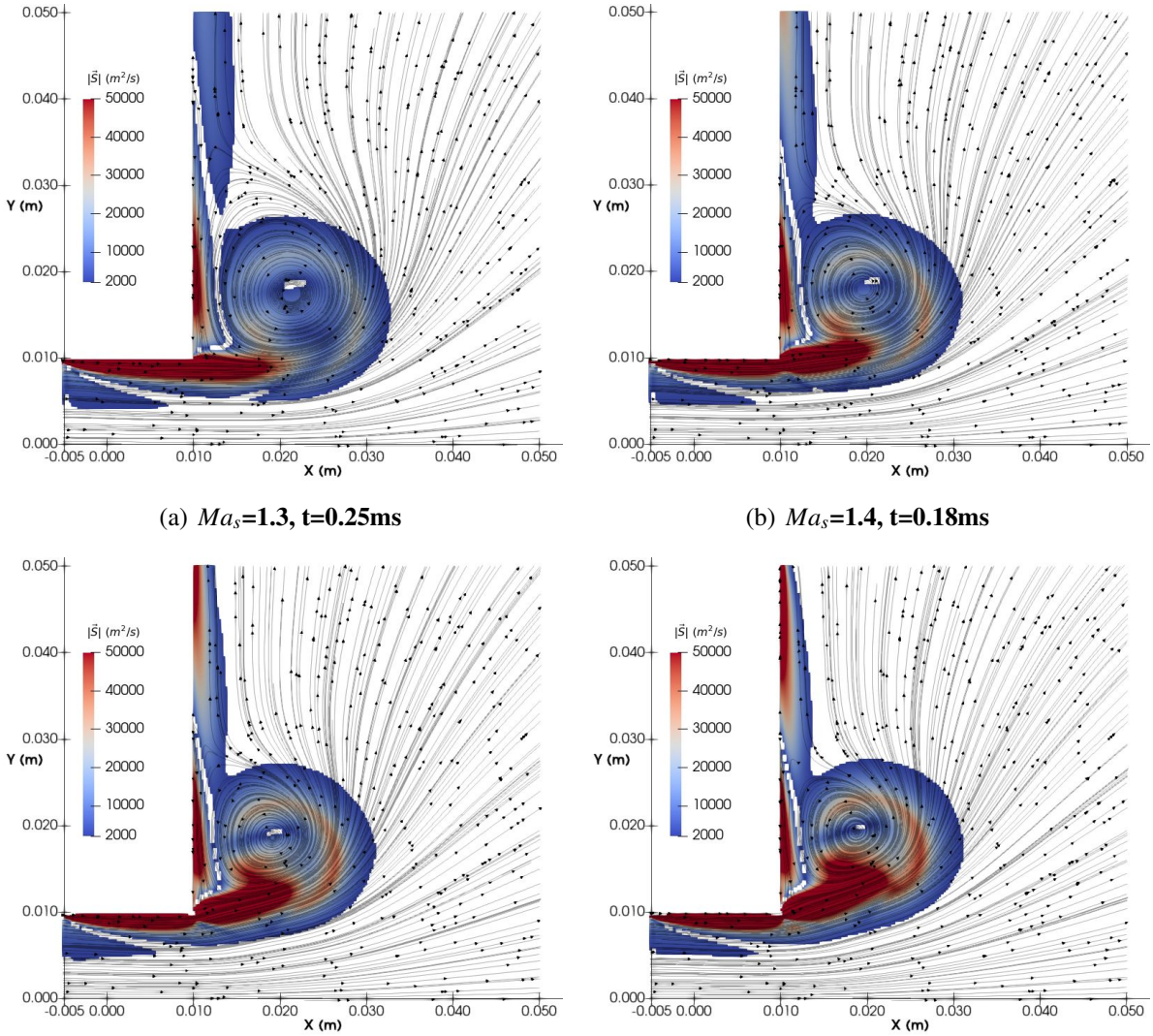

(a) Ma_s=**1.3, t=0.25ms**

(b) Ma_s=**1.4, t=0.18ms**

(c) Ma_s=**1.5, t=0.15ms**

(d) Ma_s=**1.6, t=0.13ms**

Figure 3.15: (a) - (d) **Shear vector field and streamlines calculated by *hy2Foam* with Kn = 0.005. The magnitude of the shear vector has been limited between 2** $\times 10^3$ **and 5** $\times 10^4$ m^2/s **to aid field visualisation.**

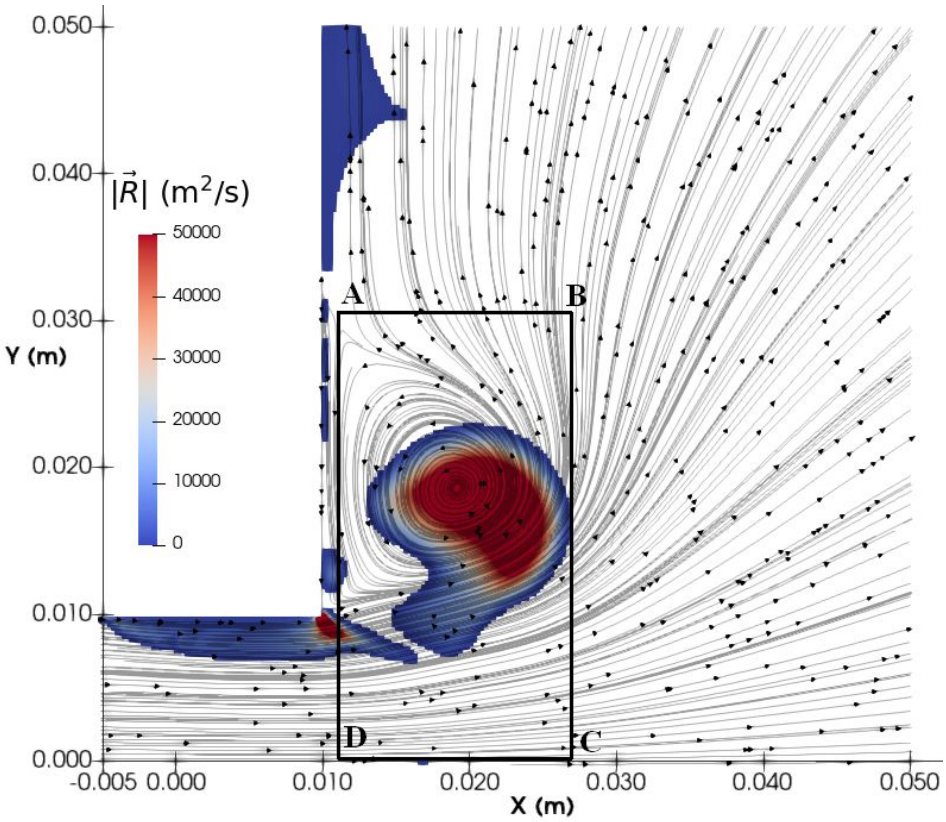

Figure 3.16: **Circulation circuit.**

Circulation is determined by taking a closed circuit around the vortex atmosphere that includes the isolated rorticity loop cross-section; circuit ABCDA shown in Figure 3.16 is an example. Substituting Equation (3.7) into Equation (3.17), the following is obtained:

$$\Gamma = \oint_A \vec{\omega} \cdot d\vec{A} = \oint_A \left(\vec{R} + \vec{S}\right) \cdot d\vec{A}, \tag{3.18}$$

and thereby

$$\Gamma = \int_A \vec{R} \cdot d\vec{A} + \int_A \vec{S} \cdot d\vec{A}. \tag{3.19}$$

Equation (3.19) suggests two properties representing the rotational strength and shear strength of a vortex as a result of the decomposition of circulation. Rorticity is a unique local vector that describes the intensity of the fluid-rotational movement or rotational deformation within the fluid domain [117]. Rorticity coincides with the local rotation axis and the rorticity line crosses the vortex cross-section. Subsequently, analogous to the definition of circulation and the expression in Equation (3.17), a new flux, called rorticity flux Φ_R, can be defined as

$$\Phi_R = \int_A \vec{R} \cdot d\vec{A}. \tag{3.20}$$

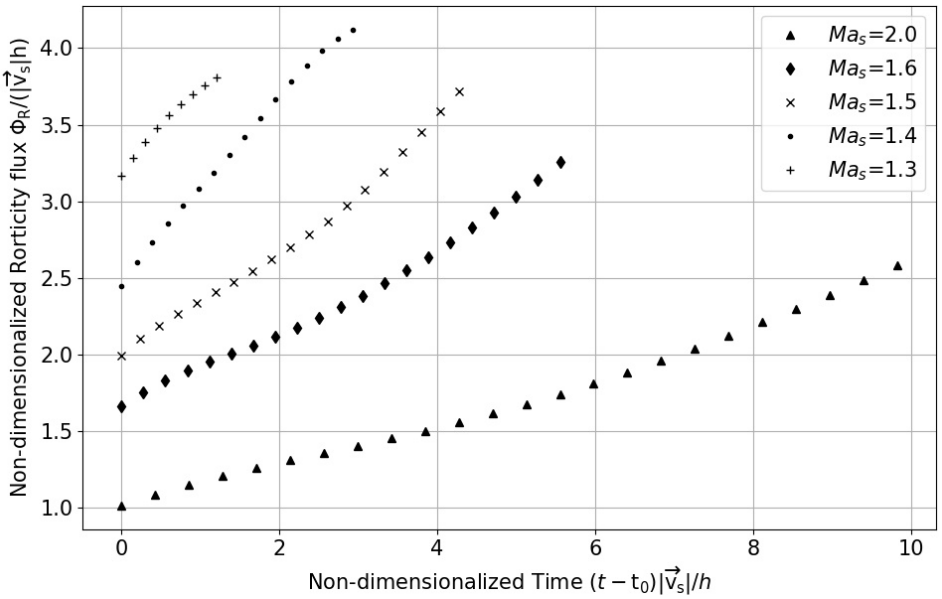

Figure 3.17: ***hy2Foam* results of non-dimensional rorticity flux at $Kn = 0.005$. $|\vec{v}_s|$ is the initial shock velocity inside the shock tube and h is the characteristic length, which is equal to semi-height of the tube. t_0 is the time that the rorticity loop formed and it is 0.25 ms, 0.18 ms, 0.15 ms, 0.13 ms, 0.1 ms for $Ma_s = 1.3$, $Ma_s = 1.4$, $Ma_s = 1.5$, $Ma_s = 1.6$, $Ma_s = 2.0$, respectively.**

This flux quantifies the vortex rotational intensity in fluid dynamics. The rorticity flux can be used to estimate the potential propagation ability of a moving vortex. A non-zero rorticity means the existence of a vortex, and the non-zero rorticity flux means that a vortex can propagate in a direction. The second term on the right hand side of Equation (3.19) can be named the shear vector flux

$$\Phi_S = \int_A \vec{S} \cdot d\vec{A}, \tag{3.21}$$

which can be used to quantify the strength of the shear movements in a vortex.

The dimensionless rorticity flux and circulation are plotted in Figures 3.17 and 3.18, respectively. The non-dimensionalised rorticity flux distribution with time changes when the shock Mach number exceeds a value in the range of 1.4 to 1.5. The units of the circulation and the rorticity flux are the same, and the magnitude of dimensionless circulation is much larger than that of dimensionless rorticity flux because the vorticity lacks movement-resolving ability. Equation (3.19) shows that both rotation and shear within a vortex loop are critical during its formation and evolution. The feature of non-linear growth of rorticity flux magnitude with time during the vortex formation is not observed in the circulation, as shown in Figure 3.18, around the vortex atmosphere [124]. The circulation of a vortex loop is usually calculated according to a manually selected circuit along the symmetry axis [74] and this circuit should cover the vortex atmosphere [124]. In addition, the lack of strict rules on the limitation of this circuit size will cause the introduction of errors. One advantage of the rorticity vector is its ability

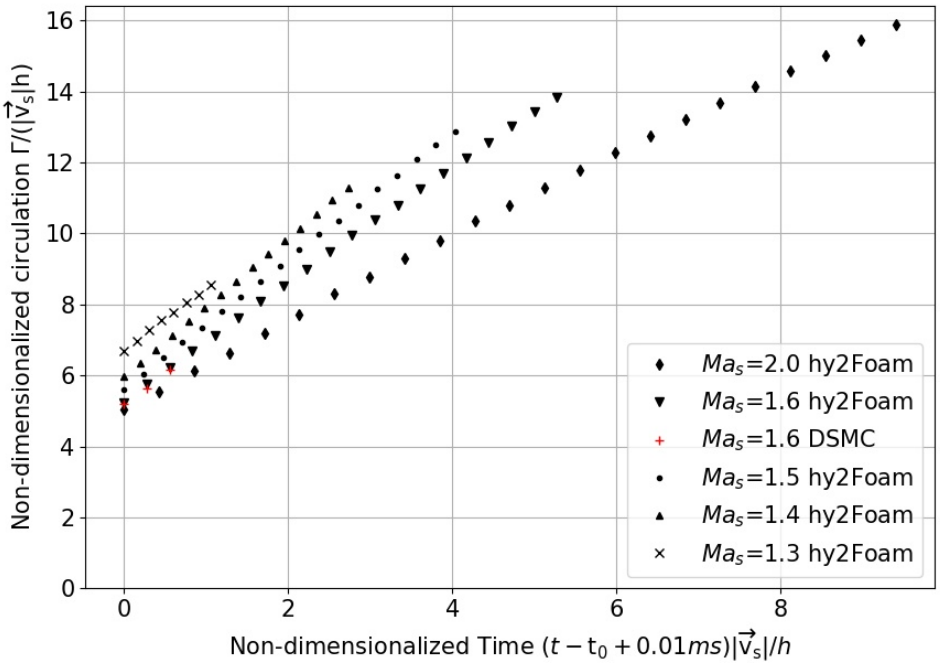

Figure 3.18: ***hy2Foam* results of non-dimensional circulation of the vortex loop at** $Kn = 0.005$**.**

to avoid contamination by shear movements so that it can use iso-surfaces to clearly represent the fluid-rotational region in the domain with a clear boundary. Subsequently, the strength of the fluid-rotation of a vortex can be accurately integrated and quantified using the rorticity flux. The introduction of rorticity can help distinguish the fluid-rotational and shear movements at any point in time inside the flow domain of interest, improving the physical understanding of vortex flows. The value of dimensionless time for each Mach number is different because of the time delay of the formation of isolated rorticity loops at different Mach numbers, and this postponement of the formation of the rorticity loop with the decrease of shock Mach number was also observed in Figures 3.13 and 3.14. The delay in the formation of the isolated rorticity loop in the cases with lower shock Mach numbers could be explained as a result of the insufficient accumulation of vorticity.

The decrease of the dimensionless rorticity flux with the increase in Knudsen number from the two solvers is presented in Figure 3.19. The results prove that a vortex loop in the slip flow regime is still able to propagate. The dimensionless rorticity flux in the near continuum flow regime ($Kn = 0.005$) from *dsmcFoamPlus* is reasonably coincident with that from CFD, and the data of $Kn = 0.025$ and $Kn = 0.05$ are in excellent agreement. The reason for the small difference of cases with $Kn = 0.005$ should be attributed to the weak embedded shock intrusion shown in Figure 3.7(d), and 3.8(a). Although the intensity of this shock intrusion is too weak to be noticeable in Figure 3.7(d) from the CFD result, it still causes the velocity gradient difference around the rorticity loop, as seen in Figure 3.20, and the subsequent rorticity flux

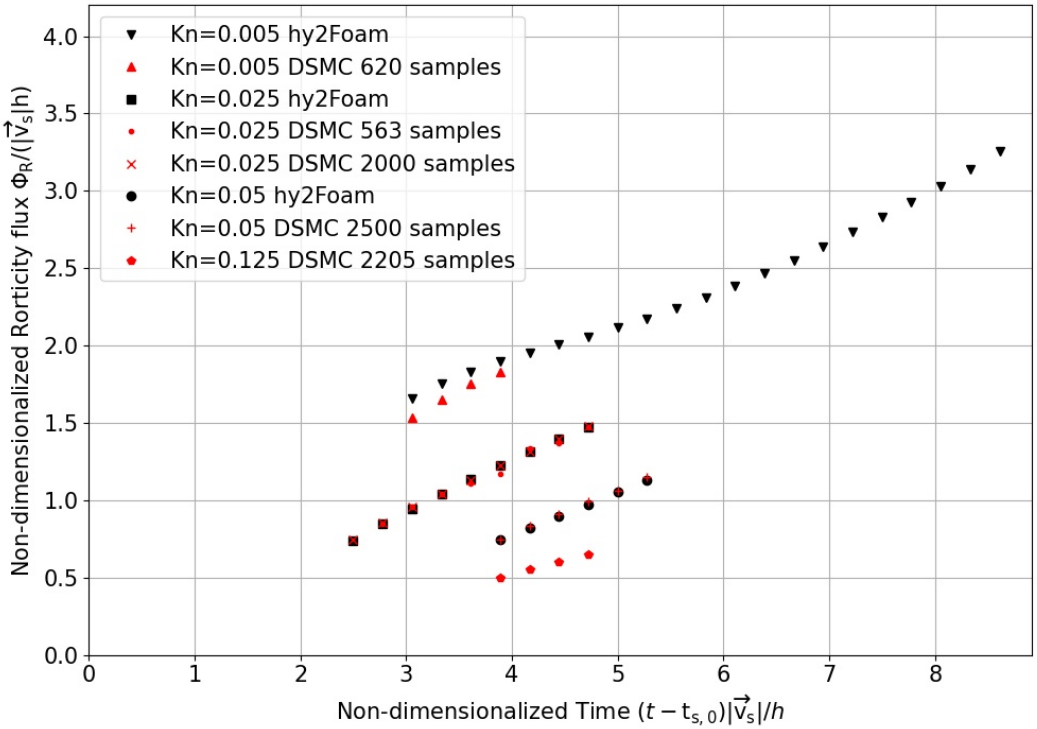

Figure 3.19: **Non-dimensionalised rorticity flux for $Ma_s = 1.6$ from *dsmcFoam* and *hy2Foam*. $t_{s,0}$ is the time when the shock wave reaches the tube exit, and here it is equal to 0.02 ms.**

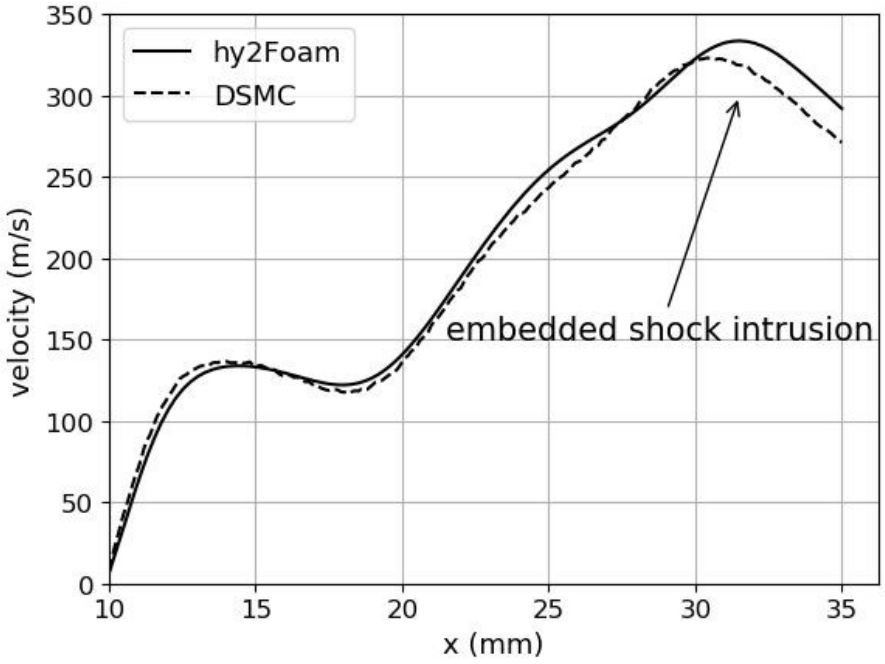

Figure 3.20: **Velocity distribution at $y = 17.5$ mm, $t = 0.16$ ms with $Ma_s = 1.6$ and $Kn = 0.005$.**

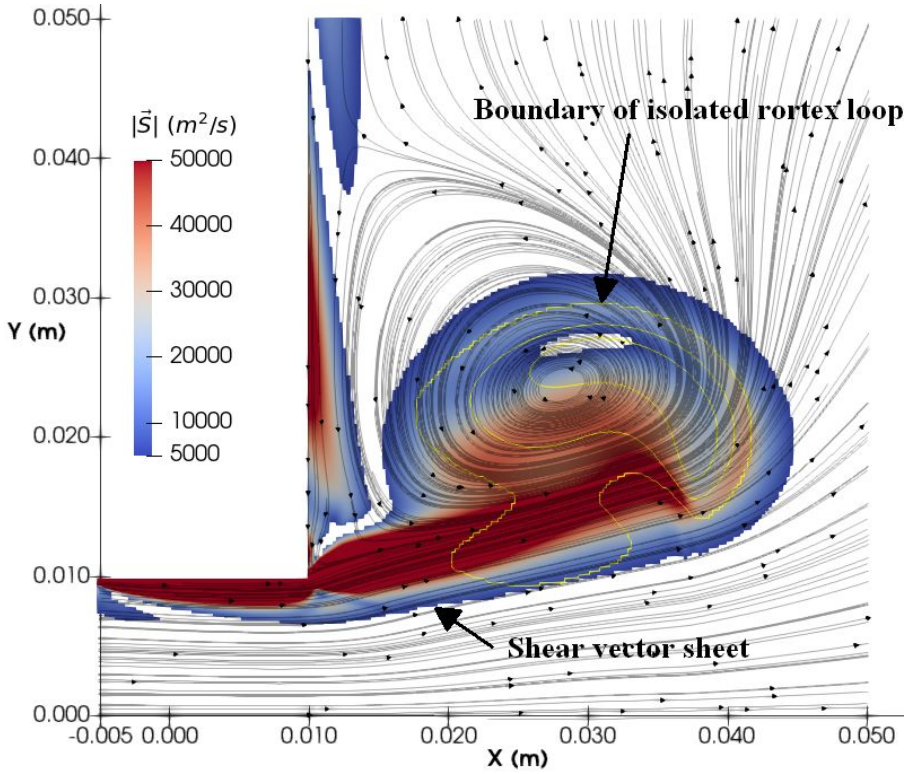

Figure 3.21: **Shear vector field and rorticity contour of** $Kn = 0.005$ **and** $Ma_s = 1.6$ **at 0.21 ms from *hy2Foam*. The closed yellow line is the boundary of the isolated rorticity loop generated from iso-surfaces. The shear vector magnitude visualisation is limited to 5** $\times 10^4$ m^2/s**.**

Table 3.4: **Circulation, rorticity flux, and shear vector flux of an isolated rorticity region at $Kn = 0.005$ and $Ma_{=}1.6$ calculated from *hy2Foam*.**

Time (ms)	Circulation (m^2/s)	Rorticity flux (m^2/s)	Shear vector flux (m^2/s)
0.21	15.1134	6.039	9.0744
0.2	14.5383	5.8718	8.6665
Difference	0.5751	0.1672	0.4079

discrepancy. In the slip flow regime, the embedded shock wave in the near continuum regime further degenerates and is deprived of the ability of influencing the calculation of rorticity flux, as shown in Figures 3.8(b) and 3.8(c), yielding excellent agreements in Figure 3.19.

In Figures 3.13 and 3.14, the rorticity field is cut off by setting a threshold of $1 \times 10^{-4}\ m^2/s$, and a clear border of the vortex loop represented by rorticity is shown. The rorticity region within a vortex atmosphere is connected to the rorticity sheet linking the wall boundary layer at the tube exit (Figures 3.13(a), 3.13(c), 3.13(e), 3.14(a), 3.14(c) and 3.14(e)) and these connections are truncated a short time afterwards (Figures 3.13(b), 3.13(d), 3.13(f), 3.14(b), 3.14(d) and 3.14(f)). This rorticity sheet works as an umbilical cord, feeding rorticity into the vortex atmosphere. When this cord is cut off and the isolated rorticity loop forms, the rorticity inside the vortex should decrease or remain constant. However, the gradual increase of rorticity flux with time presented in Figure 3.17 hints at the existence of a rorticity source leading to this continuous increase. In Figure 3.15, the shear vector sheet still connects the boundary layer with the vortex atmosphere when the independent rorticity loop occurs, so that this shear vector sheet keeps feeding the total circulation of the vortex loop. It is easy to assume that vorticity is transmitted into the rorticity loop via the closed surface of the rorticity loop or the shear vector from the interior of the rorticity loop, leading to the continuous increase of the rorticity flux of the vortex loop. As seen in Figure 3.21, the rorticity loop cross-section highlighted in the yellow line is surrounded by a shear vector field with a shear vector sheet connected to the boundary layer. Thus, the increase of the rorticity flux within the rorticity loop can only be rendered by the shear vector sheet.

The integration of the circulation, rorticity flux, and shear vector flux of an isolated rorticity loop cross-section with $Kn = 0.005$ at $t = 0.20$ ms and $t = 0.21$ ms is presented, as shown in Table 3.4. At $t = 0.2$ ms, the sum of the rorticity flux ($5.872\ m^2/s$) and the shear vector flux ($8.666\ m^2/s$) is equivalent to the total circulation ($14.538\ m^2/s$), proving the absence of the internal vorticity source. Hence, the rorticity flux increase can only be attributed to the transformation from the shear vector to rorticity or, in other words, the conversion of movement from shear to fluid-rotation, $\vec{S} \rightarrow \vec{R}$. At 0.2 ms and 0.21 ms, the decomposition of the circulation can be expressed as

$$\int_{A_{0.2ms}} \vec{\omega} d\vec{A} = \int_{A_{0.2ms}} \vec{R} d\vec{A} + \int_{A_{0.2ms}} \vec{S} d\vec{A} \tag{3.22}$$

and

$$\int_{A_{0.21ms}} \vec{\omega} d\vec{A} = \int_{A_{0.21ms}} \vec{R} d\vec{A} + \int_{A_{0.21ms}} \vec{S} d\vec{A}, \tag{3.23}$$

where $A_{0.2ms}$ and $A_{0.21ms}$ are surface areas of the isolated rorticity loop cross-section at 0.2 ms and 0.21 ms, respectively, according to Equation (3.19). Subtracting Equation (3.23) from Equation (3.22) results in

$$\Delta\Gamma = \Delta\Phi_R + \Delta\Phi_S. \tag{3.24}$$

The term on the left-hand side of Equation (3.24) is the total circulation difference of the isolated rorticity loop cross-section between two times. The first term on the right-hand side is the rorticity flux increment, and the second term is the shear vector flux increment. This equation is also proved through the data in Table 3.4. The total circulation difference, $\Delta\Gamma$, from the shear vector sheet is equal to the total shear vector flux injected into the isolated rorticity loop boundary. Hence, moving $\Delta\Phi_S$ in Equation (3.24) to the left-hand side,

$$\Delta\Gamma - \Delta\Phi_S = \Delta\Phi_R \tag{3.25}$$

is obtained, and hence,

$$\Delta\Phi_{\vec{S}_T} = \Delta\Phi_R, \tag{3.26}$$

where $\vec{S}_T$ is the transformed shear vector. The left-hand side of Equation (3.25) represents the difference between the total shear vector flux and the remaining shear vector flux within a rorticity loop, which equals the magnitude of the transformation from the shear vector flux to the rorticity flux, as shown in Equation (3.26). If the conversion between the rorticity and the shear vector does not exist, then the increment of the rorticity flux should be zero and the increase in circulation must be equal to that of the shear vector flux in Table 3.4. However, the decrease in shear vector flux equals the increase in rorticity flux. The divergence of Equation (3.7) with the introduction of vector identity in three-dimensions also implies this relationship of transformation:

$$\nabla \cdot \vec{R} = -\nabla \cdot \vec{S}. \tag{3.27}$$

Equation (3.26) can be considered the absolute integral form of Equation (3.27). Equation (3.27) demonstrates that there is a mutual transformation between the rorticity and the shear vector, or the fluid-rotation and shear movement, and the quantity of the transformation is equivalent. This equation is helpful and meaningful in the understanding of vortex formation and development, vortex interactions, and turbulent flow.

3.6.4 Geometrical characteristics of rarefied vortex loop

The geometrical characteristics of vortex loops are usually important for the understanding of the coverage in the flow field. Rorticity loop cross-section in the vortex atmosphere can be

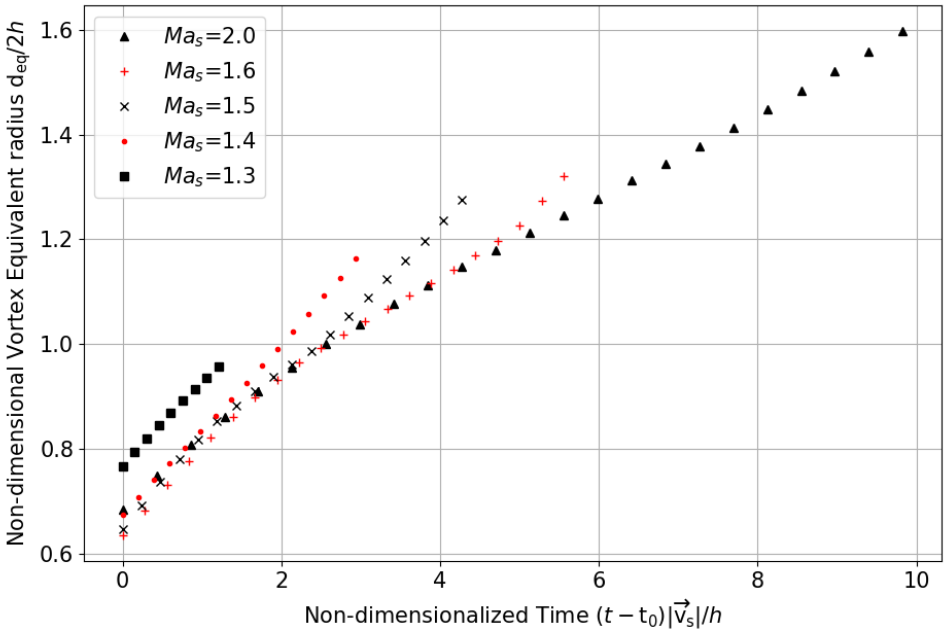

Figure 3.22: **Non-dimensionalised equivalent radius at $Kn = 0.005$, calculated with *hy2Foam*.**

defined as the rotational core. As the rorticity loop cross-section of a vortex loop core is an irregular shape, an equivalent diameter is defined as

$$d_{eq} = \sqrt{A_R/\pi}, \tag{3.28}$$

where d_{eq} is the equivalent diameter of the rotational core of a vortex loop, and A_R is the area of the rorticity loop cross-section. The non-dimensionalised equivalent radius with a different shock Mach numbers is plotted in Figure 3.22. The dimensionless time in each case begins when the rorticity loop is isolated from the rorticity sheet. In the cases of $Ma_s = 1.4$ and $Ma_s = 1.3$, a highly linear relation between the equivalent radius and non-dimensional time is observed, whereas the profile tends to be non-linear in the early stage of the formation in the cases with $Ma_s \geq 1.5$. A decrease in the slope of the distribution between the dimensionless equivalent radius and the dimensionless time can be found in the cases of $Ma_s = 1.5$, $Ma_s = 1.6$, and $Ma_s = 2.0$, indicating a deceleration of the growth rate of the equivalent radius.

Calculating the centroid of a vortex loop cross-section is important in determining its radius, provided that this vortex loop is a ring. The centroid of a vortex cross-section is conventionally determined by the distribution of vorticity [68]. Here, the centroid considered is based on the rorticity loop, so the rorticity components replace the vorticity. The centroid of the rorticity loop cross-section in the XY plane is defined as:

$$x_R = \frac{\int_A x\vec{R}d\vec{A}}{\int_A \vec{R}d\vec{A}} = \frac{\int_A xR_z dxdy}{\Phi_R}, \tag{3.29}$$

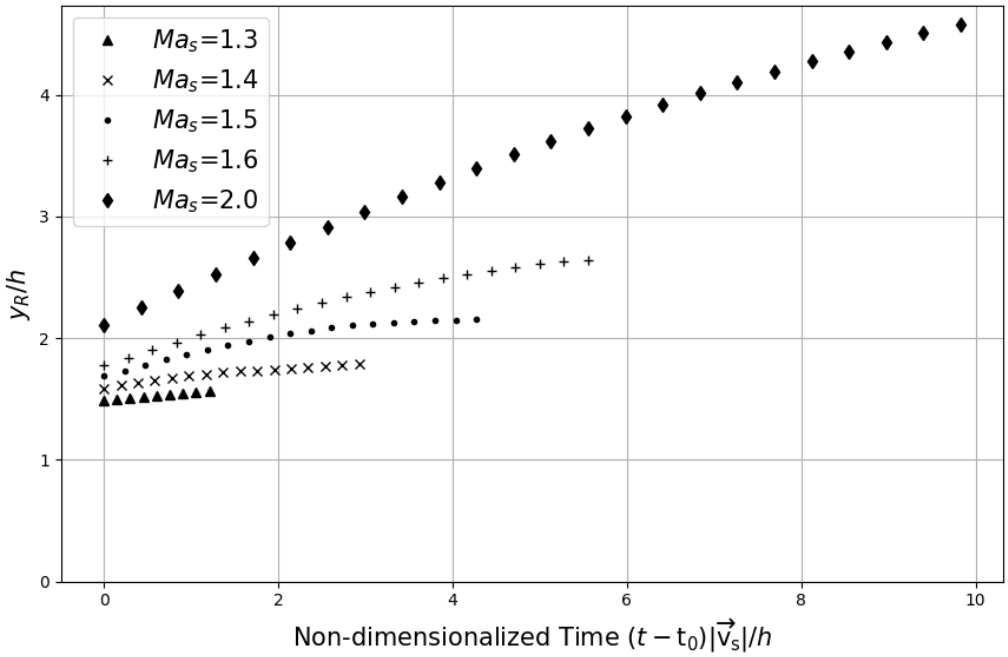

Figure 3.23: **Dimensionless y-components of the centroid of the rorticity loop with time at $Kn = 0.005$, calculated from *hy2Foam*.**

$$y_R = \frac{\int_A y\vec{R}d\vec{A}}{\int_A \vec{R}d\vec{A}} = \frac{\int_A yR_z dxdy}{\Phi_R}. \tag{3.30}$$

y_R can be considered the ring radius if the loop is a ring and it is non-dimensionlised and plotted in Figure 3.23 with dimensionless time. The radial size of the vortex loop has a positive correlation with the shock Mach number in the near continuum flow regime. It is possible for these rapidly-growing vortex loops themselves or the periphery to impinge on surfaces perpendicular to the nozzle axis or rub against surfaces parallel to the nozzle axis. The effect of rarefaction levels on the radial size of vortex loops is shown in Figure 3.24. The fast expansion due to the relatively high rarefaction level in the background yields a gradual growth of the semi-height of a vortex loop with an increase in Knudsen number. The semi-height in the transition flow regime ($Kn = 0.125$) is much larger than those in the slip flow regime and there is negligible difference in semi-height between the $Kn = 0.005$ and $Kn = 0.025$. Therefore, it can be concluded that the decrease of the environmental pressure will increase the vortex loop diameter, and the growth of the vortex ring diameter in Figures 2.9, 2.10 and 2.13 should be a result of both the increase of the shock Mach number and the reduction of the rarefaction level.

3.6.5 Failure of vortex loop formation

Figure 3.25 displays the variation of the speed contours and the streamlines due to the increase of Knudsen number with $Ma_s = 1.6$ in the slip flow regime. The Reynolds number based on the semi-height of the tube is $\mathrm{Re}_s = \rho VL/\mu$ and the result of each case is shown in Table 3.2, which

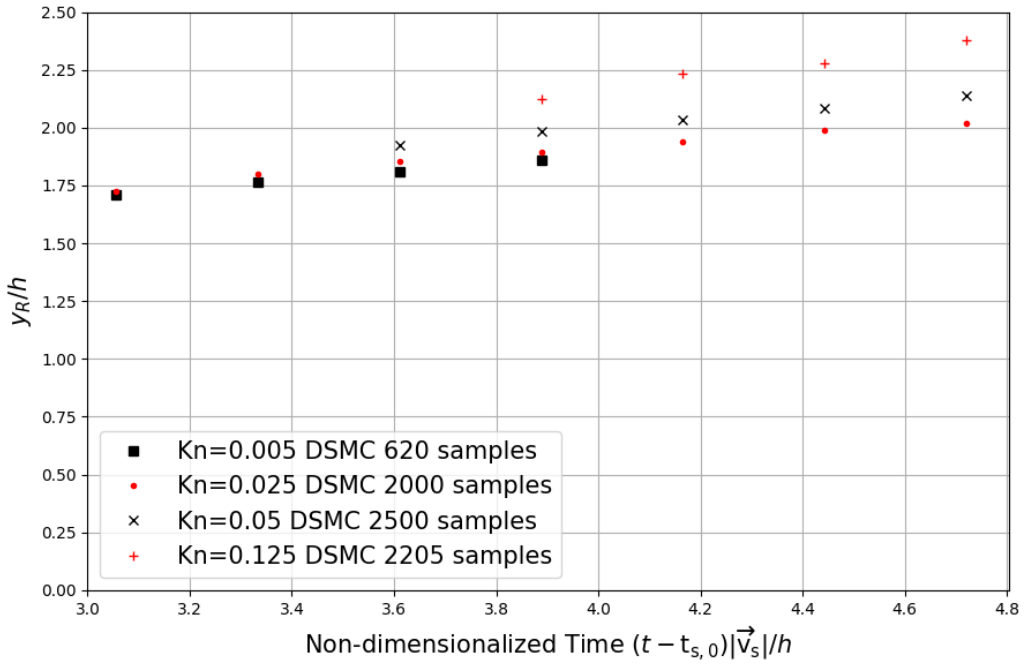

Figure 3.24: **Rarefaction effect on dimensionless semi-height with $Ma_s = 1.6$. $t_{s,0}$ is the time when the shock wave reaches the shock tube exit, and here it is equal to 0.02 ms.**

is too small to cause turbulence. The laminar flow pattern in the DSMC simulations proves that the laminar-flow assumption used in cases with *hy2Foam* solver in the near continuum flow regime is appropriate.

In Figures 3.25 and 3.26(a), vortices can be found after the shock wave diffraction in the slip flow regime. However, at 0.07 ms, a vortex occurs only in the case in the near continuum flow regime; at 0.13 ms, a clear vortex structure forms in the case with $Kn = 0.025$, whereas, a vortex-like configuration is sill in the process of formation and this vortex is not mature until $t = 0.16$ ms. The rarefaction effect on the vortex formation is severe in the case of $Kn = 0.125$. At $t = 0.16$ ms, the distinct vortex structure in the slip flow regime degenerates to a weak vortex-like configuration in the case of $Kn = 0.125$, proving a postponement in the vortex formation due to the rarefaction. In the transition regime and free-molecule regime, the flow is too rarefied to form a vortex, as shown in Figure 3.27. An early investigation of vortex formation after an obstacle with different Knudsen numbers under subsonic flow conditions can be found during the validation of the DSMC method by Bird [104]. In contrast, the limitation of the Knudsen number for vortex formation in Bird's cases is 0.88, and this critical Knudsen number was found to be 0.82 in the work of Ahangar *et al.* [125] and 0.662 in Ref. [126]. Therefore, the vortex formation is limited by a critical Knudsen number, and this Knudsen number may be a function of the flow conditions at the nozzle exit. Nevertheless, there is no full understanding of the relationship between the specific Knudsen number and vortex formation limitation. A vortex loop in the continuum flow regime entrains the background gas around it and grows in size. However, when a vortex loop is ejected into a rarefied environment, there is not sufficient gas

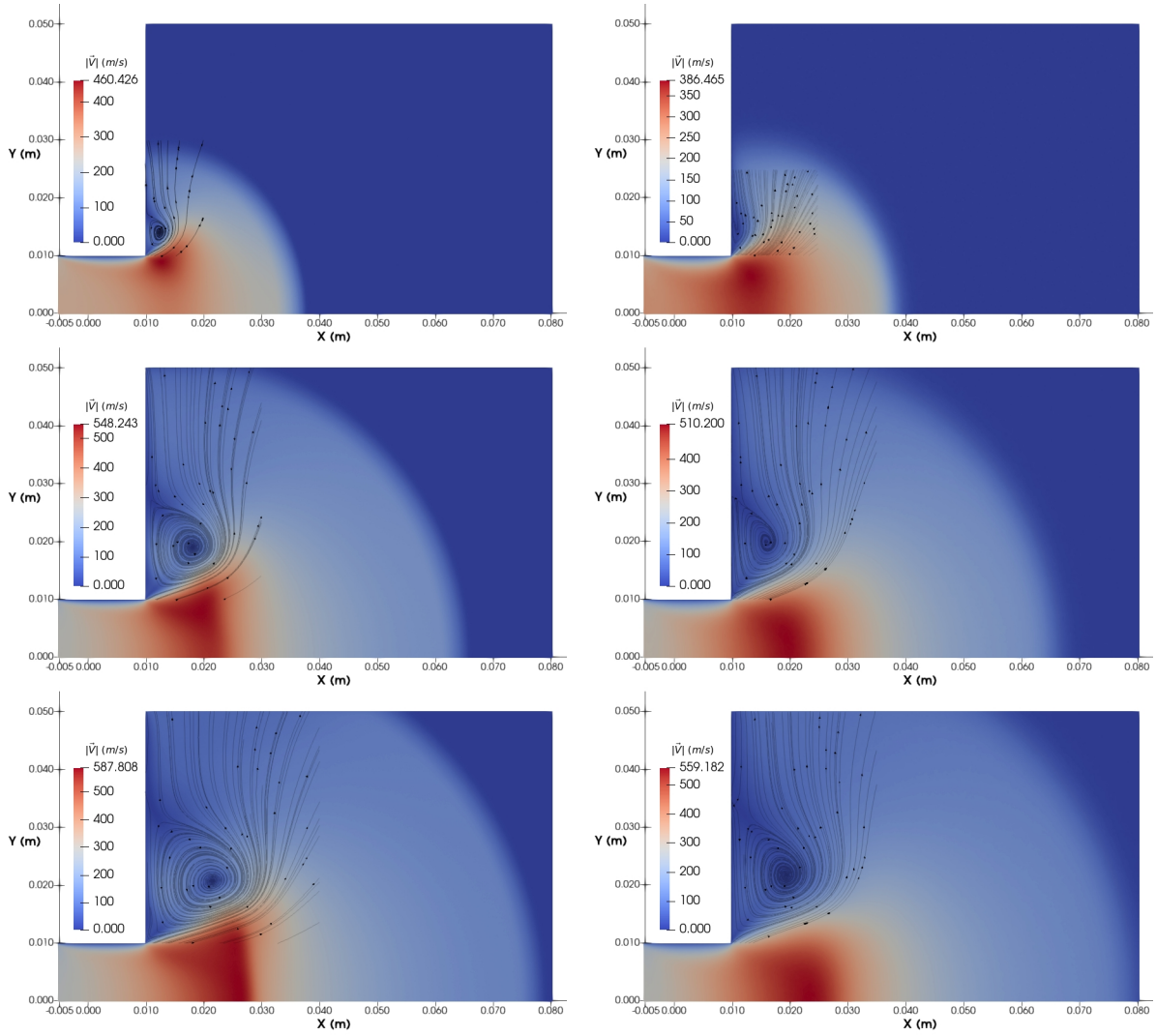

(a) Kn =**0.005** (b) Kn =**0.025**

Figure 3.25: **Velocity field and streamlines calculated by *dsmcFoamPlus* in the slip flow regime ($t = 0.07$ ms, 0.13 ms, and 0.16 ms) at $Ma_s = 1.6$ at (a) $Kn = 0.005$ and (b) $Kn = 0.025$.**

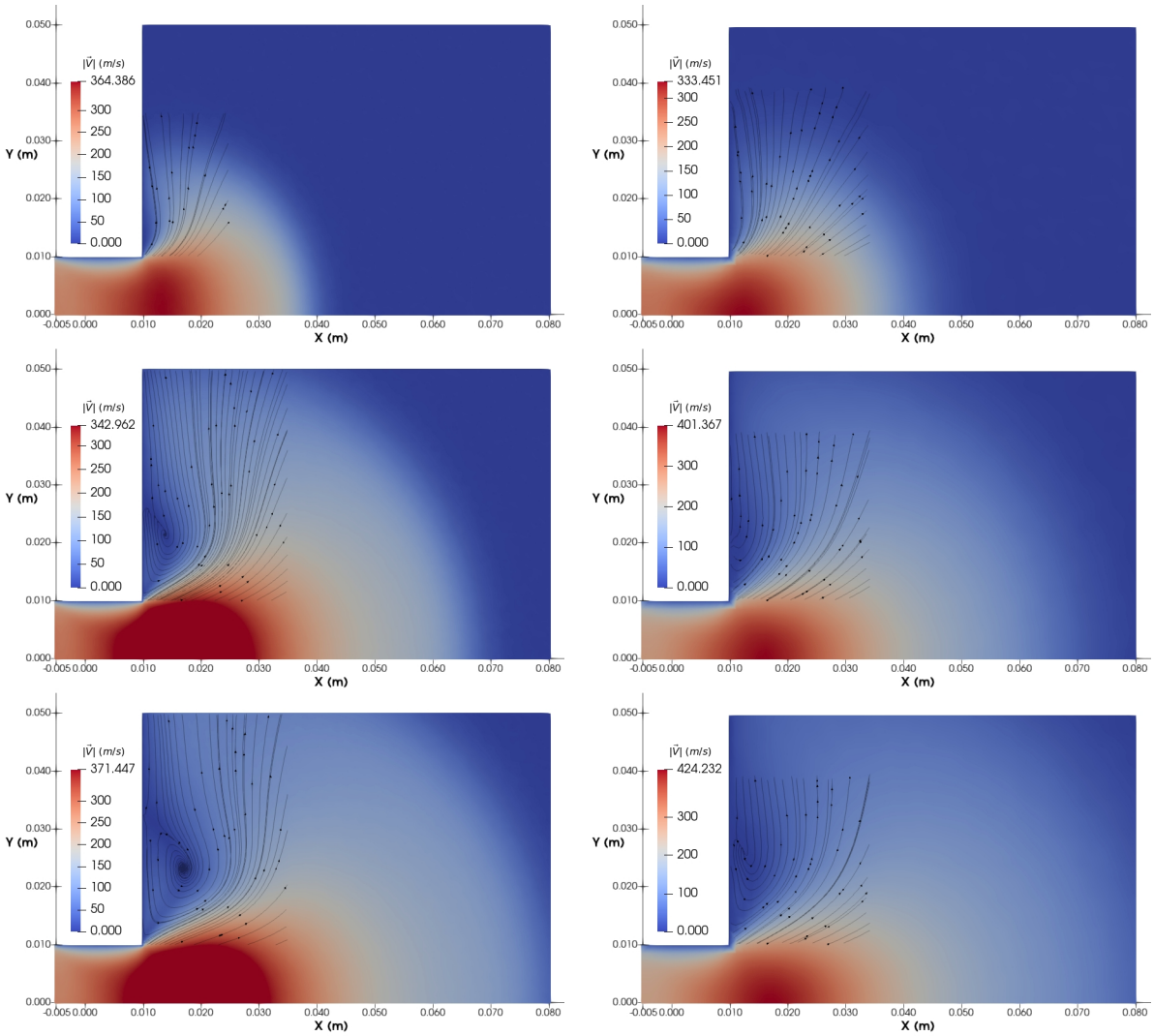

(a) Kn =**0.05** (b) Kn =**0.125**

Figure 3.26: **Velocity field and streamlines calculated by *dsmcFoamPlus* in the slip and transition flow regime ($t = 0.07$ ms, 0.13 ms, and 0.16 ms) at $M_S = 1.6$ at (a) $Kn = 0.05$ and (b) $Kn = 0.125$.**

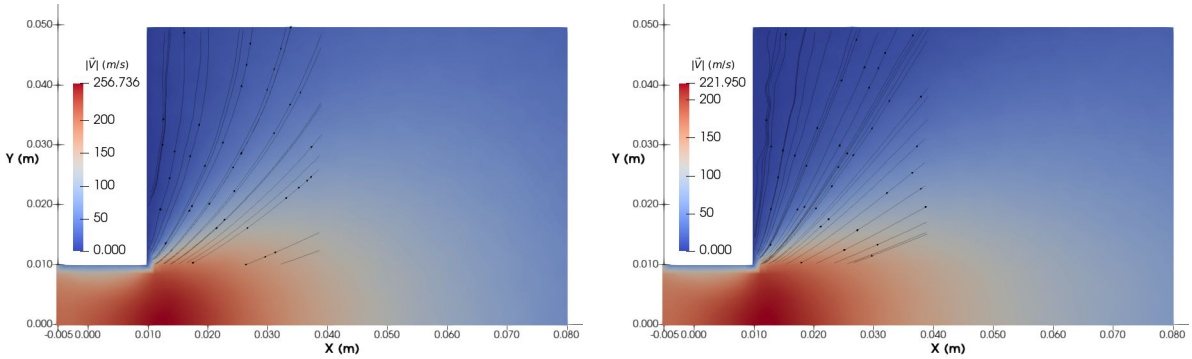

(a) Kn =**1.25** (b) Kn =**12.5**

Figure 3.27: **Velocity field and streamlines calculated by *dsmcFoamPlus* in the free molecule flow regime ($t = 0.19$ ms) at (a) $Kn = 1.25$ and (b) $Kn = 12.5$.**

for the vortex loop to entrain during its formation, and the vortex loop will be further diluted during its propagation. Eventually, the vortex loop should disappear due to gradual dissipation when the critical Knudsen number is reached. It can be concluded that this Knudsen number limit will influence the propagation of a vortex loop.

A cylindrical vortex sheet with discontinuous tangential velocity is regarded as the preconditioning of a vortex loop in continuum flow, and the vortex sheet will roll up into spirals to create a vortex loop [74]. The failure of vortex formation in the rarefied conditions can be explained from the perspective of this vortex sheet [73]. Figure 3.28(a) shows the dimensionless velocity profile inside the shock tube. The increase of the Knudsen number increases the velocity slip, resulting in higher wall velocity, as can be seen in Figure 3.28(a). The boundary layer is crucial in the development of the vortex sheet, but as the mean free path increases, the Knudsen layer, where molecules collide with the surface at a higher frequency than with other molecules, thickens. Figure 3.28(b) presents the dimensionless tangential velocity profile at 2 mm away from the tube exit and $t = 0.12$ ms. The increase in the rarefaction level thickens the vortex sheet and decreases the tangential velocity difference within the vortex sheet. Therefore, a thicker Knudsen layer, leading to higher Δy, greater wall velocity, and smaller Δu, causes the significant shrinking of the tangential velocity gradient du/dy within the boundary layer and the vortex sheet, giving rise to the subsequent failure of the mathematical precondition of discontinuous tangential velocity; the vortex sheet degenerates due to a small finite tangential velocity gradient. Hence, no vortex can be found.

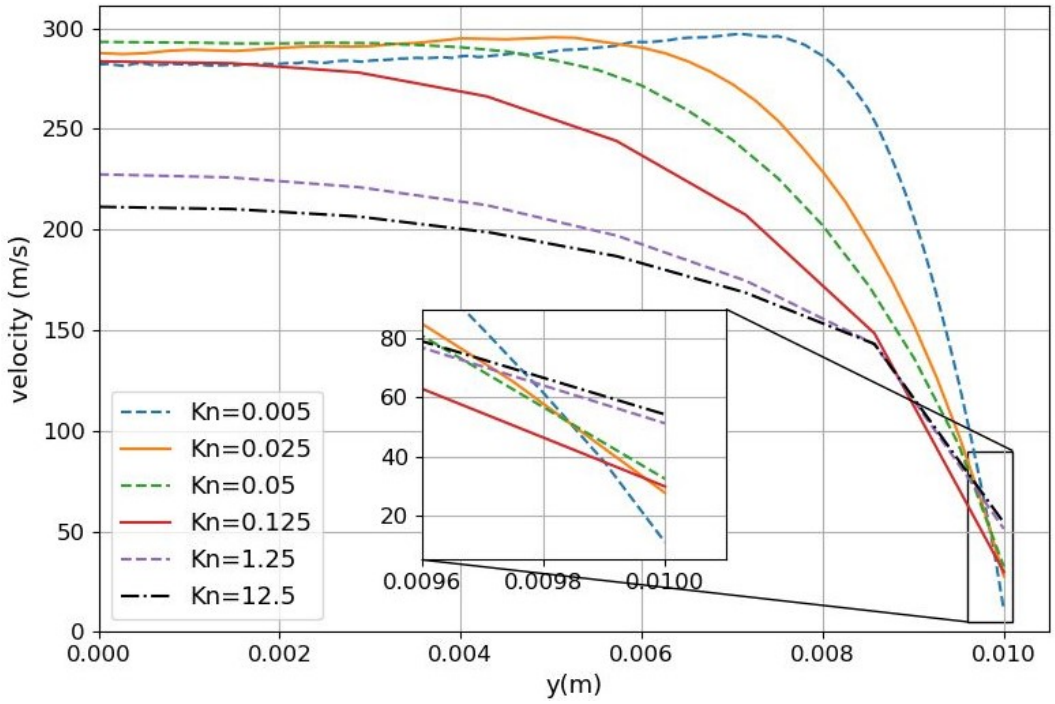

(a)

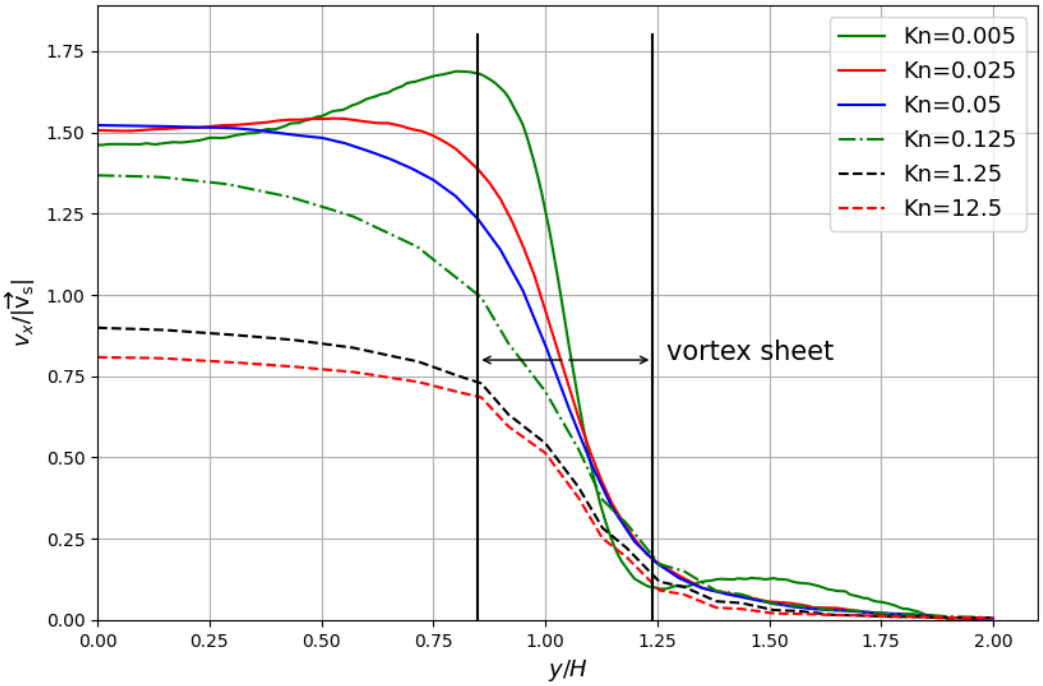

(b)

Figure 3.28: (a) **Dimensionless velocity profile inside the shock tube at** $x = 2.5$ **mm,** $t = 0.07$ **ms for different Knudsen numbers from *dsmcFoamPlus* and (b) Tangential velocity profile outside the shock tube at** $x = 12$ **mm,** $t = 0.12$ **ms for different Knudsen number with** $Ma_s = 1.6$**, as calculated from DSMC.**

3.7 Summary

In this chapter, the rorticity calculator has been validated, and an accurate decomposition of vorticity has been shown. At the same time, the mesh and time-step independence of the *hy2Foam* solver have been done before the simulations. The vortex loop formation caused by shock wave diffraction over a rectangular corner in dilute gas flows is investigated. Transient DSMC and compressible CFD simulations have been performed, and comparisons have been made between the results from the *dsmcFoamPlus* and *hy2Foam* where the Knudsen number allows.

A comparison between the flow pattern of vortex loops in this work and that in the continuum flow regime has been made, and it can be found that an increase in flow rarefaction results in the inner-structure of vortex loops becoming simpler, and the flow patterns in all the simulations of this work are laminar. Thicker primary and embedded shock waves due to flow rarefaction have been successfully captured by *dsmcFoamPlus*. The pressure distribution at the axis shows that the distribution profiles of the transition and free-molecular flow regimes are similar.

With the use of rorticity, the rotational and shear movements of the fluid can be effectively and quantitatively resolved. By integrating the equation of the decomposition of vorticity, the circulation can be decomposed into a rorticity flux that describes the fluid-rotational strength of a vortex and a shear vector flux that represents the shear strength of a vortex. Based on the rorticity field, an isolated rorticity loop forms within the vortex atmosphere described by streamlines. The calculation of rorticity flux from both *dsmcFoamPlus* and the compressible CFD solver agrees well except for a mild difference caused by the weak embedded shock wave intrusion in the near continuum flow regime ($Kn = 0.005$). The rorticity flux of the isolated rorticity loop increases with the shock Mach number non-linearly and decreases with an increasing Knudsen number. The increase of rorticity flux in the isolated rorticity loop with time is attributed to the transformation from the shear vector to rorticity, and the amount of the transformed rorticity flux is equal to the change of the shear vector flux.

According to the velocity field and streamlines in the rarefied condition, the increase of the Knudsen number postpones the vortex loop formation, and there is a maximum Knudsen number limiting the generation of a vortex. The increase in the Knudsen number will thicken the Knudsen layer and the subsequent vortex sheet, causing the failure in the condition of discontinuous tangential velocity. When the flow Knudsen number exceeds this maximum in the transition regime, no vortex loop forms. The vortex loops in the near continuum flow regime and the slip flow regime still have considerable ability to propagate forward. The radial size of the vortex loop increases with both the shock Mach number and the Knudsen number.

Chapter 2 presented the interaction between supersonic starting jet and a plane surface in low-pressure environments. If the surface is replaced by a lunar regolith surface, this flow-surface interaction will erode the regolith surface, fluidising regolith particles, and a multiphase flow will

be generated, which is called lunar plume-surface interaction (PSI). It is necessary to develop a new numerical tool to study the lunar PSI because existing codes are in-house codes. A new solver in OpenFOAM is developed for solving rarefied multiphase flows and it will be used to simulate lunar PSI. These issues will be detailed in the following chapters.

Chapter 4

New developments in rarefiedMultiphaseFoam and benchmarking

Free supersonic starting jets have been studied in Chapter 2 and 3. From this chapter on, simulating lunar PSI using the new solver developed in OpenFOAM is the main topic. The basic algorithm and the models of the open source code for solving rarefied multiphase flows – *rarefiedMultiphaseFoam* will be fully detailed after a literature review in this chapter. Before it can be used in any application, the new code must be rigorously validated. The validation of one-way coupling, which describes the momentum and heat transfer from gas atoms/molecules to a solid simulator in a computational cell, has previously been conducted and more detail can be found in Ref. [127], so it will not be presented in this thesis. This chapter focuses on benchmarking of the two-way coupling model, the phase change model, and the MPPIC method using existing analytical solutions and numerical results from the open literature.

4.1 A literature review of numerical methods for solving rarefied two-phase flows

In this thesis, rarefied two-phase flow is defined as rarefied gas flow with entrained solid particles. The numerical approach for solving rarefied two-phase flow is divided into three sections: gas phase evolution, interphase coupling calculation, and solid phase evolution. The interphase coupling model serves as a conduit for the exchange of momentum and energy between the solid and gas phases. If only the effect of the gas on the solid phase is considered in two-phase flows,

this is referred to as one-way coupling; if the opposite effect, or the effect of the solid phase on the gas phase, is also considered, this is referred to as two-way coupling. With the addition of the consideration of interactions within the liquid/solid phase, this will be called four-way coupling.

Approaches for simulating gas-particle two-phase flows in conventional CFD are often based on the Eulerian-Eulerian framework and the Eulerian-Lagrangian framework [128], where the gas phase is assumed to be continuous while the solid phase is considered to be discrete in the Eulerian-Lagrangian framework. Although it has been pointed out that the Eulerian-Eulerian framework is inapplicable to dilute flow regimes and cannot predict particle trajectories [129], it was nevertheless employed in PSI simulations on Mars with suitable modifications and models [130]. In multiphase flow simulations, the Eulerian-Lagrangian framework is more frequently used because of its advantages, such as the ability to track particles, the inclusion of particle size distribution, and interparticle forces [129]. Rahimi *et al.* [16] used the Roberts erosion model to calculate the mass flow rate of the lunar dust particles excited by the plume and showed the near-field two-phase flow results through Fluent based on the Eulerian-Lagrangian method, but because they represented the lunar surface as an inlet boundary condition for lunar dust particles, the process of cratering, similar to the work of He *et al.* [27], was unable to be found. Furthermore, the gas phase simulation is based on the Navier-Stokes-Fourier equations and the interphase calculation is built for incompressible flows. Shallcross [131] extended the Euler-Lagrangian method to compressible flows and used a deterministic approach to deal with solid particles. Gale *et al.* [130] developed and validated simulation software based on the Gas-Granular Flow Solver multi-phase flow computational framework. In this numerical tool, both the gas and solid phases were treated as Eulerian fluids. Rarefied flow regimes were considered by using the harmonic averaging procedure to correct the face viscosity. Test cases were made on spherical-particle and cylindrical-particle beds, respectively [130]. This method has proven to be reliable through simulations of plume-surface interactions on Mars [132].

Because of the continuum breakdown in the extreme conditions considered in this thesis (e.g. vacuum on the Moon or an asteroid in space), the gas phase cannot be considered continuous [128]. Without considering mass exchange, a solid particle in a gas-solid flow will theoretically experience momentum and heat exchange due to collisions with surrounding gas atoms/molecules in the Lagrangian-Lagrangian framework or from a microscopic viewpoint.

Gallis [28] successfully applied a Green's function to calculate momentum and heat transfer from a gas simulator to a spherical solid particle within a computational cell, demonstrating excellent agreement between analytical and simulation results. Burt and Boyd [29] extended the one-way coupling method to polyatomic gases and developed a two-way coupling model to bridge the gap between the influence of the solid phase on the gas phase. Gimelshein and Alexeenko [133] modelled the interaction between a thruster plume and the atmosphere at 120

km altitude via replacing Burt and Boyd's direct sampling approach [29] with an indirect one based on linear algebra. The indirect approach described by Gimelshein and Alexeenko [133] increased the efficiency of He *et al.* [134]'s simulation of the two-phase rocket plume, in which particle-particle interactions were handled using a neighboring-cell contact detection scheme and a hard sphere model [27]. They found that the solid particles increase the pressure and temperature of the gas phase in the vicinity of the nozzle axis. Morris and Goldstein *et al.* [30] treated the granular collisions as inelastic based on a stochastic method and the generalised NTC method for the selection of collision pairs in a cell because the granular volume fraction was assumed to be negligible; only binary solid-solid collisions were considered. Furthermore, instead of modelling the regolith layer, the boundary below the nozzle exit released solid particles into the domain according to an erosion model. The solver proposed in Ref. [30] was applied to simulate a multiphase flow field caused by single- and four-engine rockets in Ref. [135].

The Lagrangian-Lagrangian approach is not limited to works based on the framework proposed by Gallis [28]. Liu *et.al* [136] proposed a method for simulating PSI using a macroscopic one-way coupling method (i.e. only considering the effect of the gas phase on solid particles), but unlike He *et.al* [27] and Morris *et.al* [30], a pure DSMC simulation was performed first to obtain a steady state gas field, and then an overlay method was used to conduct one-way interphase coupling and the resulting solid particle trajectories. Li and Ren *et al.* [137] suggested a macroscopic two-way coupling approach and compared it with the microscopic method proposed by Burt and Boyd [29]. They showed that the particle velocities obtained using the microscopic approach were slower than those obtained using the macroscopic method. Chinnappan *et al.* [24] developed codes based on the DSMC framework and modelled lunar dust dispersion due to the rocket plume at different hovering altitudes using the same nozzle as in the Ref. [30]. After obtaining the gas phase steady state using the DSMC approach, the solid particles were inserted into the computational domain according to an erosion flux based on the dynamic pressure above the lunar surface, similar to the work of Liu *et.al* [136]. The solid phase evolution based on a stable gas flow field is unrealistic since the granular flow influences the gas flow field and vice versa.

Codes for solving rarefied gas-solid multiphase flows are less common, and the codes mentioned above are private with limited accessibility and extensibility to the general public. Hence, open source code is in high demand. Complex solid-solid interactions are replaced by merely binary solid-solid collisions in the aforementioned codes, which is incomplete because collisions are typically instantaneous contacts, while enduring contacts like packing have never been considered in previous PSI simulations. The lack of enduring contacts results in an unrealistic evolution of the regolith layer and the subsequent gas flow field. The first open source code for solving rarefied gas-solid multiphase flow has been developed, and the solid-solid enduring contacts are taken into account for the first time.

4.2 Numerical method III: Rarefied gas-solid flows

4.2.1 Introduction to rarefiedMultiphaseFoam

Before describing in detail the new solver, some assumptions must be highlighted:

- There is no mass exchange between the gas and solid phases.
- Solid particles are considered perfectly spherical.
- The temperature gradient of a solid particle is ignored (i.e. the particle surface temperature is equal to its core temperature).
- The volume of gas atoms/molecules is small compared to the solid particle volume.
- The local particle Knudsen number, denoted $Kn_p = \lambda / d_p$, where λ is the gas MFP and d_p is the solid particle diameter, is assumed to "be of order one or greater" [29] so that collisions between incident and reflected gas atoms/molecules in the interphase coupling model can be ignored, which will be detailed later.

The solver newly built in this thesis is formally named *rarefiedMultiphaseFoam* and it is based on the *dsmcFoamPlus* [112] solver to provide solutions for rarefied multiphase flows. The main characteristics of this solver are listed below:

- Steady and transient rarefied gas-solid simulations.
- Fully parallelised through MPI.
- Calculation of planar 2D, axisymmetric 2D, and 3D cases.
- Interphase coupling model - calculating the momentum and energy exchange between two phases.
- Solid phase change and particle size correction model - correction of temperature caused by phase change of solid phase and particle diameter correction due to phase change.
- Stochastic interparticle collisions - stochastically performing solid-solid collisions for dilute granular flows.
- MPPIC method - efficiently performing particle-particle interactions for dense granular flows.

4.2.2 Algorithmic overview of *rarefiedMultiphaseFoam*

Before the descriptions of models in the *rarefiedMultiphaseFoam*, an overview of the basic algorithm of *rarefiedMultiphaseFoam* is shown in Figure 4.1:

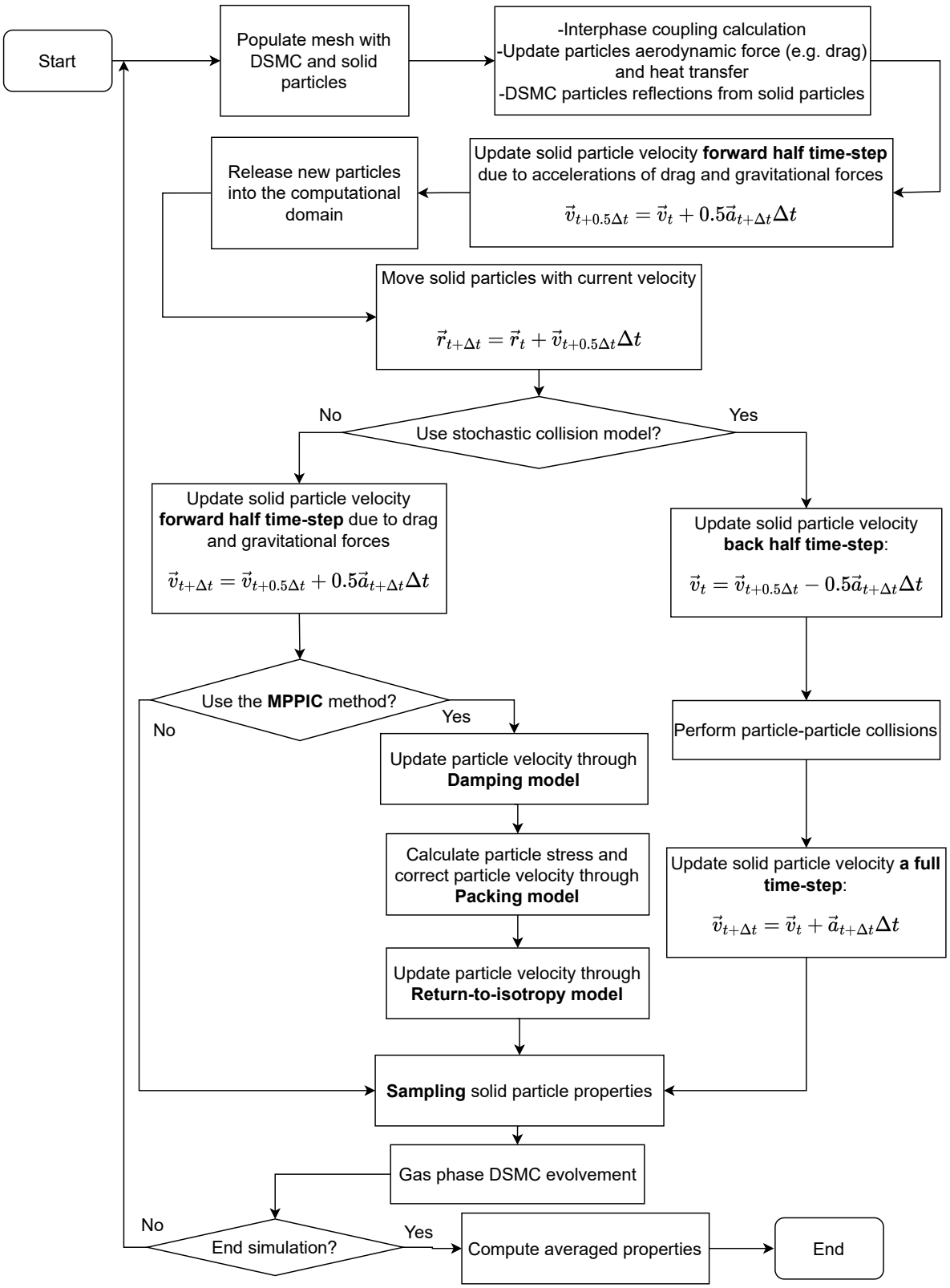

Figure 4.1: **Flow chart of *rarefiedMultiphaseFoam* solver.**

Step 1. The heat and momentum transferred from the gas phase to the solid phase are determined through the interphase one-way coupling calculation in the procedure called "Interphase coupling calculation" in Figure 4.1.

Step 2. (Optional) If the solid particle phase-change model is enabled, solid particle temperature variations are corrected through the phase change model. Otherwise, the method for updating the solid particle temperature is straightforward.

Step 3. (Optional) If the two-way coupling model is enabled, the reverse effect (i.e. the effect of the solid phase on the gas phase) is evaluated in the interphase coupling model by updating the properties of the DSMC particles that are selected to reflect from solid particle surfaces, which will be detailed in Section 4.2.3

Step 4. (Optional) Release or inject new or stuck solid particles into the computational domain through boundary conditions.

Step 5. All solid particle velocities and positions will be updated through a leapfrog algorithm to correctly account for the accelerations.

Step 6. (Optional) If the particle stochastic collision method is activated, perform solid-solid interactions with selected models, e.g. hard sphere model. Solid-solid stochastic collisions will be described later in Section 4.2.5.

Step 7. (Optional) If the MPPIC method is activated and the stochastic collision model is not activated, conduct solid-solid interactions through the MPPIC method with user-defined models, including damping, packing, and return-to-isotropy. The MPPIC method will be described in Section 4.2.6.

Step 8. Sampling solid particle properties.

Step 9. Evolution of the gas phase through the algorithm of *dsmcFoamPlus* [112].

Step 9. Calculating the required macroscopic properties of both phases.

Step 10. Go back to Step 1 until the time reaches the final calculation time.

4.2.3 Interphase coupling model

The interphase coupling model is used to quantify the momentum and heat exchange between the solid phase and the gas phase in each time-step of a two-phase flow.

Effect on gas phase from solid phase

Gallis [28] first developed the one-way coupling model for two-phase rarefied flow in the Lagrangian framework, but only gas atoms are considered in his model. The rates of momentum, $\vec{F}_\delta[\vec{v}]$, and energy, $Q_\delta[\vec{v}]$, transferred to a solid particle from each DSMC simulator are calculated as

$$\vec{F}_\delta[\vec{v}] = \frac{mW_g\left(\pi r_p^2\right)}{\mathrm{V_{cell}}}\vec{v}_r\left\{\left(1+\frac{4}{9}(1-\varepsilon)(1-\alpha)\right)|\vec{v}_r| + \frac{\sqrt{\pi}}{3}(1-\varepsilon)\alpha\sqrt{\frac{2k_BT_p}{m}}\right\} \tag{4.1}$$

and

$$Q_\delta[\vec{v}] = (1-\varepsilon)\alpha\frac{mW_g\left(\pi r_p^2\right)}{\mathrm{V_{cell}}}|\vec{v}_r|\left(\frac{1}{2}|\vec{v}_r|^2 - \left(\sqrt{\frac{2k_BT_p}{m}}\right)^2\right) \tag{4.2}$$

for a monatomic gas, where $\vec{v}_r$ is the relative velocity between a gas atom and a solid particle, $\vec{v}_r = \vec{v}_g - \vec{v}_p$, $\vec{v}_g$ is the gas atom velocity and $\vec{v}_p$ is the solid particle velocity, and k_B is the Boltzmann constant. m, W_g, V_{cell}, r_p and T_p are atomic mass, weight of DSMC particles (i.e. real number of gas atoms represented by a DSMC particle), the cell volume, the solid particle radius and solid particle temperature, respectively. ε and α are the fraction of specularly reflected gas atoms among the incident atoms and the fraction of gas atoms which experience isothermal diffuse reflection in the $(1-\varepsilon)$ fraction of incident atoms.

The model was extended to polyatomic molecules by Burt and Boyd [138] and the equations for rates of momentum and energy exchange become

$$\vec{F}_\delta[\vec{v}] = \frac{W_g\left(\pi r_p^2\right)}{\mathrm{V_{cell}}}\left(m|\vec{v}_r| + \frac{a}{3}\sqrt{2\pi m k_B T_p}\right)\vec{v}_r \tag{4.3}$$

and

$$Q_\delta[\vec{v}] = \frac{W_g\left(\pi r_p^2\right)a|\vec{v}_r|}{\mathrm{V_{cell}}}\left(\frac{1}{2}m|\vec{v}_r|^2 + e_{rot} - \left(2+\frac{1}{2}\Lambda\right)k_BT_p\right), \tag{4.4}$$

where a is the particle thermal accommodation coefficient, e_{rot} is the rotational energy of an individual gas molecule, Λ is the molecular number of degrees of freedom and m is the mass of a single gas molecule in Equations (4.3) and (4.4). It is pointed out that the influence of vibrational excitation of polyatomic gas molecules on a solid particle is negligible so that this term is removed from the energy transfer equation [29].

For each solid particle in a cell, the sum of the momentum, $\sum\vec{F}_\delta[\vec{v}]$, and energy, $\sum Q_\delta[\vec{v}]$ is calculated based on Equations (4.1) and (4.3) (or Equations (4.2) and (4.4)) and transferred to the solid particle due to the existence of all DSMC computational particles in the same computational cell. This step will loop over all the cells in the computational domain during each time-step.

Subsequently, all the solid particle temperatures and velocities are updated. The particle temperature is updated using Equation (4.5):

$$T_p(t+\Delta t) = T_p(t) + \frac{\sum Q_\delta[\vec{v}]\cdot\Delta t}{c_p m_p} \tag{4.5}$$

and the particle velocity is updated through a leapfrog algorithm (Equations (4.6) and (4.7))

$$\vec{v}_p(t+\Delta t/2) = \vec{v}_p(t) + \frac{\sum \vec{F}_\delta^{[t]}[\vec{v}]\cdot(\Delta t/2)}{m_p} \tag{4.6}$$

and

$$\vec{v}_p(t+\Delta t) = \vec{v}_p(t+\Delta t/2) + \frac{\sum \vec{F}_\delta^{[t+1]}[\vec{v}]\cdot(\Delta t/2)}{m_p}, \tag{4.7}$$

where c_p is the particle specific heat, m_p is the particle mass, t is the current computational time and Δt is the time step.

Effect on solid phase from gas phase

After the calculation of momentum and energy transferred from the gas phase to the solid phase, the effect in the opposite direction should be considered if the two-way coupling model is activated. Similar to the NTC method in standard DSMC, the number of DSMC representative particles selected to collide with a solid particle within a cell is evaluated as

$$N_{sel} = \frac{W_p N_g \pi r_p^2 (|\vec{v}_r|)_{\max}\Delta t}{\mathrm{V}_{\mathrm{cell}}}, \tag{4.8}$$

where W_p is the actual number solid particles represented by one computational solid particle in a cell, N_g is the number of DSMC particles in a cell, and $|\vec{v}_r|_{\max}$ is the maximum pre-collision relative speed over a large number of time-steps. $|\vec{v}_r|_{\max}$ will be checked when there are collision candidates and will be updated if a larger value is found. The DSMC particle will collide with a computational solid particle if [29]

$$\pi {r_p}^2 |\vec{v}_r| / \left(\pi {r_p}^2 |\vec{v}_r|\right)_{\max} > R_f \tag{4.9}$$

where R_f is a random number between 0 and 1.

Two methods currently are available for calculating the momentum and energy transfer from the solid phase to the gas phase via the DSMC method: the direct method and the indirect method. These two methods are described below.

Direct method

For a selected collision pair between a gas molecule and a solid particle, the gas molecule will experience either diffusive reflection with a probability equal to the solid particle thermal accommodation coefficient, a, or specular reflection with a probability of $1-a$.

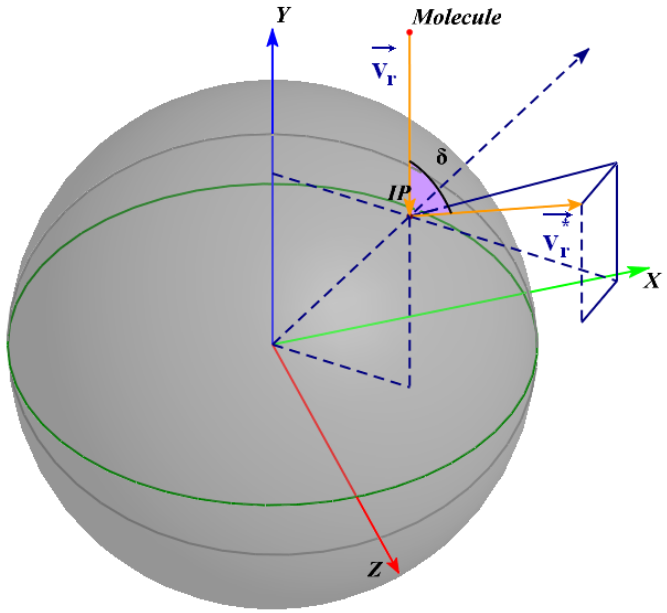

Figure 4.2: **Schematic of inter-phase collision in the direct method. δ is the deflection angle and ε is the azimuthal angle. IP is the contact point on the solid particle surface.**

As shown in Figure 4.2, when a gas particle collides with a solid particle, it is essential to determine the post-collision velocity direction. Provided that a specular reflection occurs and the direction of post-collision velocity follows the isotropic distribution according to Burt and Boyd [29], the magnitude of post-collision velocity $|\vec{v}_r^*|$ is equal to the pre-collision relative velocity magnitude. The cosine of the polar angle (χ) is sampled as $2R_f-1$ and the azimuthal (φ) angle of the post-collision velocity is sampled as $2\pi R_f$ in the global coordinate system. The unit vector of the post-collision velocity in the global coordinate system is $(cos\chi, sin\chi cos\varphi, sin\chi sin\varphi)$. The polar ($\chi$) and azimuthal ($\varphi$) angles used here are the same as those defined in Figure 5 of Ref. [27].

In diffusive collisions, the deflection angle follows a sixth-order polynomial distribution function:

$$f(\delta) = 0.02042\delta^6 - 0.2515\delta^5 + 1.104\delta^4 - 1.903\delta^3 + 0.4938\delta^2 + 1.248\delta \tag{4.10}$$

according to Burt and Boyd [29], but an explicit expression of the deflection angle is unable to be acquired through the inverse-cumulative method so that the acceptance-rejection method is implemented with an approximate maximum value of $f(\delta)_{max} = 0.72269$. δ is uniformly sampled over $[0,\pi]$. When $f(\delta)/f(\delta)_{max} < R_f$, where R_f here is a new random number, then

the deflection angle δ is selected.

In addition, the post-collision relative velocity magnitude should not be equivalent to the pre-collision one and similar to the deflection angle sampling procedures, it will be determined through the acceptance-rejection method with distribution function

$$f\left(|\vec{v}_r^*|\right) = 2\beta^4(|\vec{v}_r^*|)^3 \exp^{-\beta^2(|\vec{v}_r^*|)^2} \tag{4.11}$$

where $\beta = \sqrt{m/\left(2k_BT_p\right)}$. The maximum value of $f\left(|\vec{v}_r^*|\right)$ is calculated through $df\left(|\vec{v}_r^*|\right)/d|\vec{v}_r^*| = 0$ and it is $3\beta exp()^{1.5}\sqrt{1.5}$ in this work. An example of sampling from Maxwellian distributions has been shown in Appendix C of Ref. [104], but the range of $|\vec{v}_r^*|$ is selected as $[0, 4/\beta]$ in the code rather than $[0, 3/\beta]$ in page 425 of Ref. [104] to reduce the error.

Eventually, the post-collision relative velocity vector components will be determined with the known post-collision relative velocity magnitude, the deflection angle and the azimuthal angle according to Equation (2.22) from Bird [139] with an opposite direction due to the reflection, which is shown in Equations (4.12), (4.13), and (4.14), respectively.

$$u_r^* = \frac{|\vec{v}_r^*|}{|\vec{v}_r|}\left[-u_r\cos\delta - \sin\delta\sin\varphi\left(v_r^2 + w_r^2\right)^{1/2}\right] \tag{4.12}$$

$$v_r^* = \frac{|\vec{v}_r^*|}{|\vec{v}_r|}\left[-v_r\cos\delta - \sin\delta\left(|\vec{v}_r|w_r\cos\varphi - u_rv_r\sin\varphi\right)/\left(v_r^2 + w_r^2\right)^{1/2}\right] \tag{4.13}$$

$$w_r^* = \frac{|\vec{v}_r^*|}{|\vec{v}_r|}\left[-w_r\cos\delta + \sin\delta\left(|\vec{v}_r|v_r\cos\varphi + u_rw_r\sin\varphi\right)/\left(v_r^2 + w_r^2\right)^{1/2}\right] \tag{4.14}$$

Indirect method

The direct sampling method proposed by Burt and Boyd [29] is computationally expensive due to the random sampling through an acceptance-rejection method from multiple distribution functions for each representative DSMC particle. The so-called indirect method is based on a transformation of the coordinate system through linear algebra and a description can be found in Ref. [27]. A full description of the method is reproduced here.

A global coordinate system is denoted as *xyz* and it is transformed to a local coordinate system, denoted as $X'Y'Z'$, that moves with the solid particle with OX' in the negative direction of the relative velocity $\vec{v}_r$ through coordinate system rotation, where

$$\vec{v}_r = \vec{v}_g - \vec{v}_p. \tag{4.15}$$

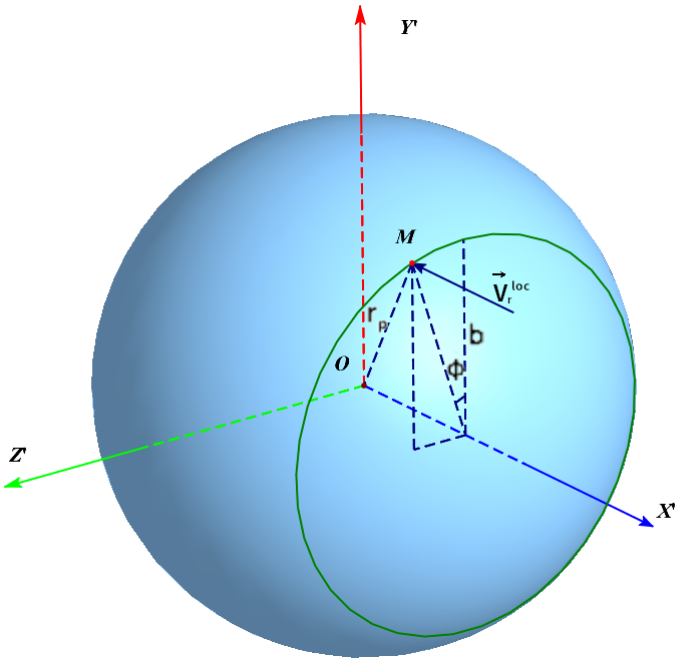

Figure 4.3: **3D Schematic of impact parameter b.**

As a result, the relative velocity, denoted as $\vec{v}_r^{loc}$, in the local system is

$$\vec{v}_r^{loc} = \begin{pmatrix} -|\vec{v}_r| \\ 0 \\ 0 \end{pmatrix}. \tag{4.16}$$

The unit vectors before and after the rotation can be calculated so that the rotation matrix $\mathbf{T}_1$ can be determined by means of Rodrigues' rotation formula,

$$\begin{pmatrix} -1 \\ 0 \\ 0 \end{pmatrix} = \mathbf{T}_1 \cdot \frac{\vec{v}_r}{|\vec{v}_r|}. \tag{4.17}$$

The reflection point M in $X'Y'Z'$ is randomly chosen on a circle with radius b normal to OX', as shown in Figure 4.3. The impact parameter b is stochastically selected as $r_p\sqrt{R_f}$ and the components of M are defined as

$$\begin{pmatrix} \sqrt{r_p^2 - b^2} & b\cos\phi & b\sin\phi \end{pmatrix}, \tag{4.18}$$

where $\phi = 2\pi R_f$.

Secondly, the local coordinate system will be transformed into a normal coordinate system $X_2Y_2Z_2$ with OM in the OX_2 direction. With the help of the unit vector of OM, the rotation

matrix $\mathbf{T}_2$ can be calculated through Rodrigues' rotation formula as

$$\begin{pmatrix} 1 \\ 0 \\ 0 \end{pmatrix} = \mathbf{T}_2 \cdot \frac{OM}{|OM|}. \tag{4.19}$$

Then, the relative velocity in $X'Y'Z'$ coordinate system, noted as $\vec{p}$, will be

$$\vec{p} = \mathbf{T}_2 \cdot \vec{v}_r^{loc} = \begin{pmatrix} \mathrm{p_x} \\ \mathrm{p_y} \\ \mathrm{p_z} \end{pmatrix}. \tag{4.20}$$

Subsequently, the post-collision relative velocity will be evaluated, denoting the normal component as U and the tangential component as V. In the case of a specular reflection, the normal component is inverted and the tangential component remains the same, resulting in

$$\vec{p}^* = \begin{pmatrix} -\mathrm{p_x} \\ \mathrm{p_y} \\ \mathrm{p_z} \end{pmatrix}. \tag{4.21}$$

In the case of a diffusive reflection, the normal (U) and tangential (V) components are based on the Maxwellian velocity distributions:

$$\begin{cases} f\left(\beta^2 U^2\right) = e^{-\beta^2 U^2} \\ f\left(\beta^2 V^2\right) = e^{-\beta^2 V^2} \end{cases} \tag{4.22}$$

where β is the same as that in Equation (4.11).

The normal and tangential components will be sampled as $\sqrt{-\ln\left(R_f\right)}\Big/\beta$. The reflection azimuthal angle φ is randomly chosen in the range of $[0, 2\pi]$ with uniform distribution. Therefore, the post-collision relative velocity in $X_2Y_2Z_2$ is

$$\vec{p}^* = \begin{pmatrix} U \\ V\cos\varphi \\ V\sin\varphi \end{pmatrix}. \tag{4.23}$$

After the calculation of an atom/molecules' post-collision relative velocity in the $X_2Y_2Z_2$ system, the relative velocity in the global coordinate system can be acquired by

$$\vec{v}_r^* = \mathbf{T}_2^{-1}\mathbf{T}_1^{-1}\vec{p}. \tag{4.24}$$

The indirect method does not include any sampling over a distribution function so this method is more efficient. Finally, the absolute molecule velocity vector will be recovered from the local collision coordinate system by adding the particle velocity

$$\vec{v}_g\left(t+\Delta t\right)=\vec{v}_r^*+\vec{v}_p\left(t\right). \tag{4.25}$$

It must be mentioned that no matter if the direct or indirect method is used, the rotational energy for a molecule, e_{rot}, should be updated in the case of diffuse reflection [29]:

$$e_{rot}=-\ln\left(R_f\right)k_BT_p \tag{4.26}$$

where R_f is a random number in the range of $(0,1]$ here.

4.2.4 Solid particle phase change model and particle size correction

Phase change model

The particle phase change will influence the variation of particle temperature when the solid particle temperature is high enough. Burt and Boyd [140] provided a simple phase change model following the theory of Hunter *et al.* [141] to correct the solid particle temperature, but they considered the solid particle diameter as constant, which is unrealistic because the phase change will significantly change the size of the substance. This simple phase change model is reproduced and a particle size correction scheme is added into it. Two essential temperatures must be specified: the nucleation temperature, T_f, and the equilibrium melting temperature, T_m. Combined with a ratio of the crystallisation front radius to the particle radius, r_1, the two temperatures divide the phase change process into 4 parts:

1. If the particle temperature $T_p<T_f$ and $r_1=0$, then the particle is in the pure solid phase.

2. If $T_p<T_f$ and $r_1=1$, which means particle is in the pure liquid phase, but it is supercooled to a low temperature, or if the $T_p<T_m$ and $0<r_1<1$, which means the internal part of this particle is liquid and the shell is solid, as shown in Figure 4.4(a), then the particle is considered in the solidification process. The variation of r_1 is updated through

$$\Delta r_1=-\frac{\mathrm{A}}{r_p}(T_m-T_p)^{1.8}\Delta t, \tag{4.27}$$

where 1.8 is the index according to Plastinin *et.al* [142], A is a constant that depends on material; it is 2.7×10^{-6} $\mathrm{ms^{-1}K^{-1.8}}$ for Al_2O_3. The heat transferred to the gas phase from the solid particles includes the heat due to solidification. Hence, the particle temperature calculated through Equation (4.5) should be corrected by removing the part due to solidification, which is expressed as $\Delta\left(r_1^3\right)h_f/c_p$, where h_f is the latent heat of fusion and $\Delta\left(r_1^3\right)$

is the variation of r_1^3 of a solid particle within Δt.

3. If $T_p > T_m$ and $r_1 < 1$, this condition means that the core of the particle is solid but the shell is in the liquid phase, as shown in Figure 4.4(b). In the condition that this particle absorbed heat and $Q_\delta[\vec{v}] > 0$, then this particle is melting. The new r_1 is acquired by solving the equation:

$$\frac{\sum Q_\delta |\vec{v}| \Delta t}{c_p m_p} = \frac{h_f}{c_p} \Delta \left(r_1^3\right) \tag{4.28}$$

and the temperature variation is calculated through

$$\Delta T_p = \frac{h_f}{c_p} \left(r_1^3 - 1\right). \tag{4.29}$$

4. If $T_p > T_m$ and $r_1 = 0$, the particle is in the pure liquid phase.

More detail of this phase change model can be found in Ref. [140].

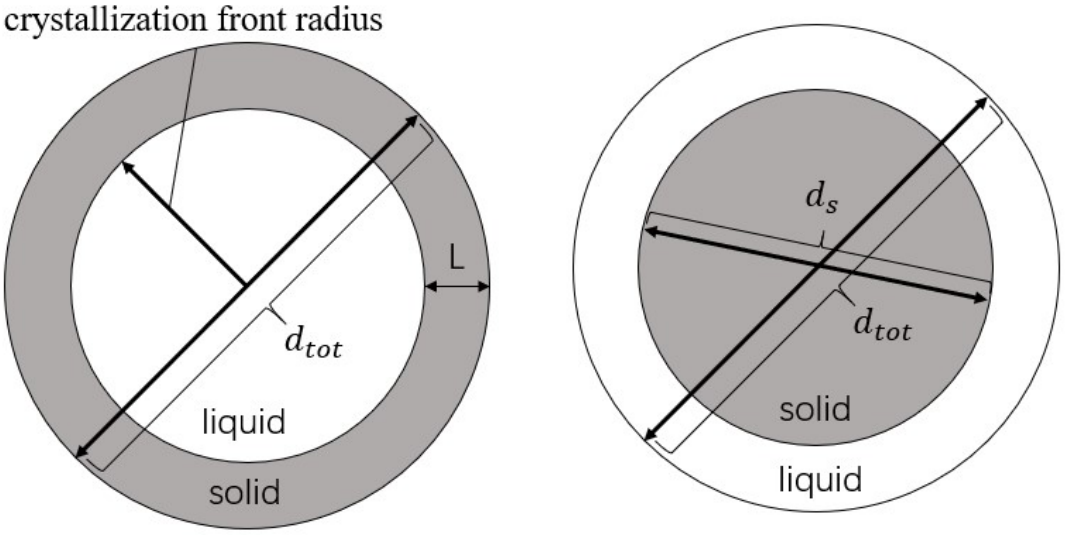

Figure 4.4: **Schematic of particle (a) solidification and (b) melting processes.**

Particle size correction

When solid particles experience phase change, the particle diameter change caused by the material density variation will affect the number of reflections of DSMC particles from a solid particle through Equation (4.8) so that it is worthy of consideration. Hence, if the particle temperature is over the equilibrium melting temperature, then the total diameter of the solid particle is corrected through density correction, whereas, if the particle temperature is lower than the equilibrium melting temperature, the granular particle diameter is considered to be constant.

Although the particle core is in the liquid phase, the value of temperature which is lower than the equilibrium melting temperature is beyond the definition areas of the relation of $\rho_{p,lp} - T_p$.

First, if a particle is in the solid phase and is to melt to the pure liquid phase, the particle diameter is corrected through:

$$d_p = \left(\frac{6m_p}{\pi \rho_{p,lp}} \right)^{1/3}, \tag{4.30}$$

where m_p is the particle mass, which is invariable due to mass conservation, $\rho_{p,L}$ is the particle liquid phase density and it is a single value function of particle temperature according to Equation (7) in Ref. [141].

Second, if the core of the particle is in the solid phase while its shell is in the liquid phase; for instance, when a particle is experiencing melting, then according to mass conservation

$$m_p = m_{p,lp} + m_{p,sp} \tag{4.31}$$

and

$$m_p = \frac{1}{6}\pi \left(d_{p,tot}^3 - d_{p,sp}^3 \right) \rho_{p,lp} + \frac{1}{6}\pi d_{p,sp}^3 \rho_{p,sp}, \tag{4.32}$$

where $m_{p,lp}$ is the particle mass of liquid phase and $m_{p,sp}$ is the particle mass of solid phase. As mentioned in Ref. [140], in the process of melting, r_1 represents the cube-root of the liquid volume fraction so that

$$r_1 = \left(1 - \left(d_{p,sp} / d_{p,tot} \right)^3 \right)^{1/3}. \tag{4.33}$$

Substituting $d_{p,sp}$ into Equation (4.32), the following is obtained

$$d_{p,tot} = \left\{ \frac{m_p}{\frac{1}{6}\pi \left[\left(1 - r_1^3 \right) \rho_{p,sp} + r_1^3 \rho_{p,lp} \right]} \right\}^{1/3}. \tag{4.34}$$

4.2.5 Stochastic interparticle collision model

The stochastic collision method deals with solid-solid collisions by selecting collision pairs at random in a computational cell. Stochastic collision methods are extensively implemented in Lagrangian simulations [143]. The stochastic method has an advantage over deterministic methods because it saves computational time while searching for collision pairs [143]. A representative stochastic collision method is the O'Rourke method [144], which has been a standard method in some commercial codes [143] and has been used in modelling spray dryers [145], but the O'Rourke method suffers from an unthorough collision kernel, unconvincing collision determination, and an unlimited time step [146]. The NTC method [143] and the "Collision Zhang&Bo" method [146] were derived according to the O'Rourke method to improve the accuracy and effi-

ciency. The generalised NTC method was used to model PSI-induced lunar regolith dispersion in Ref. [30].

After the collision pairs are determined, collisions are executed to calculate the post-collision velocities using either the hard sphere model or the soft sphere model [147]. The soft sphere model, also known as the discrete element method, is based on mechanical elements such as a spring and a dash-pot, and collisions and contacts are handled by integrating the equations of motion, leading to substantially higher computational cost [147]. The hard sphere model has a low computational cost and explicitly expresses particle post-collision velocities; however, the hard sphere model is designed for dilute granular flows (i.e. the solid particle number density is assumed to be low) and only binary collisions are considered [147]. In this thesis, only the hard sphere model is taken into account for simplicity.

Collision detection scheme

The NTC method is that in each cell, the number of inter-particle (ip) collision pairs that should be selected and tested for collision, N_{ip}, is

$$N_{ip} = \frac{W_p N_p (N_p - 1) \left(\left| \vec{v}_{r,ip} \right| \sigma_{ip} \right)_{\max} \Delta t}{2 \mathrm{V}_{\mathrm{cell}}}, \tag{4.35}$$

where W_p is the number of real solid particles that each simulator represents, N_p is the instantaneous number of simulator particles in the cell, $\left(\left| \vec{v}_{r,ip} \right| \sigma_{ip} \right)_{\max}$ is the maximum value of the product of the collision cross-section, σ_{ip}, and the relative speed of a particle pair, $|\vec{v}_{r,ip}|$, Δt is the time-step, and $\mathrm{V}_{\mathrm{cell}}$ is the cell volume. Collision pairs accepted for collision if

$$\frac{\left| \vec{v}_{r,ip} \right| \sigma_{ip}}{\left(\left| \vec{v}_{r,ip} \right| \sigma_{ip} \right)_{\max}} > R_f.$$

Hard sphere model

The hard sphere model is widely used to simulate rocket plume and lunar dust interactions [27, 30, 148]. It explicitly expresses the post-collision velocity via the coefficients of restitution and friction. For simplicity, solid particle-particle sliding [147] is ignored and the granular hard sphere model used in Ref. [30] is repeated here. The post-collision velocity is updated via

$$\vec{v}^{*}_{p_i} = \vec{v}_m + \mathrm{e} \left| \vec{v}_{p_i} - \vec{v}_m \right| \vec{e} \tag{4.36}$$

and

$$\vec{v}^{*}_{p_j} = \vec{v}_m - \mathrm{e} \left| \vec{v}_{p_j} - \vec{v}_m \right| \vec{e}, \tag{4.37}$$

where $\vec{e}$ is a vector randomly sampled from a unit sphere and

$$\vec{v}_m = \frac{m_{p_i}\vec{v}_{p_i} + m_{p_j}\vec{v}_{p_j}}{m_{p_i} + m_{p_j}}. \tag{4.38}$$

To ensure energy conservation, when the restitution coefficient, e, is smaller than 1, a fraction of the kinetic energy of an individual particle is transformed into internal energy through

$$\Delta T = 0.5 \times ((\vec{v}_p^*)^2 - (\vec{v}_p)^2)/c_p, \tag{4.39}$$

leading to an increase in the solid particle temperature.

4.2.6 The multipahse particle-in-cell (MPPIC) method

The MPPIC method, pioneered by Andrews and O'Rourke [149], is a method developed in computational particle fluid dynamics for efficiently treating the interactions of a dense solid phase (i.e. high solid particle number density) in simulations of multiphase flows, e.g. fluidised beds [128]. The solid phase in the MPPIC method is expressed in the Lagrangian framework, similar to the DSMC method, and each solid simulator particle represents a large number of real solid particles with the same location, size, density, and velocity. When modelling solid-solid collisions, the method avoids computationally expensive particle collision detection schemes.

The solid phase transport equation of the particle probability distribution function f_p without the consideration of any collision terms is

$$\frac{\partial f_p}{\partial t} + \frac{\partial (f_p \vec{v})}{\partial \vec{r}} + \frac{\partial (f_p \vec{a}_{tot})}{\partial \vec{v}} = 0 \tag{4.40}$$

where the terms on the left hand side are the variation of the particle distribution function with time, convection in physical space, and external body forces in velocity space, respectively [150]. Generally, the total acceleration, $\vec{a}_{tot}$, of a solid particle is expressed as

$$\vec{a}_{tot} = \vec{a}_{drag} - \frac{1}{\rho_p}\nabla p + \vec{g} - \frac{1}{\theta_p \rho_p}\nabla \tau_p \tag{4.41}$$

in the MPPIC method, where θ_p is the local solid phase volume fraction, ρ_p is the solid particle mass density, ∇p is the gas phase pressure gradient, $\vec{g}$ is the gravitational acceleration, and τ_p is the interparticle stress, which is also called particle normal stress (if the off-diagonal elements of the stress tensor are neglected) [150] and particle contact stress [151]. The first two terms on the right hand side are the acceleration due to drag force and buoyancy, and the final term models enduring contacts, rather than collisions, between solid particles in a dense solid phase [151].

The final term in Equation (4.41) is evaluated through a packing model (explicit/implicit) in-

corporating a solid particle stress model (e.g. the Harris and Crighton model [152] or Lun's model [153]). The implicit packing model suffers from difficulty in solving highly nonlinear volume fraction equations, resulting in high computational cost. Furthermore, there is a possibility of yielding an unphysical negative volume fraction using the implicit packing model because of the existence of gradients of the particle interpolation operators in the linearised volume fraction equations [150]. Unlike the implicit packing model, the explicit packing model is robust and fast because the requirement for an implicit solution for particle stress is removed via including the stress gradient, making it ideal for three-dimensional simulations. In the explicit packing model, a continuous calculation of the particle pressure is used to simulate the particle stress, and the resulting stress force is applied to discrete particles. The packing model limits and corrects the velocity of the solid particles by increasing the interparticle stress to infinity, preventing them from entering closely-packed cells that they may move towards [151].

A packing model, however, is insufficient to fully characterise solid-solid interactions because it does not account for the effect of solid-solid collisions. It has been demonstrated that through solid-solid collisions, the particle velocity distribution eventually tends to an isotropic, Gaussian distribution, and that high-frequency collisions in dense granular flow enhance particle stresses [154]. Therefore, the damping and the return-to-isotropy models are also derived and included in the MPPIC method.

Particle collisional exchanges of mass, momentum, and energy between particles were considered using a Bhatnagar, Gross, and Krook (BGK) model added on the right hand side of Equation (4.40) to evaluate the rates of local equilibration of particle velocities and the masses, compositions, and temperatures of liquid films on bed particles due to collisions [154]. The transport equation of the solid phase with additional collision terms is

$$\frac{\partial f_p}{\partial t} + \frac{\partial \left(f_p \vec{v}\right)}{\partial \vec{r}} + \frac{\partial \left(f_p \vec{a}_{tot}\right)}{\partial \vec{v}} = \frac{f_{D'} - f_p}{t_D} + \frac{f_{G'} - f_p}{t_G}, \tag{4.42}$$

where $f_{D'}$ is the "particle distribution function obtained by collapsing the velocity dependence of f to a delta function centered about the local mass-averaged particle velocity" [151], and $f_{G'}$ is the isotropic Gaussian particle distribution function [155]. On the right hand side of Equation (4.42), the first term, called the collisional damping term, demonstrates that particle velocities relax to the mass-averaged velocity within a damping time t_D and it is an improved version that takes the effects of the particle coefficient of restitution and of non-equilibrium particle collision frequency into account [151]; the second term, named the return-to-isotropy term, ensures that particle distributions tend to isotropy within a relaxation time named the return-to-isotropy time, t_G. The time of the relaxation to an equilibrium distribution caused by collisions is assumed to be proportional to the particles' collision time [154]. The final

expression for the damping time is

$$\frac{1}{t_D} = \frac{2\sqrt{2}}{3\pi}\frac{\theta_p}{r_{32}^3}\frac{\sum_p W_p (r_p + r_{32})^4 \left(\vec{v}_{p,i} - \bar{\vec{v}}\right)^2}{\sum_p W_p (r_p + r_{32})^2 \sqrt{\left(\vec{v}_{p,i} - \bar{\vec{v}}\right)^2}}\frac{\theta_{cp}}{\theta_{cp} - \theta_p}\left(1 - \mathrm{e}^2\right), \tag{4.43}$$

where r_{32} is known as the Sauter mean radius, $\sum_p$ is the summation done in a computational cell, $\bar{\vec{v}}$ is the averaged particle velocity of a cell, θ is the solid volume fraction, θ_{cp} is the solid close-packing volume fraction and e is the particle restitution coefficient [151]. With the introduction of Equation (4.43), improvements can be found in the test of colliding particle jets with the participation of the damping model in Ref. [155] while the results were still not sufficiently realistic because no particle scattering can be observed in the downstream. The particle dispersion downstream in the colliding jets is observed in the tests of Ref. [155] and the return-to-isotropy time, t_G, is expressed as

$$\frac{1}{t_G} = \frac{8\sqrt{2}}{5\pi}\frac{\theta_p}{r_{32}^3}\frac{\sum_p W_p (r_p + r_{32})^4 \left(\vec{v}_{p,i} - \bar{\vec{v}}\right)^2}{\sum_p W_p (r_p + r_{32})^2 \sqrt{\left(\vec{v}_{p,i} - \bar{\vec{v}}\right)^2}}\frac{\theta_{cp}}{\theta_{cp} - \theta_p}\frac{1+\mathrm{e}}{2}\left(2 - \frac{1+\mathrm{e}}{2}\right). \tag{4.44}$$

The code for modeling the damping term and the return-to-isotropy term was previously well-developed in OpenFOAM. More detail of the derivation of the damping model and the return-to-isotropy model can be found in Refs. [151] and [155] respectively.

The MPPIC method described thus far is embedded in the Euler-Lagrangian framework with the Navier-Stokes equations for solving continuum gas phase and it is not capable of simulating multiphase flow when the gas phase is rarefied. Therefore, the *rarefiedMultiphaseFoam* and the MPPIC method both being implemented within OpenFOAM are combined together. The MPPIC method is reproduced in *rarefiedMultiphaseFoam* source code and has been improved to model axisymmetric geometries by the addition of radial weighting factors. The DSMC method controls the gas-phase evolution, while the MPPIC method is fully responsible for solid-solid interactions at high solid number density. The accelerations due to the gas phase, incorporating the drag and buoyancy forces in Equation (4.41), are updated through the interphase coupling model in Section 4.2.3.

4.3 Benchmarking tests

4.3.1 DSMC particle reflection from the surface of a stationary solid particle

The momentum and energy exchange from a solid particle to a gas atom or molecule is accomplished by collisions of gas atoms/molecules on the solid particle's surface. The reflection

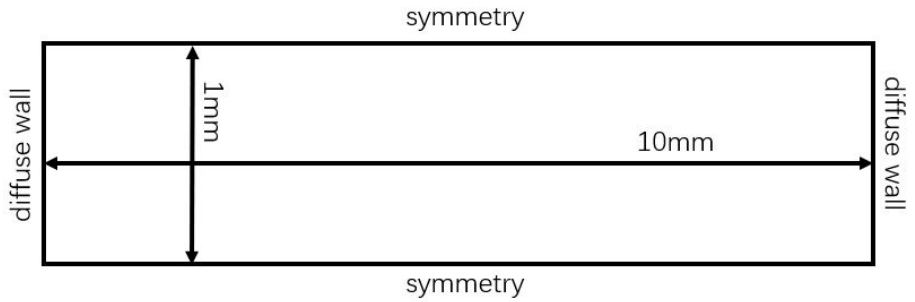

Figure 4.5: **Computational domain for calculating DSMC particles reflection from a stationary solid particle.**

shown in Ref. [27] is duplicated to validate *rarefiedMultiphaseFoam* solver. In this validation case, a real stationary solid particle is fixed at $(0,0,0)$ in the domain, and the atoms/molecules in the surrounding gas will collide with and then reflect from the surface of this solid particle. The computational geometry and corresponding boundary conditions are shown in Figure 4.5. The cell size is 5×10^{-5} m and the gas number density is uniform in the domain with a value of 3.54×10^{21} m^{-3}. The gas type is not important and the molecule mass is 5×10^{-26} kg. The solid particle temperature is 1000 K. One million samples are collected for each case.

Specular reflection

To observe the distributions of the azimuthal angle and the polar angle of post-collision velocities, the relative velocity between the solid particles and gas molecules/atoms has been fixed as $(100,10,20)$ m/s to cancel the impact of the variations of the relative velocity on the results of the distributions. The angle of incidence equals the angle of reflection in specular reflection, and the magnitude of the relative velocity remains constant. The direction of reflection is distributed uniformly in space [27]. The results of azimuthal angle and the cosine of polar angle are plotted in Figures 4.6. The fluctuations from both methods are caused by random sampling, and the positions of peaks will change with the number of samples. As expected, the azimuthal angles from both direct and indirect methods are uniformly distributed between 0 to 2π and the cosines of polar angles from both methods are evenly distributed in the range of $[-1,1]$, which is in excellent agreement with the results of Ref. [27].

Diffuse reflection

In diffuse reflections, the angle of reflection is not equivalent to the angle of incidence and the post-collision velocity magnitude ($|\vec{v}^*|$) changes. As shown in Equation 4.11, the post-collision speed of gas atoms/molecules is relative to the particle mass and temperature, and the post-collision speed should follow the distribution of Equation (4.11). The final profile of the

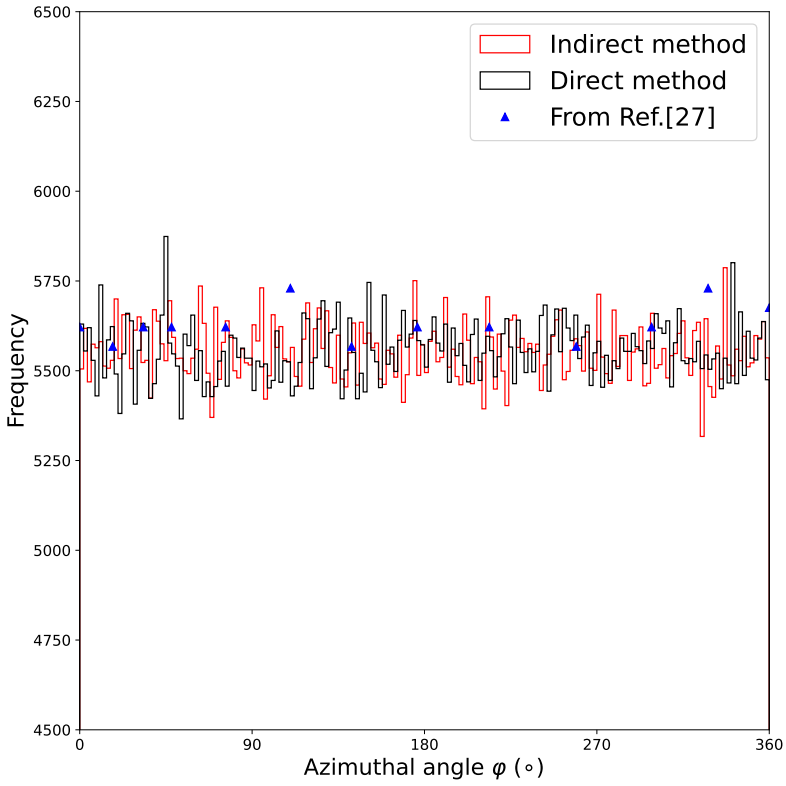

(a)

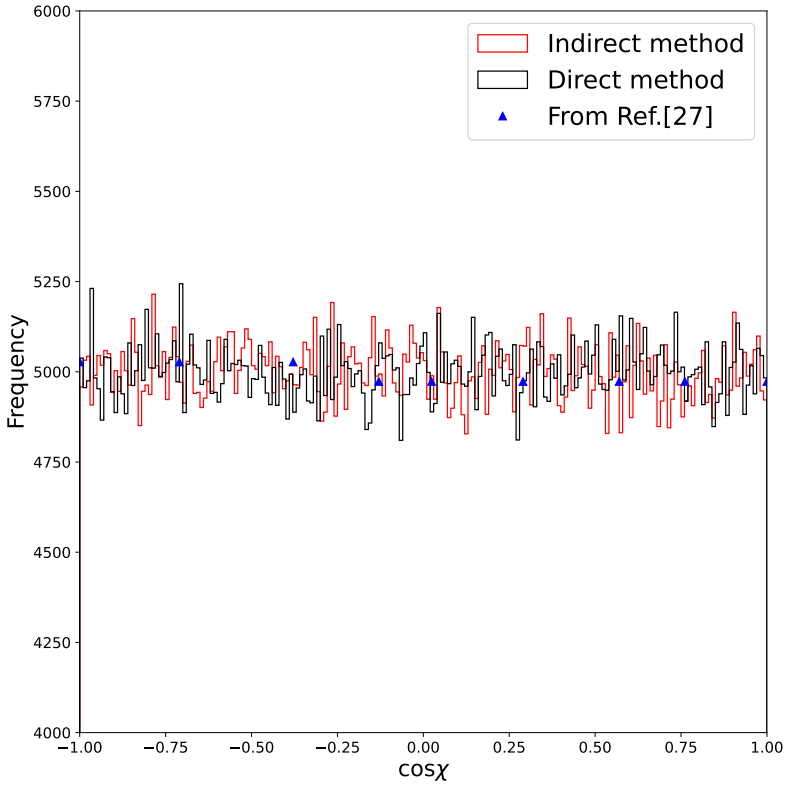

(b)

Figure 4.6: **(a) Azimuthal angle distribution and (b) cosine distribution of polar angle in specular reflection from the direct and indirect methods in two-way coupling model.**

histograms from both methods is presented in Figure 4.7 and they are in good agreement, with a tiny difference caused by the statistical error due to sampling. Both methods also have excellent agreement with the theoretical profile that indicates the kinetic energy change of reflected gas atoms/molecules after a diffuse reflection from a solid particle surface. Good agreements can also be found in the distribution of the post-collision azimuthal angle and the cosine of the polar angle in Figures 4.8 of this work and Figures 8 and 9 in Ref. [27], proving that both methods are equivalent. In comparison with the profiles in Figure 4.6, the post-collision polar and azimuthal angle distributions of diffuse reflection shown in Figure 4.8 do not follow a uniform distribution, which is expected for diffuse reflections.

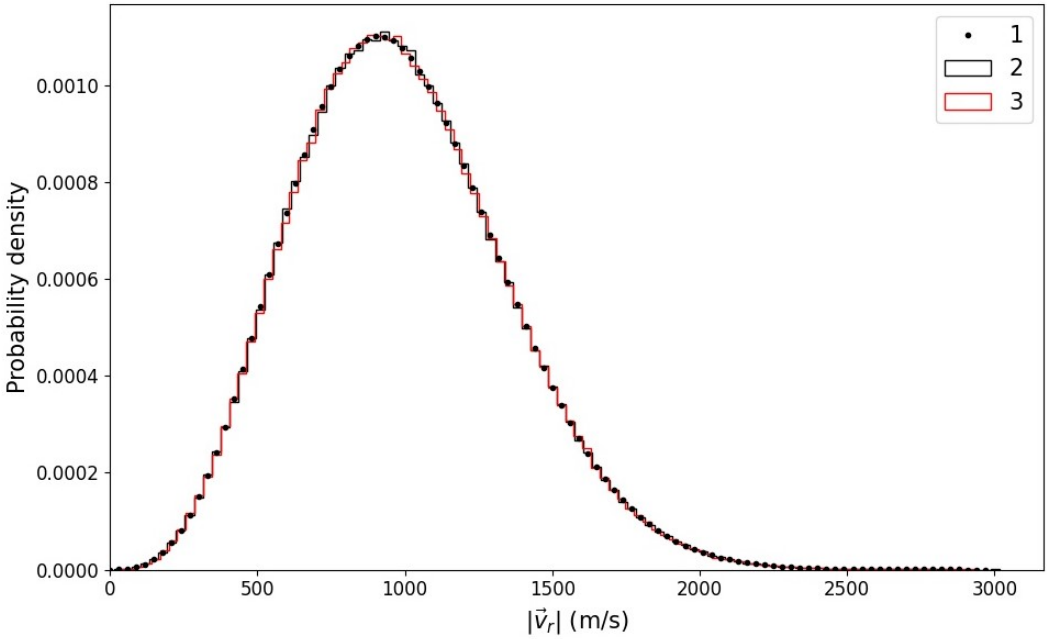

Figure 4.7: **Post-collision relative velocity distribution in diffuse reflection from the direct and indirect methods. The black line is the distribution function of Equation (12) in Ref. [29]. The number of samples is 1 million. 1: Theoretical distribution of Equation** (4.11)**, 2: Result from indirect method, 3: Result from direct method based on Equation (2.22) from Ref. [104]. The probability density is calculated as** $M_j / \sum_{j=1}^{bins} M_j \times \frac{x_{\max} - x_{\min}}{bins}$**, where** M_j **is the number of samples,** $bins$ **is the number of bins in the histogram and** x_{max} **and** x_{min} **are the maximum and minimum of the horizontal ordinate.**

4.3.2 Solid particles in a uniform gas flow

A simple case of a uniform two-phase flow, which was published by Burt and Boyd [29], is repeated here for validation of the effectiveness and accuracy of the two-way coupling method in *rarefiedMultiphaseFoam*. The computational domain is a 0.1 mm $\times$ 20 mm 2D rectangle, as shown in Figure 4.9, divided into 5000 cells (5×1000) with a cell size of 2×10^{-5} m. The

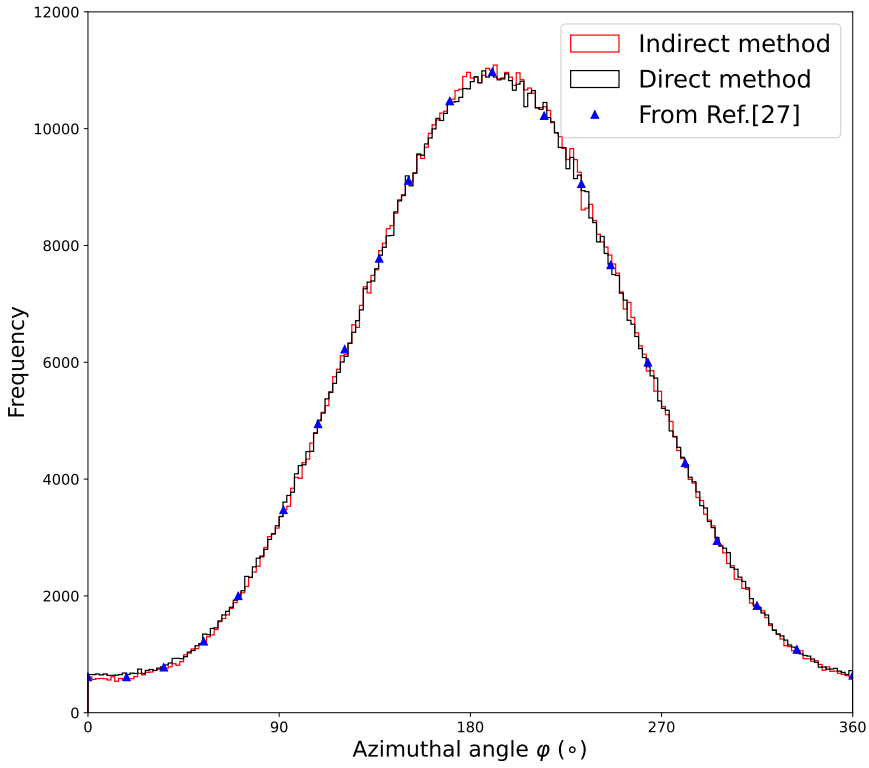

(a)

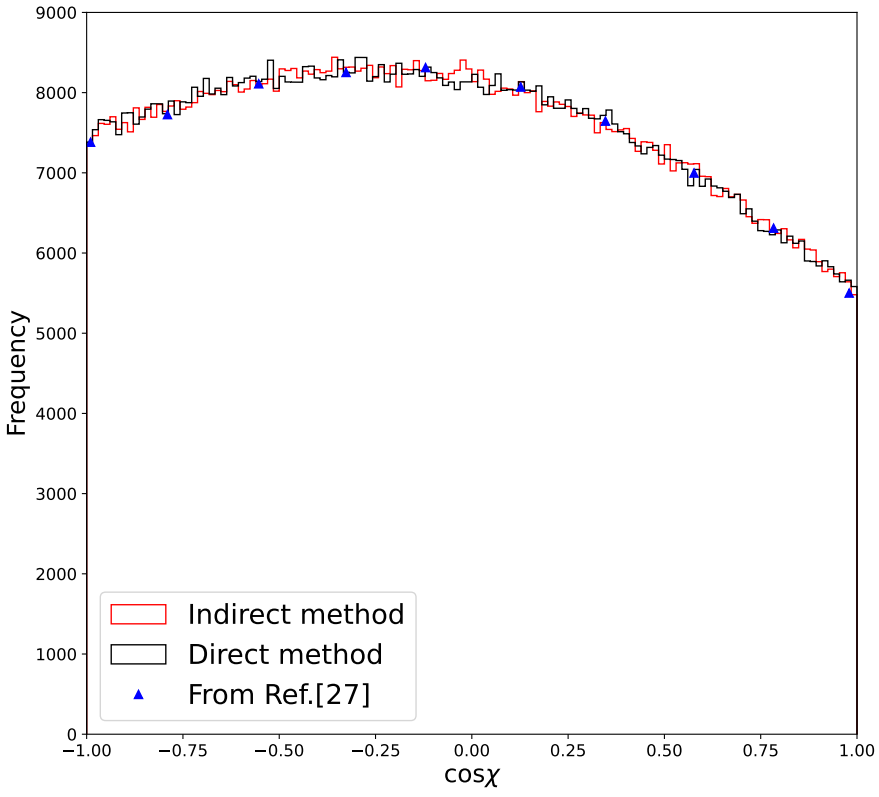

(b)

Figure 4.8: **(a) Azimuthal angle distribution and (b) cosine distribution of polar angle in diffuse reflection from the direct and indirect methods.**

Table 4.1: **Parameters of particle acceleration in a uniform gas flow in the validation of *rarefiedMultiphaseFoam***

	Gas phase		
Species	H_2	N_2	CO
Diameter (m)	3.34×10^{-27}	4.65×10^{-26}	4.65×10^{-26}
Number density (m^{-3})	2×10^{23}	1×10^{23}	1×10^{23}
Speed (m/s)		2000	
Temperature (K)		1000	
	Solid phase		
Species		A	B
Diameter (m)		3×10^{-6}	6×10^{-6}
Number density (m^{-3})		9.896×10^{10}	1.237×10^{10}
Speed (m/s)		1200	
Temperature (K)		2200	
Material density (kg/m^3)		3970	
Specific heat $(J/(kg \times K))$		765	
Surface thermal accommodation coefficient		0.89	

Variable Hard Sphere (VHS) model and the Larsen-Borgnakke model for calculating the redistribution of energy within the gas phase are used in the DSMC simulation. The computational parameters are presented in Table 4.1. Additionally, 2×10^5 samples have been collected after the steady state for averaging.

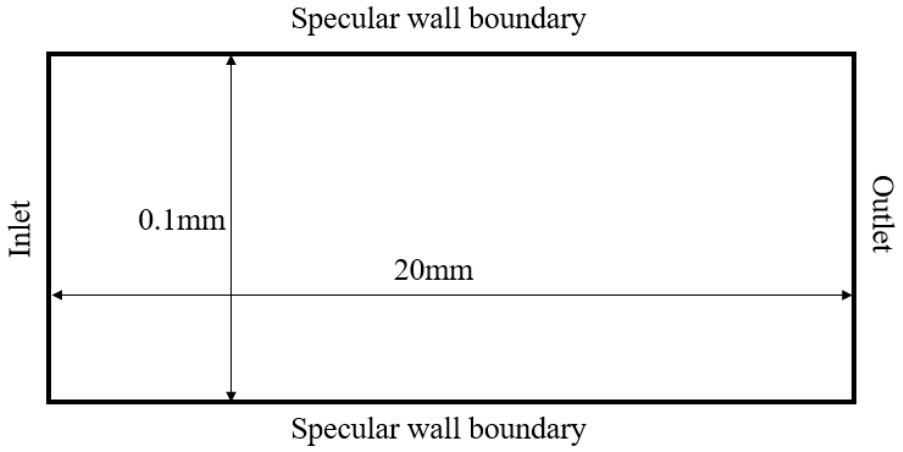

Figure 4.9: **Dimensions and boundary conditions of the computational domain used for particle acceleration in a uniform gas flow.**

The comparisons of the number density, temperature, and speed of the solid phase and gas phase between the results from Ref. [29], Ref. [156] and *rarefiedMultiphaseFoam* have been made in Figures 4.10–4.12. The results from the new solver are obtained by averaging the 5 cell values in the direction perpendicular to the flow direction to decrease the statistical noise. The gas properties all perfectly agree with those in Ref. [29], and the solid phase properties are in excellent agreement with the results of Ref. [156], but have discrepancies with the solid phase

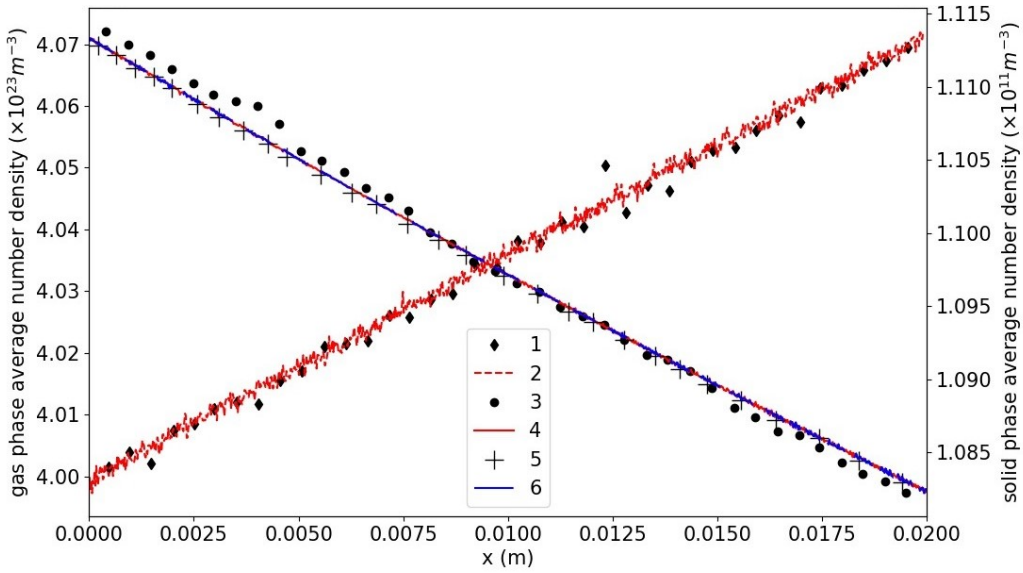

Figure 4.10: **Average number density of gas phase and solid phase. 1: Result of gas phase from Ref. [29], 2: Result of gas phase from *rarefiedMultiphaseFoam*, 3: Result of solid phase from Ref. [29], 4: Result of solid phase from *rarefiedMultiphaseFoam*, 5: Result of solid phase from Ref. [156], 6: Result of solid phase based on Equation (14) of Ref. [29] from *rarefiedMultiphaseFoam***

results in Ref. [29].

As specular wall boundary conditions are used, the total energy and momentum of both phases are conservative. Linear variations of the properties of both phases due to momentum and energy exchange have been successfully reproduced, indicating that *rarefiedMultiphaseFoam* is able to provide physical results. In Figure 4.11, hot solid particles were cooled down linearly during the movement in x-direction, and the heat was transferred to the gas phase. Different averaging methods were implemented in the calculation of the average temperature of the solid phase in each cell by Burt and Boyd [29] and Li *et al.* [156]. Burt and Boyd [29] used the arithmetic average temperature, which is calculated through:

$$\bar{T} = \frac{\sum\sum T_{p,ij} N_{p,ij}}{\sum\sum N_{p,ij}}, \tag{4.45}$$

while Li *et al.* [156] used the weighted averaged temperature

$$\bar{T}_w = \frac{\sum\sum c_{p,i} m_{p,i} T_{p,ij} N_{p,ij}}{\sum\sum c_{p,i} m_{p,i} N_{p,ij}}, \tag{4.46}$$

where i is the index of the solid particle species and j is the index of solid particles of a specific specie within a cell. Figure 4.12 manifests acceleration of solid particles caused by fast-moving gas flow. Solid particles are finally accelerated to about 1227 m/s using *rarefiedMultiphaseFoam*, which is about 4% different from the final speed of the solid particles in Ref. [29].

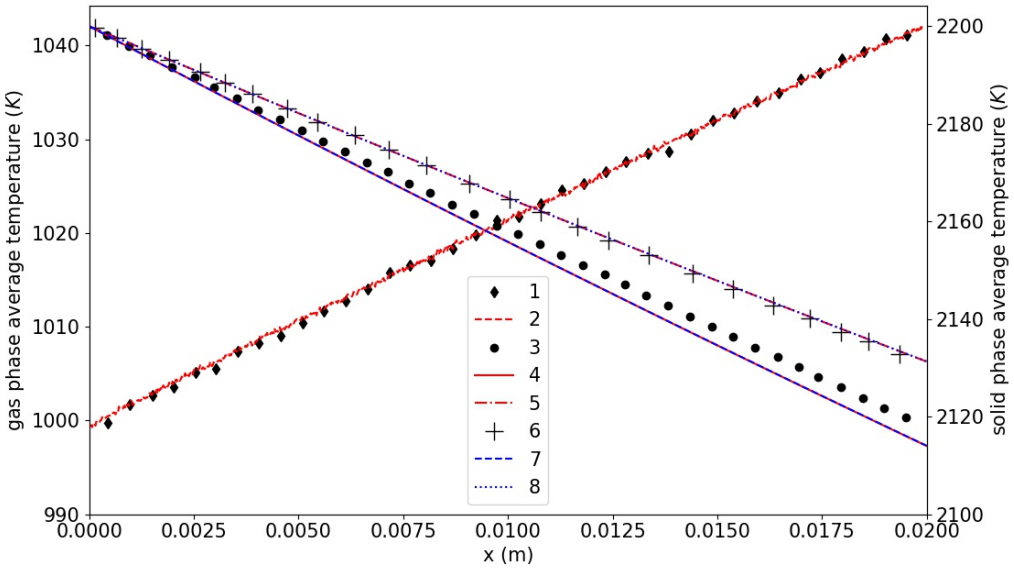

Figure 4.11: **Average temperature of gas phase and solid phase. 1: Result of gas phase from Ref. [29], 2: Result of gas phase from *rarefiedMultiphaseFoam*, 3: Result of solid phase from Ref. [29], 4: Result of solid phase arithmetic average temperature from *rarefiedMultiphaseFoam*, 5: Result of solid phase weighted average temperature from *rarefiedMultiphaseFoam*, 6: Result of solid phase weighted average temperature from Ref. [156], 7: Result of solid phase arithmetic average temperature based on Equation (14) of Ref. [29] from *rarefiedMultiphaseFoam*, 8: Result of solid phase weighted average temperature based on Equation (14) of Ref. [29] from *rarefiedMultiphaseFoam***

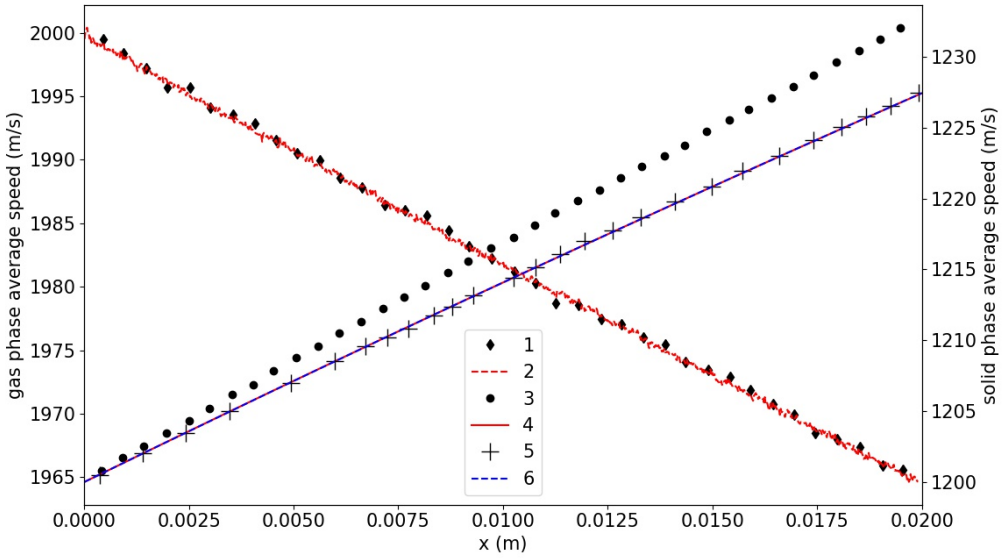

Figure 4.12: **Average speed of gas phase and solid phase. 1: Result of gas phase from Ref. [29], 2: Result of gas phase from *rarefiedMultiphaseFoam*, 3: Result of solid phase from Ref. [29], 4: Result of solid phase from *rarefiedMultiphaseFoam*, 5: Result of solid phase from Ref. [156], 6:Result of solid phase based on Equation (14) of Ref. [29] from *rarefiedMultiphaseFoam***

4.3.3 Particle phase change

The particle phase change model will be validated to determine if a solid particle can experience a continuous and physical phase change process. By using the same computational domain in Section 4.3.1, a real stationary solid particle, whose weight is 1, is deployed at $(0,0,0)$ and the gas flow passes across the solid particle and results in either solidification or melting of this solid particle. The simulation detail is shown in Table 4.2. The boundary conditions on the left and right surfaces are inlet and outlet boundary conditions, and the top and bottom surfaces are specular wall boundary conditions for the gas phase. The NTC method and variable soft sphere model are selected to conduct collisions of the gas phase. The particle diameter of the solid phase is 7×10^{-5} m. The material density and specific heat capacity is 3970 kg/m^3 and 765 J/kgK, respectively. α_p and ε_p in Equation (4.1) are 1 and 0. The equilibrium melting temperature, the nucleation temperature, and the constant A of Equation (10) in Ref. [140] for Al_2O_3 are 2313 K, 1970 K, and 2.7×10^{-6} ms^{-1}/K$^{-1.8}$ [157], respectively. The heat of fusion is 1.07×10^6 J/kg for Al_2O_3 particles here. The particle size correction model is embedded in the phase change model to correct the particle diameter due to the density variation.

Figures 4.13 and 4.14 manifest the relationship of $T_p - D_p$ and $T_p - r_1$ of the two cases. The particle will not melt until its temperature exceeds the melting temperature, which is 2313 K here. As the solid particle melts towards the internal part, its total diameter, which includes the

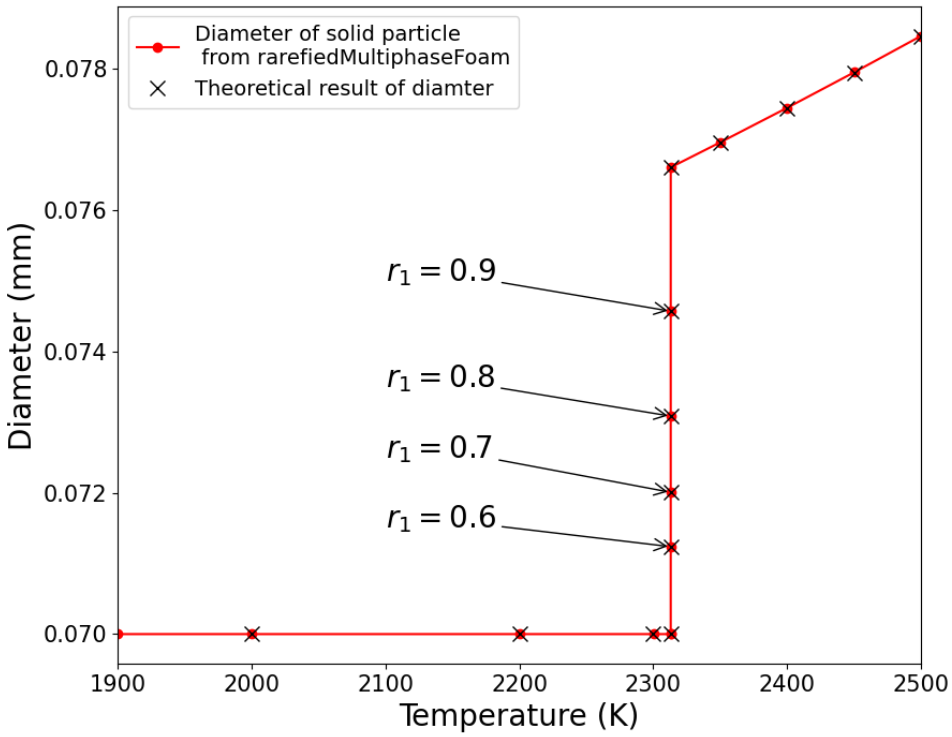

(a)

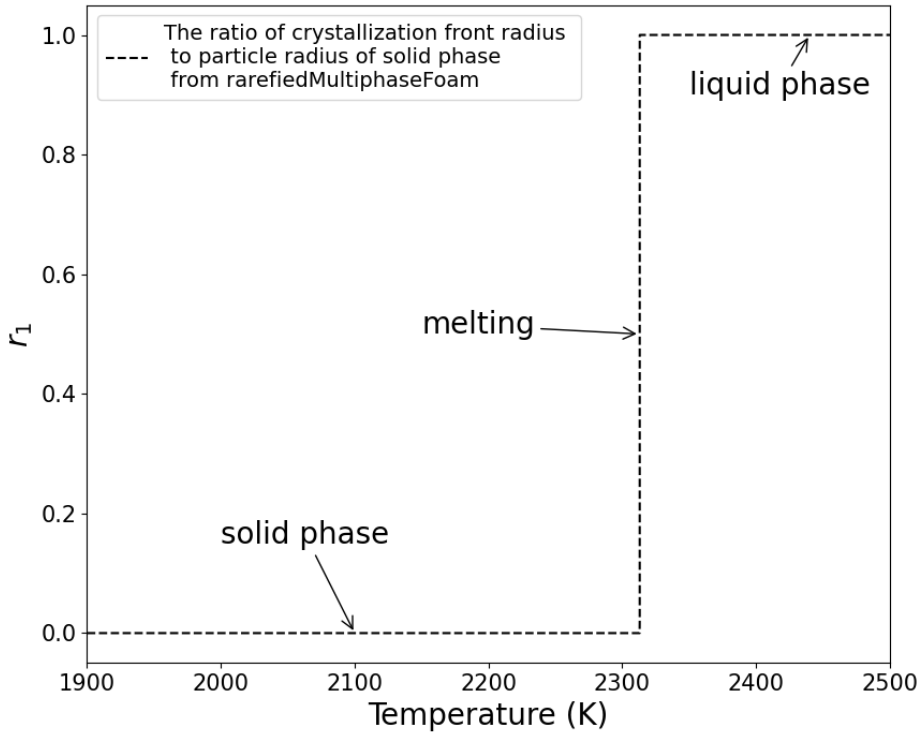

(b)

Figure 4.13: **Results of particle heating process.**

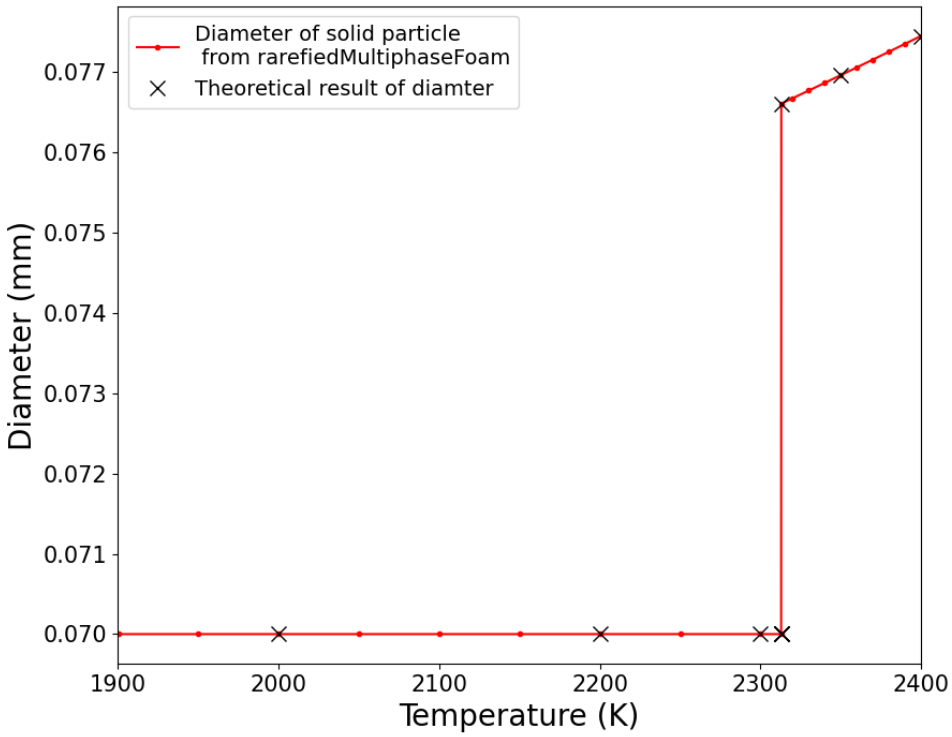

(a)

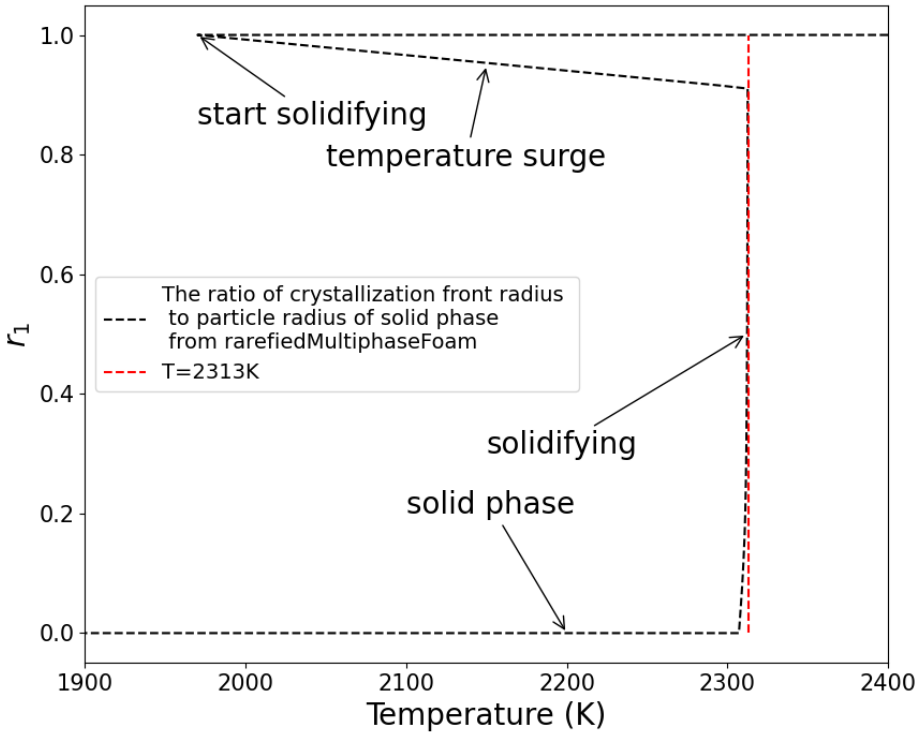

(b)

Figure 4.14: **Results of particle cooling process.**

Table 4.2: **Parameters of particle phase change cases in the validation of *rarefiedMultiphaseFoam*.**

Cooled particle				
Phase	Material type	Velocity (m/s)	Temperature (K)	Inlet number density $(/m^3)$
Gas	Argon	(337.2,0,0)	1000	3.54×10^{21}
Solid	Aluminum Oxide	(0,0,0)	2400	1×10^{12}
Heated particle				
Phase	Material type	Velocity (m/s)	Temperature (K)	Inlet number density $(/m^3)$
Gas	Argon	(337.2,0,0)	3000	3.54×10^{21}
Solid	Aluminum Oxide	(0,0,0)	1900	1×10^{12}

diameter of the solid sphere core and twice the thickness of the liquid shell, will increase in the condition of constant particle temperature. When it is completely melted into the liquid phase, the particle diameter will increase to the maximum value and remain constant. For heating cases, the solver can provide a solution that is in excellent agreement with the theoretical results.

As expected, the solid particle diameter will be reset to 7×10^{-5} m when its temperature reaches the melting temperature, and as assumed, the solidification process starts when the particle temperature is lower than the nucleation temperature, as shown in Figure 4.14(a). It is worthy to note that the temperature surge in the relationship of $T_p - r_1$ in Figure 4.14(b) is caused by existence of the term of latent heat of fusion representing the transition from the liquid phase to stable $\alpha-$phase of alumina, which is mentioned in Equation (12) of Ref. [140] to simplify the crystallisation process, and this temperature variation prevents the particle temperature from exceeding the melting temperature, which can be observed from the red dash line representing the melting temperature.

To sum up, the phase change model with the size correction proposed here allows a solid particle to experience a continuous phase change and diameter change. However, the collision between these liquid droplets or particles mixed with both phases and the droplet-wall interaction have not been considered yet. Currently, the thermophysical properties of Al_2O_3 [141] and ZrO_2 [158] are well-defined, but the thermophysical properties of other materials can be extended in the future.

4.3.4 Particle sedimentation using the MPPIC method

In Section 4.2.6, the MPPIC method have been reviewed, which is responsible for the simulations of solid particles interactions, including enduring and transient contacts. Before any application, a gravity-dominated sedimentation case in Ref. [150] is repeated with no gas phase in the domain to allow us to focus on the correctness of the reproduced MPPIC method in the *rarefiedMultiphaseFoam*.

The domain is a $0.138 \times 0.138 \times 0.3$ m hexahedron and it is decomposed into 9000 cells ($15 \times$

15×40). The boundary conditions of the six surfaces are all diffuse wall boundary conditions. The particle material density is 2500 kg/m^3 and the diameter is 0.3 mm. The number of solid simulator particles in the domain is 162232 and each parcel represents 749 real solid particles. The gravitational acceleration is 9.8 m/s^2 and the time-step is 0.001 s. All particles are stationary after the initialisation and distributed uniformly throughout the domain. The dual averaging method and the extended Harris and Crighton particle stress model [150, 152] are used. The interparticle stress is expressed as

$$\tau_p = \frac{P_s \theta_p^{\beta}}{\max\left[\left(\theta_{cp} - \theta_p\right), \varepsilon\left(1 - \theta_p\right)\right]} \tag{4.47}$$

according to the extended Harris and Crighton model, where P_s is a constant in the range of 5 to 200 with a unit of pressure [159], β is suggested to be a constant between 2 and 5 by Auzerais *et.al* [160], ε is 1×10^{-7}, θ_p is solid particle volume fraction, and θ_{cp} is the close-packing volume fraction. Here P_s , β and θ_{cp} are 10 Pa, 2 and 0.6 respectively according to Ref. [150].

The results of the particle distribution is shown in Figure 4.15. When t= 0.01 s, particles with a volume fraction of 0.3 are initialised uniformly in the domain. As the particles begin to accelerate under the action of the applied gravity, the volume fraction at the top approaches zero, while the volume fraction at the bottom approaches the close-packing value. When all of the particles have settled, there is an evident cut off at half the domain's height where no solid particles remain above ($t = 0.6$ s).

The particle volume fractions with time are compared quantitatively in Figure 4.16. The volume fraction values in Figure 4.16 are averaged ones in the $x-$ and $y-$directions at each layer to reduce the statistical noise. At $t = 0.1$ s, 0.2 s and 0.6 s, the volume fractions agree well with those from Ref. [150]. If the statistical noise is neglected, the cause of the difference at $t = 0.15$ s is most likely the drag force and coefficient of restitution. To begin with, no drag force is acting on the solid particles due to the absence of the gas phase in this test while the gas phase is present in the test case of Ref. [150], with a gas density of 1.093 kg/m^3. The sedimentation speed of solid particles is faster than that with the appearance of drag forces, leading to a higher volume fraction between 0.08 m and 0.125 m and a smaller volume fraction between 0.19 m and 0.21 m.

In addition, at 0.2 s in Figure 7 of Ref. [150] and at 0.15 s in Figure 4.15, a small amount of particles bouncing back from the top sedimentation layer are noticeable, but the volume fraction distribution near the top of the sedimentation layer appears to be different in the two figures, which might be a result of a difference in the coefficient of restitution used in the validation case. The coefficient of restitution in current test is 0.85, but it is not mentioned in Ref. [150]. Figure 4.17 presents a comparison of the effects of the coefficient of restitution with the same physical properties except for the difference in the coefficient of restitution. A higher restitution

coefficient means less kinetic energy lost during collisions. The particles with a higher coefficient of restitution obviously bounce back higher than those with a smaller coefficient, proving the significance of the coefficient of restitution.

4.4 Summary

In this chapter, the open source DSMC solver – *dsmcFoamPlus* has been updated to include a two-way coupling model to calculate the momentum and heat exchange between the gas and solid phases, a solid particle phase change model with particle size correction, the solid stochastic collision model for dilute granular phases, and the MPPIC method to solve dense granular flows.

Some benchmarkings of an open source DSMC-based solver in OpenFOAM for two-phase rarefied flow called *rarefiedMultiphaseFoam* have been undertaken. Results from *rarefiedMultiphaseFoam* have been compared with the theoretical and previous simulation results.

The results of azimuthal and polar angle distributions of specular and diffuse reflections of DSMC particles from the stationary solid particle surface through the indirect method are in excellent agreement with those obtained through the direct method, proving the equivalence between the two methods. The post-collision relative speed through both methods has been compared with the theoretical result and shows good agreement.

The case of solid particles injected into a uniform gas flow is reproduced. The results are physical and in good agreement with that shown in Ref. [29].

The reproduced MPPIC code in *rarefiedMultiphaseFoam* is validated through a gravity-controlled sedimentation case. The results of the volume fraction of the solid phase are logical and agree well with that in Ref. [150], indicating the effectiveness of the MPPIC method.

The results of the phase change model are presented by calculating the process of cooling and heating of a stationary solid particle. The results show that a solid particle can experience a physical and continuous phase change with the use of the phase change model.

After rigorous validations and benchmarkings, the solver can be applied to the simulation of lunar PSI and the simulation parameters and results will be discussed in the next chapter.

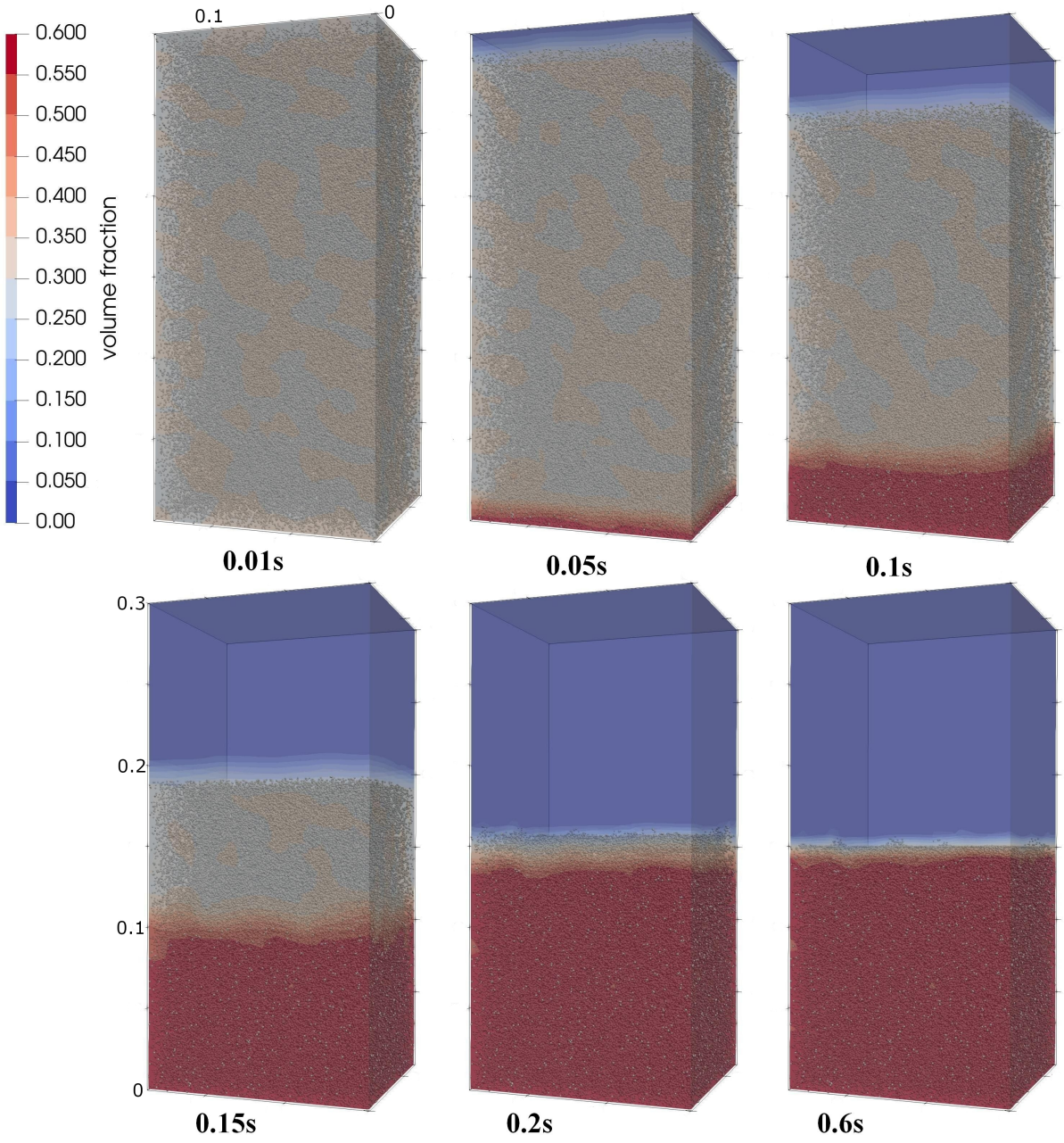

Figure 4.15: **Particle distribution variation with times during the process of sedimentation.**

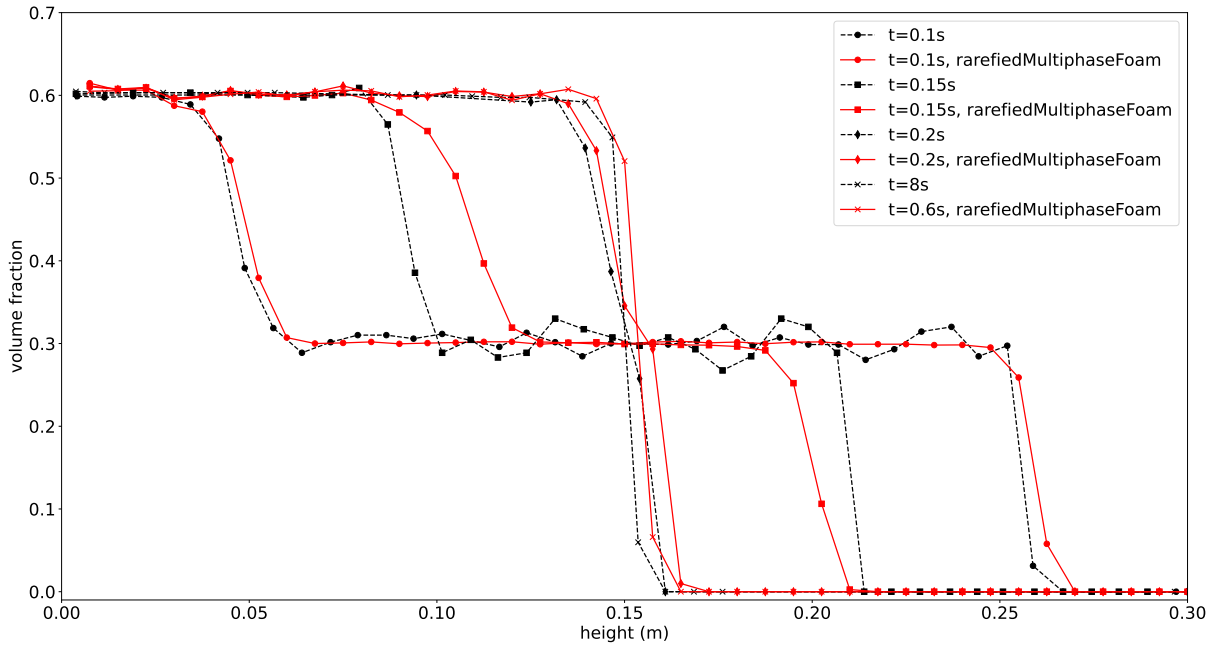

Figure 4.16: **Comparison of solid phase volume fraction distribution. Red: from *rarefiedMultiphase*. Black: from Ref. [150].**

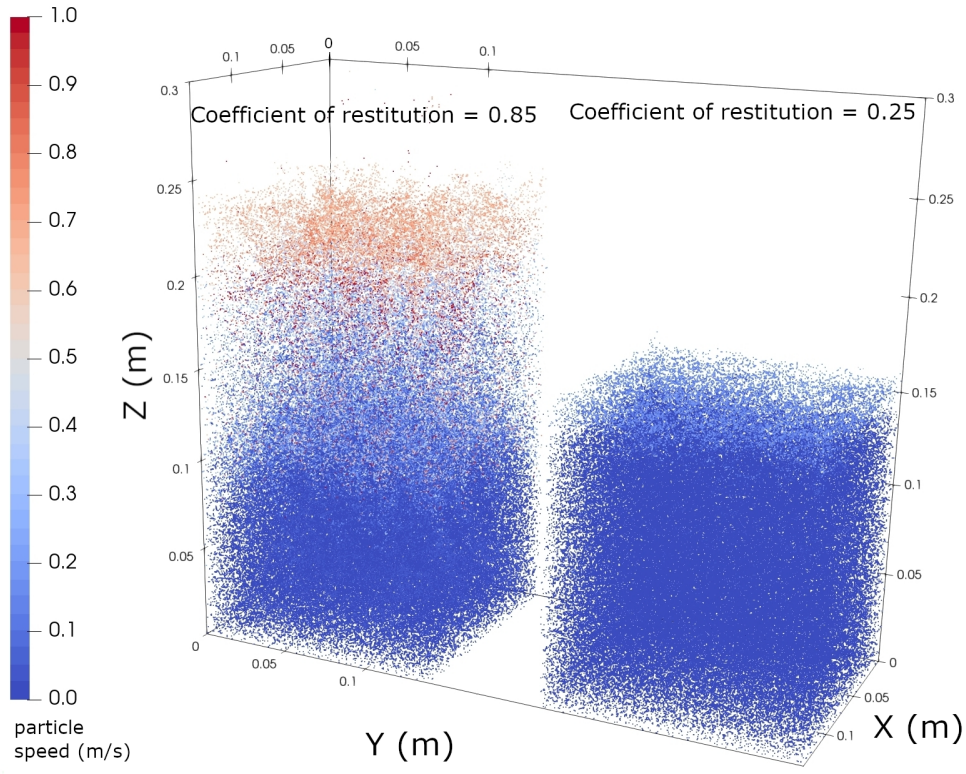

Figure 4.17: **Comparison of the particle distribution with different coefficient of restitution at 0.2 s.**

Chapter 5

Application of rarefiedMultiphaseFoam: lunar plume-surface interactions

Chapters 2 and 3 studied supersonic starting free jet flows and their impingement on a flat plate. This chapter will replace the plate with a regolith-coated surface, and the supersonic starting jet and eventual exhaust plume from a nozzle will impinge on and interact with the dust layer. The multiphase solver benchmarked in Chapter 4 – *rarefiedMultiphaseFoam* solver will be used to simulate PSI. To begin with, a short literature review of PSI will be presented, followed by the details of the simulation parameters. The transient effect and influence of the solid-solid enduring contacts on the gas field and the lunar regolith layer will be discussed.

5.1 A review of PSI

PSI is a multi-phase and multi-system complex discipline that details the phenomenon caused by the impingement of a rocket exhaust on planetary body regolith; including cratering physics, ejecta dynamics, and plume flow physics [26].

Much effort was devoted to investigating PSIs during NASA's Apollo and Viking projects, since this phenomenon has the potential to have an influence on human activities in the extraterrestrial environment and has become one of the most challenging problems in lunar missions [161]. When the Apollo 12 lunar module landed on the Moon, permanent marks caused by sandblast induced by PSIs were observed on the surfaces of the Surveyor 3 spacecraft, which was located 155 m away from the Apollo 12 landing site [162]. In addition, the 11°-tilt caused by PSI during the landing of the Apollo 15 lunar module, shown in Figure 5.1, threatened the progress of the mission [163]. Small particles released are believed to have achieved escape velocity because

Figure 5.1: **Apollo 15 Lunar Module tilted 11 degrees into a crater [21].**

of the near vacuum environment on the Moon, posing risks to orbital facilities [164]. When improved rocket engines with considerably higher thrust are deployed in the future, PSIs will be a significant worry [21].

Future spacecraft must be constructed to withstand the resulting dust or sand shower caused by PSIs. PSIs on Mars also attracted attention. Soil bearing capacity failure, liquefaction, and eruptions were found during the tests of the descent engines of the Viking landers [165, 166]. The Mars lander in the Mars Science Lab was designed to use a sky-crane manoeuvre to remit the plume-dust interaction, but computational fluid dynamics (CFD) simulations showed that the plume-dust interaction was inevitable [167]. The plume-dust interaction will always be a concern as long as humans seek to explore other extraterrestrial planets, moons, and asteroids. The risk control of the plume-dust interaction necessitates a thorough knowledge of multiphase dynamics [164].

The actual behaviour of the PSIs is related to the nozzle thrust, height, angle of the jet, the period of firing, and soil physical properties [168]. Because of its multiphase and multi-system characteristics, this phenomenon poses a difficulty during the landing or launch procedure on the moon and Mars, and it is not fully understood and explained. The trajectories of bed particles have been shown to be dependent on a variety of factors, including plume structure, which is affected by nozzle height, stagnation pressure in the combustion chamber, and nozzle geometry, particle geometry, and physical properties, which include size, shape, and density, and particle-particle interactions [169].

5.1.1 Direct plume impingement

The plume impingement can be divided into two types: direct, where the core of the plume directly impinges on a surface, and indirect, where the periphery or the backflow of the plume impinges on a surface [170]. The plume impingement from a landing module leading to the dust layer erosion belongs to the first kind. According to Donaldson *et. al* [171], the structure of impinging steady jet flows consists of a free jet, an impingement zone, and a wall jet. The supersonic exhaust gas from a rocket nozzle produces a Mach disc, followed by expansion waves

and a standoff shock immediately above the surface [164]. A plume in a rarefied extraterrestrial environment will experience multiple flow regimes and a schematic of the plume-dust interaction is been shown in Figure 1.5.

The earliest model of plume impingement was developed by Roberts [172] for the preparation of the Apollo program [170]. The relation between the pressure of the stagnation point, denoted as p_{stag}, and the chamber of the thruster, denoted as p_c, was presented when the altitude, denoted as H, is smaller than $R_n\sqrt{(\kappa+2)/2}$, where $\kappa = \gamma(\gamma-1)Ma_n^2$:

$$\frac{p_{stag}}{p_c} = \left(1+\gamma Ma_n^2\right)\left(1+\frac{\gamma-1}{2}Ma_n^2\right)^{-\gamma/(\gamma-1)}, \tag{5.1}$$

where Ma_n is the nozzle Mach number. Otherwise, when the hovering altitude is higher than $R_n\sqrt{(\kappa+2)/2}$, the equation becomes

$$\frac{p_{sp}}{p_c} = \frac{\kappa+2}{2}\left(\frac{H}{R_n}\right)^{-2}\left(1+\gamma Ma_n^2\right)\left(1+\frac{\gamma-1}{2}Ma_n^2\right)^{-\gamma/(\gamma-1)}. \tag{5.2}$$

The pressure at the stagnation point is of great importance because the surface shear stress and the dust erosion rate hinge on it [170].

As the deflected flow enters the rarefied flow regime in the radial direction, the strong shock wave thickens in the radial direction, eventually entering the free-molecular regime. A boundary layer forms on the dust layer, which thickens in the radial direction and tends to be a Knudsen layer. According to Mehta *et. al* [173], although most plumes from a descent engine on Mars or the moon are under-expanded, the atmospheric difference between the moon and Mars causes a significant change in plume structure. The plume may be deflected when the landing module approaches the ground, and this deflected plume impingement on the landing module's components may raise loads and heat fluxes [16].

The continuum, transition, and free-molecular flow regimes are present in the gas flow field due to the direct plume impingement on the moon. CFD is suitable for the continuum flow regime which is close to the nozzle and possibly the stagnation region, while the rarefied flow regimes can be solved by the DSMC method. Efforts have been made to combine these two methods together through the communications at the interfaces between continuum and other regimes [161]. The hybrid CFD/DSMC method was first realized by Wadsworth and Erwin [174] through interpolation of the flux properties at the interfaces, but it was implemented to simulations of one-dimensional shock waves. A continuum-particle method which can automatically adjust the interfaces between regimes was developed by Schwartzentruter *et.al* [123] and was successfully used in simulations of hypersonic problems [175–177]. Yang *et.al* [178] coupled a CFD code, Nozzle Flow, with a DSMC code, Plume Work Station, to study the impingement of

a thruster plume on the surface of a circular cone. Marichalar *et. al* [179] modelled the plume impingement during the ascent stage of a lunar lander through a loosely coupled CFD/DSMC method. An alternative method is a unified continuum-rarefied solver by combining a Boltzmann kinetic solver with gas kinetics-based continuum flow solvers, which was proposed by Tosh and Liever *et. al* [180]. The simulation results of the size of the standoff shock, surface pressure, and shear stress distribution of the plume impingement under lunar conditions with different altitudes in their work were compared with the experimental results and good agreements were found. Ye *et.al* [181] use a CFD/DSMC method considering the CFD result as the input of the DSMC simulation to investigate the vacuum plume diversion technique outside the earth.

5.1.2 Cratering physics and particle ejecta

Videos recorded during the descent of the Apollo Lunar Module provided a wealth of information, including the estimation of the particle ejection angle (around 1-3°) and the number density of lifted particles (around $10^8 - 10^{13}$ m^{-3}) [20]. However, the quantity and quality of desired data are insufficient due to the limited number of landing missions [131].

Extensive lab experiments on the jet and granular bed interactions have been conducted to understand the complex mechanisms. Metzger *et al.* [17] have concluded that the plume impingement will move dust particles owing to a combination of any four mechanisms: viscous erosion, diffused gas eruption, bearing capacity failure, and diffusion-driven shearing. Viscous erosion is

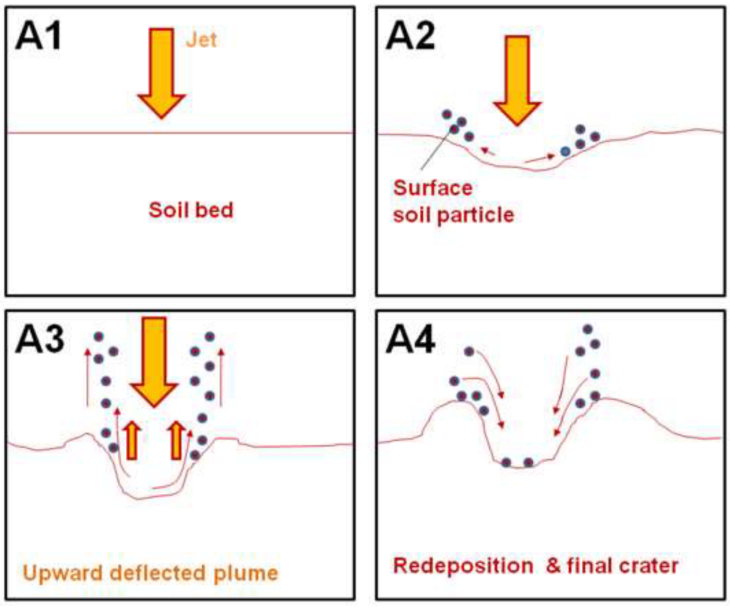

Figure 5.2: **Schematic of viscous shear erosion [26].**

common when the size of the solid particles is small, and it is mainly associated with the lifting and rolling of granules in the top layer, as shown in Figure 5.2. The diffused gas eruption occurs

when gas penetrates and pressurises the porous structure of the dust layer bed, causing the dust layer bed to fluidise. Bearing capacity failure is the creation of a depression when the stagnation

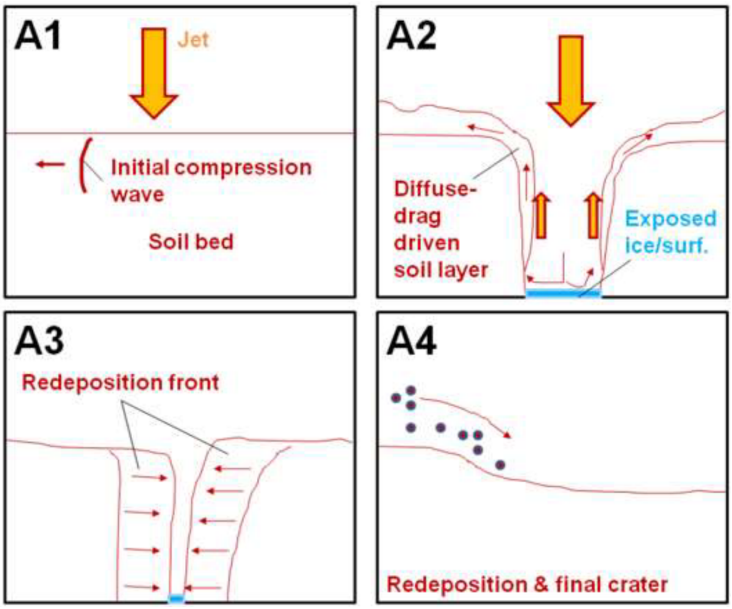

Figure 5.3: **Schematic of bearing capacity failure [26].**

pressure exceeds the dust bearing capacity, as shown in Figure 5.3. Diffusion-driven shearing is a process in which soil internal motions are caused by enough body force from the gas inside the porous structures of the soil [169]. A new erosion mechanism called diffusive gas explosive erosion, presented in Figure 5.4, was found during the Phoenix spacecraft mission; it is a result of pulsed supersonic jet impingement on a porous dust layer that leads to local fluidisation and shock wave formation and propagation in a dilute gas environment [18].

The geometric information of craters under different conditions is also collected through laboratory experiments. Haehnel *et. al* [182] proposed an empirical method to evaluate the crater sidewall slope and the crater depth that takes into account the experimental results of the impingement of a subsonic jet on a cohesionless granular bed. Guleria and Patil [169] observed craters in five different forms, including saucer, parabolic, parabolic with an intermediate region, U, and conical slants with a curved bottom. Their experiments proved that the particle size and distribution have a significant impact on the crater shape, dimension, and the formation mechanism. As a result, the cratering process on various landing sites on the moon and Mars is complicated by dust particles with varied particle sizes and distributions. The experiments mentioned above were conducted intrusively with the nozzle close to a transparent board to allow observation of the crater formation. To some extent, the flow field with a board is different from that without one. To circumvent this problem, Stubbs *et. al* [25] used the stereo-photogrammetry technique in atmospheric conditions to record a three-dimensional image of the crater and conduct measurements non-intrusively. This new visualisation method successfully captured the time-resolved and stereo-geometrical information of the crater formation process.

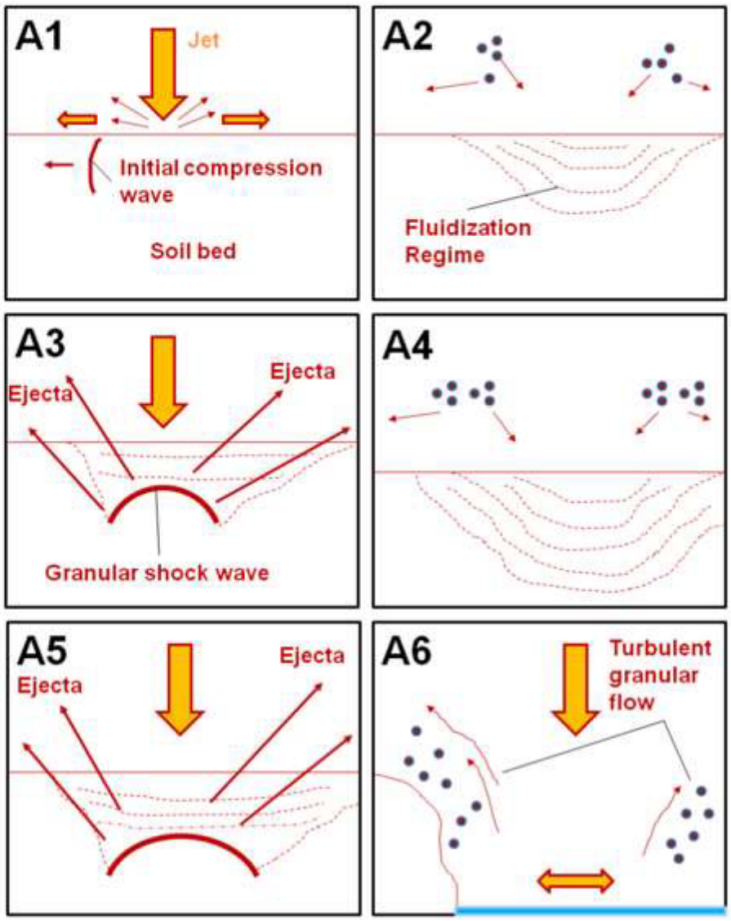

Figure 5.4: **Schematic of explosive erosion [26].**

Lunar particles are magnetic and have low DC conductivity and dielectric loss due to abundant iron material, so lunar particles are prone to adhere to each other and cause static electricity under vacuum. It should be highlighted that glass bubbles, sand, and volcanic ash are commonly used to simulate the real lunar regolith granules because of insufficient lunar regolith samples, but experimental results using simulator particles in atmosphere are usually different from that using real lunar particles [161].

Unfortunately, it is highly difficult to mimic a planetary environment, including high vacuum, strong cosmic radiation and electric field, and low gravity [161], in a laboratory experiment. The lab experiments mentioned were conducted in the atmosphere rather than in a vacuum chamber that creates a rarefied environment. Metzger [183] mentioned a series experiments for scaling the dust particle erosion rate in lunar and Martian conditions in NASA. He recorded a figure of the crater formed under the conditions of a lunar and Martian rocket plume. The size of the crater formed in rarefied conditions was bigger than that in atmospheric conditions, and neither an intermediate region nor a rim [169] was found in this crater. Metzger [183] recognised that the surface erosion rate according to experiments in the continuum flow regime resulted in an under-estimation in the transition flow regime and implied that the Knudsen number exacer-

bated the complexity of the plume erosion physics. In NASA's Physics Focused Ground Test campaign [184], a series of scaled ground tests have been conducted to provide benchmarking data of plume-surface interactions in low-pressure environment for numerical tools. In their experiments, a splitter plate with a 38° leading edge was implemented to bisect the plume and allowed the observation of two-dimensional soil erosion [184]. Quantities considered in the scaling of the experiments include the non-dimensional altitude, the ratio of kinetic-to-internal energy of the plume gas, the solid particle Reynolds number, the particle Knudsen number, the densimetric Froude number, soil strength, dimensionless threshold friction velocity, and dimensionless pressure gradient, but it is pointed out that these quantities are unable to be perfectly scaled in the ground tests [184]. Efforts were also made to acquire results from an experiment conducted in a chamber falling from a tower [185] to replicate the extraterrestrial gravity field, but the experiments were limited by the size of the chamber.

Early efforts [186, 187] have been done to relate the crater formation and the erosion with the nozzle heights and pressure ratios. Experimental studies were further extended to model the erosion rate, total quantity of ejected soil, and soil ejection angle because these parameters are considered three important properties to quantify the damage to the spacecraft itself and the hardware around it [21]. It has been found that viscous erosion is the most important mechanism during the period of landing [188] and it is important in widening the crater size [183]. The derivation of the Roberts model [172] was dependent on the viscous erosion. In the Roberts model [172], which is used in Refs. [16, 24, 30, 135, 137, 189, 190], the erosion rate, $\dot{m}$ (kg/(s m^2)), is assumed to be proportional to the difference between the surface shear stress and a threshold stress which is calculated through the Mohr-Coulomb equation:

$$0.5a\left|\vec{v}_g\right|\dot{m} = \tau_{ss} - \tau_{ts} \tag{5.3}$$

and

$$\tau_{ts} = \tau_{co} + p\tan\varphi_0, \tag{5.4}$$

where $\dot{m}$ is the mass erosion rate, τ_{ss} is the surface shear stress, τ_{ts} is the threshold stress, τ_{co} is the cohesive stress and φ_0 is the repose angle of soil. a is an empirical dimensionless parameter representing the fraction of gas velocity that a particle acquires [191] because of the loss of the momentum and energy during impingement and the uncertainty of the landing position (i.e. the difference of physical properties of the regolith particles at different locations). It has been found that decreasing a will increase the crater size. Metzger *et al.* [191] modified the Roberts' model by considering the ejection angles of particles and adding a material damage model. The Roberts' model, on the other hand, isn't the only one employed in plume-regolith interactions. For instance, Morris [170] implemented a relation

$$\dot{m} = 0.0022\tau_{ss} \tag{5.5}$$

to evaluate the mass erosion rate per time-step. As the dust erosion rate is proportional to the local gas dynamic pressure [24], the gas dynamic pressure above the lunar surface at 10 cm or 5 cm was calculated as the shear stress τ_{ss} for the estimation of dust erosion rate in the work of Refs. [170] and [24]. On the other hand, Lane and Metzger [192] provided theoretical equations for determining the erosion rate and total mass of lunar dust excited. A simple relationship based on data from the Apollo project through the weather radar technique between the mass erosion rate of lunar dust and the surface shear stress was proposed. The analytical approach of Metzger [192] was used to investigate the soil erosion during the landing of Chang'E-4, which is part of the China Lunar Exploration Project by You and Zhang *et al.* [193]. They improved the theoretical erosion rate equation and suggested that further improvements could be made in the consideration of particle ejection angle distribution. There is limited literature focusing on the particle ejection angle in the erosion model. In Ref. [137], Li and Ren *et. al* compared the particle injection angle acquired from the result of their private code with that from Refs. [27,30,135]. They concluded that smaller particles have a larger ejection angle than larger particles, and that the particle ejection angle increases in the nozzle radial direction, but there is a noticeable difference in the ejection angles in the same test case using different interphase calculation methods.

The expression of the erosion rate modelled from these experimental studies provided useful information for numerical simulations of PSIs, but solid-solid interaction models without the consideration of close-packing limits and enduring contacts, such as merely considering binary collisions or replacing the regolith layer with a plane surface in Refs. [16, 24, 30, 136, 137, 189], give rise to unrealistic sedimentation and inaccurate movements. Replacing the regolith layer with a plane surface leads to the failure to capture transient gas flow field variations caused by cratering. In addition, the amount of regolith particles injected into the computational domain according to Equation (5.3) is unbounded. In practice, the actual number of lifted particles is associated with the surface shear stress caused by the plume and must be finite and decrease with time as the dust layer is eroded due to mass conservation. However, with the consideration of the mass conservation, overestimation of the number of entrained dust particles occurs when the simulation is run to acquire a steady granular flow.

To summarise, experiments are inevitable and essential for the validation and uncertainty estimation of numerical tools, but an effective and open-source code is cost-effective to promote the understanding of the plume-surface interactions. Solid-solid binary collisions or overly simplified models of dust layers in previous PSI simulation results are unable to correctly simulate the transient interaction between the plume and the regolith-coated surface. Both instantaneous and enduring contacts should be considered at the same time in the simulation of PSI. In Section 4.2, the basic theory of the simulations of gas-solid flows in rarefied conditions have been detailed and the models have been validated in Chapter 4. The numerical result of the lunar

plume-surface interactions with the MPPIC method where the solid-solid enduring contacts are considered will be presented for the first time and it will be compared with the result with the solid stochastic collision model. The effect of the transient effect and the enduring solid-solid contacts will be discussed.

5.2 PSI simulation

To ensure a secure landing on the Moon, the primary thruster will activate before the landing module impacts the surface. The module can be seen as being suspended above the lunar surface just before the reverse thruster fires. Since the flow field inside the nozzle is not taken into account in this study, the entire nozzle is substituted by a nozzle exit surface. When the nozzle starts to discharge, a high-speed gas flow impacts the ground and interacts with the lunar surface and the regolith particles that are lying on it. The regolith layer may be represented mathematically as a collection of particles lying on a solid surface using the stochastic collision and MPPIC methods, from which regolith particles are entrained in the gas flow and expelled into the domain, resulting in a cratering and dispersal process.

In Figure 8(b) of Ref. [30], the lunar descent engine from the Apollo era is modelled. The nozzle exit radius was 0.81 m, and the standoff height was 2 m. To save computational costs, the nozzle exit radius and stand-off height are scaled down by a factor of 100 in the current study. This has the consequence of increasing the Knudsen number while decreasing the Reynolds number of this problem. The nozzle stagnation temperature and pressure remain unchanged from the early studies, and the profiles for velocity, density, and temperature at the nozzle exit are simply scaled down. Figure 5.5 presents the dimensions of the axisymmetric computational geometry. A simple diffuse wall boundary condition with a coefficient of restitution in the normal direction is applied to the bottom surface of the computational domain to substitute the specular wall in Ref. [27] and the time-step of both cases is 2.5×10^{-9} s.

Water vapour is selected as the working gas in this simulation, as it has been in previous simulations of PSIs with the larger Apollo nozzle, with molecular mass and diameter of 2.99×10^{-26} kg and 4.5×10^{-10} m, respectively. The number of rotational degrees of freedom and number of vibrational modes are both 3. For the variable hard sphere collision model, the exponent of the viscosity-temperature power law is 0.75. The vibrational modes are modelled using a harmonic oscillator model, with characteristic vibrational temperatures of 2294 K, 5261 K, and 5432 K for the bending, symmetric stretch, and asymmetric stretch modes, respectively. The profiles of the number density, temperature, and velocity (both radial and axial components) at the nozzle exit are extracted from the distribution profiles in Figure 5 of Ref. [30] (and scaled down to fit the smaller nozzle exit radius in the current work) because the distributions are not uniform.

The models applied in the DSMC method are identical to those in Chapter 3. The NTC method

is applied to determine collision partners for the DSMC simulators, and the variable hard sphere model with the Larsen-Borgnakke energy redistribution model is used to determine the post-collision properties. The indirect interphase coupling model is used in this work to quantify the momentum and energy exchange between the gas and solid phases.

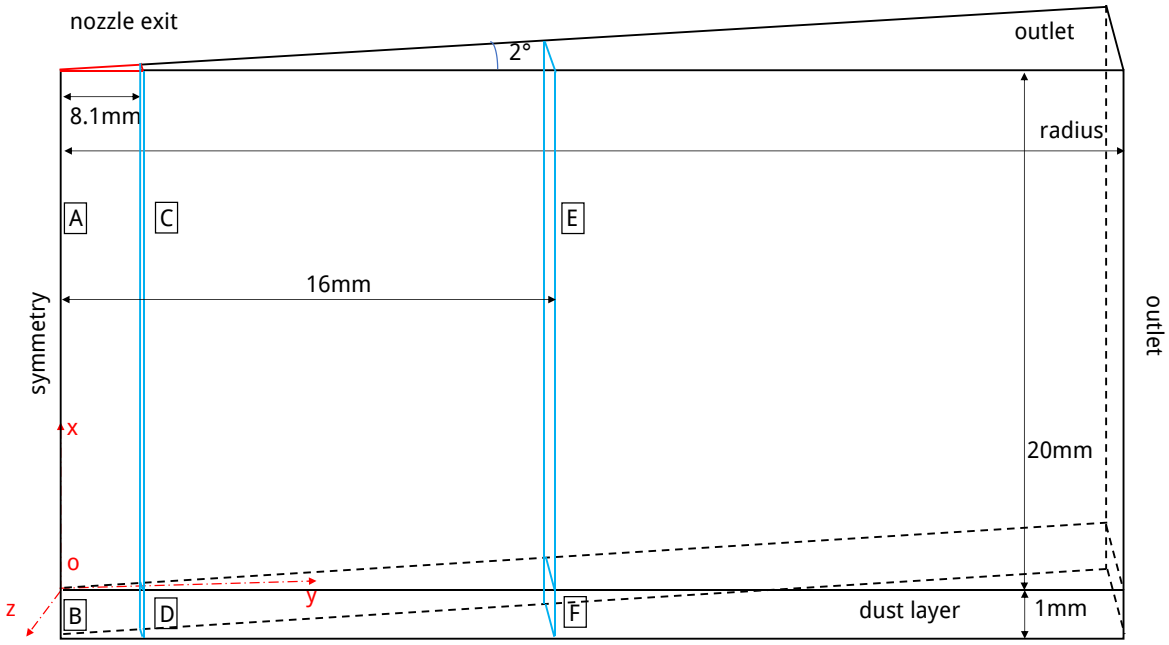

Figure 5.5: **Computational domain for the plume-surface interaction study.**

Regarding the regolith material, solid particles are assumed to be unconsolidated with a diameter of 2.8×10^{-7} m to attempt to ensure the particle local free-molecular assumption ($Kn_p > 10$) [28]. The regolith material density, the specific heat capacity and the surface thermal accommodation coefficient are 3100 kg/m^3, 2180 J/kgK and 0.89, respectively. The coefficient of restitution of lunar regolith particles is sensitive to the material, direction of impact, and coefficient of friction [194], which is not the topic of the current work. For the sake of simplicity, it is assumed that solid particles lose 15% of their momentum due to collisions and that the coefficient of restitution is 0.85. After initialisation, the velocity and temperature of each regolith particle are $(0, 0, 0)$ m/s and 200 K, respectively, and all particles are dispersed in the 'dust layer' shown in Figure 5.5.

The PSI simulations were conducted on the regional high performance computing machine ARCHIE-WeSt, using 40 cores per task and each simulation required 2 weeks of wall time.

5.2.1 Case I: stochastic particle collision model

The mesh parameters of the six blocks in Figure 5.5 are detailed in Table 5.1. The radius of the domain (i.e. y direction) is 45 mm. The stochastic collision model is applicable to the

Table 5.1: **Mesh detail with stochastic collision model.**

Block ID	Cell numbers ($X \times Y$)	Cell edge grading (X Y Z)
A	775×775	(7.5 7.5 1)
B	40×775	(7.5 7.5 1)
C	775×294	(7.5 6.7 1)
D	40×294	(7.5 6.7 1)
E	775×370	(7.5 1.7 1)
F	40×370	(7.5 1.7 1)

Table 5.2: **Mesh detail with the MPPIC method.**

Block ID	Cell numbers ($X \times Y$)	Cell edge grading (X Y Z)
A	775×775	(7.5 7.5 1)
B	40×775	(7.5 7.5 1)
C	775×294	(7.5 6.7 1)
D	40×294	(7.5 6.7 1)
E	775×626	(7.5 1.7 1)
F	40×626	(7.5 1.7 1)

dilute granular phase and the dust particle number density is 2.175×10^{16} m^{-3}, corresponding to a volume fraction of 0.0025%. The weight of each solid particle simulator is 25 (i.e. one simulator represents 25 real regolith particles.). The gravitational field is effective in the domain above the 'dust layer' in Figure 5.5. There are approximately 100,000 solid simulator particles. The domain contains roughly 13.7 million DSMC simulator particles at the simulation end time which is 0.375 ms. The DSMC does not achieve a 'steady-state' due to the solid particles travelling through the domain and the two-way coupled characteristics of the simulation, and both phases are entirely transient.

5.2.2 Case II: MPPIC method

The radius of Case II is extended to 65 mm and the mesh details are presented in Table 5.2. It is suggested that the best estimate of the bulk density of the lunar regolith is 1500 kg/m^3 [195], which would result in a close-packing state in each cell, and that it would thereby take a relatively long time (in comparison to the time step) to allow the plume to entrain the regolith particles, resulting in an unaffordable computational cost for the current work. Hence, the regolith number density is given as 2.175×10^{18} m^{-3}, corresponding to a volume fraction of 2.5% and the bulk density of around 77.5 kg/m^3 (i.e. the collision-dominated granular flow regime). Approximately 1 million solid simulators are initialised in the 'dust layer' and the weight of the solid simulators is 376. The highest volume fraction of a container filled with perfect same-size spheres has been determined to be about 0.64 [196], but in this test scenario, the close-packing volume fraction is reduced to 0.62.

The Harris and Crighton model is implemented to calculate the interparticle stress. It is well

understood that P_s must be sufficiently large to avoid exceeding the close packing volume fraction in dynamic calculations. Small values of P_s will yield longer relaxation times for an over-packing cell to balance to the close-packing value; extremely small P_s will result in failure of expelling particles from an over-packing or close-packing cell. In low volume fraction locations, increasing the exponent β can constrain particle dispersion [159]. Yet, the choice of P_s and β is empirical, and no studies of the impact of both parameters in PSI simulations can be found. Therefore, typical values of P_s and β are given to ensure for a stable result, which is 50 Pa and 3, respectively. Explicit packing model, damping model with the damping time expressed in Equation (4.43), and return-to-isotropy model with the return-to-isotropy time shown in Equation (4.44) are used and the dual averaging method in OpenFOAM is implemented. Similar to Case I, this simulation is fully transient and no 'steady-state' for either phases is achieved; approximately 16.7 million DSMC particles are distributed in the domain at the final time-step.

5.3 Results and discussions

Figures 5.6 and 5.7 show the developments of the gas-solid flow in both cases. A strong normal shock wave above the dust layer rapidly decelerates the gas flow. The normal shock wave moves towards to the dust layer after its formation and then reverses its direction and eventually resides at a position close to $X = 10$ mm. The somewhat unusual shock wave caused by the nozzle exit conditions and the stand-off height was also noticed by Morris *et.al* [30]. The evolution of the regolith layer can be separated into two stages: cratering and dispersal. An evident boundary layer has formed above the dust layer in Case II with the MPPIC method, shown in Figure 5.7 at $t = 7.5 \times 10^{-6}$ s and Figure 5.8, while this boundary layer is not observed when the stochastic method is used, see Figure 5.6, at the same time, suggesting that the top surface of the regolith layer acts as a diffuse wall in Case II. In Figure 5.8, an increase of the boundary layer thickness can be observed due to the escalation of the rarefaction level in the radial direction. The regolith granules in the vicinity of $Y = 15$ mm have been transported towards and away from the nozzle axis at 3.75×10^{-4} s in Case I while a full layer of dust particles exists at 5×10^{-4} s in Case II. The cratering process is slower with the MPPIC method than with the stochastic collision method. The evolution of the solid phase will be comprehensively discussed later.

5.3.1 Gas flow field

The gas speed field is compared in Figure 5.9 between the stochastic collision model and MPPIC method. The basic structures, including the normal and oblique shock waves, and the vortex after the shock waves, are similar to, but not identical with those presented in Figure 8(b) of Ref. [30], most likely because of the increased Knudsen number and decreased the Reynolds number where the nozzle dimension, scaled down by a factor of 100 here, is considered as the characteristic length. The high-speed jet is impeded and decelerated in a short distance

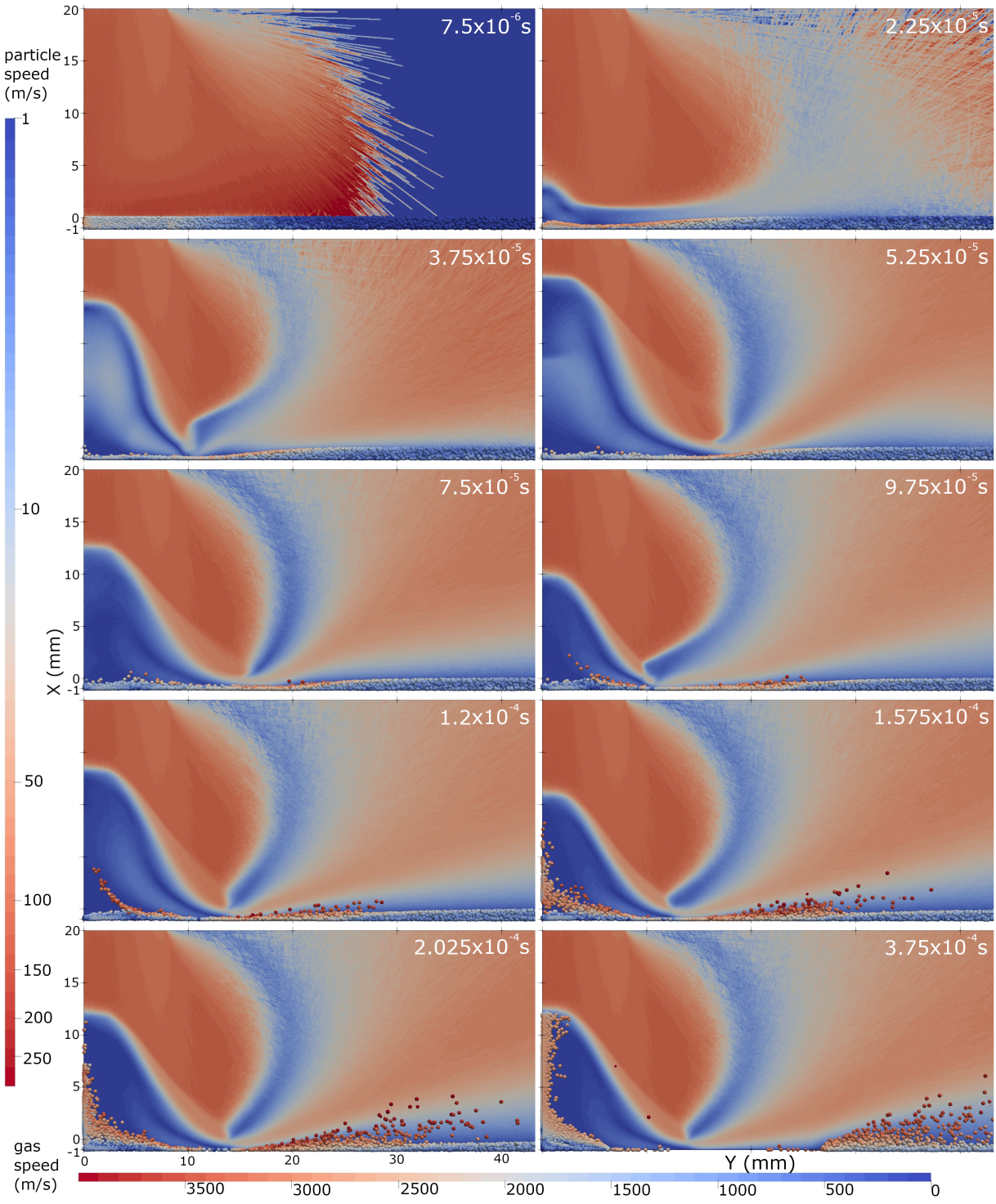

Figure 5.6: **Overview of the two-phase flow evolution with the stochastic method.**

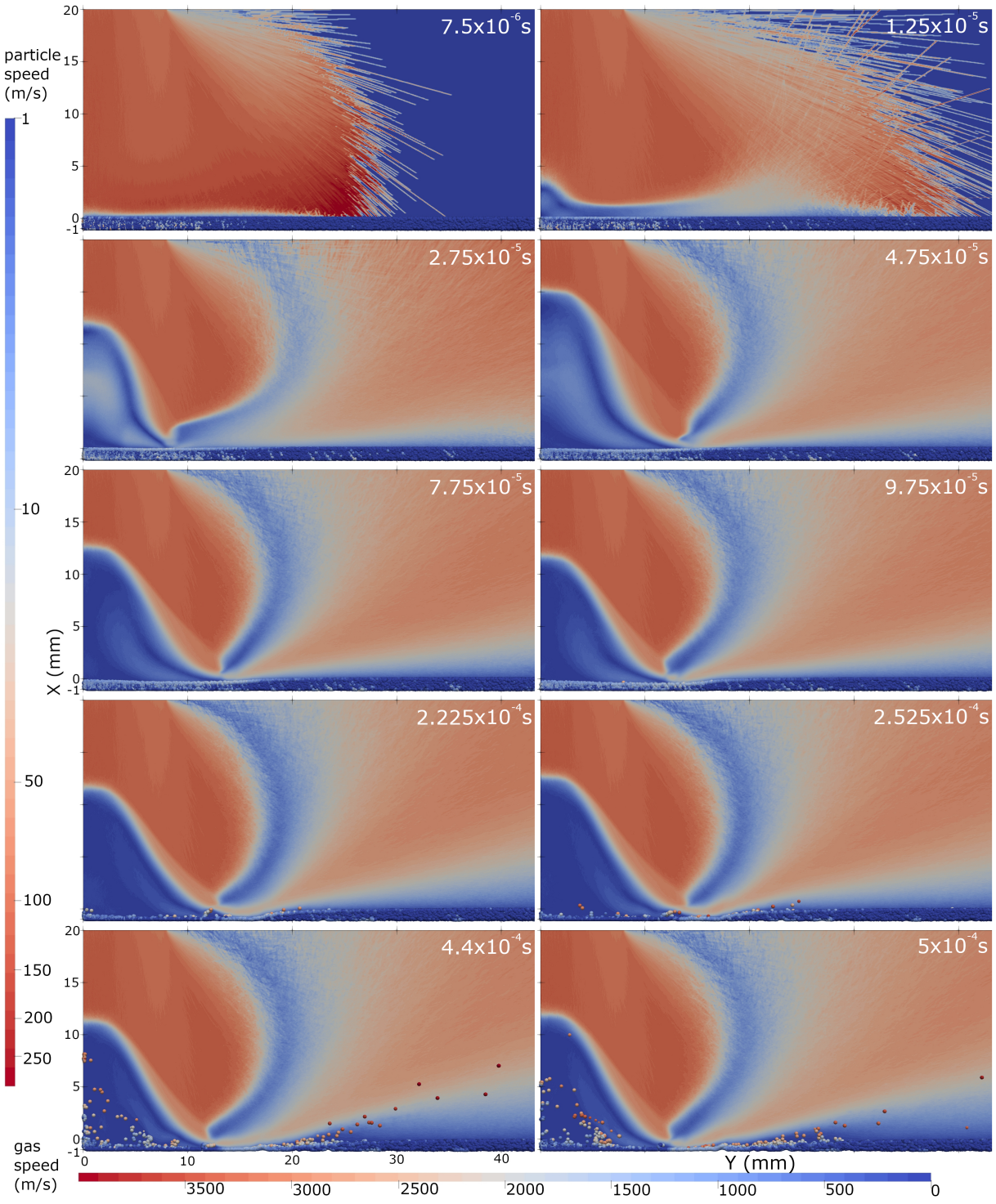

Figure 5.7: **Overview of the two-phase flow evolution with the MPPIC method.**

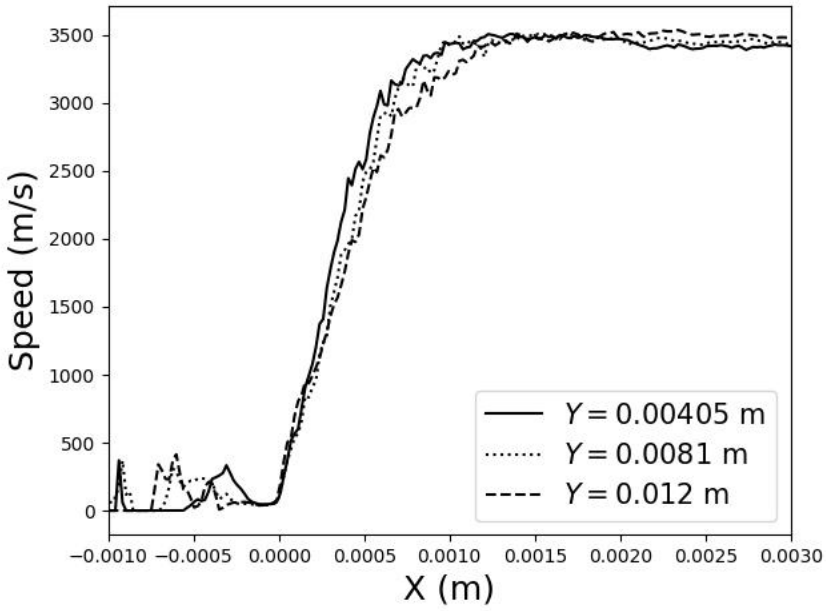

Figure 5.8: **Boundary layer thickness at t =7.5$\times 10^{-6}$ s of Case II.**

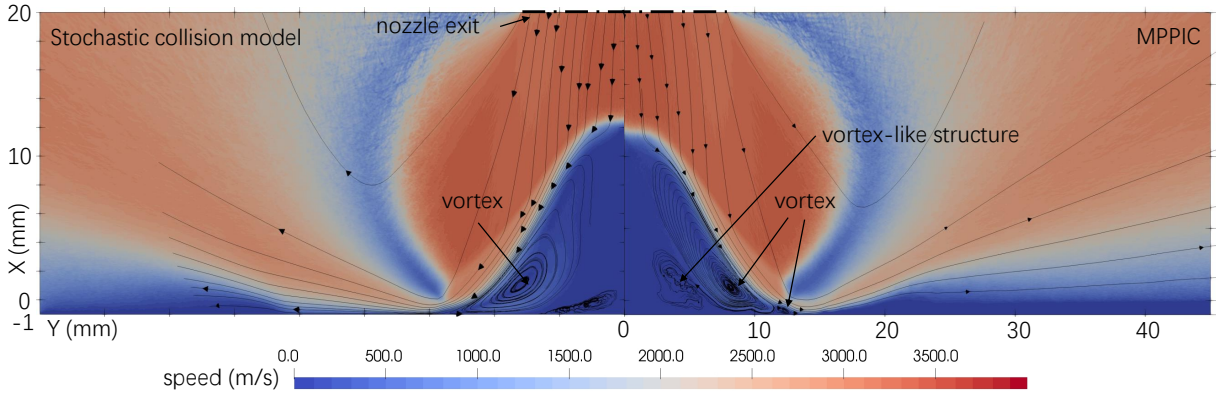

Figure 5.9: **Comparison of gas velocity field between case I and II at $t = 0.375$ ms.**

by the lunar surface through the strong normal shock wave. In the radial direction, the pressure difference between the stagnation region with high pressure and the far-field region with rarefied environment is balanced through a relatively weak oblique shock wave [30]. This oblique shock wave connected with the strong normal shock wave at around $Y = 2$ mm and the curved shock at $Y = 14$ mm. Similar to Case II, the top layer of the regolith layer should behave like a diffuse wall for the gas phase gradually permeating through the porous medium and the lunar regolith starts to be eroded due to the pressure and shear stress on the surface, shown in Figure 5.10, but the gas flow crosses the lunar regolith and impinges on the lunar surface because of the small volume fraction in Case I with the stochastic collision model; this not realistic. Marked by the dashed lines in Figure 5.10, the particle ejection angle increases with time because of the erosion of the dust layer with time.

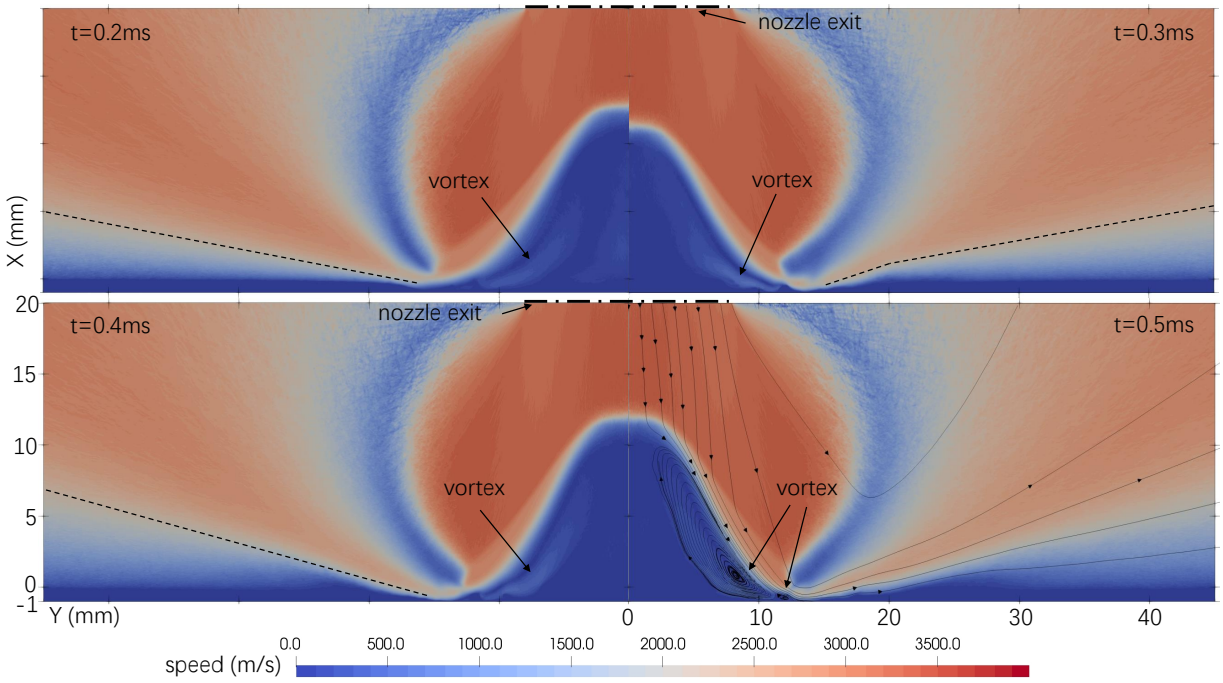

Figure 5.10: **Gas speed field of case II.**

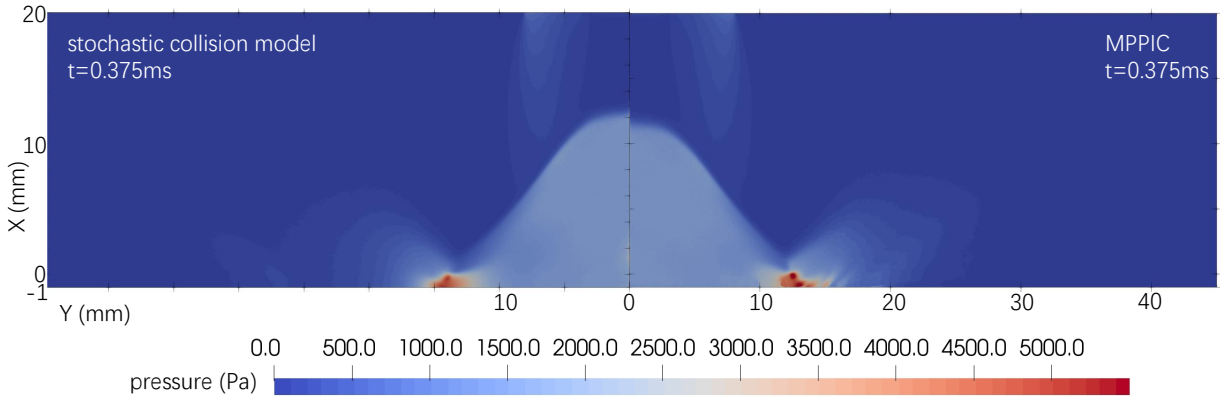

Figure 5.11: **Comparison of gas pressure field between case I and case II.**

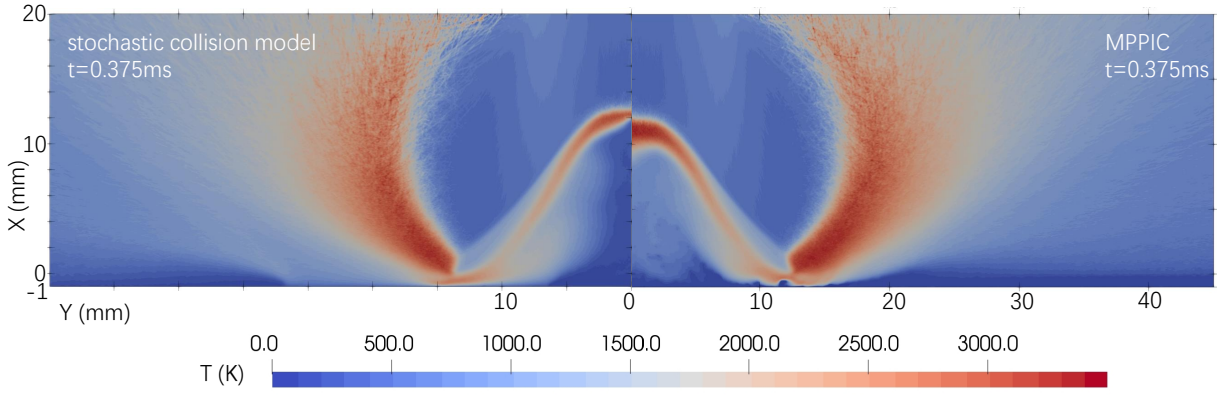

Figure 5.12: **Comparison of gas overall temperature field between case I and case II.**

Even if the initial environment is vacuum, a vortex still appears after the shock wave because the Knudsen number near the stagnation region is higher than the critical Knudsen number characterising the vortex formation mentioned in Chapter 3. The wall vortex downstream of the strong normal shock wave in Figure 5.9 is distorted due to the erosion and the cratering changing the shape of the regolith layer. It should be mentioned that there is a vortex-like structure below the main wall vortex in both cases, shown in Figure 5.9 and the positions of this structure in both cases coincide with the location where a large number of solid particles are entrained, see Figures 5.6 and 5.7, indicating that this structure may be a result of the amount of entrained particles. Furthermore, the difference in height and size of the vortex-like structure in both situations may be related to different particle distributions in the region downstream of the normal shock wave. In particular, there is small secondary vortex at 0.5 ms of Case II owing to the entrained dust particles. Figures 5.11 and 5.12 compare the gas pressure and temperature fields of both cases at 0.375 ms. The gas pressure located at the joint of the oblique and curved shocks (around $Y = 14$ mm), corresponding to the deepest erosion, is much higher than the other places in both cases and the pressure value increases with time. The gas pressure at the normal shock wave in both cases seems to be similar, but the pressure distributions downstream of the curved shock are different in the two cases. The temperature fields at the curved shock are similar while they are distorted at the normal shock and oblique shock waves and their downstream field close to the stagnation regions. Specifically, the normal shock wave at $X = 12$ mm of Case II is thicker than that of Case I in Figure 5.12.

The gas pressure, temperature, and velocity profiles along the nozzle symmetry axis of the MP-PIC case is shown in Figure 5.13. The normal shock wave moving back and forth between $t = 0.45$ ms and $t = 0.5$ ms can be observed from the pressure and axial velocity component distributions. This fluctuation of the normal shock wave is also presented in the pressure and temperature distributions of Figure 5.14. The distortion of the gas flow field due to the entrained solid particles can also be proved by the pressure and temperature distribution downstream of the normal shock wave in Figure 5.14. However, the entrained solid particles seem to have limited impact on the gas radial velocity because the gas radial velocity component along the symmetry axis changes little.

The height of the normal shock wave varies in Figures 5.11 and 5.12 because of the different evolution process of the solid phase. First, the gas field in both cases will not reach a steady state until the regolith layer stops evolving. There are more solid particles in Case II than that in Case I, and solid particles are accelerated slower with the MPPIC method due to the presence of multiple collisions and enduring contacts. The increase of the number of entrained solid particles delays the time for the gas phase to acquire a pseudo-steady state. Secondly, the cratering significantly influences the gas flow field evolution. The gas in the stagnation region of the MPPIC case moves downwards as the crater deepens, followed by the movement of the

normal shock wave shown in Figures 5.6 and 5.7.

It should be noted that the influence of the gas flow field caused by cratering and dispersal of the regolith layer will definitely affect the surface properties on top of the regolith layer, particularly the surface shear stress. This suggests that an approach that simulates PSIs using an erosion model using the dynamic pressure above the surface to calculate erosion flux and replacing the lunar surface with a simple plane surface is not appropriate.

5.3.2 Regolith layer evolution

The cratering, as a result of the early stages of the plume impingement, is presented in Figures 5.15 and 5.16, as scatter plots of dust particle speeds with time, for Case I with the stochastic collision method and II with the MPPIC method, respectively. The gas flow rapidly compresses and penetrates the lunar dust layer in Case I where the close-packing limit is not considered; this is not physical and realistic since solid particles should not have full access to a cell with the local volume fraction approaching the close-packing value. The gas atoms/molecules should contact and reflect from the top of the regolith layer or gradually permeate the pores in the dust layer. It can be observed that at 0.05 ms, the solid particles in Case I are about to be dispersed while the regolith layer with the MPPIC method is still in the early stages of cratering; this is because the granular phase in Case I is dilute and only binary collisions are involved in the stochastic collision model, leading to fast response of solid particles to the gas field. The postponement of cratering and the smaller speed of the regolith particles using the MPPIC method suggests that the regolith layer with high volume fractions hinders the gas from spreading into the pores and that enduring contacts between solid particles restrict their movements, which is more natural and realistic. It is reasonable to conclude that the MPPIC method is better suited for PSI simulations.

Two different processes have been found to contribute to the particle dispersal from the lunar regolith layer after the cratering. Firstly, at 0.2 ms and 0.28 ms of Figure 5.17, a considerable number of particles are entrained by the wall vortex formed beneath the strong normal shock wave and then assemble nearby the nozzle axis. Some of these lifted particles move towards the strong normal shock wave, but the normal shock wave prevents these particles from crossing the shock wave and swimming upstream. Then, these particles travel off the symmetry axis along the oblique shock wave and the curved shock wave, see $t = 0.375$ ms of Figure 5.17. Meanwhile, particles are lifted upwards and ejected radially outwards at $Y = 15$ mm. Almost all the solid particles between $Y = 5$ mm and 25 mm at $t = 0.375$ ms are blown or ejected off the axis. Similar particle dispersion form with distinct structures of the regolith layer has also been observed in Figure 5.18 using the MPPIC method. It takes a longer time scale for particles in Case II to disperse. The existence of the aforementioned vortex downstream of the oblique shock wave in Figure 5.10 significantly influences the particle movements and distribution between

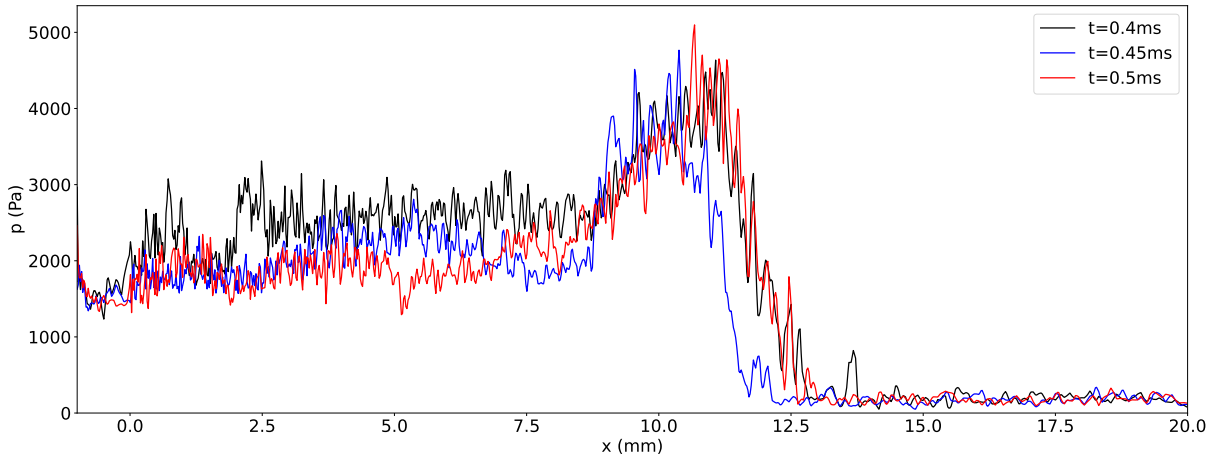
t=0.4ms
t=0.45ms
t=0.5ms
p (Pa)
x (mm)

(a)

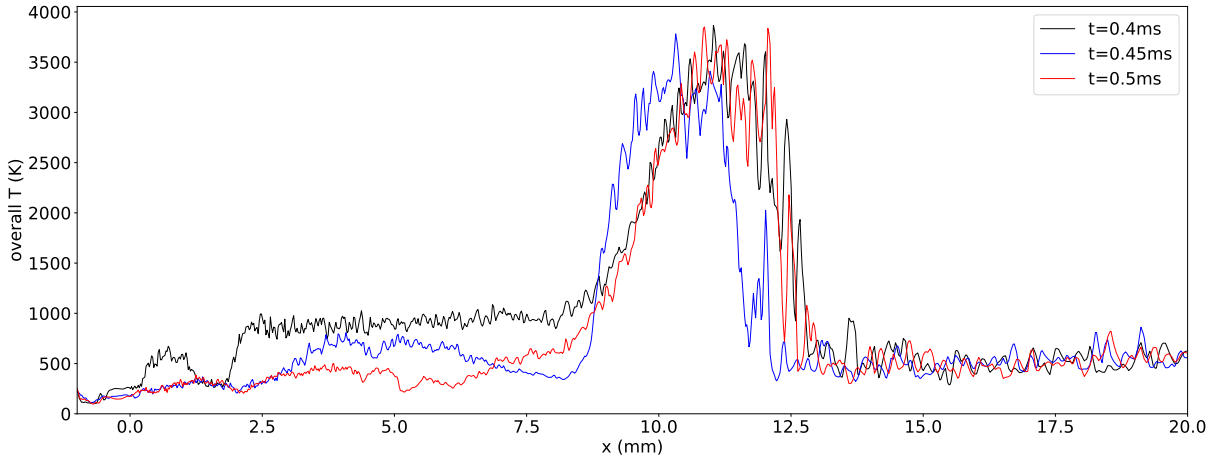
t=0.4ms
t=0.45ms
t=0.5ms
overall T (K)
x (mm)

(b)

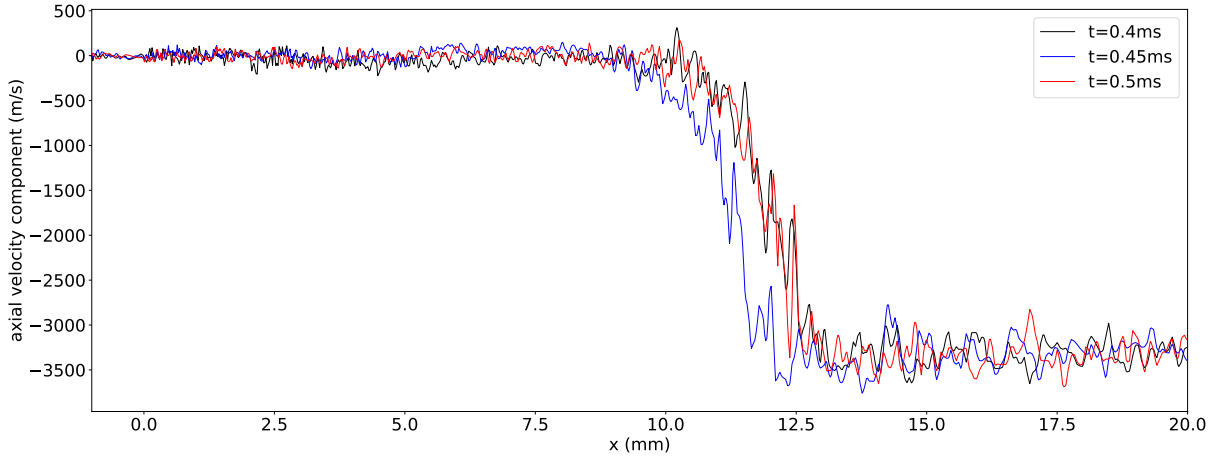
t=0.4ms
t=0.45ms
t=0.5ms
axial velocity component (m/s)
x (mm)

(c)

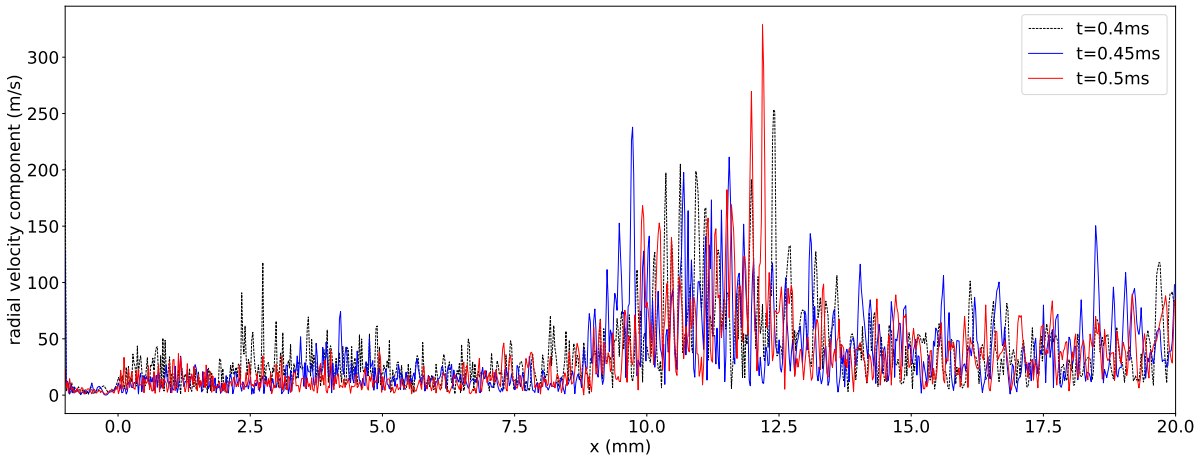

(d)

Figure 5.13: **Physical properties at nozzle axis of case II.**

$Y = 5$ mm and 10 mm. It is interesting that some particles are entrained by a small secondary vortex between $Y = 11$ mm and 15 mm and the regolith surface in the range of $Y = 25$ mm to 40 mm becomes uneven and forms a wave-like structures in Figure 5.18 due to the scouring of the gas flow in the radial direction; analogous phenomenon can be seen in sand surfaces scoured by the wind in deserts, for example Figures 26(b) and 26(f) in Ref. [197]. Particles are accelerated to 50–100 m/s when they are ejected from the dust layer. Taking $Y = 13$ mm as the boundary to determine the proportion of particles that move towards or away from the symmetry axis, approximately 6.35% particles move towards the axis using the stochastic collision method while this fraction decreases to 3.62% in the MPPIC case, because of the consideration of more types of solid-solid interactions in the MPPIC method.

The solid volume fraction distribution of the MPPIC case at three times is presented in Figure 5.19. It is found as expected that the solid volume fraction at the top of the dust layer increases at 0.1 ms due to a downwards force exerted by the plume on the solid particles. At 0.02 ms, the maximum solid volume fraction in the domain exceeds the close-packing value and this value decreases to around 0.66 at 0.5 ms, leading to numerical phenomenon called over-packing. This phenomenon seems to be cause of the simultaneous use of the damping model with the packing and return-to-isotropy models in the MPPIC method, which has been noticed in Ref. [198]. The damping model is suggested to be implemented in the closely-packed region [198], however, systematic investigation of the influence of combinations of the MPPIC submodels on the PSI simulation cannot be found.

Figure 5.20 presents the contours of the local particle Knudsen number, Kn_p, at different times of the MPPIC case. As mentioned in Section 4.2.1, the locally free-molecular assumption is the prerequisite of the interphase coupling model, but this assumption is not valid in the vortex, at the top of the regolith layer, and near the stagnation region. The range where the assumption is

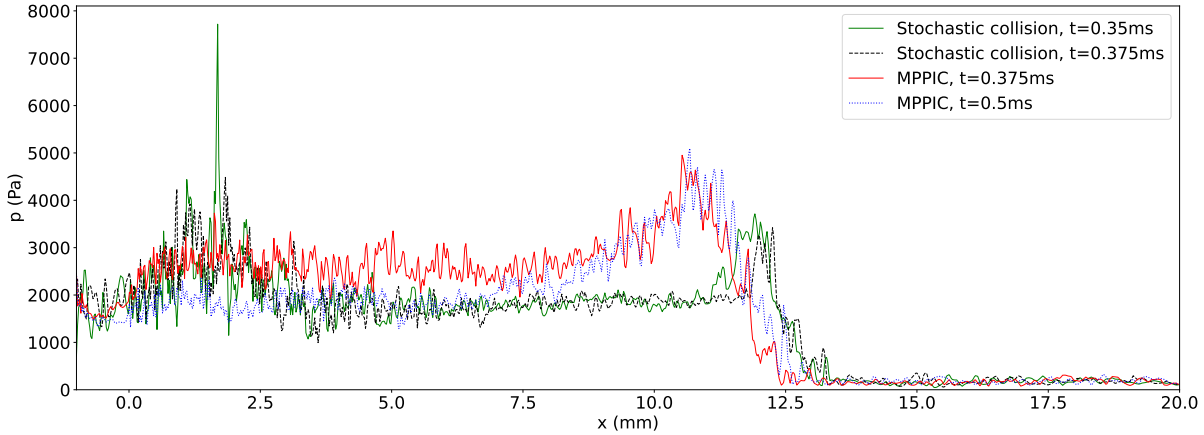
Stochastic collision, t=0.35ms
Stochastic collision, t=0.375ms
MPPIC, t=0.375ms
MPPIC, t=0.5ms
p (Pa)
x (mm)

(a)

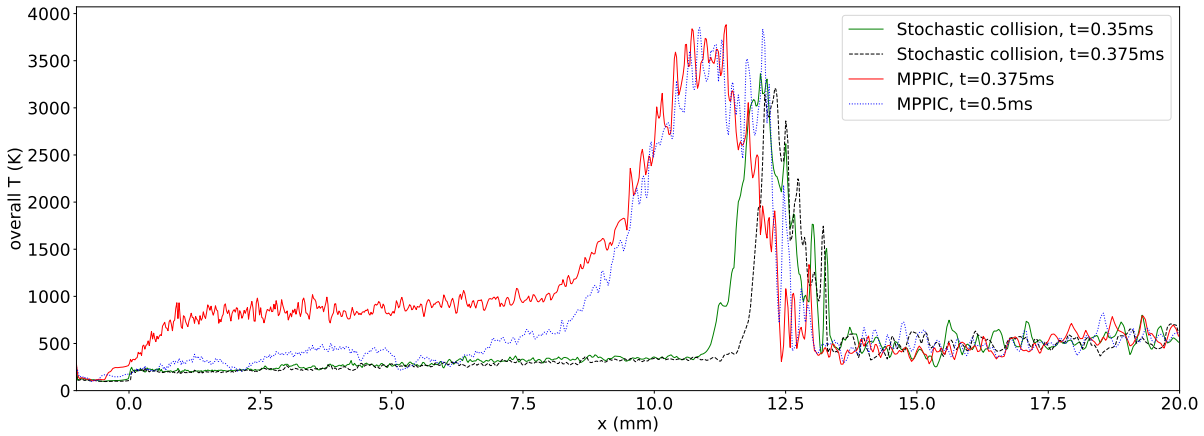
Stochastic collision, t=0.35ms
Stochastic collision, t=0.375ms
MPPIC, t=0.375ms
MPPIC, t=0.5ms
overall T (K)
x (mm)

(b)

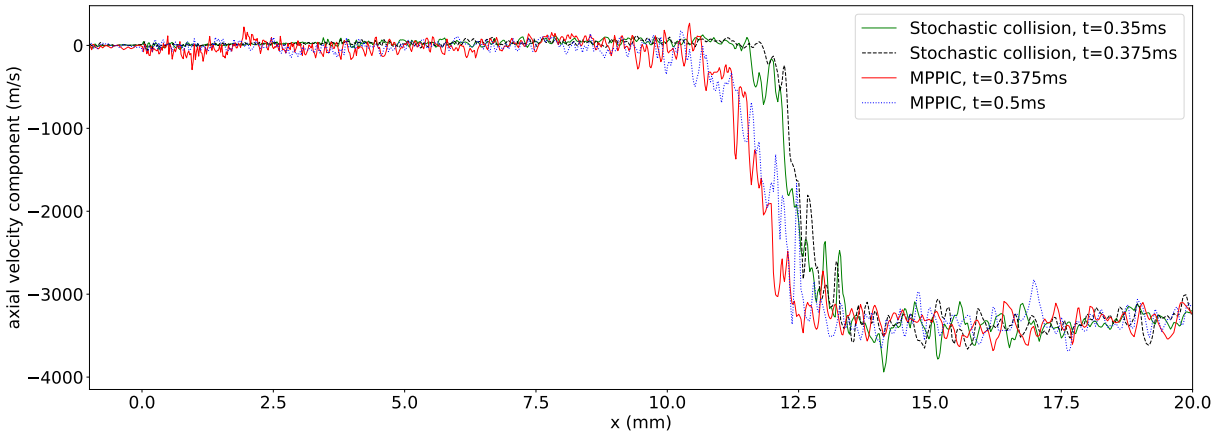
Stochastic collision, t=0.35ms
Stochastic collision, t=0.375ms
MPPIC, t=0.375ms
MPPIC, t=0.5ms
axial velocity component (m/s)
x (mm)

(c)

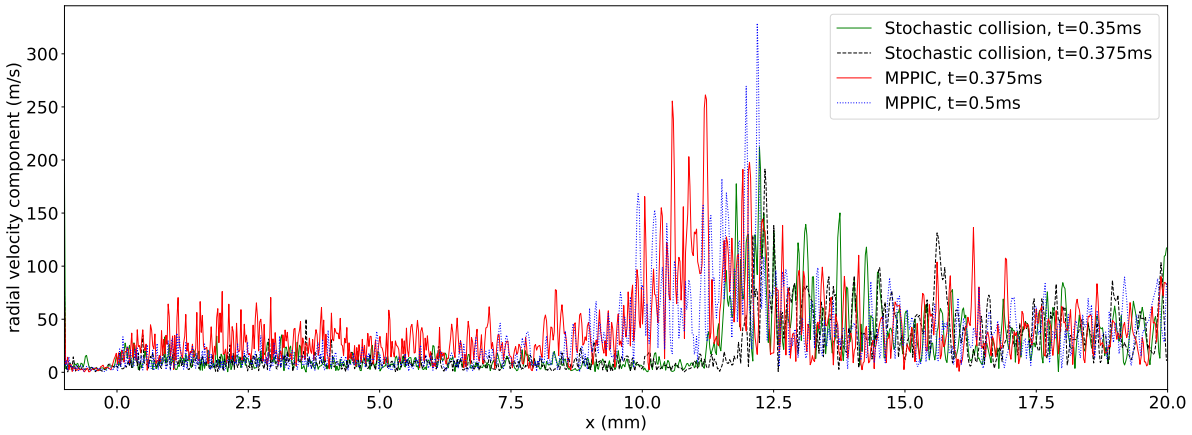

(d)

Figure 5.14: **Comparison of physical properties at nozzle axis between case I and case II.**

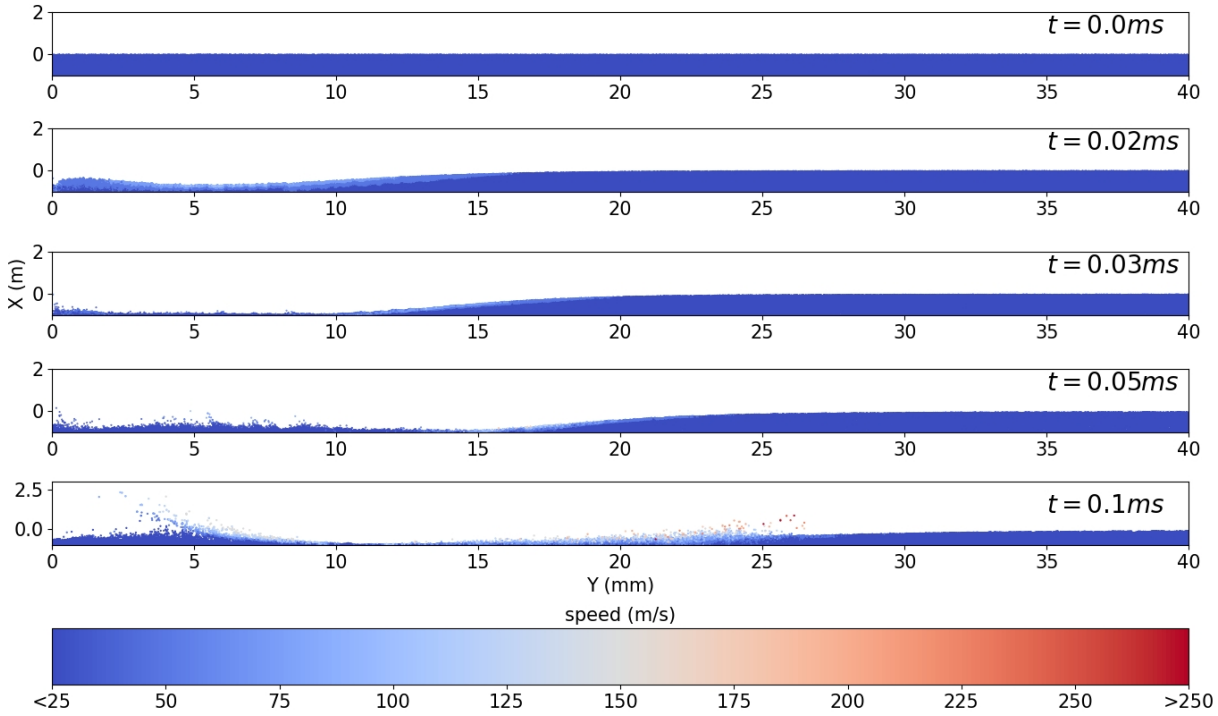

Figure 5.15: **Cratering in case I.**

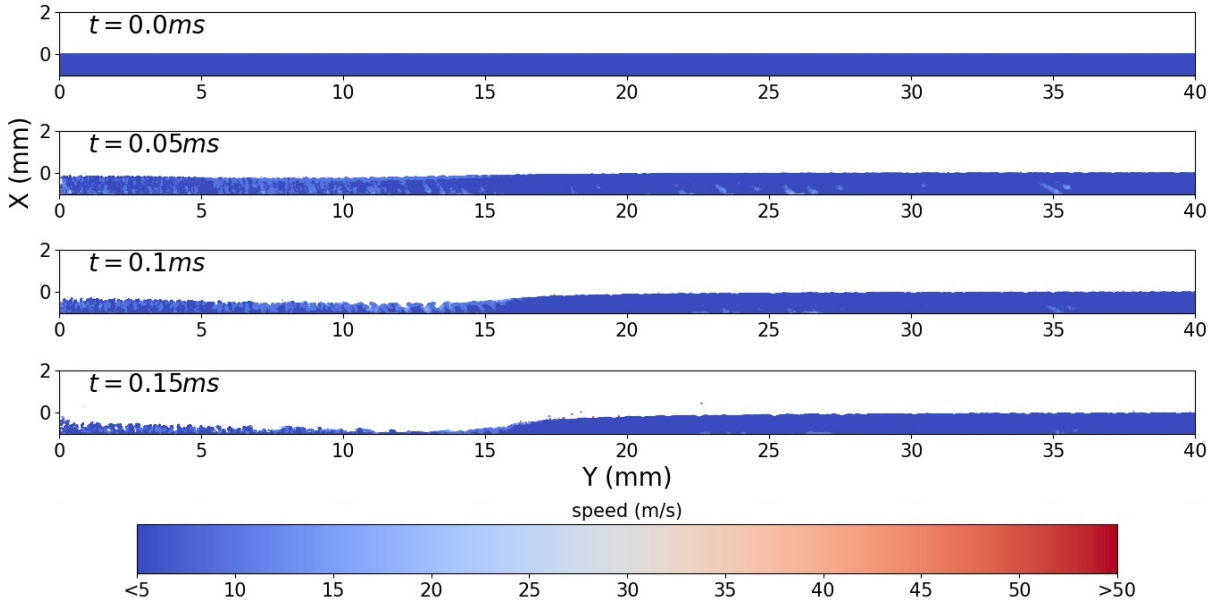

Figure 5.16: **Cratering in case II.**

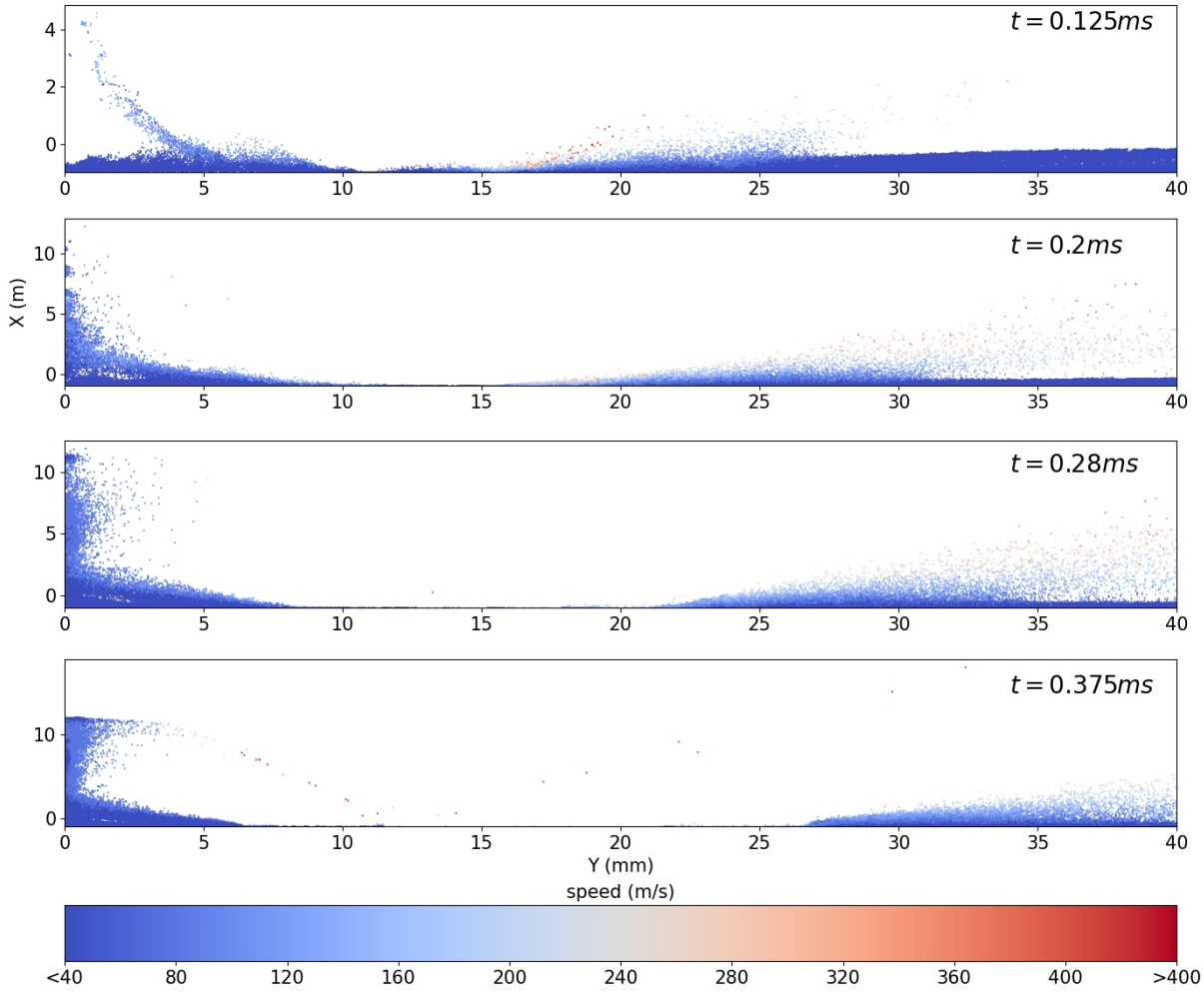

Figure 5.17: **Regolith dispersal in case I.**

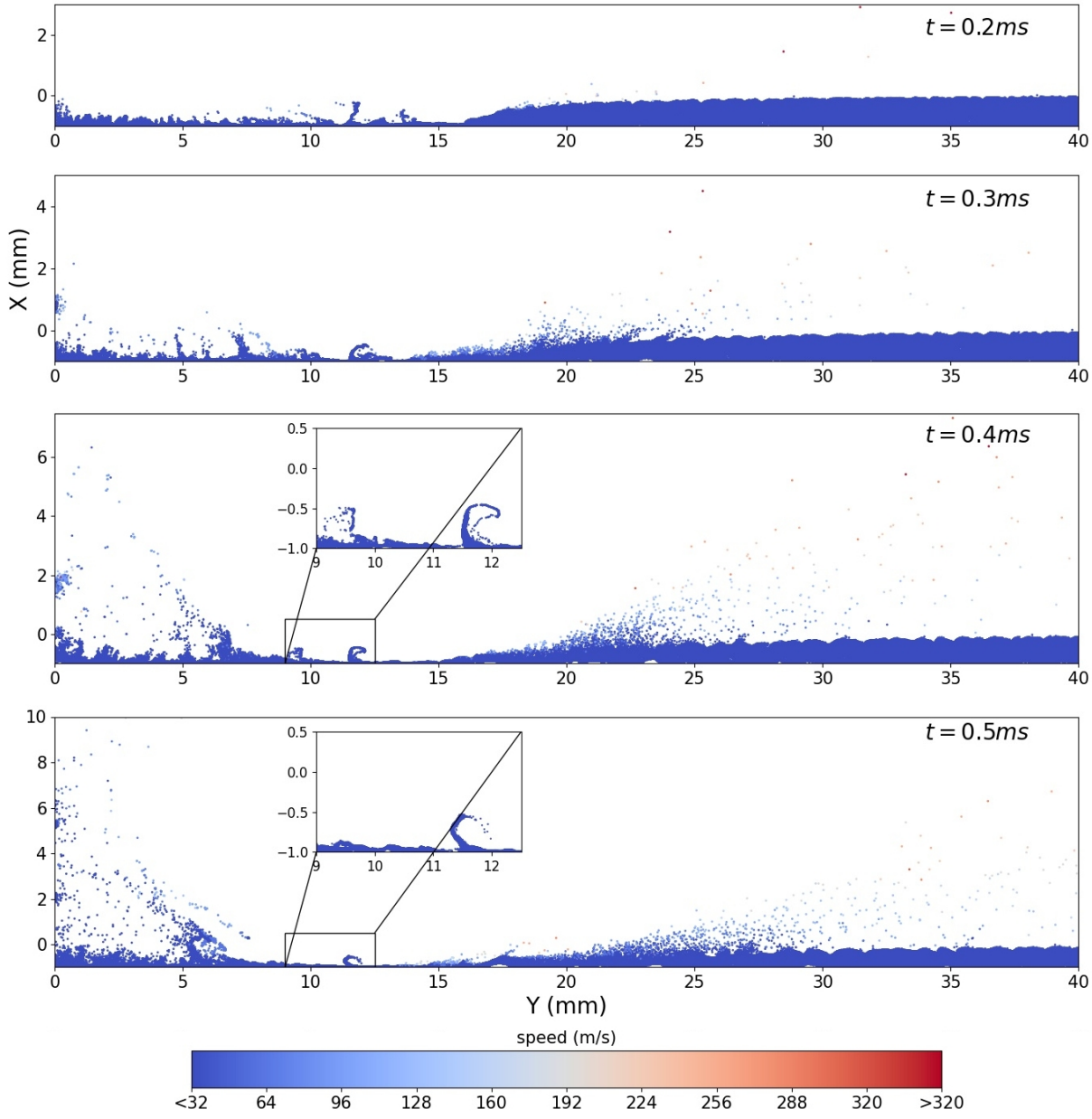

Figure 5.18: **Regolith dispersal in case II.**

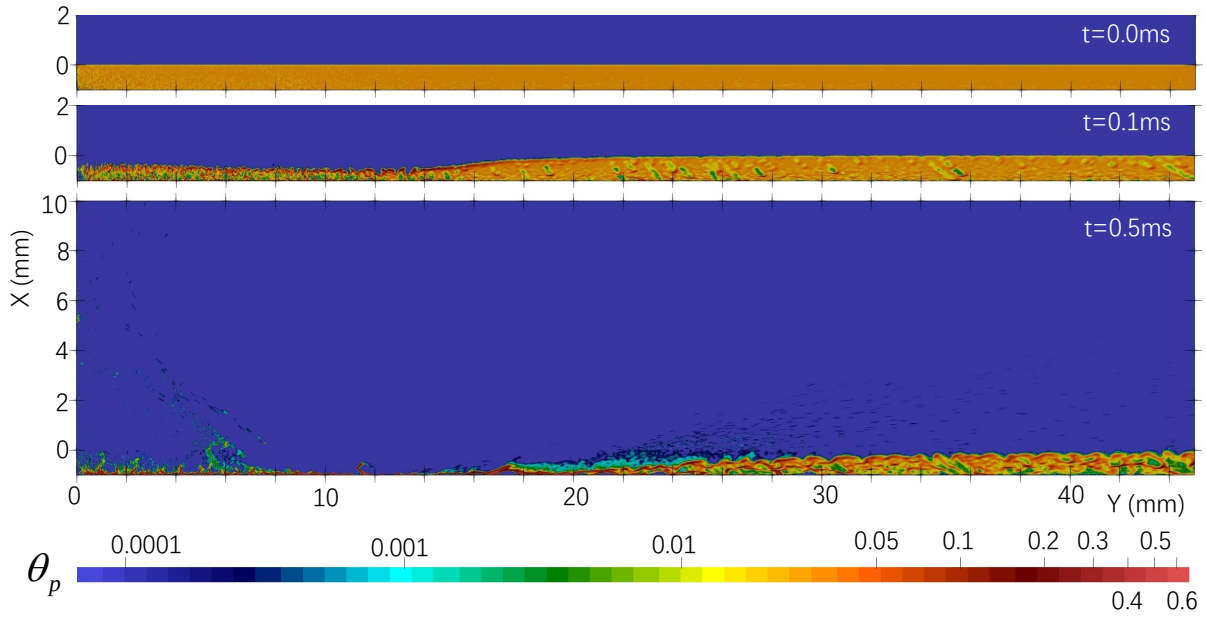

Figure 5.19: **Solid phase volume fraction of case II.**

invalid gradually increases with time as the shock wave forms and the gas permeates through the regolith layer, especially at the location between $Y = 10$ mm and 15 mm with Kn_p entering the slip flow regime, see Figure 5.11, at 0.3 ms and 0.5 ms. The breakdown of the free-molecular assumption introduces errors to the calculation of momentum and heat fluxes from the gas phase to the solid phase, causing the subsequent inaccurate solid particle paths and distribution, which is also noticed in Ref. [200]. A comparison between the particle drag coefficient based on a free-molecular model (i.e. Equation (7.11) of Ref. [104]) and that according to equations of the improved Loth empirical model [199] is shown in Figure 5.21, which clearly shows that Kn_p significantly increases the discrepancies. When the gas Mach number is 0.5, the differences of the drag coefficient between the free-molecular model and the Loth equation is 13.36% for $Kn_p = 1$ and 5.97% for $Kn_p = 3$, respectively. Kn_p at the stagnation region in Figure 5.20 is 2 to 8, corresponding to an error smaller than 10%, but the error increases in the small vortex at $Y = 12$ mm because Kn_p is smaller than 1. Further extension and correction of the calculation of the drag force in the interphase coupling model is necessary.

The solid particle temperature distributions at the end of the two cases are presented in Figure 5.22. The maximum particle temperature is 1326 K in the case using the stochastic collision method while it is 739 K in the MPPIC case due to the delay of the dispersal with the MPPIC method. Particles lifted and move radially off the axis to the far-field are heated, however, it is unexpected that the particles in the regolith layer from $Y = 0$ mm to $Y = 10$ mm, whose initial temperature is 200 K, are cooled down to a range of 100 - 130 K, especially the particles in the small secondary vortex between $Y = 10$ mm and 15 mm in the MPPIC case. This unnatural cooling should be attributed to the inaccurate calculation of the heat flux in the interphase

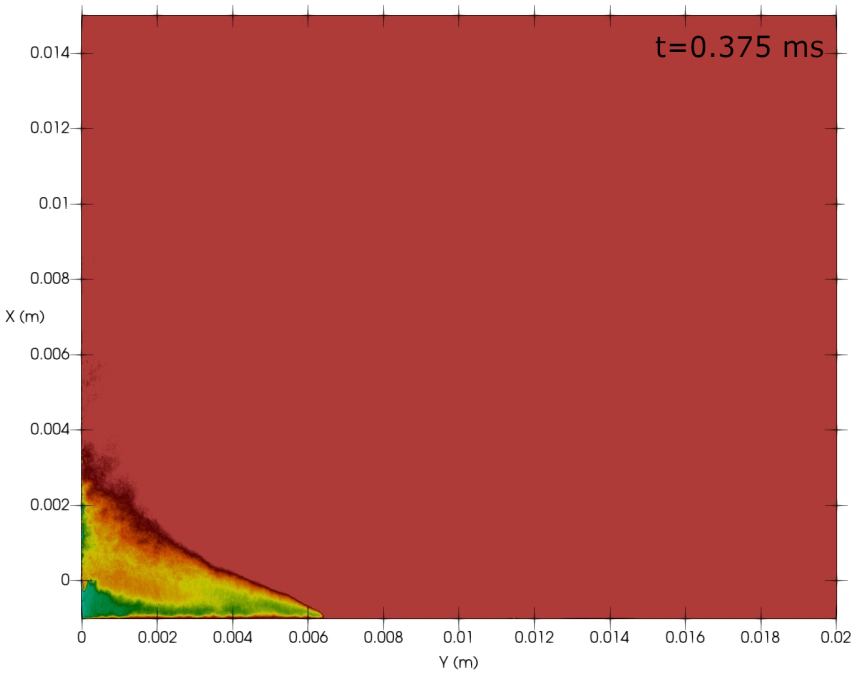

(a) Case I

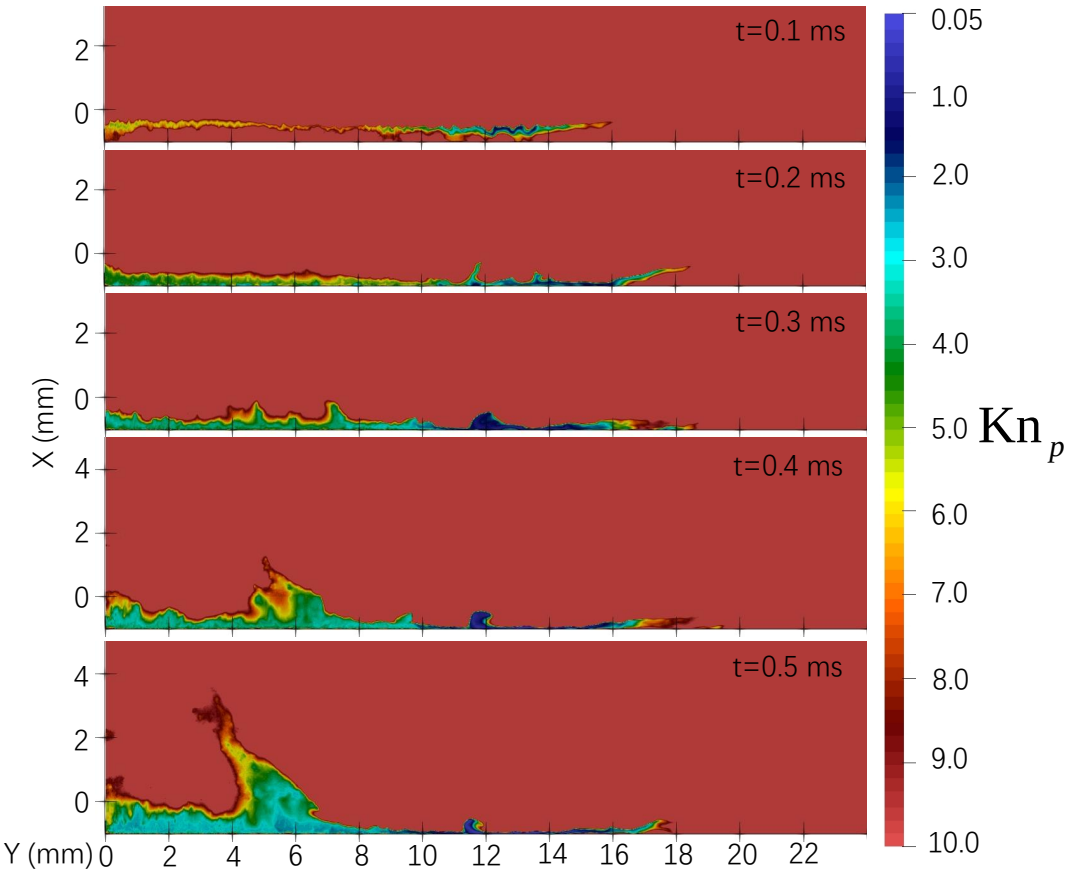

(b) Case II

Figure 5.20: **Distribution of Kn_p, where Kn_p is the ratio of the local gas MFP and the solid particle diameter.**

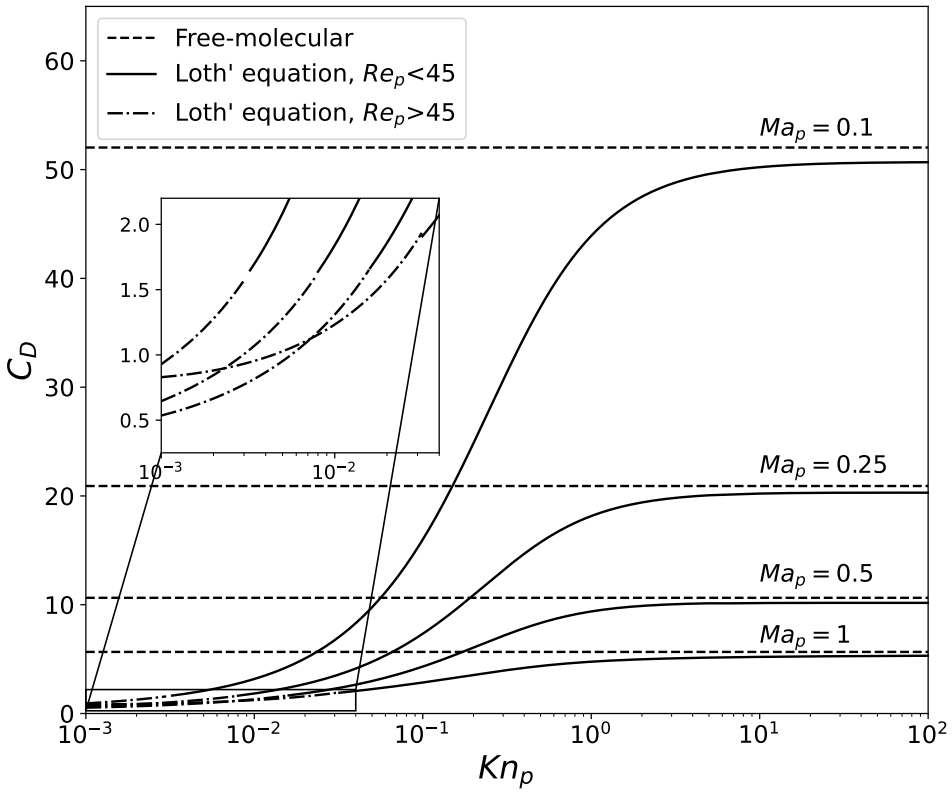

Figure 5.21: **Drag coefficient vs particle Knudsen number for Loth's equations [199] and the free-molecular model [104] in subsonic flow conditions.** $Ma_p = |\vec{v}_r|/\mathrm{a_g}$ **and** $Re_p = \rho_g|\vec{v}_r|d_p/\mu_g$**, where** $\vec{v}_r$ **is the particle-gas relative velocity,** $\mathrm{a_g}$ **is the speed of sound,** ρ_g **is the gas mass density,** d_p **is the particle diameter, and** μ_g **is the gas dynamic viscosity [199]. The calculation of the coefficient is based on the assumption of equivalence of the particle temperature and the gas temperature and the specific heat ratio is 1.3.**

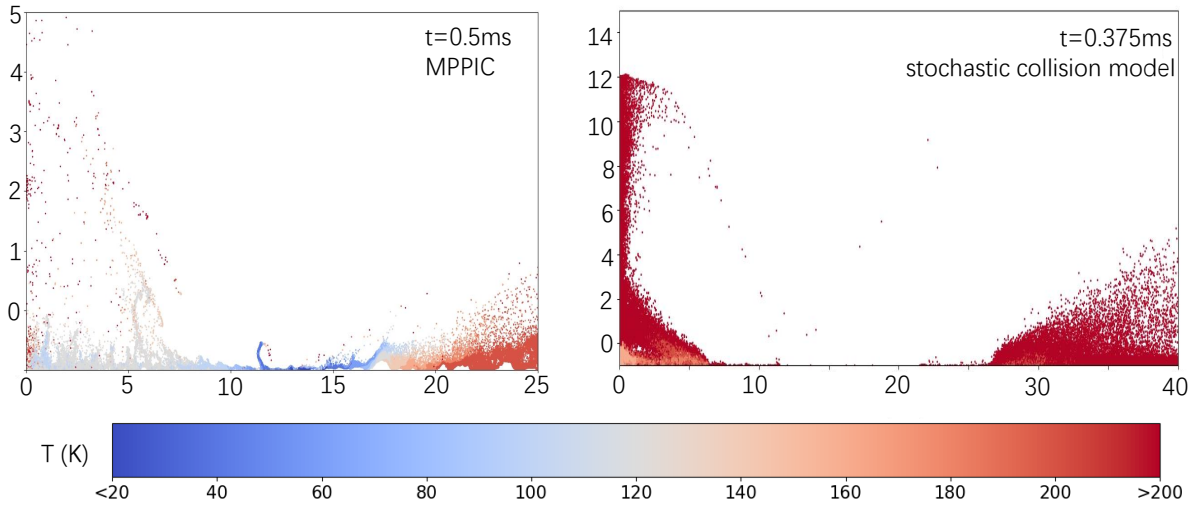

Figure 5.22: **Examples of particle temperature distributions using the MPPIC method (left) and the stochastic collision model (right).**

coupling model (similar to the inappropriate calculation of momentum flux and drag force mentioned above), indicating that the interphase heat transfer is more sensitive to Kn_p than the drag forces. The calculations of the drag force and the heat flux share the same local free-molecular condition ($Kn_p > 10$) in current interphase coupling model, but the MFP at the position where particles are cooled down is smaller than this assumption. This conclusion can also be proven by Figures 5.22 and 5.20 where the locations with solid particles cooled down in the two cases coincide with the regions with Kn_p is 2 to 5 and therefore in the transition flow regime.

5.4 Summary

In this chapter, the updated *rarefiedMultiphaseFoam* solver is used to simulate lunar PSI due to the exhaust plume from a scaled-down version of the lunar module descent engine from the Apollo era with two different situations; dilute granular case (i.e. low solid volume fraction) with the stochastic collision model and dense granular case (i.e. higher solid volume fractions) with the MPPIC method. The transient results using the two solid-solid interaction methods have been compared.

An importing finding is that the transient influence is of great importance to the gas phase, with the shock structure and stand-off height changing significantly as the regolith layer is eroded by the plume. Similar regolith cratering and particle dispersion processes are captured with both methods. It has been observed that the entrained dust particles significantly affect the gas flow development, including additional vortex formation, the fluctuation of the shock waves' positions, and the reflected flow towards to far field.

The MPPIC method accounting for close-packing limits and enduring contacts can yield a more realistic regolith layer evolution in PSI simulations. The top of the regolith layer is closer to a diffuse wall boundary condition for the DSMC particles and the regolith layer evolution is slowed down because of the more complicated solid-solid interactions in the MPPIC method. Despite the fact that initial solid volume fraction is low, the stochastic collision approach, which does not account for the close-packing limit, becomes unreliable because the gas compresses the regolith layer.

The calculation of drag forces and heat transfer in the interphase two-way coupling model based on the theory of Gallis [28] is found to be sensitive to particle Knudsen number, introducing considerable inaccuracies in the calculated solid particle temperatures.

Chapter 6

Conclusions and future work

6.1 Conclusions

The aim of this research was to examine transient phenomena that occurs when a high-speed gas is ejected from a supersonic nozzle and impinges on a regolith-coated surface in low-pressure environments.

The impact of the low-pressure environment on the shock wave diffraction and the vortex ring evolution has been experimentally studied using a shock tube working in a vacuum chamber. It has been confirmed that the reduction of the environmental pressure will increase of the thickness of the primary and embedded shock wave of vortex rings. The CRVR sill can be found in rarefied environments as long as the pressure ratio reaches the threshold values, but its strength decreases during its propagation. The trend of the flow structure degeneration during the propagation of the vortex ring as the environmental pressure decreases is observed. The environmental pressure limit of the schlieren imaging system used to recognise the vortex structure is found to be 0.2 bar.

Due to the limitation of the experimental apparatus, the influence of the rarefaction level and the shock Mach number on the vortex loop formation due to shock wave diffraction in rarefied ($Kn > 0.001$) conditions is investigated using various numerical tools, including CFD, DSMC and a new post-processing method called "rorticity" to identify the internal structures of vortex loops. It is found that an increase in flow rarefaction results in the simplification of the internal structures of vortex loops and that laminar flow patterns occur in all the simulation cases. The distribution profiles of the transition and free-molecular flow regimes are similar. With the use of rorticity, the rotational and shear movements of the fluid can be effectively and quantitatively resolved. By integrating the equation of the decomposition of vorticity, the circulation can be

decomposed into a rorticity flux that describes the fluid-rotational strength of a vortex and a shear vector flux that represents the shear strength of a vortex. The rorticity flux of the isolated rorticity loop increases with the shock Mach number non-linearly and decreases with increasing Knudsen number. The increase of rorticity flux in the isolated rorticity loop with time is attributed to the transformation from the shear vector to rorticity, and the amount of the transformed rorticity flux is equal to the change of the shear vector flux. According to the velocity field and streamlines in the rarefied condition, the increase of the Knudsen number postpones the vortex loop formation, and there is a maximum Knudsen number limiting the generation of a vortex. The increase in the Knudsen number will thicken the Knudsen layer and the subsequent vortex sheet, causing the failure in the condition of discontinuous tangential velocity. When the flow Knudsen number exceeds this maximum in the transition regime, no vortex loop forms. The vortex loops in the near continuum flow regime and the slip flow regime still have considerable ability to propagate forward. The radial size of the vortex loop increases with both the shock Mach number and the Knudsen number.

To study the impingement of rocket exhaust on a regolith-coated layer, an open source DSMC-based solver in OpenFOAM for two-phase rarefied flow called *rarefiedMultiphaseFoam* is developed and benchmarked it using analytical solutions and previous simulation results. The enduring solid-solid contacts are considered in the new solver. This thesis presented the direct and indirect interphase two-way coupling models, extended the solid particle phase change model with a correction to the particle diameter due to the phase change process, and updated the solver with the stochastic collision method for a dilute solid phase and the MPPIC method for solving dense solid phases. The benchmarking results of the indirect interphase two-way coupling model are in excellent agreement with those obtained through the direct method, proving the equivalence between the two methods. A test case of a uniform gas-solid flow was reproduced and the results are physical and agree well with previous simulation results in the literature. The updated solid particle phase change model allows a solid particle to experience a physical and continuous phase change and diameter variation. A gravity-controlled sedimentation case was used to validate the reproduced MPPIC code and the result was in good agreement with that in previous literature.

After the benchmarking, the *rarefiedMultiphaseFoam* was used to simulate lunar PSI due to the exhaust plume from a scaled-down version of the lunar module descent engine from the Apollo era with two different situations; a dilute granular case (i.e. low solid volume fraction) with the stochastic collision model and a dense granular case (i.e. higher solid volume fractions) with the MPPIC method. The effect of the enduring solid-solid interactions has been evaluated, and the transient plume-dust layer interaction has been studied. It is found that the transient influence is of great importance to the gas phase as the regolith layer is eroded by the plume. The entrained dust particles significantly affect the gas flow development, including additional

vortex formation, the fluctuation of shock waves positions, and reflected flow towards to far field. The MPPIC method, which accounts for close-packing limits and enduring contacts, can yield a more realistic regolith layer evolution in PSI simulations. Despite the fact that the initial solid volume fraction is low, the stochastic collision approach, which cannot account for the close-packing limit, becomes unreliable because the gas compresses the regolith layer. It must be mentioned that the evaluation of drag forces and heat transfer in the interphase two-way coupling model of this thesis is found to be sensitive to particle Knudsen number, introducing considerable inaccuracies in the calculated solid particle temperatures.

6.2 Future work

From the current work, the following areas can be investigated further:

1. The formation of a vortex loop in the slip flow regime has been confirmed, but the exact relation between the Kn and the vortex loop formation is still unknown. The influence of the initial conditions and the Knudsen number on the vortex loop formation can be investigated.

2. The influence of the nozzle geometry on the vortex loop formation and propagation ability in rarefied conditions can be investigated since the nozzle exit geometry is an effective passive thrust control method. Moreover, in practice, multiple nozzles are widely used and rarefied vortex loop interactions would also be of interest to study.

3. With the solid particle stochastic collision method, simulations can be conducted to investigate particle-laden flow impingement on sensitive surfaces in space. The code can be extended to have the ability to calculate the heat transfer due to solid particles to evaluate the heat flux on the surfaces.

4. The *rarefiedMultiphaseFoam* solver does not include a model describing interactions between droplets and a wall and within droplets. These models can be built to study topics with nozzle flows with liquid droplets in space. Provided that droplets are able to be modelled, a more realistic flow can be simulated with the phase change model.

5. A detailed study of the influence of all parameters in the MPPIC method on simulations of PSIs has not been conducted and this test is necessary to provide a guideline for subsequent users.

6. The *rarefiedMultiphaseFoam* solver can be used to simulate the impingement of two-phase flow due to PSIs with landing pads and berms to study nearby facility protection techniques in rarefied environments.

Appendix A

Transient simulations with *dsmcFoamPlus*

Obtaining time-averaged results for a steady-state flow in the DSMC method is standard, but in a transient case, it is necessary to perform the same simulation many times and average the results for each individual time interval.

A boolean variable *steadyStateCase* is introduced in the *dsmcDynamicLoadBalancing* class and can be specified in *system/loadBalanceDict*. If *steadyStateCase* is set as *true*, the simulation is running in the steady-state mode and the previous time directories will be deleted as the simulation progresses, since in those cases only the data with the most samples and lowest scatter is desired. However, if *steadyStateCase* is set *false*, all the time directories written out are saved to disk in order to perform an ensemble average.

A Python script called "*dsmcFoamPlusTransientAverageLoadBalance*" has been developed to run the simulations multiple times and perform the ensemble averaging. It can be found at *https://github.com/Kevin-Cao-gla/TransientDSMC-and-Rortex-scripts*. This script must be located in the base directory of a simulation, along with a *loadBalance* script, which has previously been described in Ref [112]. The Python code that the user can alter is shown in Table A.1. This script will perform the first simulation, then copy the result of each written time to a newly-created directory called "*FirstCalculation*", then clean the case directory to start the next ensemble until the number of samples that is defined by "*nCalculations*" is reached. The results generated in each ensemble are then averaged and written to the "*FirstCalculation*" directory. In the current work, the macroscopic properties of interest are pressure, velocity, and temperature, so only the results of these properties are ensemble-averaged.

The script can also be used to start the simulation again in the case of a halted system and power-off when using a personal computer, job time limitation on an high performance computing (HPC), or simply when a user needs to increase the number of samples and continue the simulation. The number of completed ensembles is defined by *nComplete* in the script, and a

Table A.1: **User defined part in the Python script.**

```
##################BEGINNING OF USER DEFINE PART#####################
# ——————————————————————————————————
caseName = "XXXXXX/" #slash must be kept
# ——————————————————————————————————
#the working directory path = "/home/XXXX/OpenFOAM/XXXX-2.4.0-MNF/run/"
#the directory where new data computed by another computer is saved
externalDataPath = "/home/XXXX/OpenFOAM/XXXX-2.4.0-MNF/run/"
# ——————————————————————————————————
# Important! number of calculations needed.
nCalculations = 0
#How many times it has been calculated?
nComplete = 0
#Is the calculation interrupted?
calcInteruption = False
#Just do superposition for two individual data?
externalNumComplete=0
# ——————————————————————————————————
######################END OF USER DEFINE PART######################
```

boolean variable called *calcInteruption* is defined to check if the simulation has been interrupted. As an illustration, if it is desired to run the simulation 10 times, but it stopped in the middle of the eighth calculation, one could set *nCalculations* and *nComplete* as 3 and 7 respectively because the eighth was not completed and set *calcInteruption* as *True*.

If the user wants to use two personal computer (PC)s or the combination of PC and HPC to calculate one case in order to improve the speed of calculation, the variable *externalNumComplete* can be used. For instance, if the HPC finished a simulation 20 times, which is considered as external data, and the PC finished it 40 times, and the data from both has already been ensemble-averaged separately, then *nComplete* can be defined as 40 and *externalNumComplete* as 20. The script will merge both results and average them. It is worth mentioning that when *externalNumComplete* is non-zero, the number in *nCalculations* will not work because the script is working in data-merging mode. Also, the *externalDataPath* should be set to the relevant case directory.

Appendix B

Rorticity Calculator

Two methods to calculate the rorticity are given in Ref. [117] and [121]. The first uses the Newton iteration method [117] and the second is based on Schur decomposition [121]. The detail of definition, derivation and calculation procedures of rorticity is given in Ref. [117] and [121] and is not repeated here.

The calculation of rorticity in this work is based on the real Schur decomposition because of the method's high efficiency. Schur decomposition is already included in the *scipy* module in Python. The calculator used here reads the data or result files created through user-defined post-processing utilities or executable commands and then finds the rotational part in the domain. These utilities are rewritten by means of the vorticity utility in *OpenFOAM/applications/utilities/postProcessing/velocityField/vorticity* to read the velocity data *UMean* of each computational cell from a *dsmcFoamPlus* simulation or *U* from CFD method and to calculate the corresponding velocity gradient tensor and vorticity vector. Interpolation schemes for *gradSchemes* in the *system/fvSchemes* file of each case must be declared before typing any executable commands. In this work, the second-order central difference scheme *Gauss linear* is used.

If higher version of OpenFOAM is used, such as OpenFOAM-v2112, the calculation of the vorticity and the velocity gradient should be conducted through the following commands

- *postProcess -func vorticity*
- *postProcess -func grad(U)*

, respectively.

The order of the velocity gradient tensor in OpenFOAM is:

$$\frac{\partial u}{\partial x}, \frac{\partial v}{\partial x}, \frac{\partial w}{\partial x}, \frac{\partial u}{\partial y}, \frac{\partial v}{\partial y}, \frac{\partial w}{\partial y}, \frac{\partial u}{\partial z}, \frac{\partial v}{\partial z}, \frac{\partial w}{\partial z}$$

Appendix C

Downloading, installing and using rarefiedMultiphaseFoam

C.1 Solver directory structure

The solver directory structure can be found in Figure C.1. The existing DSMC library is completely in charge of the gas phase evolution. Each solid simulator particle, which represents a number of real solid particles, is built in a class called *solidParticleCoupling* in the *parcels* directory, and a newly-built class in the *clouds* directory, *solidParticleCouplingCloud*, is responsible for the solid phase evolution. The interphase coupling model, which will be described in detail in Section 4.2.3, is built in a class named *interphaseCoupling* in the *interphaseCoupling* directory. The particles of both phases are intialised in the same computational domain through the *rarefiedMultiphaseInitialise* executable. All calculations, including the gas phase evolution, interphase coupling, and solid phase evolution, are realised using the *rarefiedMultiphaseFoam* executable. These underlying classes are saved in *src/lagrangian/rarefiedMultiphase*.

C.2 Downloading and installing

Two versions of the source code for OpenFOAM-2.4.0-MNF and OpenFOAM-v2112 are presented.

For OpenFOAM-2.4.0-MNF, the new solver can be downloaded from the associated Computer Physics Communications library entry. Detailed instructions of installing and building of *rarefiedMultiphaseFoam* for a chosen platform has been presented in *doc/Multiphase/ multiphaseInstallGuide.pdf* of the main directory. A version for OpenFOAM-v2112 is provided and it can be found in the *multiphase-ZCao-devel* branch at

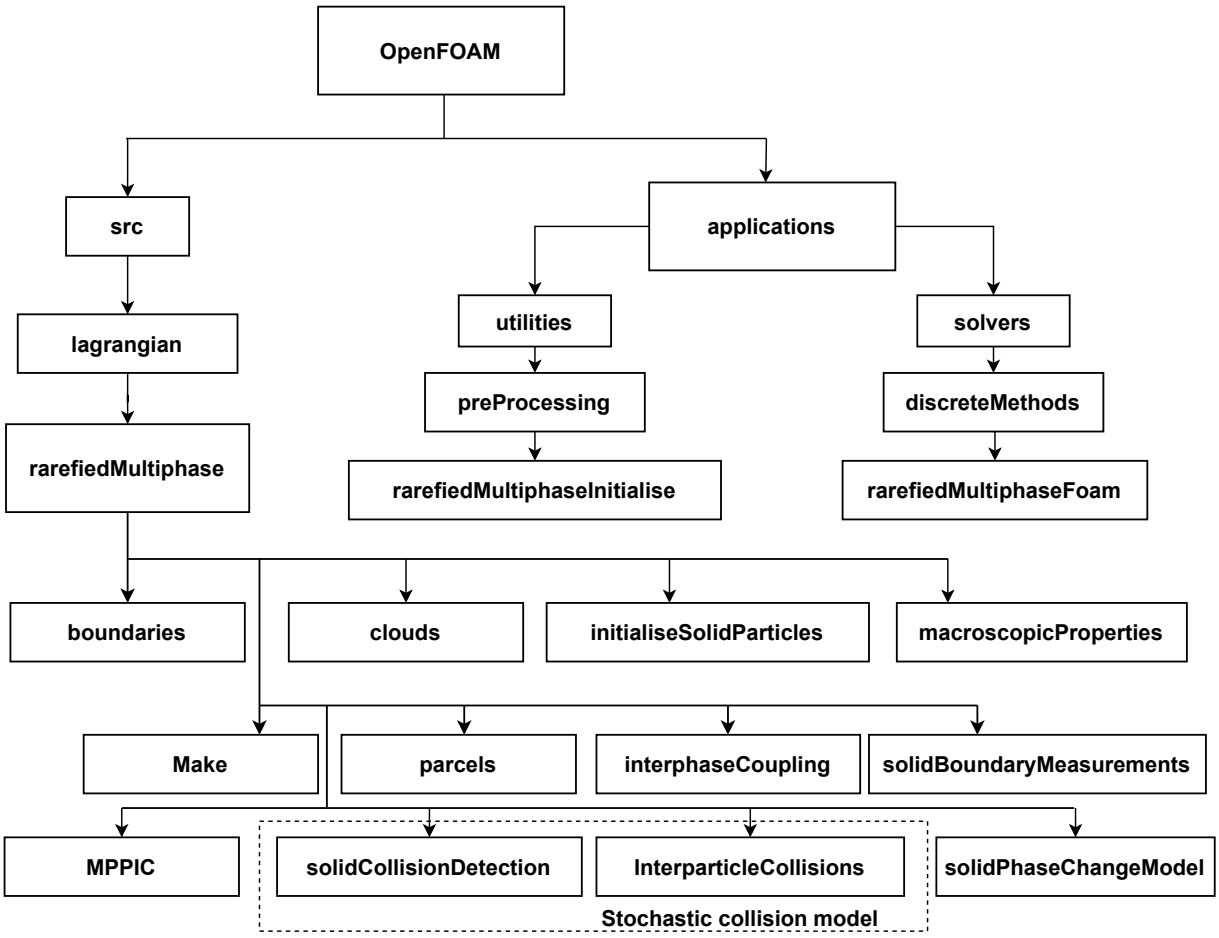

Figure C.1: **Directory structure of the *rarefiedMultiphaseFoam* solver.**

https://github.com/MicroNanoFlows/MNF-v2112

The source code for the libraries can be found in *src/lagrangian/rarefiedMultiphase* and the executables for initialising and running the solver can be found in *applications/utilities/preProcessing/rarefiedMultiphaseInitialise* and *applications/solvers/discreteMethods/rarefiedMultiphaseFoam*.

C.3 Using rarefiedMultiphaseFoam

Using rarefiedMultiphaseFoam will be very simple for users who are already familiar with an application from the OpenFOAM suite. Since this solver is based on the *dsmcFoamPlus* [112] solver, the gas phase simulations, including mesh creation, time control, initialisation, and post-processing, are identical and be found in Section 4 of Ref. [112]. The method to define solid particle properties, the particle initial state and to use the MPPIC method will be presented. The example is the benchmark case in Section 4.3.2 and only one solid specie is presented. The example of the use of the MPPIC method is the benchmark case in Section 4.3.4.

C.3.1 Solid particle properties

Constant solid particle properties are defined for each type of solid material added in a simulation; the values of these properties are given in a file located at *[case]/constant/spcProperties*. An example of this file of the benchmark case in Section 4.3.2 is shown in Table C.1. Here, the particle name *Al2O33* means Al_2O_3 particles with a diameter of 3 microns. The content of this file resembles that in Section 4.1.2 of Ref. [112]. Line 2 in Table C.1 defines the type of interphase coupling model. Users need to provide a list of solid particle names on Line 5 and the physical properties of each name should be defined in **solidProperties**. Line 8 defines the real number of solid particles or weight. Line 10 defines the collision detection scheme of the stochastic collision model, and the **solidNoTimeCounter** is the NTC method detailed in Ref. [30]. The collision model with the necessary coefficients is specified in Line 12–18 and the **solidHardSphereModel** is the hard sphere model considering solid binary collisions and it is described in Ref. [147]. Line 10 is set to **false**, Line 11–18 do not work. For a spherical solid particle, Line 26–32 are of great importance in interphase coupling calculation, velocity, and temperature update. Line 19–20, and 40–44 are prepared for the solid phase change model. Since Line 19 is set to **false**, Line 40–44 does not work. Line 34–39 are used for nonspherical solid particles detailed in Ref. [29].

Table C.1: **User defined part in spcProperties.**

```
1  // * * * * * * * * * * * * * * * * * * * * * * * * * * * * * * * * * * * * * * * * * //
2  InterphaseCouplingModel TwoWayCouplingIndirectMethod;
3
4  // Particle species
5  typeIdList (Al2O33);
6
7  nEquivalentSolidParticles 0.00044;
8
9  //- Stachastic collision model
10 enableParticleParticleCollisions    false;
11 solidCollisionDetection             solidNoTimeCounter;
12 solidBinaryCollisionModel           solidHardSphereModel;
13 solidHardSphereModelCoeffs
14 {
15    enableParticleSlide            false;
16    CoeffResituation               0.9;
17    CoeffFriction                  0;//- only effective when particle slides
18 }
19 enableParticlePhaseChangeModel      false;
20 materialList (AluminumOxide);
21
22 solidProperties
23 {
24    Al2O33
25    {
26        Diameter 3e-6;// m
27        epsilonSolid 0;//for monatomic gas only
28        alphaSolid 1;//for monatomic gas only
29        rhoSolid 3970;
30        specificHeatSolid 765;// (J/(kg*K))
31        muSolid 1;
32        tauSolid 0.89;
33
34        nonSphericalParticle false;
35        nonSphericalModelProperties
36        {
37          nonsphericalParticleVolume 0.0;
38          nonsphericalParticleSuperficialArea 0.0;
39        }
40         phaseChangeModelProperties
41        {
42           equilibriumMeltingTemperature 2313;// K
43           nucleationTemperature 1970;// K
44        }
45    }
46 }
47 // * * * * * * * * * * * * * * * * * * * * * * * * * * * * * * * * * * * * * * * * * //
```

C.3.2 Solid particle initialisation

After the definition of the case, all the particles, including the DSMC and the solid particles, can be initialised into the computational domain by using the command *rarefiedMultiphaseInitialise*. The initialisation of the DSMC particles is controlled in the file called *dsmcInitialiseDict*, which can be found in Ref. [112]. The initial state of solid particles is defined in *solidInitialiseDict* and the example of the benchmark case in Section 4.3.2 is shown in Table C.2.

Line 3 defines the selected initialisation method. The selected method, **solidMeshFill**, will fill the whole computational domain with solid particles. Other methods, such as **solidZoneFill**, can be used to fill user-defined regions of the mesh with solid particles. It must be highlighted that the solid particle name at Line 6, 12, 22, 26, and 30 should be the same as that in the **tybeIdList** in Table C.1. Line 33 defines the initial guess of relative speed in Equation 4.8. This value should not only be large enough to allow the occurrence of reflections of the DSMC particles from a solid particle, but also be small enough to avoid nonphysical collisions.

C.3.3 Using the MPPIC method

Table C.3 shows an example of defining properties of the MPPIC method in the benchmark case of particle sedimentation in Section 4.3.4. Line 3 defines the type of packing model, and line 19 defines the averaging method for calculating the average properties of the solid phase in a cell at each time-step. The particle stress model is defined at Line 4–17. Here, the Harris and Crighton model [150] is selected and the corresponding properties of this model are defined at line 6–11. **alphaPacked** is the close-packing volume fraction of the solid phase. Line 13–17 is used for velocity corrections after particle velocity updates in the packing model. The damping model type and the return-to-isotropy model type, as well as their properties, are defined in lines 21–27 and 29–35, respectively. In this benchmark case, no damping model and the return-to-isotropy model were used, so properties in Line 22–27 and 30–35 were not read. The alternatives to these two models are **RelaxationDamping** and **StochasticIsotropyModel**, respectively. Once these two models are activated, properties must be given and Line 24 and 32 define the calculation of the time scale defined in Equation 4.43 and 4.44.

Table C.2: **User defined part in solidInitialiseDict.**

```
configuration
{
    type solidMeshFill;
    numberDensities
    {
        Al2O33 9.896144e10;
    };
    CzRatios
    {
    //- define the ratio of the crystallization front radius to the particle radius
    //- range [0,1]
         Al2O33 0;
    };

    //- define the particle phase state
    //- "0" means pure solid phase
    //- "1" means unsteady phase but the core part is liquid
    //- "2" means unsteady phase but the core part is solid
    //- "3" means pure liquid phase
    phaseStates
    {
        Al2O33 0;
    };
    velocities
    {
        Al2O33 (1200 0 0);
    };
    temperatures
    {
        Al2O33 2200;
    }
     // for initialising "sigmaTcRMax" for DSMC particle reflection from solid particle surface
        interphaseInitialRelativeSpeed 200;
}
```

Table C.3: **User defined part in mppicPropertiesDict.**

```
1  enableMPPICMethod true;
2
3  MPPICPackingModel ExplicitPacking;
4  mppicParticleStressModelType HarrisCrightonModel;
5  alphaPacked 0.5;//close packed volume fraction
6  HarrisCrightonModelProperties
7  {
8     pSolid 100;//Pa
9     beta 3.0;
10    eps 1e-7;
11 };
12
13 mppicCorrectionLimitingMethods absoluteMethod;
14 absoluteMethodProperties
15 {
16    elasticRestitutionFactor 0.85;
17 };
18
19 mppicAveragingMethod DualMethod;
20
21 MPPICDampingModel NoMppicDamping;
22 MPPICDampingModelProperties
23 {
24    TimeScaleModel equilibrium;
25    alphaPacked 0.5;
26    e 0.85;
27 };
28
29 MPPICIsotropyModel NoIsotropyModel;
30 MPPICIsotropyModelProperties
31 {
32    TimeScaleModel equilibrium;
33    alphaPacked 0.5;
34    e 0.85;
35 };
```

Appendix D

Drawings of the shock tube

This section presents the drawings of the parts of the shock tube connected to the vacuum chamber used in this work. The unit of sizes shown in the following figures is millimeter.

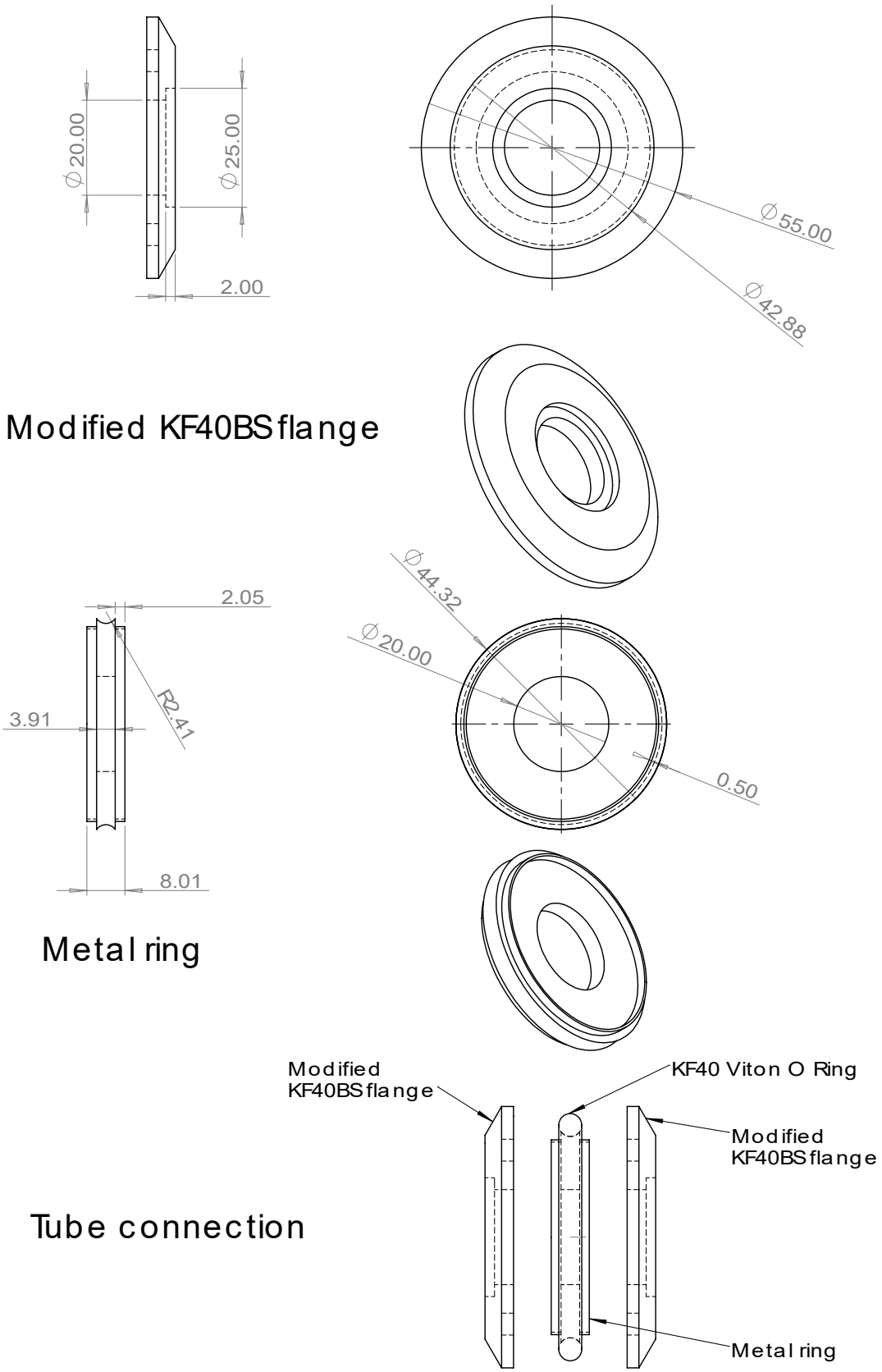

Figure D.1: Design of modified KF40BS flanges and the metal ring.

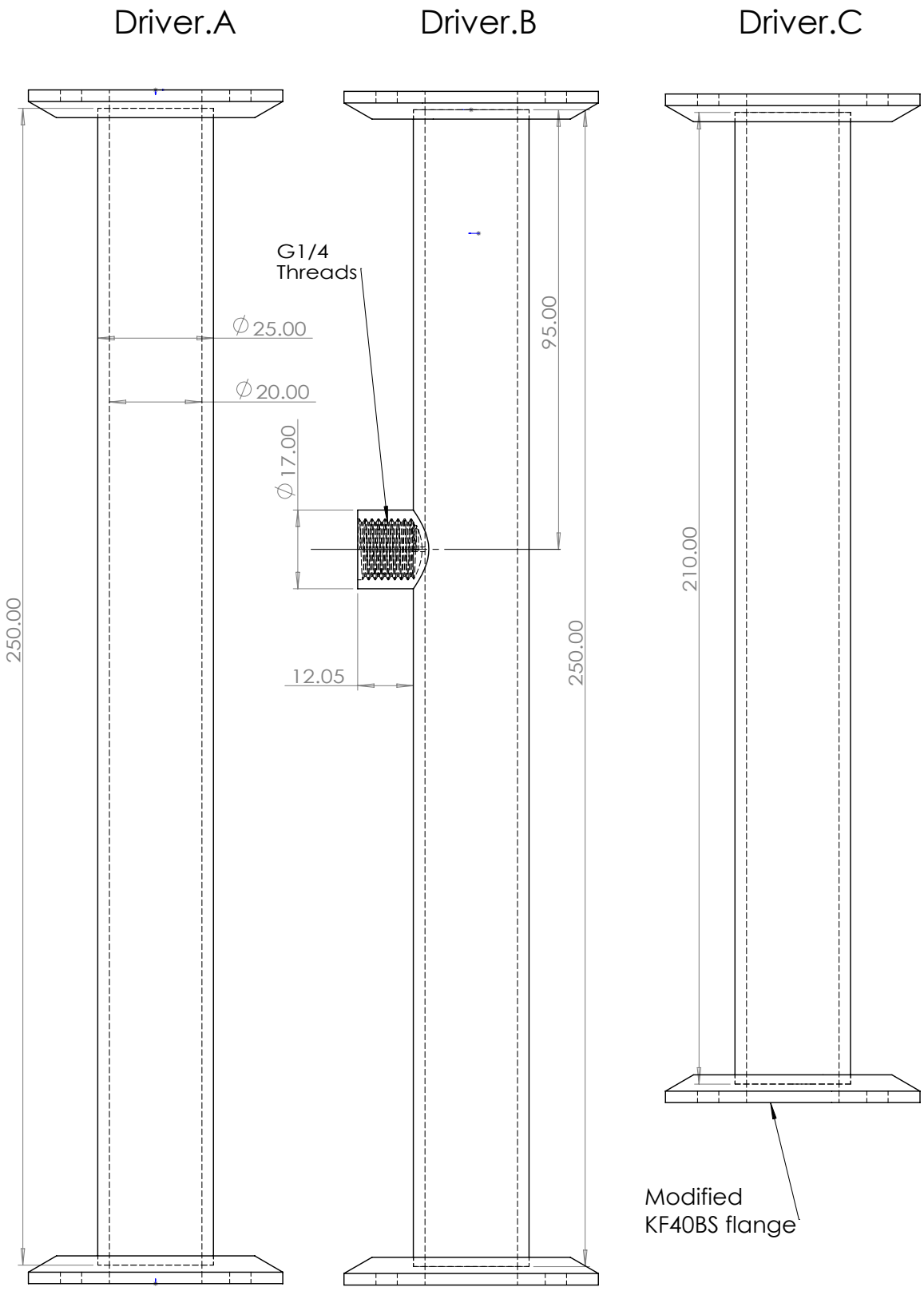

Figure D.2: Design of the driver section.

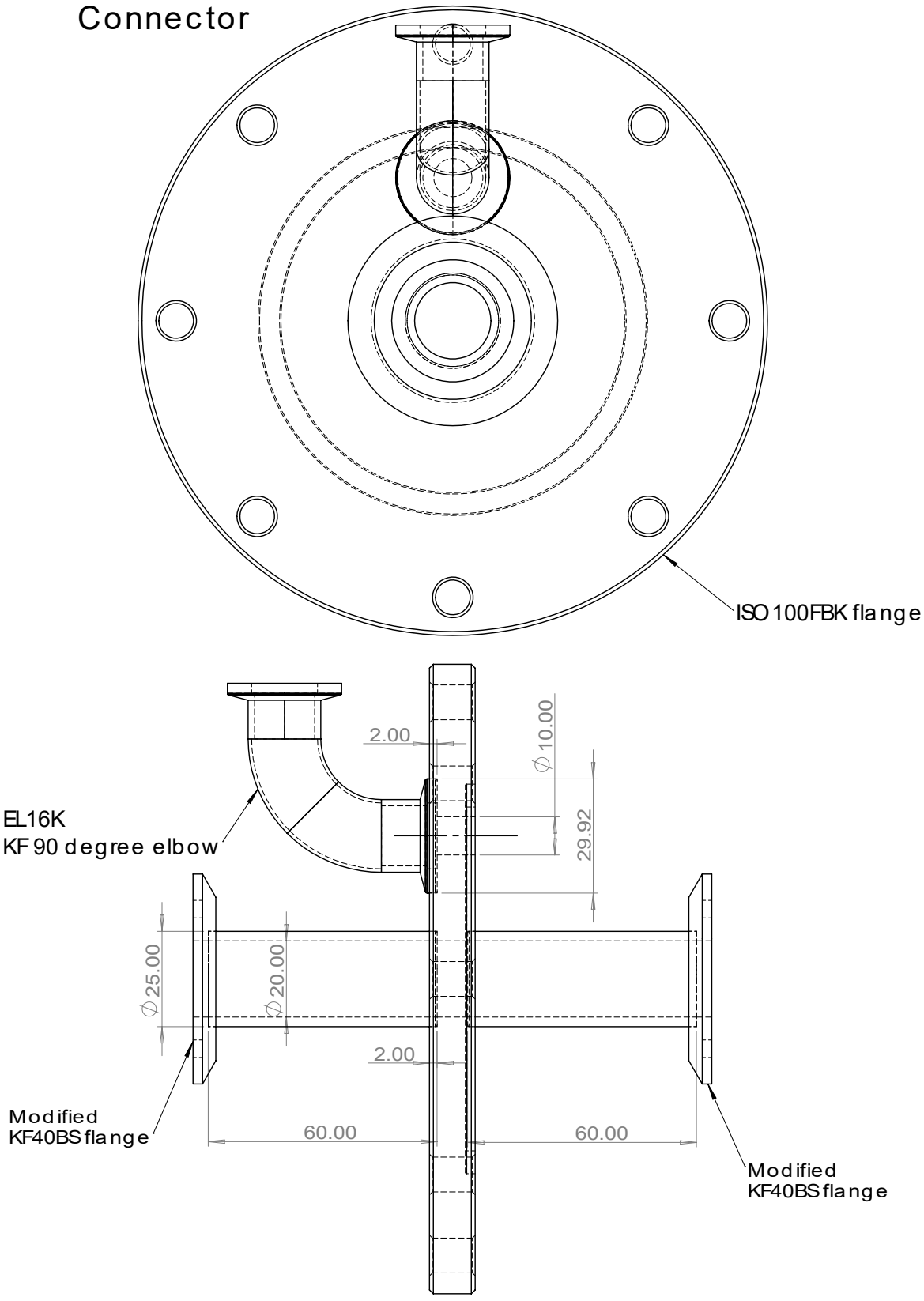

Figure D.3: Design of the connector for linking the shock tube and the vacuum chamber.

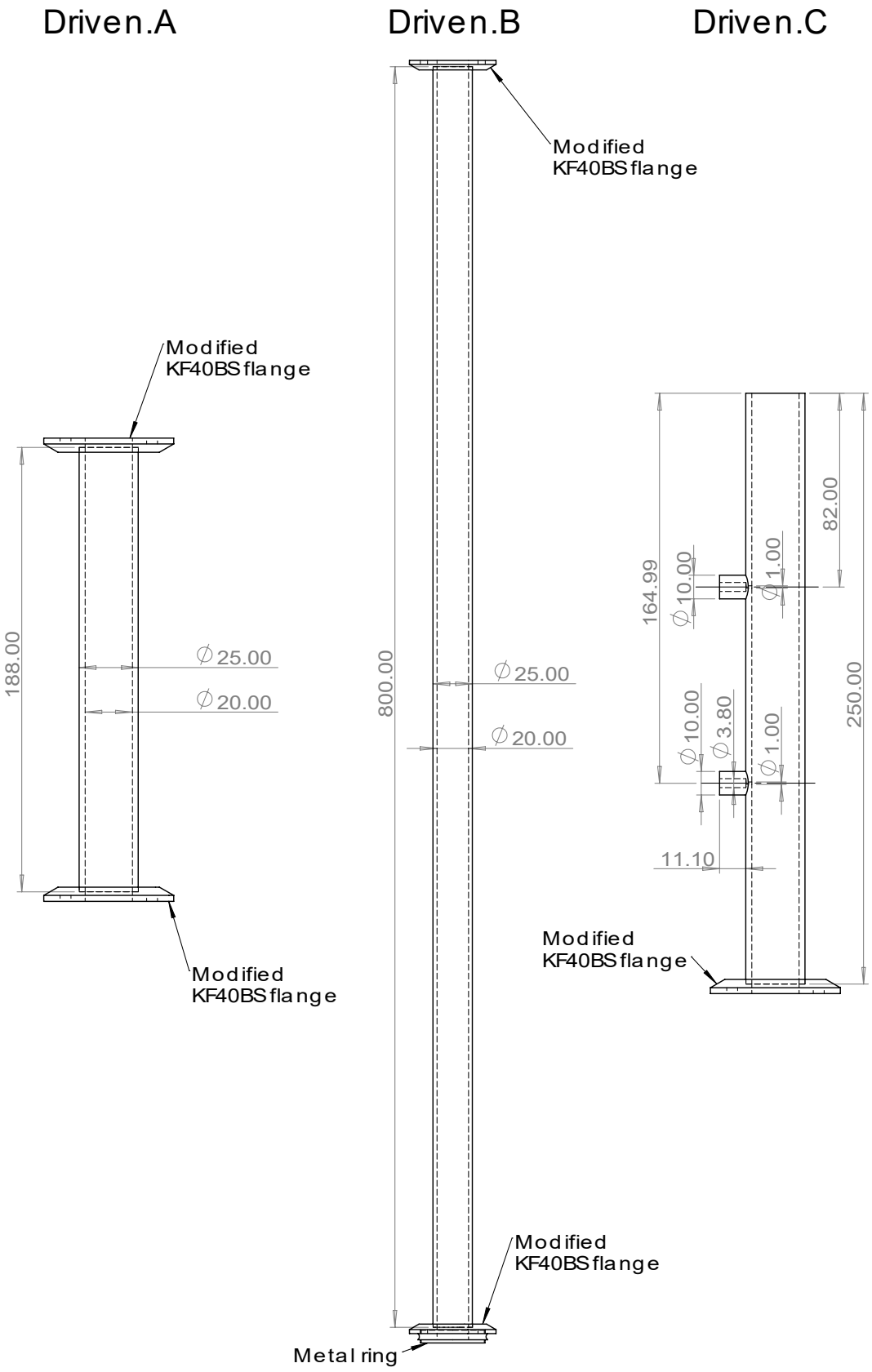

Figure D.4: Design of the driven section.

Bibliography

[1] T. R. Deschenes and J. Grot, "Prediction of rarefied micro-nozzle flows using the SPARTA library," in *AIP Conference Proceedings*, vol. 1786(1), p. 080002, AIP Publishing LLC, 2016.

[2] R. Ranjan, S. Chou, F. Riaz, and K. Karthikeyan, "Cold gas micro propulsion development for satellite application," *Energy Procedia*, vol. 143, pp. 754–761, 2017.

[3] Y. Qian, L. Xiao, S. Zhao, J. Zhao, J. Huang, J. Flahaut, M. Martinot, J. Head, H. Hiesinger, and G. Wang, "Geology and scientific significance of the Rümker region in northern Oceanus Procellarum: China's Chang'E-5 landing region," *Journal of Geophysical Research: Planets*, vol. 123(6), pp. 1407–1430, 2018.

[4] K. A. Farley, K. H. Williford, K. M. Stack, R. Bhartia, A. Chen, M. de la Torre, K. Hand, Y. Goreva, C. D. Herd, R. Hueso, *et al.*, "Mars 2020 mission overview," *Space Science Reviews*, vol. 216(8), pp. 1–41, 2020.

[5] D. Lauretta, S. Balram-Knutson, E. Beshore, W. Boynton, C. Drouet d'Aubigny, D. DellaGiustina, H. Enos, D. Golish, C. Hergenrother, E. Howell, *et al.*, "OSIRIS-REx: sample return from asteroid (101955) Bennu," *Space Science Reviews*, vol. 212(1), pp. 925–984, 2017.

[6] C. White, "Benchmarking, development and applications of an open source DSMC solver," 2013.

[7] F. La Torre, S. Kenjereš, J.-L. Moerel, and C. Kleijn, "Hybrid simulations of rarefied supersonic gas flows in micro-nozzles," *Computers & fluids*, vol. 49, no. 1, pp. 312–322, 2011.

[8] J. J. Peña Fernández and J. Sesterhenn, "Compressible starting jet: pinch-off and vortex ring–trailing jet interaction," *Journal of Fluid Mechanics*, vol. 817, pp. 560–589, 2017.

[9] K. H. Lee, "Plume influence analysis of small bipropellant thruster on solar array of GEO satellite," *Plos one*, vol. 13(9), p. e0199667, 2018.

[10] S. Vereen, "Orion Begins Checkouts, Completes First Service Module Course Correction Burn." https://blogs.nasa.gov/artemis/2022/11/16/orion-begins-checkouts-completes-first-service-module-course-correction-burn/. 2022, Nov 16.

[11] K. Shariff and A. Leonard, "Vortex rings," *Annual Review of Fluid Mechanics*, vol. 24, no. 1, pp. 235–279, 1992.

[12] J. Martinez and E. Worthy, "International Space Station (ISS) Thruster Plume Contamination and Erosion Control for Visiting Spacecraft," *Microscopy and Microanalysis*, vol. 26, no. S2, pp. 2238–2239, 2020.

[13] M. Orlandi, A. Passaro, and R. Rampini, "Need for a tool for the preliminary analysis of bipropellant plume impingement effects on contamination sensitive surfaces," in *Systems Contamination: Prediction, Control, and Performance 2016*, vol. 9952, p. 995209, International Society for Optics and Photonics, 2016.

[14] P. H. Oosthuizen and W. E. Carscallen, *Introduction to compressible fluid flow*. CRC press, 2013.

[15] A. R. Tummala and A. Dutta, "An overview of cube-satellite propulsion technologies and trends," *Aerospace*, vol. 4(4), p. 58, 2017.

[16] A. Rahimi, O. Ejtehadi, K. Lee, and R. Myong, "Near-field plume-surface interaction and regolith erosion and dispersal during the lunar landing," *Acta Astronautica*, vol. 175, pp. 308–326, 2020.

[17] P. T. Metzger, R. C. Latta III, J. M. Schuler, and C. D. Immer, "Craters formed in granular beds by impinging jets of gas," in *AIP Conference Proceedings*, vol. 1145(1), pp. 767–770, American Institute of Physics, 2009.

[18] M. Mehta, N. O. Renno, J. Marshall, M. R. Grover, A. Sengupta, N. A. Rusche, J. F. Kok, R. E. Arvidson, W. J. Markiewicz, M. T. Lemmon, *et al.*, "Explosive erosion during the phoenix landing exposes subsurface water on mars," *Icarus*, vol. 211(1), pp. 172–194, 2011.

[19] J. R. Gaier, K. Journey, S. Christopher, and S. Davis, "Evaluation of brushing as a lunar dust mitigation strategy for thermal control surfaces," in *International Conference on Environmental Systems*, 2011.

[20] C. Immer, J. Lane, P. Metzger, and S. Clements, "Apollo video photogrammetry estimation of plume impingement effects," *Icarus*, vol. 214(1), pp. 46–52, 2011.

[21] P. T. Metzger, J. E. Lane, C. D. Immer, and S. Clements, "Cratering and blowing soil by rocket engines during lunar landings," 2008.

[22] Y. Zou, W. Li, and Z. Ouyang, "China's deep space exploration to 2030," *China National COSPAR report*, 2014.

[23] G. Kminek, M. A. Meyer, D. W. Beaty, B. L. Carrier, T. Haltigin, and L. E. Hays, "Mars Sample Return (MSR): planning for returned sample science," *Astrobiology*, no. ja, 2022.

[24] A. K. Chinnappan, R. Kumar, and V. K. Arghode, "Modeling of dusty gas flows due to plume impingement on a lunar surface," *Physics of Fluids*, vol. 33, no. 5, p. 053307, 2021.

[25] D. C. Stubbs, L. Silwal, B. S. Thurow, M. Hirabayashi, V. Raghav, and D. E. Scarborough, "Three-Dimensional Measurement of the Crater Formation During Plume–Surface Interactions Using Stereo-Photogrammetry," *AIAA Journal*, pp. 1–16, 2021.

[26] M. Mehta, "Rocket Plume Interactions for NASA Landing Systems," 2019.

[27] X. He, B. He, and G. Cai, "Simulation of rocket plume and lunar dust using dsmc method," *Acta Astronautica*, vol. 70, pp. 100–111, 2012.

[28] M. Gallis, J. Torczynski, and D. Rader, "An approach for simulating the transport of spherical particles in a rarefied gas flow via the direct simulation Monte Carlo method," *Physics of Fluids*, vol. 13, no. 11, pp. 3482–3492, 2001.

[29] J. Burt and I. Boyd, "Development of a two-way coupled model for two phase rarefied flows," in *42nd AIAA Aerospace Sciences Meeting and Exhibit*, p. 1351, 2004.

[30] A. B. Morris, D. B. Goldstein, P. L. Varghese, and L. M. Trafton, "Approach for modeling rocket plume impingement and dust dispersal on the moon," *Journal of Spacecraft and Rockets*, vol. 52, no. 2, pp. 362–374, 2015.

[31] P. F. Penko, I. Boyd, D. Meissner, and K. J. DeWitt, "Measurement and analysis of a small nozzle plume in vacuum," *Journal of Propulsion and Power*, vol. 9(4), pp. 646–648, 1993.

[32] T. Niimi, "Optical diagnostics of nonequilibrium phenomena in highly rarefied gas flows," in *AIP Conference Proceedings*, vol. 663, pp. 1025–1032, American Institute of Physics, 2003.

[33] G. Dettleff and M. Grabe, "Basics of plume impingement analysis for small chemical and cold gas thrusters," tech. rep., DEUTSCHES ZENTRUM FUR LUFT-UND RAUMFAHRT (DLR) GOETTINGEN (GERMANY) INSTITUT . . . , 2011.

[34] B. He, J. Zhang, and G. Cai, "Research on vacuum plume and its effects," *Chinese Journal of Aeronautics*, vol. 26(1), pp. 27–36, 2013.

[35] H. W. Liepmann, A. Roshko, D. Coles, and B. Sturtevant, "A 17-Inch Diameter Shock Tube for Studies in Rarefied Gasdynamics," *Review of Scientific Instruments*, vol. 33(6), pp. 625–631, 1962.

[36] H. Zare-Behtash, K. Kontis, N. Gongora-Orozco, and K. Takayama, "Compressible vortex loops: effect of nozzle geometry," *International Journal of Heat and Fluid Flow*, vol. 30, no. 3, pp. 561–576, 2009.

[37] J. D. Anderson Jr, *Fundamentals of aerodynamics*. Tata McGraw-Hill Education, 2010.

[38] J. D. Anderson, *Modern compressible flow: with historical perspective*, vol. 12. McGraw-Hill New York, 1990.

[39] P. G. Saffman, *Vortex dynamics*. Cambridge university press, 1995.

[40] J. J. P. Fernández and J. Sesterhenn, "Compressible starting jet: pinch-off and vortex ring–trailing jet interaction," *Journal of Fluid Mechanics*, vol. 817, pp. 560–589, 2017.

[41] H. Zhang, Z. Chen, X. Jiang, and Z. Huang, "The starting flow structures and evolution of a supersonic planar jet," *Computers & Fluids*, vol. 114, pp. 98–109, 2015.

[42] T. Murugan, S. De, C. Dora, and D. Das, "Numerical simulation and PIV study of compressible vortex ring evolution," *Shock waves*, vol. 22, no. 1, pp. 69–83, 2012.

[43] J. M. Delery, "Shock wave/turbulent boundary layer interaction and its control," *Progress in Aerospace Sciences*, vol. 22(4), pp. 209–280, 1985.

[44] D. S. Dolling, "Fifty years of shock-wave/boundary-layer interaction research: what next?," *AIAA journal*, vol. 39(8), pp. 1517–1531, 2001.

[45] G. Ben-Dor and G. Ben-Dor, *Shock wave reflection phenomena*, vol. 2. Springer, 2007.

[46] R. C. Mehta, "Numerical Simulation of Base Pressure and Drag of Space Reentry Capsules at High Speed," in *Hypersonic Vehicles-Past, Present and Future Developments*, IntechOpen, 2019.

[47] G. Li, *Experimental studies on shock wave interactions with flexible surfaces and development of flow diagnostic tools*. PhD thesis, University of Glasgow, 2020.

[48] A. H. Shapiro, "The dynamics and thermodynamics of compressible fluid flow," *New York: Ronald Press*, 1953.

[49] F. Gnani, K. Lo, H. Zare-Behtash, and K. Kontis, "Experimental investigation on shock wave diffraction over sharp and curved splitters," *Acta Astronautica*, vol. 99, pp. 143–152, 2014.

[50] V. Soni, A. Chaudhuri, N. Brahmi, and A. Hadjadj, "Turbulent structures of shock-wave diffraction over 90 convex corner," *Physics of Fluids*, vol. 31(8), p. 086103, 2019.

[51] B. W. Skews, "The perturbed region behind a diffracting shock wave," *Journal of Fluid Mechanics*, vol. 29(4), pp. 705–719, 1967.

[52] M. Sun and K. Takayama, "A note on numerical simulation of vortical structures in shock diffraction," *Shock Waves*, vol. 13, no. 1, pp. 25–32, 2003.

[53] M. Sun and K. Takayama, "Vorticity production in shock diffraction," *Journal of Fluid Mechanics*, vol. 478, pp. 237–256, 2003.

[54] B. Skews, C. Law, A. Muritala, and S. Bode, "Shear layer behavior resulting from shock wave diffraction," *Experiments in fluids*, vol. 52(2), pp. 417–424, 2012.

[55] B. W. Skews, "The shape of a diffracting shock wave," *Journal of Fluid Mechanics*, vol. 29(2), pp. 297–304, 1967.

[56] T. Bazhenova, L. Gvozdeva, and Y. V. Zhilin, "Change in the shape of the diffracting shock wave at a convex corner," in *Gasdynamics of Explosions and Reactive Systems*, pp. 401–412, Elsevier, 1980.

[57] F. Gnani, K. H. Lo, H. Zare-Behtash, and K. Kontis, "Shock wave diffraction phenomena around slotted splitters," *Aerospace*, vol. 2, no. 1, pp. 1–16, 2015.

[58] F. Gnani, K. H. Lo, H. Zare-Behtash, and K. Kontis, "Shock wave diffraction in the presence of a supersonic co-flow jet," *Shock Waves*, vol. 26(3), pp. 253–262, 2016.

[59] R. Paton, B. Skews, and A. Saligram, "Visualisation of plane shock wave diffraction from the curved exit of a shock tube," *Journal of Visualization*, vol. 18(3), pp. 493–499, 2015.

[60] B. Skews and J. Bentley, "Merging of two independent diffracting shock waves," *Shock Waves*, vol. 26(3), pp. 327–331, 2016.

[61] S. Cooppan and B. Skews, "Three-dimensional shock wave diffraction off a discontinuous edge," *Shock Waves*, vol. 27, no. 2, pp. 131–142, 2017.

[62] F. Elder Jr and N. De Haas, "Experimental study of the formation of a vortex ring at the open end of a cylindrical shock tube," *Journal of Applied Physics*, vol. 23, no. 10, pp. 1065–1069, 1952.

[63] K. Kontis, R. An, and J. A. Edwards, "Compressible vortex-ring interaction studies with a number of generic body configurations," *AIAA journal*, vol. 44, no. 12, pp. 2962–2978, 2006.

[64] M. Gharib, E. Rambod, and K. Shariff, "A universal time scale for vortex ring formation," *Journal of Fluid Mechanics*, vol. 360, pp. 121–140, 1998.

[65] M. Brouillette and C. Hebert, "Propagation and interaction of shock-generated vortices," *Fluid dynamics research*, vol. 21, no. 3, pp. 159–169, 1997.

[66] J. Baird, "Supersonic vortex rings," *Proceedings of the Royal Society of London. A. Mathematical and Physical Sciences*, vol. 409, no. 1836, pp. 59–65, 1987.

[67] R. Hillier, "Computation of shock wave diffraction at a ninety degrees convex edge," *Shock waves*, vol. 1(2), pp. 89–98, 1991.

[68] L. Qin, Y. Xiang, H. Lin, and H. Liu, "Formation and dynamics of compressible vortex rings generated by a shock tube," *Experiments in Fluids*, vol. 61(3), pp. 1–16, 2020.

[69] H. Zare-Behtash, K. Kontis, and N. Gongora-Orozco, "Experimental investigations of compressible vortex loops," *Physics of Fluids*, vol. 20, no. 12, p. 126105, 2008.

[70] M. Thangadurai and D. Das, "Characteristics of counter-rotating vortex rings formed ahead of a compressible vortex ring," *Experiments in fluids*, vol. 49, no. 6, pp. 1247–1261, 2010.

[71] C. Dora, T. Murugan, S. De, and D. Das, "Role of slipstream instability in formation of counter-rotating vortex rings ahead of a compressible vortex ring," *Journal of fluid mechanics*, vol. 753, pp. 29–48, 2014.

[72] H. Zhang, Z. Chen, B. Li, and X. Jiang, "The secondary vortex rings of a supersonic underexpanded circular jet with low pressure ratio," *European Journal of Mechanics-B/Fluids*, vol. 46, pp. 172–180, 2014.

[73] P. G. Saffman, *Vortex dynamics*. Cambridge university press, 1992.

[74] S. Green, *Fluid vortices*, vol. 30. Springer Science & Business Media, 2012.

[75] H. Ahmad, N. Hasan, and S. Sanghi, "On the influence of co-flow on the shocks and vortex rings in the starting phases of under-expanded jets," *Physics of Fluids*, 2022.

[76] B. K. Shivamoggi, "Hydrodynamic impulse in a compressible fluid," *Physics Letters A*, vol. 374(47), pp. 4736–4740, 2010.

[77] D. W. Moore, "The effect of compressibility on the speed of propagation of a vortex ring," *Proceedings of the Royal Society of London. A. Mathematical and Physical Sciences*, vol. 397, no. 1812, pp. 87–97, 1985.

[78] R. Mariani and K. Kontis, "Effects of exit nozzle diameter on compressible vortex rings flow structure," in *47th AIAA Aerospace Sciences Meeting Including The New Horizons Forum and Aerospace Exposition*, p. 410, 2009.

[79] L. Qin, Y. Xiang, S. Qin, and H. Liu, "On the structures of compressible vortex rings generated by the compressible starting jet from converging and diverging nozzles," *Aerospace Science and Technology*, vol. 106, p. 106188, 2020.

[80] E. J. Gutmark and F. F. Grinstein, "Flow control with noncircular jets," *Annual review of fluid mechanics*, vol. 31(1), pp. 239–272, 1999.

[81] H. Zhang, Z. Chen, Z. Guo, and X. Sun, "Characteristic behavior of shock pattern and primary vortex loop of a supersonic square jet," *International Journal of Heat and Mass Transfer*, vol. 115, pp. 347–363, 2017.

[82] H. Zhang, Z. Chen, X. Jiang, and Z. Guo, "The initial flow characteristics of supersonic jets with different geometries," *Physics Letters A*, vol. 379, no. 18-19, pp. 1256–1262, 2015.

[83] R. Mariani, K. Kontis, and N. Gongora-Orozco, "Head on collisions of compressible vortex rings on a smooth solid surface," *Shock Waves*, vol. 23(4), pp. 381–398, 2013.

[84] A. Szumowski, G. Sobieraj, W. Selerowicz, and J. Piechna, "Starting jet–wall Interaction," *Journal of sound and vibration*, vol. 232, no. 4, pp. 695–702, 2000.

[85] T. Minota, M. Nishida, and M. Lee, "Shock formation by compressible vortex ring impinging on a wall," *Fluid dynamics research*, vol. 21(3), pp. 139–157, 1997.

[86] T. Murugan and D. Das, "Structure and acoustic characteristics of supersonic vortex rings," in *FLUCOME 2007 (9th International Symposium on Fluid Control, Measurement and Visualization)*, pp. 16–19, 2007.

[87] T. Murugan and D. Das, "On evolution and acoustic characteristics of a compressible vortex ring," *International Journal of Aeroacoustics*, vol. 7(3-4), pp. 199–222, 2008.

[88] T. Murugan and D. Das, "Characteristics of noise produced during impingement of a compressible vortex ring on a wall," *International Journal of Aeroacoustics*, vol. 9(6), pp. 849–858, 2010.

[89] M. Downey, T. Cloete, and A. Yates, "A rapid opening sleeve valve for a diaphragmless shock tube," *Shock Waves*, vol. 21(4), pp. 315–319, 2011.

[90] D. C. Taylor, *The Characterization and Feasibility of a Low-Duty-Cycle Diaphragmless Shock Tube*. PhD thesis, Texas A & M University, 2012.

[91] M. Samimi, J. Zamani, and F. Sardarzadeh, "Shock wave pressure and velocity measuring using a novel optic sensor in a newly designed diaphragm-less shock tube," *Experimental Techniques*, vol. 45(1), pp. 55–66, 2021.

[92] G. Li, T. Ukai, and K. Kontis, "Characterization of a novel open-ended shock tube facility based on detonation transmission tubing," *Aerospace Science and Technology*, vol. 94, p. 105388, 2019.

[93] Y. Kai, W. Garen, T. Schlegel, and U. Teubner, "A novel shock tube with a laser–plasma driver," *Laser and Particle Beams*, vol. 35(4), pp. 610–618, 2017.

[94] J. N. Bradley, *Shock waves in chemistry and physics*. Methuen & Co.Ltd, 1963.

[95] G. S. Settles, *Schlieren and shadowgraph techniques: visualizing phenomena in transparent media*. Springer Science & Business Media, 2001.

[96] M. J. Hargather, G. S. Settles, and M. J. Madalis, "Schlieren imaging of loud sounds and weak shock waves in air near the limit of visibility," *Shock Waves*, vol. 20(1), pp. 9–17, 2010.

[97] G. Li, M. B. Agir, K. Kontis, T. Ukai, and S. Rengarajan, "Image processing techniques for shock wave detection and tracking in high speed schlieren and shadowgraph systems," in *Journal of Physics: Conference Series*, vol. 1215, p. 012021, IOP Publishing, 2019.

[98] S. Paris, "A gentle introduction to bilateral filtering and its applications," in *ACM SIGGRAPH 2007 courses*, pp. 3–es, 2007.

[99] R. Szeliski, *Computer vision: algorithms and applications*. Springer Nature, 2022.

[100] K. Kontis, R. An, H. Zare-Behtash, and D. Kounadis, "Head-on collision of shock wave induced vortices with solid and perforated walls," *Physics of Fluids*, vol. 20(1), p. 016104, 2008.

[101] J. Maxwell, "On stresses in Rarefied Gases Arising from Inequalities of Temperature," vol. 170, pp. 231–256, 1879.

[102] M. v. Smoluchowski, "Ueber w¨armeleitung in verd¨unnten Gasen," vol. 64, pp. 101–130, 1898.

[103] V. Casseau, *An open-source CFD solver for planetary entry*. PhD thesis, University of Strathclyde, 2017.

[104] G. A. Bird and J. Brady, *Molecular gas dynamics and the direct simulation of gas flows*, vol. 42. Clarendon press Oxford, 1994.

[105] H. M. Mott-Smith, "The solution of the boltzmann equation for a shock wave," *Physical Review*, vol. 82(6), p. 885, 1951.

[106] H. Struchtrup and M. Torrilhon, "Regularization of Grad's 13 moment equations: Derivation and linear analysis," *Physics of Fluids*, vol. 15(9), pp. 2668–2680, 2003.

[107] X.-j. Gu and D. R. Emerson, "A high-order moment approach for capturing non-equilibrium phenomena in the transition regime," *Journal of fluid mechanics*, vol. 636, pp. 177–216, 2009.

[108] P. Bhathnagor, E. Gross, and M. Krook, "A model for collision processes in gases," *Physical Review*, vol. 94(3), p. 511, 1954.

[109] F. Pellicani, "Atmosphere Re-Entry Simulation Using Direct Simulation Monte Carlo (DSMC) Method," 2016.

[110] H. Mao, D. Fu, and X. Bao, "Engineering method of predicting rocket exhaust plumes at middle and low altitudes," *Journal of Spacecraft and Rockets*, vol. 54, no. 5, pp. 1170–1177, 2017.

[111] M. D. Weinberg, "Direct Simulation Monte Carlo for astrophysical flows–I. Motivation and methodology," *Monthly Notices of the Royal Astronomical Society*, vol. 438, no. 4, pp. 2995–3006, 2014.

[112] C. White, M. K. Borg, T. J. Scanlon, S. M. Longshaw, B. John, D. Emerson, and J. M. Reese, "dsmcFoam+: An OpenFOAM based direct simulation Monte Carlo solver," *Computer Physics Communications*, vol. 224, pp. 22–43, 2018.

[113] C. Shu, X. Mao, and Y. Chew, "Particle number per cell and scaling factor effect on accuracy of DSMC simulation of micro flows," *International Journal of Numerical Methods for Heat & Fluid Flow*, 2005.

[114] S. Stefanov, "On DSMC Calculations of Rarefied Gas Flows with Small Number of Particles in Cells," *SIAM J. Scientific Computing*, vol. 33, pp. 677–702, 01 2011.

[115] E. Roohi, S. Stefanov, A. Shoja-Sani, and H. Ejraei, "A generalized form of the Bernoulli Trial collision scheme in DSMC: Derivation and evaluation," *Journal of Computational Physics*, vol. 354, pp. 476–492, 2018.

[116] N. G. Hadjiconstantinou, A. L. Garcia, M. Z. Bazant, and G. He, "Statistical error in particle simulations of hydrodynamic phenomena," *Journal of computational physics*, vol. 187, no. 1, pp. 274–297, 2003.

[117] S. Tian, Y. Gao, X. Dong, and C. Liu, "Definitions of vortex vector and vortex," *Journal of Fluid Mechanics*, vol. 849, pp. 312–339, 2018.

[118] C. Liu, Y. Wang, Y. Yang, and Z. Duan, "New omega vortex identification method," *Science China Physics, Mechanics & Astronomy*, vol. 59(8), pp. 1–9, 2016.

[119] Y. Gao and C. Liu, "Rortex and comparison with eigenvalue-based vortex identification criteria," *Physics of Fluids*, vol. 30, no. 8, p. 085107, 2018.

[120] V. Kolář, J. Šístek, F. Cirak, and P. Moses, "Average corotation of line segments near a point and vortex identification," *AIAA journal*, vol. 51(11), pp. 2678–2694, 2013.

[121] C. Liu, Y. Gao, S. Tian, and X. Dong, "Rortex—A new vortex vector definition and vorticity tensor and vector decompositions," *Physics of Fluids*, vol. 30, no. 3, p. 035103, 2018.

[122] M. Darbandi and E. Roohi, "A hybrid DSMC/Navier–Stokes frame to solve mixed rarefied/nonrarefied hypersonic flows over nano-plate and micro-cylinder," *International Journal for Numerical Methods in Fluids*, vol. 72, no. 9, pp. 937–966, 2013.

[123] T. E. Schwartzentruber and I. D. Boyd, "A hybrid particle-continuum method applied to shock waves," *Journal of Computational Physics*, vol. 215(2), pp. 402–416, 2006.

[124] D. G. Akhmetov, *Vortex rings*. Springer Science & Business Media, 2009.

[125] E. K. Ahangar, M. B. Ayani, and J. A. Esfahani, "Simulation of rarefied gas flow in a microchannel with backward facing step by two relaxation times using Lattice Boltzmann method–Slip and transient flow regimes," *International Journal of Mechanical Sciences*, vol. 157, pp. 802–815, 2019.

[126] A. Gavasane, A. Agrawal, and U. Bhandarkar, "Study of rarefied gas flows in backward facing micro-step using Direct Simulation Monte Carlo," *Vacuum*, vol. 155, pp. 249–259, 2018.

[127] Z. Cao, M. Agir, C. White, and K. Kontis, "An open source code for two-phase rarefied flows: rarefiedmultiphasefoam," *Computer Physics Communications*, vol. 276, p. 108339, 2022.

[128] W. K. H. Ariyaratne, E. V. P. J. Manjula, C. Ratnayake, and M. C. Melaaen, "CFD approaches for modeling gas-solids multiphase flows–A review," in *Proceedings of The 9th EUROSIM Congress on Modelling and Simulation, EUROSIM 2016, The 57th SIMS Conference on Simulation and Modelling SIMS 2016*, no. 142, pp. 680–686, Linköping University Electronic Press, 2018.

[129] Y. Zhang, X.-B. Lu, and X.-H. Zhang, "An optimized Eulerian–Lagrangian method for two-phase flow with coarse particles: Implementation in open-source field operation and manipulation, verification, and validation," *Physics of Fluids*, vol. 33(11), p. 113307, 2021.

[130] M. Gale, K. Buettner, R. Mehta, P. A. Liever, and J. Curtis, "Gas-granular flow solver for plume surface interaction and cratering simulations," in *23rd AIAA Computational Fluid Dynamics Conference*, p. 4503, 2017.

[131] G. Shallcross, *Modeling Particle-Laden Compressible Flows with an Application to Plume-Surface Interactions*. PhD thesis, 2021.

[132] P. A. Liever, M. P. Gale, R. S. Mehta, and J. S. West, "Gas-Granular simulation framework for spacecraft landing plume-surface interaction and debris transport analysis," in *Earth and Space 2018: Engineering for Extreme Environments*, pp. 39–48, American Society of Civil Engineers Reston, VA, 2018.

[133] S. Gimelshein, A. Alexeenko, D. Wadsworth, and N. Gimelshein, "The influence of particulates on thruster plume/shock layer interaction at high altitudes," in *43rd AIAA Aerospace Sciences Meeting and Exhibit*, p. 766, 2004.

[134] X. HE, B. HE, and G. CAI, "Two-phase Coupled Model for DSMC Plume Simulation," *Journal of Propulsion Technology*, vol. 2, 2011.

[135] A. B. Morris, D. B. Goldstein, P. L. Varghese, and L. M. Trafton, "Lunar Dust Transport Resulting from Single-and Four-Engine Plume Impingement," *AIAA Journal*, vol. 54, no. 4, pp. 1339–1349, 2016.

[136] D. Liu, S. Yang, Z. Wang, H. Liu, C. Cai, and D. Wu, "On rocket plume, lunar crater and lunar dust interactions," in *48th AIAA Aerospace Sciences Meeting Including the New Horizons Forum and Aerospace Exposition*, p. 1161, 2010.

[137] Y. Li, D. Ren, Z. Bo, W. Huang, Q. Ye, and Y. Cui, "Gas-particle two-way coupled method for simulating the interaction between a rocket plume and lunar dust," *Acta Astronautica*, vol. 157, pp. 123–133, 2019.

[138] J. M. Burt and I. D. Boyd, "Evaluation of a Monte Carlo model for two phase rarefied flows," in *36 th AIAA Thermophysics Conference*, 2003.

[139] G. A. Bird, *The DSMC method*. CreateSpace Independent Publishing Platform, 2013.

[140] J. Burt and I. Boyd, "Monte Carlo Simulation of a Rarefied Multiphase Plume Flow," in *AIAA Aerospace Sciences Meeting & Exhibit*, 2005.

[141] S. Hunter, S. Cherry, and J. Kliegel, "Gas-particle nozzle flows with reaction and particle size change," *AIAA Journal*, 2006.

[142] Y. Plastinin, N. Anfimov, G. Baula, G. Karabadzhak, B. Khmelinin, and A. Rodionov, "Modeling of aluminum oxide particle radiation in a solid propellant motor exhaust," in *31st Thermophysics Conference*, p. 1879, 1996.

[143] D. P. Schmidt and C. Rutland, "A new droplet collision algorithm," *Journal of Computational Physics*, vol. 164(1), pp. 62–80, 2000.

[144] P. O'Rourke, "Collective drop effects on vaporizing sprays," *Princeton University, United States (Ph. D. Thesis)*, 1981.

[145] M. Mezhericher, A. Levy, and I. Borde, "Probabilistic hard-sphere model of binary particle–particle interactions in multiphase flow of spray dryers," *International Journal of Multiphase Flow*, vol. 43, pp. 22–38, 2012.

[146] H. Zhang, Q. Liu, B. Qin, and H. Bo, "Simulating particle collision process based on Monte Carlo method," *Journal of Nuclear Science and Technology*, vol. 52(11), pp. 1393–1401, 2015.

[147] C. T. Crowe, J. D. Schwarzkopf, M. Sommerfeld, and Y. Tsuji, *Multiphase flows with droplets and particles*. CRC press, 2011.

[148] G. Zheng, Y. Cui, W. Yu, D. Ren, Q. Ye, and D. Geng, "Method on calculation of lunar soil particles trajectories considering collision effect," *Chin. J. Space Sci.*, vol. 35, pp. 486–494, 2015.

[149] M. J. Andrews and P. J. O'Rourke, "The multiphase particle-in-cell (MP-PIC) method for dense particulate flows," *International Journal of Multiphase Flow*, vol. 22(2), pp. 379–402, 1996.

[150] D. M. Snider, "An incompressible three-dimensional multiphase particle-in-cell model for dense particle flows," *Journal of computational physics*, vol. 170(2), pp. 523–549, 2001.

[151] P. J. O'Rourke and D. M. Snider, "An improved collision damping time for MP-PIC calculations of dense particle flows with applications to polydisperse sedimenting beds and colliding particle jets," *Chemical Engineering Science*, vol. 65(22), pp. 6014–6028, 2010.

[152] S. Harris and D. Crighton, "Solitons, solitary waves, and voidage disturbances in gas-fluidized beds," *Journal of Fluid Mechanics*, vol. 266, pp. 243–276, 1994.

[153] C. Lun, S. B. Savage, D. Jeffrey, and N. Chepurniy, "Kinetic theories for granular flow: inelastic particles in Couette flow and slightly inelastic particles in a general flowfield," *Journal of fluid mechanics*, vol. 140, pp. 223–256, 1984.

[154] P. J. O'Rourke, P. P. Zhao, and D. Snider, "A model for collisional exchange in gas/liquid/solid fluidized beds," *Chemical Engineering Science*, vol. 64(8), pp. 1784–1797, 2009.

[155] P. J. O'Rourke and D. M. Snider, "Inclusion of collisional return-to-isotropy in the MP-PIC method," *Chemical engineering science*, vol. 80, pp. 39–54, 2012.

[156] P. A. Li Z., Li Z. and W. J., "A numerical method for simulating rarefied two phase flow (in chinese)," *ACTA AERODYNAM ICA SINICA*, vol. 33, no. 2, pp. 266–271, 2015.

[157] Y. Plastinin, H. Sipatchev, G. Karabadzhak, B. Khmelinin, E. Szhenov, A. Khlebnikov, and Y. Shishkin, "Experimental investigation of alumina particles' phase transitions and radiation," in *36th AIAA Aerospace Sciences Meeting and Exhibit*, p. 862, 1998.

[158] W. K. Kim, J. H. Shim, and M. Kaviany, "Thermophysical properties of liquid UO2, ZrO2 and corium by molecular dynamics and predictive models, journal = Journal of Nuclear Materials," vol. 491, pp. 126–137, 2017.

[159] D. M. Snider, P. J. ORourke, and M. J. Andrews, "An incompressible two-dimensional multiphase particle-in-cell model for dense particle flows," tech. rep., Los Alamos National Lab., NM (United States), 1997.

[160] F. Auzerais, R. Jackson, and W. Russel, "The resolution of shocks and the effects of compressible sediments in transient settling," *Journal of Fluid Mechanics*, vol. 195, pp. 437–462, 1988.

[161] Y. Cui, J. Wang, and Y. Xie, *Interactions between lunar particles and engine plumes (in Chinese)*. Beijing Science Press, 2021.

[162] P. T. Metzger and B. T. Vu, "Rocket Exhaust Cratering: Lessons Learned from Viking and Apollo," tech. rep., 2004.

[163] J. McDivitt *et al.*, "Apollo 15 Mission Report, MSC-05161," *NASA Johnson Space Center, Houston, TX*, 1971.

[164] J. Capecelatro, "Modeling high-speed gas-particle flows relevant to spacecraft landings: A review and perspectives," *arXiv preprint arXiv:2109.02523*, 2021.

[165] R. Hutton, H. Moore, R. Scott, R. Shorthill, and C. Spitzer, "Surface erosion caused on Mars from Viking descent engine plume," *The moon and the planets*, vol. 23(3), pp. 293–305, 1980.

[166] J. Vizcaino and M. Mehta, "Quantification of plume-soil interaction and excavation due to the Mars Science Laboratory Sky Crane Descent Phase," in *8th Symposium on Space Resource Utilization*, p. 1649, 2015.

[167] A. Sengupta, J. Kulleck, S. Sell, J. Van Norman, M. Mehta, and M. Pokora, "Mars lander engine plume impingement environment of the Mars Science Laboratory," in *2009 IEEE Aerospace conference*, pp. 1–10, IEEE, 2009.

[168] R. F. Scott and H.-Y. KO, "Transient rocket-engine gas flow in soil.," *AIAA Journal*, vol. 6, no. 2, pp. 258–264, 1968.

[169] S. D. Guleria and D. V. Patil, "Experimental investigations of crater formation on granular bed subjected to an air-jet impingement," *Physics of Fluids*, vol. 32(5), p. 053309, 2020.

[170] A. B. Morris *et al.*, *Simulation of rocket plume impingement and dust dispersal on the lunar surface*. PhD thesis, The University of Texas at Austin, 2012.

[171] C. D. Donaldson, R. S. Snedeker, and D. P. Margolis, "A study of free jet impingement. Part 2. Free jet turbulent structure and impingement heat transfer," *Journal of Fluid Mechanics*, vol. 45(3), pp. 477–512, 1971.

[172] L. Roberts, "The interaction of a rocket exhaust with the lunar surface(Rocket exhaust jet interaction with lunar surface dust layer)," *Agard the Fluid Dyn. Aspects of space flight*, vol. 2, 1966.

[173] M. Mehta, A. Sengupta, N. O. Renno, J. W. V. Norman, P. G. Huseman, D. S. Gulick, and M. Pokora, "Thruster plume surface interactions: Applications for spacecraft landings on planetary bodies," *AIAA journal*, vol. 51(12), pp. 2800–2818, 2013.

[174] D. Wadsworth and D. Erwin, "One-dimensional hybrid continuum/particle simulation approach for rarefied hypersonic flows," in *5th Joint Thermophysics and Heat Transfer Conference*, p. 1690, 1990.

[175] T. E. Schwartzentruber, L. C. Scalabrin, and I. D. Boyd, "A modular particle–continuum numerical method for hypersonic non-equilibrium gas flows," *Journal of Computational Physics*, vol. 225(1), pp. 1159–1174, 2007.

[176] T. E. Schwartzentruber, L. C. Scalabrin, and I. D. Boyd, "Hybrid particle-continuum simulations of hypersonic flow over a hollow-cylinder-flare geometry," *AIAA journal*, vol. 46(8), pp. 2086–2095, 2008.

[177] T. E. Schwartzentruber, L. C. Scalabrin, and I. D. Boyd, "Hybrid particle-continuum simulations of nonequilibrium hypersonic blunt-body flowfields," *Journal of Thermophysics and Heat Transfer*, vol. 22(1), pp. 29–37, 2008.

[178] Z. Yang, Z.-Y. Tang, G.-B. Cai, and B.-J. He, "Development of a coupled NS-DSMC method for the simulation of plume impingement effects of space thrusters," *Thermophysics and Aeromechanics*, vol. 24(6), pp. 835–847, 2017.

[179] J. Marichalar, A. Prisbell, F. Lumpkin, and G. LeBeau, "Study of plume impingement effects in the lunar lander environment," in *AIP Conference Proceedings*, vol. 1333(1), pp. 589–594, American Institute of Physics, 2011.

[180] A. Tosh, P. A. Liever, R. R. Arslanbekov, and S. D. Habchi, "Numerical analysis of spacecraft rocket plume impingement under lunar environment," *Journal of Spacecraft and Rockets*, vol. 48(1), pp. 93–102, 2011.

[181] Q. Ye, Y. Shu, X. Zhang, Z. Xing, L. Wang, and B. He, "Research on simulation and test of vacuum plume diversion technique based on vehicles taking off outside the earth (in Chinese)," *Journal of Aerospace power*, 2020.

[182] R. B. Haehnel, W. B. Dade, and B. Cushman-Roisin, "Crater evolution due to a jet impinging on a bed of loose particles," in *Earth & Space 2008: Engineering, Science, Construction, and Operations in Challenging Environments*, pp. 1–10, 2008.

[183] P. T. Metzger, "Rocket exhaust blowing soil in near vacuum conditions is faster than predicted by continuum scaling laws," in *Earth and Space 2016: Engineering for Extreme Environments*, pp. 58–66, American Society of Civil Engineers Reston, VA, 2016.

[184] A. M. Korzun, C. J. Eberhart, J. West, P. Liever, A. Weaver, J. Mantovani, A. Langton, B. Kemmerer, and A. Atkins, "Design of a Subscale, Inert Gas Test for Plume-Surface Interactions in a Reduced Pressure Environment," in *AIAA Scitech 2022 Forum*, p. 1808, 2022.

[185] M. Kuhns, P. Metzger, A. Dove, J. Byron, S. Lamb, T. Roberson, L. Lohman, W. Chambers, G. Rixon, R. Kuhns, *et al.*, "Deep Regolith Cratering and Plume Effects Modeling for Lunar Landing Sites," in *Earth and Space 2021*, pp. 62–78, 2021.

[186] L. Roberts, "The action of a hypersonic jet on a dusty surface," in *Proceedings of 31st Annual Meeting of the Institute of Aerospace Science*, pp. 63–50, 1963.

[187] N. S. Land and L. V. Clark, *Experimental investigation of jet impingement on surfaces of fine particles in a vacuum environment*. National Aeronautics and Space Administration, 1965.

[188] P. T. Metzger, J. Smith, and J. E. Lane, "Phenomenology of soil erosion due to rocket exhaust on the Moon and the Mauna Kea lunar test site," *Journal of Geophysical Research: Planets*, vol. 116, no. E6, 2011.

[189] D. Geng, D. Ren, Q. Ye, Y. Ma, G. Zheng, and Y. Cui, "A New Computational Method for the Interaction Between Plume Field and Soil Particles," *Journal Of Astronautics*, vol. 35, pp. 884–892, 2014.

[190] A. Morris, D. Goldstein, P. Varghese, and L. Trafton, "Plume impingement on a dusty lunar surface," in *AIP Conference Proceedings*, vol. 1333(1), pp. 1187–1192, American Institute of Physics, 2011.

[191] P. T. Metzger, J. E. Lane, and C. D. Immer, "Modification of Roberts' Theory for Rocket Exhaust Plumes Eroding Lunar Soil," in *Earth & Space 2008: Engineering, Science, Construction, and Operations in Challenging Environments*, pp. 1–8, 2008.

[192] J. E. Lane and P. T. Metzger, "Estimation of Apollo lunar dust transport using optical extinction measurements," *Acta Geophysica*, vol. 63, no. 2, pp. 568–599, 2015.

[193] J. You, X. Zhang, H. Zhang, C. Li, Y. Xu, Q. Yan, H. Yu, J. Liu, Y. Li, Y. Wang, *et al.*, "Analysis of plume–lunar surface interaction and soil erosion during the Chang'E-4 landing process," *Acta Astronautica*, vol. 185, pp. 337–351, 2021.

[194] E. Willert, *Stoßprobleme in Physik, Technik und Medizin: Grundlagen und Anwendungen*. Springer Nature, 2020.

[195] W. D. Carrier III, G. R. Olhoeft, and W. Mendell, "Physical properties of the lunar surface," *Lunar sourcebook*, pp. 475–594, 1991.

[196] S. Torquato, T. M. Truskett, and P. G. Debenedetti, "Is random close packing of spheres well defined?," *Physical review letters*, vol. 84(10), p. 2064, 2000.

[197] J. F. Kok, E. J. Parteli, T. I. Michaels, and D. B. Karam, "The physics of wind-blown sand and dust," *Reports on progress in Physics*, vol. 75(10), p. 106901, 2012.

[198] U. Caliskan and S. Miskovic, "A chimera approach for mp-pic simulations of dense particulate flows using large parcel size relative to the computational cell size," *Chemical Engineering Journal Advances*, vol. 5, p. 100054, 2021.

[199] E. Loth, J. Tyler Daspit, M. Jeong, T. Nagata, and T. Nonomura, "Supersonic and hypersonic drag coefficients for a sphere," *AIAA journal*, vol. 59(8), pp. 3261–3274, 2021.

[200] A. Morris, D. Goldstein, P. Varghese, and L. Trafton, "Modeling the interaction between a rocket plume, scoured regolith, and a plume deflection fence," *Earth and space*, vol. 2012, pp. 189–198, 2012.